Exploiting Passive Microwave Observations for Sea Ice Emissivity and Cloud Characterization in the Arctic

Inaugural-Dissertation

zur

Erlangung des Doktorgrades

der Mathematisch-Naturwissenschaftlichen Fakultät

der Universität zu Köln

vorgelegt von

Nils Risse

angenommen im Jahr 2025

Abstract

Passive microwave observations from polar-orbiting satellites contain information on both the sea ice and clouds, which are essential components of the Arctic climate system. Retrieving this information requires physical or empirical simulations of the surface radiative transfer. Intricate processes of the Arctic climate system govern the spatiotemporal variability of sea ice optical properties and limit climate record capabilities from historic observations and the exploitation of recently launched submillimeter missions. This thesis exploits multi-platform sub-orbital passive microwave observations to improve the understanding of the spatiotemporal variability of the sea ice emissivity at millimeter and submillimeter waves and its representation in physical radiative transfer models, and to assess cloud liquid water path retrieval accuracy over sea ice.

Sea ice and its snow cover are spatially heterogeneous due to the ice deformation, drift, and its formation history. Hence, the sea ice emissivity is expected to vary at small spatial scales that are not resolved by coarse satellite footprints. Airborne sea ice emissivity observations obtained from field campaigns between 89 and 340 GHz allow for a quantification of this small-scale spatial variability at hectometer-scale resolution relevant for new submillimeter satellite missions. A clustering technique is used to identify distinct sea ice emissivity spectra. The four identified spectra are related to specific sea ice types using visual camera imagery with similar sea ice and snow properties. Each cluster exhibits a low spectral emissivity variability from 183 to 340 GHz. The spatial variability strongly depends on the footprint size and reduces by 50% from the hectometer resolution to the typical size of satellite footprints at 340 GHz. Collocations with satellite observations show low spectral gradients from 89 to 340 GHz at the scale of satellite footprints as small-scale features average out.

The sea ice microwave emissivity varies temporally due to changes in its macro- and microphysical properties, especially around surface freeze onset at the end of summer. Ship-based observations over two months from two scanning microwave radiometers between 22 and 243 GHz capture this temporal surface emissivity evolution at the meter scale. During new ice formation, the surface emissivity transitions from the open water signature to nilas. This transition is resolved continuously and found to be highly correlated across all frequencies. Subsequent snowpack formation and related volume scattering by snow grains reduce the emissivity at 183 and 243 GHz from 0.95 to about 0.6, while almost no change occurs at lower frequencies (22 to 51 GHz) where scattering is lower. A novel regression model is applied, which predicts the emissivity at 243 GHz from grayscale camera images. This method highlights the role of snow presence

for the emissivity reduction. Radiative transfer model simulations of bare and snow-covered new ice were found to statistically match the observed frequency, angular, and polarization-dependent emissivity signature observed along the ship trajectory.

Cloud liquid water path (CLWP) retrievals from passive microwave observations over Arctic sea ice require a separation of the sea ice and atmospheric radiative contributions. An optimal estimation retrieval that inverts a coupled physical sea ice–atmosphere radiative transfer model is applied to airborne passive microwave radiometer data from 22 to 183 GHz. The retrieval is evaluated against collocated airborne reference observations, such as cloud liquid layers detection from lidar. The cloud liquid water path detectability, defined as the 95th percentile of falsely-detected CLWP under clear-sky conditions, is about $50\,\mathrm{g\,m^{-2}}$ in the Central Arctic and increases up to $350\,\mathrm{g\,m^{-2}}$ toward the marginal ice zone. The relative retrieval accuracy improves with increasing CLWP to below 50 % for CLWP above $100\,\mathrm{g\,m^{-2}}$. The main challenge for the CLWP retrieval is the similarity between CLWP emission and surface signals due to scattering in the upper snowpack and emission by nilas in leads. Moreover, atmospheric events, such as melt-freeze cycles during warm air intrusions, cause retrieval uncertainties by changing the optical properties of the snowpack.

Zusammenfassung

Passive Mikrowellenbeobachtungen von polarumlaufenden Satelliten enthalten Informationen sowohl über das Meereis als auch über Wolken, die wesentliche Bestandteile des arktischen Klimasystems sind. Die Gewinnung dieser Informationen erfordert physikalische oder empirische Simulationen des Strahlungstransfers an der Oberfläche. Komplexe Prozesse des arktischen Klimasystems bestimmen die räumlich-zeitliche Variabilität der optischen Eigenschaften des Meereises und schränken die Möglichkeiten der Klimaaufzeichnung aus historischen Beobachtungen und der Nutzung kürzlich gestarteter Submillimeter-Missionen ein. Diese Arbeit nutzt suborbitale passive Mikrowellenbeobachtungen von mehreren Plattformen, um das Verständnis der räumlich-zeitlichen Variabilität der Emissivität von Meereis bei Millimeter- und Submillimeterwellen und deren Darstellung in physikalischen Strahlungstransfermodellen zu verbessern und die Genauigkeit der Ermittlung des Flüssigwasserpfads von Wolken über Meereis zu bewerten.

Meereis und seine Schneebedeckung sind aufgrund der Eisverformung, der Drift und ihrer Entstehungsgeschichte räumlich heterogen. Daher ist zu erwarten, dass die Emissivität des Meereises auf kleinen räumlichen Skalen variiert, die von groben Satelliten-Footprints nicht aufgelöst werden. Luftgestützte Beobachtungen der Emissivität von Meereis, die im Rahmen von Feldkampagnen zwischen 89 und 340 GHz gewonnen wurden, ermöglichen eine Quantifizierung dieser kleinräumigen räumlichen Variabilität mit einer Auflösung im Hektometerbereich, die für neue Submillimeter-Satellitenmissionen relevant ist. Zur Identifizierung unterschiedlicher Emissivitätsspektren des Meereises wird eine Klassifizierungsmethode verwendet. Die vier identifizierten Spektren werden anhand von Bildern einer visuellen Kamera mit ähnlichen Meereis- und Schneeeigenschaften bestimmten Meereistypen zugeordnet. Jeder Cluster weist eine geringe spektrale Emissivitätsvariabilität von 183 bis 340 GHz auf. Die räumliche Variabilität hängt stark von der Auflösung ab und verringert sich um 50 % von der Hektometerauflösung auf die typische Größe von Satellitenmessungen bei 340 GHz. Kollokationen mit Satellitenbeobachtungen zeigen geringe spektrale Gradienten von 89 bis 340 GHz auf der Skala der Satellitenmessungen, da kleinräumige Merkmale sich ausgleichen.

Die Mikrowellenemissivität des Meereises variiert zeitlich aufgrund von Veränderungen seiner makro- und mikrophysikalischen Eigenschaften, insbesondere zu Beginn der Oberflächenvereisung am Ende des Sommers. Schiffsgestützte Beobachtungen über zwei Monate hinweg mit zwei abtastenden Mikrowellenradiometern zwischen 22 und 243 GHz erfassen diese zeitliche Entwicklung der Oberflächen-Emissivität im Meterbereich. Während der Neubildungsphase des

Eises wandelt sich die Oberflächen-Emissivität von der Signatur offenen Wassers zu Nilas. Dieser Übergang wird kontinuierlich aufgelöst und weist eine hohe Korrelation über alle Frequenzen hinweg auf. Die anschließende Schneedeckenbildung und die damit verbundene Volumenstreuung durch Schneekörner reduzieren die Emissivität bei 183 und 243 GHz von 0,95 auf etwa 0,6, während bei niedrigeren Frequenzen (22 bis 51 GHz), bei denen die Streuung geringer ist, fast keine Veränderung auftritt. Es wird ein neuartiges Regressionsmodell angewendet, das die Emissivität bei 243 GHz aus Graustufen-Kamerabildern vorhersagt. Diese Methode unterstreicht die Rolle des Schneevorkommens für die Verringerung der Emissivität. Simulationen mit Strahlungstransfermodellen von blankem und schneebedecktem neuem Eis stimmten statistisch mit der entlang der Schiffsroute beobachteten frequenz-, winkel- und polarisationsabhängigen Emissivitätssignatur überein.

Die Ermittlung des Wolkenflüssigwasserpfades (cloud liquid water path; CLWP) aus passiven Mikrowellenbeobachtungen über dem arktischen Meereis erfordert eine Trennung der Strahlungsbeiträge des Meereises und der Atmosphäre. Ein Optimal Estimation-Retrieval, das ein gekoppeltes physikalisches Meereis-Atmosphäre-Strahlungstransfermodell invertiert, wird auf Daten eines luftgestützten passiven Mikrowellenradiometers von 22 bis 183 GHz angewendet. Das Retrieval wird anhand von kollokierten luftgestützten Referenzbeobachtungen, wie z. B. der Erkennung von Wolkenflüssigkeitsschichten mittels Lidar, bewertet. Die Nachweisbarkeit des flüssigen Wasserpfads in Wolken, definiert als das 95. Perzentil des falsch-detektierten CLWP unter wolkenfreien Bedingungen, beträgt in der zentralen Arktis etwa $50\,\mathrm{g\,m^{-2}}$ und steigt in Richtung der Randzone des Meereises auf bis zu $350\,\mathrm{g\,m^{-2}}$ an. Die relative Genauigkeit des Retrievals verbessert sich mit zunehmendem CLWP auf unter 50 % für CLWP über $100\,\mathrm{g\,m^{-2}}$. Die größte Herausforderung bei der CLWP-Ermittlung ist die Ähnlichkeit zwischen CLWP-Emission und Oberflächensignalen aufgrund von Streuung in der oberen Schneedecke und Emissionen durch Nilas in Rinnen. Darüber hinaus verursachen atmosphärische Ereignisse wie Schmelz-Gefrier-Zyklen während Warmlufteinbrüchen Unsicherheiten bei dem Retrieval, da sie die optischen Eigenschaften der Schneedecke verändern.

Contents

Chapter 1

Introduction

1.1 Motivation

Remote sensing instruments onboard satellite platforms capture information about the Earth system encoded in electromagnetic radiation. This signal can be converted into physical properties of the Earth's atmosphere, ocean, land, and cryosphere using geophysical retrieval methods. While active remote sensing instruments transmit radiation and measure the signal scattered back to the sensor, passive instruments receive radiation emitted from the sun and scattered to the sensor or emitted and scattered by the Earth system. The expansion of global observing system capabilities and improvements in assimilating observations into numerical weather prediction models at global scales significantly enhanced the weather prediction accuracy over the past decades (Bauer et al., 2015). Moreover, the continuous multi-decade time series of satellite remote sensing data are the basis for understanding processes and changes in the Earth system, especially in regions sparsely covered with conventional ground-based measurement networks. In the Arctic, polar-orbiting satellites provide the only long-term data source with complete spatial coverage. This global view from satellites is complemented by targeted field campaigns and long-term ground-based measurement sites that resolve processes at regional and local scales.

Observations in the Arctic record a near-surface air temperature increase in response to the anthropogenic emission of greenhouse gases, which increase the atmospheric absorption and re-emission of thermal radiation emitted at the surface (Serreze and Francis, 2006). This near-surface air temperature increase exceeds global warming by a factor of 2–4, known as Arctic amplification (Rantanen et al., 2022; Chylek et al., 2022). Arctic amplification results from various dominant positive feedback mechanisms unique to the Arctic climate system that enhance the external greenhouse gas forcing (Wendisch et al., 2023) modulated by internal cli-

mate variability (Zhou et al., 2024; Sweeney et al., 2023). A key positive feedback is the surface albedo feedback, which describes the amplified warming in response to increased absorption of solar radiation when high-albedo surfaces, such as sea ice and snow cover, melt. The observed extension of the melt season duration (Stroeve et al., 2014) and summer sea ice area decline (Fig. 1.1; Stroeve et al., 2007) contribute to the surface albedo feedback. The observed sea ice area decline is related to greenhouse gas emissions (Notz and Stroeve, 2016) and projected to continue in the future (Wang and Overland, 2012; Notz and SIMIP Community, 2020). A reduction and additional thinning of sea ice cover (Soriot et al., 2024) also increases the heat flux from the upper ocean to the atmosphere (Screen and Simmonds, 2010). This additional warming near the surface often remains within the surface inversion in the Arctic (lapse rate feedback; Linke et al., 2023). The near-surface temperature increase exhibits seasonal (Serreze et al., 2009; Maturilli et al., 2015) and regional variations owing to the complexity of coupled processes in the Arctic climate system (sea ice, snow, clouds, and water vapor), and atmosphere and ocean circulation (Screen and Simmonds, 2010; Screen et al., 2012; Pithan et al., 2014). While climate projections of Arctic amplification magnitude are uncertain due to the various feedback processes involved, there is high confidence that Arctic amplification will continue over the 21st century (IPCC, 2021, Chapter 4).

Clouds play a delicate role in the Arctic climate system through precipitation formation as part of the water cycle (Bengtsson, 2010) and the surface energy budget (Bennartz et al., 2013). While snow accumulation on land and sea ice changes the surface albedo and heat flux, liquid precipitation modifies snowpack properties with implications for wildlife (Bartsch et al., 2023). The net radiative effect of clouds largely depends on microphysical (particle phase, shape, size, and number concentration) and macrophysical properties (cloud height and thickness). Clouds cool the surface by reflecting incoming shortwave radiation, which modulates the strength of the surface albedo feedback in autumn (Kay et al., 2016), and warm the surface through the emission of longwave radiation (Shupe and Intrieri, 2004; Shupe et al., 2015; Kay and L'Ecuyer, 2013). This longwave emission mostly depends on the amount of cloud liquid water (Ebell et al., 2020; Nomokonova et al., 2020), which typically occurs together with frozen hydrometeors at temperatures as low as -40° C (Shupe et al., 2011). Such mixed-phase clouds frequently occur in the Arctic (Cesana et al., 2012; Nomokonova et al., 2019; Gierens et al., 2020) and can persist for several days through various local feedback mechanisms (Morrison et al., 2012). The distinct signature of mixed-phase clouds on the longwave radiative flux (Stramler et al., 2011) is challenging to represent in climate models (Pithan et al., 2014).

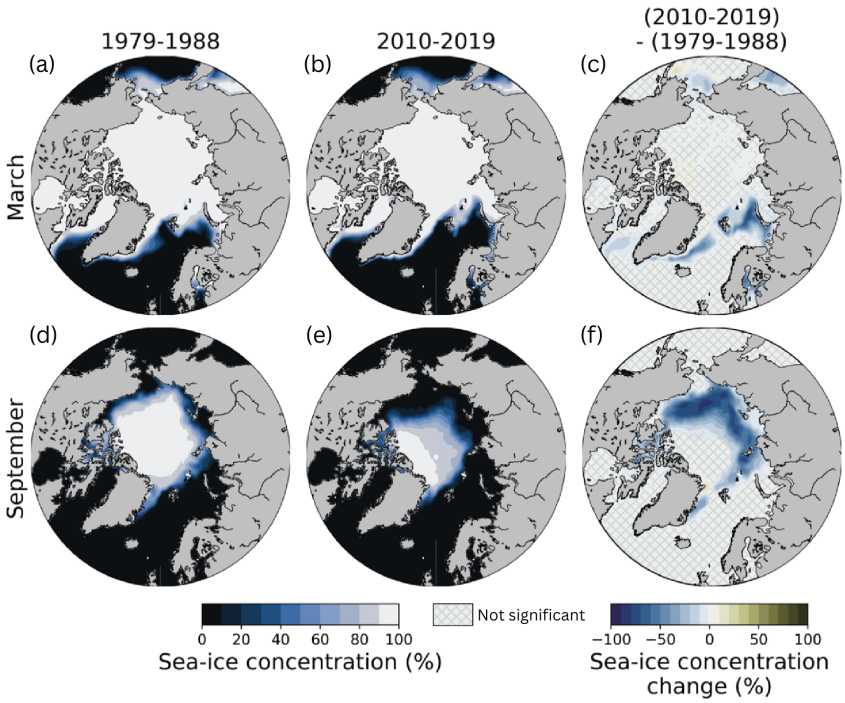

Figure 1.1: Arctic mean sea ice concentration based on satellite observations in (a, b) March and (d, e) September for the decades (a, d) 1979–1988 and (b, e) 2010–2019. The absolute change in sea ice concentration over the 31 years is shown for (c) March and (f) September, where negative values correspond to a reduction in sea ice concentration from 1979–1988 to 2010–2019. Sea ice concentrations are derived from passive microwave observations with the Bootstrap algorithm version 3 (Comiso, 2017). This figure is adapted from Fig. 9.13 in the Intergovernmental Panel on Climate Change (IPCC) Sixth Assessment Report (AR6) (IPCC, 2021).

Improved understanding of the surface and atmospheric properties in the Arctic can be achieved by a range of satellite instruments. Regarding the surface, passive microwave observations can monitor key geophysical sea ice parameters, such as sea ice cover and extent, sea ice type, sea ice surface temperature, thin sea ice thickness, sea ice drift, and snow depth on first-year ice (Lucas et al., 2023). These parameters are typically derived from observations at frequencies between 1.4 and 91 GHz, which we define as low frequencies ($\leq$ 91 GHz), while high frequencies ($>$ 91 GHz) are typically not incorporated in sea ice products. These passive microwave observations are complemented by spectrometers, infrared radiometers, scatterometers, imaging synthetic aperture radar (SAR), radar altimeters, and lidar altimeters (Lucas et al., 2023). Spectrometer and infrared radiometer observations of sea ice are limited to cloud-free conditions, and the passive observations in the visible spectrum are further unavailable during polar night. Microwave radiometers and radars partly close this gap by providing information also under cloudy conditions year-round.

Passive microwave radiometers also allow monitoring of key atmospheric parameters, including clouds and precipitation (e.g., Boukabara et al., 2011; Pfreundschuh et al., 2024). An important cloud property is the total amount of cloud liquid water in the atmospheric column, i.e, liquid water path. The liquid water path is operationally derived from passive microwave observations over open ocean (e.g., Elsaesser et al., 2017) using an accurately estimated background surface emissivity based on the sea state, i.e., sea surface temperature, sea surface salinity, and near-surface wind (Kilic et al., 2023). Over sea ice, no operational product is yet available from passive microwave observations. An accurate observation of liquid cloud occurrence is available from spaceborne lidars (Kay et al., 2016), but the observations are often attenuated by the topmost liquid layer. Visual and near infrared imagers are important in the summer and provide information on the effective radius, optical depth, and cloud liquid water path from solar reflectance measurements (Platnick et al., 2001). Over sea ice, these methods exploit the spectral dependence of absorption by liquid cloud droplets above 1000 nm (Platnick et al., 2001; Klingebiel et al., 2023), but need to account for surface albedo uncertainties related to variations in the snow grain size (Ehrlich et al., 2017).

Frozen hydrometeors can also be detected with passive microwave observations, but the mixed signal from the surface and hydrometeors makes the retrieval challenging (Milani and Kidd, 2023). In the Arctic, spaceborne Cloud Profiling Radars (CPRs) onboard CloudSat (Stephens et al., 2002, 2008) and EarthCARE (Illingworth et al., 2015; Wehr et al., 2023) provide high sensitivity to the vertical distribution of precipitation. Thus, they are used as ground truth for passive microwave retrieval evaluation and development (Camplani et al., 2024a), but often miss clouds and precipitation below about 1 km height due to surface clutter (Maahn et al., 2014; Schirmacher et al., 2023). Observations of cloud ice properties, i.e., ice water path, are poorly constrained by current observations and thus largely differ among climate models (Duncan and Eriksson, 2018; Eliasson et al., 2011). Novel submillimeter wave satellite missions will fill this gap (Buehler et al., 2012; Eriksson et al., 2020; May et al., 2024; Wang et al., 2017a) as demonstrated from airborne observations (Brath et al., 2018; Pfreundschuh et al., 2022). While the higher frequencies are less sensitive to the surface, surface contributions are relevant up to about 480 GHz (Wang et al., 2017b).

The satellite observations in Fig. 1.2 demonstrate the combined surface and atmosphere sensitivity of passive microwave observations in the Arctic at three frequencies on 10 April 2025. At 23 GHz, the sea ice is clearly separable from open water due to its high emissivity at this frequency. At 89 GHz, various structures can be detected over sea ice, such as leads and large-scale gradients, which indicate

the importance of spatial and temporal variations in sea ice and snow properties and sea ice rheology (Ólason et al., 2025), which are challenging to simulate. At 325.15 GHz, water vapor and scattering by ice clouds dominate the signal, but surface influence is clearly visible under very dry conditions, such as a lead north of the Arctic Archipelago and the ice edge in the Fram Strait. Thus, the Central Arctic between Svalbard and the Arctic Archipelago likely receives a significant surface contribution that needs to be considered for cloud ice and water vapor retrievals.

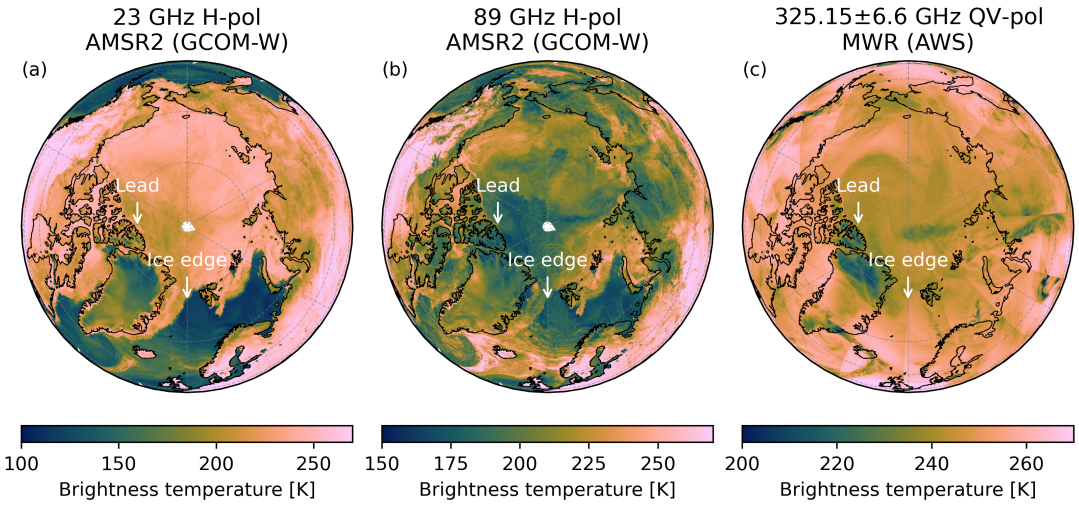

Figure 1.2: Passive microwave observations in the Arctic on 10 April 2025. (a) Advanced Microwave Scanning Radiometer - 2 (AMSR2) at 23 GHz at horizontal polarization (H-pol), (b) AMSR2 onboard the GCOM-W satellite at 89 GHz at H-pol, and (c) Microwave Radiometer (MWR) onboard the Arctic Weather Satellite (AWS) mission at 325.15±6.6 GHz at quasi-vertical polarization (QV-pol). Arrows indicate the presence of the ice and a lead visible at 325.15±6.6 GHz. Note that the incidence angle of AMSR2 is constant with 55°, while it varies with scan position between ±54° for the cross-track scanning MWR onboard AWS. GCOM-W AMSR2 data is obtained from Berg (2022b) and AWS MWR data is obtained from EUMETSAT (2025).

Lawrence et al. (2019) identified that passive microwave, conventional, and infrared observations have the largest impact on short-range tropospheric forecasts in the Arctic. Microwaves are most important in summer, while conventional observations are most important in winter. This difference is due to the challenge in simulating the microwave emission of sea ice and snow-covered land during winter from model equivalents. At the same time, this joint sensitivity of passive microwave observations to the Arctic atmosphere and surface provides an opportunity for coupled data assimilation (De Rosnay et al., 2022). Coupled data assimilation aims at improving the assimilation in one domain by using observations in another domain (Penny et al., 2017) and improves model forecast skill

(Browne et al., 2019). This is particularly important over sea ice, where sea ice and snow temperature are important input parameters of the observation operator that are needed to estimate atmospheric contributions to the measured signal. Improving the assimilation of satellite observations in the Arctic will also improve weather forecasts in mid-latitudes, depending on the large-scale atmospheric flow (Day et al., 2019). Additionally, refined assimilation of observations from current and future satellites will enhance global reanalysis products (ECMWF, 2025) and thus data-driven weather prediction models (e.g., Lam et al., 2023).

There are several methods to account for the surface emission over sea ice and snow for a given location and time. These are climatological emissivity atlases, empirical models, and physical radiative transfer models. Advances in each of the tools will improve physical retrievals, data assimilation, and radiative transfer modeling (Kubota et al., 2025; Sandells et al., 2025). Emissivity atlases are based on a satellite climatology and provide a globally mapped monthly mean and standard deviation of the emissivity (Munchak et al., 2020; Wang et al., 2017b). A widely used atlas is the Tool to Estimate Land Surface Emissivity from Microwave to Submillimeter Waves (TELSEM^2; Wang et al., 2017b), which parametrizes monthly statistics of the emissivity as a function of frequency, angle, and polarization. These atlases also provide a baseline for the incorporation of other tools that account for temporal variability. The operational Microwave Integrated Retrieval System (MiRS; Boukabara et al., 2011) by the National Oceanic and Atmospheric Administration (NOAA) simultaneously derives atmospheric and surface properties over all surfaces globally. The algorithm derives the surface emissivity dynamically from background values depending on the surface type using the Community Radiative Transfer Model (CRTM). The retrieved sea ice emissivity spectra are then converted into geophysical properties (sea ice concentration and age) using sea ice and snow radiative transfer models during post-processing (Boukabara et al., 2018; Kongoli et al., 2011).

The long time series of satellite microwave observations provides large amounts of data to train large-scale machine learning models that learn the spatial and temporal variability of the microwave signature (Geer, 2024a). When predicting the emissivity with a machine learning model, as in Geer (2024a), an atmospheric model is required to provide the atmospheric upwelling radiation and transmissivity for direct comparison with satellite radiances. The method by Geer (2024a) learns an underlying empirical state and an empirical emissivity model, which converts the state into an emissivity. The empirical sea ice state can be interpreted as a compression of sea ice properties that are relevant for the radiative signature, such as polarization effects and spectral gradients. This approach requires careful consideration of model errors that might potentially affect model weights during

training. An application of this framework in numerical weather prediction models enables improved timeliness for assimilating sea ice concentration fields (Geer, 2024b). Recently, De Gélis et al. (2025) developed an empirical emissivity model from 1.4–89 GHz based on a single-layer feedforward neural network for snow on land using reanalysis, satellite products, and emissivity climatology as predictors. Their model improved the estimates compared to a monthly emissivity climatology.

Radiative transfer models for sea ice and snow simulate the microwave emissivity spectrum from first principles using layered geophysical properties as input, such as temperature, thickness, density, salinity, and grain size. An established sea ice and snow radiative transfer model is the Microwave Emission Model of Layered Snowpacks (MEMLS; Wiesmann and Mätzler, 1999; Mätzler and Wiesmann, 1999), with extensions for sea ice (Tonboe et al., 2006) and for active simulations (Proksch et al., 2015b). Around the same time, the semi-empirical Helsinki University of Technology (HUT) snow emission model was developed (Pulliainen et al., 1999), which differs in various assumptions from MEMLS, but shows comparable results (Pan et al., 2016). To facilitate comparisons between electromagnetic theories within the same framework, the Snow Microwave Radiative Transfer model (SMRT) was developed and extended to sea ice surfaces (Picard et al., 2018).

An application of sea ice and snow emission models is to identify surface parameters that influence satellite measurements and retrievals. Rahimi et al. (2022) perform sensitivity tests to quantify the impact of snow properties (depth, density, and grain size) on the emissivity at high frequencies (89 and 166 GHz) over northern hemisphere land surfaces with the dense media radiative transfer quasi-crystalline approximation (DMRT-QCA) theory (Tsang et al., 2000). The scattering signal of frozen hydrometeors at these frequencies is used to derive snowfall over land from the Global Precipitation Measurement (GPM) Microwave Imager (GMI) instrument. Thus, small changes in the surface snow properties would impact the snowfall retrieval accuracy. Density and snow depth based on the land surface hydrology model of the European Centre for Medium-Range Weather Forecasts (ECMWF) Integrated Forecasting System (IFS), Integrated Hydrology Tiled ECMWF Scheme for Surface Exchanges over Land (HTESSEL; Balsamo et al., 2015, 2009), are used to map regions where snowfall retrievals are vulnerable to snow emissivity changes. Potential accumulation of snow by the precipitation event itself would change the underlying emissivity at high frequencies.

Several physical retrieval approaches have been developed to derive atmospheric properties from surface-sensitive passive microwave observations over sea

ice, which often requires a combination of radiative transfer models developed separately by the cryosphere and atmosphere communities. Rückert et al. (2023b) couple the sea ice version of MEMLS with the atmospheric model by Wentz and Meissner (2000) to simultaneously retrieve snow and sea ice parameters (sea ice concentration, multiyear ice fraction, snow thickness, and temperature) and atmospheric parameters (liquid water path and integrated water vapor) from Advanced Microwave Scanning Radiometer - 2 (AMSR2) observations. Their retrieval is also applicable over the open ocean, where additionally the sea surface temperature and wind speed are derived based on the ocean emissivity model by Meissner and Wentz (2012). This retrieval builds on an earlier version that used an empirical emissivity (Mathew et al., 2009) estimated from satellite observations over first-year and multiyear ice instead of the physical radiative transfer model (Scarlat et al., 2017, 2020). An evaluation of this earlier version showed lower accuracy in water vapor estimates compared to other satellite and reanalysis products (Crewell et al., 2021). Incorporating a more physical approach for the surface improved the retrieval result. An advantage of using a physical radiative transfer model is also that it allows the use of spatially and temporally varying inputs from thermodynamic sea ice and snow models. Kang et al. (2023) use a thermodynamic sea ice and snow model and couple the radiative transfer models MEMLS for sea ice (Tonboe, 2010; Tonboe et al., 2011) and Radiative Transfer for TOVS (RTTOV; Saunders et al., 2018) to retrieve the atmospheric temperature profile from Advanced Technology Microwave Sounder (ATMS) observations at the Multidisciplinary drifting Observatory for the Study of Arctic Climate (MOSAiC; Nicolaus et al., 2022) site. Improvements in the retrieved atmospheric temperature profile were detected when including surface-sensitive oxygen sounding channels in the retrieval.

The physical snow radiative transfer model HUT was tested in a data assimilation context over snow-covered land (Hirahara et al., 2020). The main difference to sea ice is the underlying soil and potential embedded or emerging vegetation and its interaction with microwave radiation, and more diverse large-scale topography. Simulating the physical inputs required for radiative transfer models is challenging, as found by Prigent et al. (2015) when comparing simulations with CRTM over land with an emissivity climatology (Aires et al., 2011). Hirahara et al. (2020) use model fields on snow properties (thickness, temperature, density, liquid water content, and snow water equivalent), from a multi-layer snow model (Arduini et al., 2019) of the land surface model HTESSEL. Data assimilation experiments showed improvements when using the HUT model over an emissivity atlas at low frequencies. However, the improvements were limited by systematic deficiencies in the emissivity modeling at frequencies above 20 GHz.

Radiative transfer models for the sea ice and snow can be applied to evaluate general circulation models (GCMs) in the Arctic against microwave observations from satellites (Burgard et al., 2020b; Smith et al., 2022). In analogy to data assimilation for numerical weather prediction, this approach avoids the impact of geophysical retrieval uncertainties on quantities predicted by the model, such as sea ice concentration. Burgard et al. (2020a) developed the Arctic Ocean Observation Operator (ARC3O) to convert the GCM output on physical properties of the sea ice, snow, ocean, and atmospheric parameters into brightness temperatures. The MEMLS sea ice version is used as a module to simulate the emission and reflection of sea ice during the cold season. The input to MEMLS is taken directly from the GCM, with additional assumptions about microphysical properties not simulated directly. ARC3O is applied to evaluate the GCM against observations at 6.9 GHz (Burgard et al., 2020a) and 18 GHz (Smith et al., 2022). The applicability to higher frequencies requires consideration of the spatial and temporal evolution of snowpack properties (density, grain size, and layering), which is not yet available from the sea ice module of the GCM.

Spaceborne passive microwave observations are recently advancing toward improved spatial resolution, extended spectral regions, and higher temporal coverage. Improved spatial resolution will be achieved by the conically-scanning multi-frequency microwave radiometer (1.4–36 GHz) Copernicus Imaging Microwave Radiometer (CIMR) (Donlon et al., 2023). At 18 and 36 GHz, the resolution will be 4×6 and 3×5 km, reducing the footprint radius by a factor of about three compared to AMSR2 due to the large antenna of CIMR. This will enable the development of sea ice concentration maps at a much finer resolution and improved accuracy (Kilic et al., 2018) with implications for observing leads and estimating surface fluxes. Moreover, CIMR continues the time series of thin ice thickness based on 1.4 GHz observations, which can fully penetrate newly formed sea ice of 50 cm thickness (e.g., Kaleschke et al., 2010; Tian-Kunze et al., 2014; Huntemann et al., 2014; Scarlat et al., 2020; Paţilea et al., 2019) based on the Soil Moisture and Ocean Salinity (SMOS; Barre et al., 2008) and Soil Moisture Active-Passive (SMAP; Entekhabi et al., 2010) missions. With the launch of AMSR3 (Kachi et al., 2023) in 2025, the spatial resolution at high frequencies (about 5 km at 165.5 and 183.31 GHz) also increases by a factor of 2–3 compared to similar sensors in the polar orbit. Moreover, AMSR3 will continue the time series of its predecessors, AMSR2 (JAXA, 2016) and AMSR-E (Kawanishi et al., 2003). An even higher resolution of less than 1 km will be achieved by the Wind Velocity Radar Nephoscope (WIVERN; Illingworth et al., 2018), a conically scanning 94 GHz Doppler radar measuring wind, clouds, and precipitation, and a radiometer mode sensitive to both atmosphere and sea ice properties.

Extensions in the spectral region from typically below 200 GHz toward the submillimeter wave up to 660 GHz will be implemented with the European Polar System - Second Generation (EPS-SG) Ice Cloud Imager (ICI; Kangas et al., 2014a) by the European Organisation for the Exploitation of Meteorological Satellites (EUMETSAT). The ICI instrument will be onboard the Metop-SG-B satellite together with the MicroWave Imager (MWI), covering the frequency range from 18.7 to 660 GHz on a single platform. The submillimeter waves fill the gap between the microwave and thermal infrared spectrum and are highly sensitive to the scattering by cloud ice (Buehler et al., 2007). Long-term observations of ICI onboard three consecutive satellites are expected to improve the understanding of global occurrence of cloud ice and their representation in weather and climate models (Eliasson et al., 2011; Duncan and Eriksson, 2018). First measurements up to 204 GHz were conducted with the Time-Resolved Observations of Precipitation structure and storm Intensity with a Constellation of Smallsats - 01 (TROPICS-01) Pathfinder mission in a polar orbit from June 2021 to December 2023 (Blackwell, 2022). The Arctic Weather Satellite (AWS), launched in 2024, provides first observations up to frequencies of 325 GHz (Eriksson et al., 2025). The Microwave Sounder (MWS) onboard the Metop-SG-A satellite launched in 2025 extends the time series of its predecessors, Advanced Microwave Sounding Unit - A (AMSU-A), AMSU-B, and Microwave Humidity Sounder (MHS), and provides an additional high-frequency channel at 229 GHz (Kangas et al., 2014b).

Multiple satellites similar to AWS will be arranged in the EPS-Sterna constellation, enabling higher temporal coverage in polar regions. While temporal coverage in the Arctic is already higher than in other regions, the EPS-Sterna enables the monitoring of rapidly developing storms, such as polar lows (Melsheimer et al., 2016), with positive impact on numerical weather prediction skill (Lean et al., 2025; Rivoire et al., 2024). Fully exploiting its capabilities will require knowledge of the emissivity at 325 GHz.

1.2 Field campaigns

Four field campaigns that include microwave radiometer observations over sea ice with channels above 100 GHz and ancillary instruments to characterize the surface, clouds, and atmosphere, were carried out within the framework of the Transregional Collaborative Research Center TRR 172 on "Arctic amplification: Climate Relevant Atmospheric and Surface Processes and Feedback Mechanisms ($\mathcal{AC}$)^3" (Wendisch et al., 2023): Arctic Cloud Observations Using Airborne Measurements During Polar Day (ACLOUD; Wendisch et al., 2019), Airborne Measurements of Radiative and Turbulent Fluxes of Energy and Momentum in the

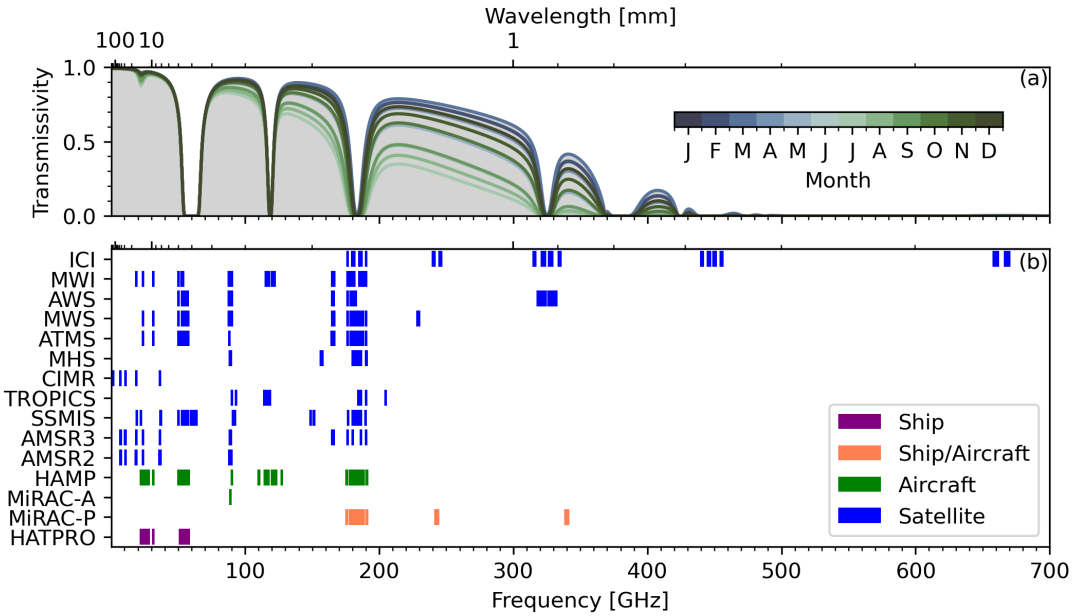

Figure 1.3: Spectrum of the atmospheric transmissivity and location of instrument band passes. (a) Nadir transmissivity under clear-sky conditions from 1 to 700 GHz simulated with the Passive and Active Microwave radiative TRAnsfer (PAMTRA; Mech et al., 2020) model based on monthly mean radiosonde profiles launched from 2018 to 2022 at 12 UTC in Ny-Ålesund, Svalbard (Maturilli, 2020). (b) Band passes of satellite instruments as provided by RTTOV (EUMETSAT NWP-SAF, 2019) and instruments deployed during field campaigns in a downward-looking geometry (see Sect. 1.2). Band passes with a bandwidth of less than 1 GHz are set to 1 GHz for better visibility.

Arctic Boundary Layer (AFLUX; Mech et al., 2022a), HALO–$(\mathcal{AC})^3$ (Wendisch et al., 2024), and Water Vapor, Mixed-Phase Clouds, and Sea Ice Emissivity over the Central Arctic Ocean (VAMPIRE; Rabe and Geibert, 2025). The microwave radiometer observations over sea ice during ACLOUD, AFLUX, and HALO–$(\mathcal{AC})^3$ campaigns were implemented with aircraft, and during the VAMPIRE campaign from a research vessel (Table 1.1). The instruments provide observations at surface-sensitive satellite channels at frequencies above 200 GHz similar to current and future satellite instruments (Fig. 1.3).

During ACLOUD, measurements with the *Polar 5* research aircraft were conducted in the Fram Strait from May to June 2017 (Ehrlich et al., 2019b). *Polar 5* carried the nadir-viewing Microwave Radar/radiometer for Arctic Clouds (MiRAC; Mech et al., 2019), consisting of a combined active–passive component MiRAC-A with a 94 GHz cloud radar and an 89 GHz radiometer channel, and a solely passive component MiRAC-P (183–340 GHz). MiRAC-A and MiRAC-P were also operated onboard the same aircraft during AFLUX in the Fram Strait from March to April 2019 (Mech et al., 2022a). During this time period, the atmospheric transmissivity reaches its maximum in the Arctic (Fig. 1.3). Hence,

the AFLUX campaign provides the highest quality of 340 GHz sea ice emissivity data among the field campaigns analyzed here.

The HALO–$(\mathcal{AC})^3$ campaign from March to April 2022 focused on air mass transformations during cold air outbreaks and warm air intrusions in the Fram Strait and Central Arctic (Wendisch et al., 2024). The *High Altitude and Long Range Research Aircraft (HALO)* carried the nadir-viewing HALO Microwave Package (HAMP) consisting of a 35 GHz cloud radar (Ewald et al., 2019) and 22–183 GHz microwave radiometer (Mech et al., 2014). *HALO* allows for passive microwave observations of deeper cloud systems and includes observations in the Central Arctic not available from the low-flying *Polar 5* aircraft.

The VAMPIRE campaign was performed during R/V *Polarstern* cruise PS144 around the surface freeze onset (August to October 2024) in the Central Arctic (Rabe and Geibert, 2025). Its instrumentation for sea ice observations includes MiRAC-P and the Humidity and Temperature Profiler (HATPRO; Rose et al., 2005) with channels between 22 and 58 GHz. HATPRO and MiRAC-P scanned upwelling and downwelling radiation at various incidence angles regularly during the cruise with a smaller footprint size compared to the aircraft observations. The passive microwave radiometer observations were complemented by ancillary instruments, including two surface cameras (visual and thermal infrared), two cloud radars, radiosondes, and a disdrometer. The VAMPIRE campaign is an extension of the Water Vapor, Cloud Liquid Water, and Surface Emissivity over the Arctic Marginal Ice Zone in Summer (WALSEMA) setup (Rückert et al., 2025) implemented onboard R/V *Polarstern* cruise PS131 during the summer melt period from June to August 2022 in the Fram Strait (Kanzow, 2023). VAMPIRE captures the temporal evolution of the sea ice emissivity after surface freeze onset at 243 GHz and its angular dependence for the first time.

Each field campaign provides high-quality observations of the surface and atmospheric radiation over Arctic sea ice. They are suitable for analyzing the spatiotemporal variability of sea ice emissivity and the retrieval capabilities of surface and atmospheric properties.

Table 1.1: Overview of the field expeditions ACLOUD, AFLUX, HALO–$(\mathcal{AC})^3$, and VAMPIRE.

Mission	Platform	Type	Frequencies [GHz]	Time
ACLOUD	*Polar 5*	Aircraft	89–340	May–Jun 2017
AFLUX	*Polar 5*	Aircraft	89–340	Mar–Apr 2019
HALO–$(\mathcal{AC})^3$	*HALO*	Aircraft	22–183	Mar–Apr 2022
VAMPIRE	R/V *Polarstern*	Ship	22–340	Aug–Oct 2024

1.3 Thesis objectives

Passive microwave observations from polar-orbiting satellites allow long-term monitoring of the surface and atmospheric state of the Arctic climate system. This provides observational evidence for changes in the cryosphere and atmosphere in response to global warming. Moreover, their assimilation in numerical weather prediction models improves weather forecasting in the high and mid latitudes and reanalysis. However, there are still challenges in interpreting and simulating surface-sensitive passive microwave observations over snow and sea ice from existing and novel satellite missions with high-frequency channels. Challenges include the representation of its spatial variability at small scales, which are typically not resolved by satellites but influence the measured signal. Moreover, the temporal evolution of the emissivity at high frequencies and its atmospheric drivers that couple the cryosphere and atmosphere are not well understood due to the lack of detailed observations. Additionally, physical radiative transfer models need to be evaluated against field observations over sea ice. Finally, field observations provide high-resolution reference observations to evaluate passive microwave retrievals based on physical radiative transfer models.

The ACLOUD, AFLUX, HALO–$(\mathcal{AC})^3$, and VAMPIRE expeditions provide an opportunity to improve the understanding and simulation of spaceborne surface-sensitive passive microwave observations at high frequencies over Arctic sea ice. These observations are used to identify physical sea ice and snow properties that influence the emissivity up to submillimeter wavelengths. Moreover, the temporal evolution of sea ice emissivity at high frequencies is related to surface and atmospheric processes, such as new ice formation and snowfall. The spatial variability of the high-resolution emissivity is analyzed within satellite footprints. Additionally, the representation of sea ice emissivity in a snow and sea ice microwave radiative transfer model is assessed using the field observations. The applicability is tested with a physical forward operator consisting of an atmospheric and surface radiative transfer model to simultaneously retrieve surface parameters and cloud liquid water path. The detectability of the cloud liquid water path retrieval is assessed using ancillary airborne observations, and the accuracy is quantified from synthetic retrieval experiments. This dissertation aims to answer the following research questions (RQs):

RQ1: How does sea ice emissivity vary spatially within satellite footprints, and how is this reflected in the spectral variability at the satellite scale toward submillimeter wavelengths? (addressed in Study 1)

RQ2: Which atmospheric processes influence sea ice emissivity toward high frequencies? (addressed in Studies 2 and 3)

RQ3: How representative are sea ice and snow radiative transfer simulations at high frequencies? (addressed in Studies 2 and 3)

RQ4: How accurately can we retrieve cloud liquid water path from passive microwave observations over sea ice? (addressed in Study 3)

The next section provides an overview of the studies addressing the RQs. Afterward, the theoretical background is introduced in Chapter 2. The Chapters 3, 4, and 5 present the three studies outlined below. Finally, Chapter 6 concludes this thesis and provides an outlook.

1.4 Overview of the studies

Study 1: Spatial emissivity variability up to 340 GHz

Satellite observations of MWS, AWS, and ICI above 200 GHz are partly sensitive to the surface, especially under cold and dry conditions during polar night (Fig. 1.3). To derive surface and atmospheric properties from these observations, the sea ice microwave emission at high frequencies and its spatial variability must be known. Therefore, the first study assesses sea ice microwave emissivity from 89 to 340 GHz using airborne observations from the ACLOUD and AFLUX field campaigns (Chapter 3; Risse et al., 2024b). The field observations provide sea ice emissivity estimates during clear-sky flights at frequencies similar to those of the satellite instruments. Moreover, frequent collocations with large-scale satellite observations provide insights into the role of small-scale emissivity variations for the large-scale satellite footprint.

Study 2: Microwave signature of snow accumulation

The temporal evolution of sea ice and snow microwave emissivity at small spatial scales is often not captured by field observations due to their short duration, and is unresolved by large satellite footprints. Especially at high frequencies (183 and 243 GHz), no observations are yet available that capture the small-scale emissivity change during the transition from summer melt to autumn freeze-up, including the formation of new ice and snow accumulation on newly formed sea ice. The second study uses VAMPIRE observations to analyze the sea ice microwave emissivity at frequencies up to 243 GHz and assesses the performance of the Snow Microwave Radiative Transfer (SMRT; Picard et al., 2018) model at high frequencies (Chapter 4). These observations allow us to assess the role of snow scattering for the sea ice emissivity at 183 and 243 GHz. Moreover, the spectral, angular, and polarization dependence of SMRT over sea ice can be

compared to long-term high-resolution emissivity observations of diverse sea ice conditions.

Study 3: Sea ice–atmosphere retrieval

Several studies developed physical sea ice–atmosphere retrievals for satellite passive microwave observations (e.g., Kang et al., 2023; Rückert et al., 2023b). However, little is known about the retrieval performance regarding cloud liquid water path, i.e., detectability and retrieval accuracy, due to the scarcity of reference observations from field measurements or collocated spaceborne lidar observations. Airborne passive microwave observations, combined with collocated reference observations from cloud radar, lidar, and thermal infrared, provide an opportunity for retrieval evaluation along the flight track under diverse atmospheric conditions. The third study develops a physical optimal estimation sea ice–atmosphere retrieval algorithm for airborne passive microwave observations that inverts a physical forward operator consisting of SMRT and the Passive and Active Microwave radiative TRAnsfer (PAMTRA; Mech et al., 2020) model (Chapter 5). The retrieval estimates cloud liquid water path and snow layer properties based on observations during the HALO–$(\mathcal{AC})^3$ campaign.

Chapter 2

Theoretical background

This chapter provides an overview of the two radiative transfer models used in this thesis, i.e., the Passive and Active Microwave radiative TRAnsfer (PAMTRA; Mech et al., 2020) model for the atmosphere (Sect. 2.1) and the Snow Microwave Radiative Transfer (SMRT; Picard et al., 2018) model for the sea ice and its snow cover (Sect. 2.2). Both models receive physical input parameters and convert them to optical properties to solve the radiative transfer equation. In order to retrieve geophysical parameters using radiative transfer models, the geophysical retrieval problem needs to be solved. Here, the optimal estimation (Rodgers, 2000) method is used and described in Sect. 2.3. The emissivity definition and assumptions for the emissivity estimation from microwave radiometer data are outlined in Sect. 2.4. Finally, machine learning methods are introduced to solve unsupervised clustering tasks and regression tasks (Sect. 2.5).

2.1 Atmospheric radiative transfer

2.1.1 PAMTRA model

The PAMTRA model (Mech et al., 2020) allows for both active and passive microwave radiative transfer simulations, including absorption and scattering by hydrometeors. In this thesis, the passive mode is used for the simulation of ship, airborne, and satellite geometries. PAMTRA solves the monochromatic one-dimensional vector radiative transfer equation for a plane-parallel, horizontally homogeneous atmosphere with azimuthal homogeneity (Evans and Stephens, 1993, Eq. (2.22))

$$\mu \frac{d\mathbf{I}(z,\mu)}{dz} = \mathbf{K}(z,\mu)\mathbf{I}(z,\mu) - 2\pi \int_{-1}^{1} \mathbf{M}(z,\mu,\mu')\mathbf{I}(z,\mu')\, d\mu' - \boldsymbol{\sigma}(z,\mu)B[T(z)], \quad (2.1)$$

with the vector of I (total intensity) and Q (difference between horizontal and vertical polarization) Stokes parameters $\mathbf{I}$, scattering matrix $\mathbf{M}$, extinction matrix $\mathbf{K}$, emission vector $\boldsymbol{\sigma}$, temperature T, Planck function B, height coordinate z, and cosine of the zenith angle μ. Positive μ corresponds to the downward direction. The equation is solved with the doubling and adding method (e.g., Mätzler, 2006) implemented in the polarized radiative transfer code RT4 (Evans and Stephens, 1995). The output of PAMTRA is the horizontally and vertically polarized equivalent blackbody temperature at 16 discrete quadrature angles for both the upwelling and downwelling directions. By specifying an instrument height, the output corresponds to sensor geometries within the atmosphere (ship, aircraft) or satellite geometries. The inputs to PAMTRA are atmospheric profiles (temperature, relative humidity, and pressure), hydrometeor profiles, and surface boundary conditions.

2.1.2 Atmospheric gases

PAMTRA accounts for the absorption by atmospheric gases from resonant lines (water vapor and oxygen) and the water vapor and dry continuum (Mech et al., 2020). The gas absorption coefficients are computed in this thesis with the line-by-line model by Rosenkranz (1998) with modifications for the water vapor continuum (Turner et al., 2009) and the line width modification of the 22.235 GHz water vapor line (Liljegren et al., 2005). Accounting for the gaseous absorption is important near absorption lines and toward high frequencies where the water vapor continuum absorption increases (243 and 340 GHz). The microwave radiometers used in this thesis measure along the rotational water vapor absorption lines at 22.235 and 183.31 GHz, the oxygen absorption complex between 50 and 60 GHz, and the oxygen absorption line at 118.75 GHz.

2.1.3 Cloud liquid water

Liquid clouds are a two-phase medium consisting of almost spherical liquid water droplets suspended in air (Mätzler, 2006). Their diameter is much smaller than the wavelength at microwave frequencies (about 10 µm), and therefore interact with microwave radiation mostly through emission and absorption. In the Arctic, liquid clouds occur at temperatures as low as −40°C. Thus, simulating their interaction with microwave radiation requires a realistic representation of the dielectric permittivity of liquid water at supercool temperatures (Kneifel et al., 2014; Rosenkranz, 2015). Turner et al. (2016) developed a parameterization for temperatures as low as −35°C based on field observations at supercool temperatures and laboratory data, which is implemented in PAMTRA. The fre-

quency and temperature dependence of the dielectric permittivity is expressed by a double-Debye equation (Debye, 1929; Ellison, 2007). Based on the dielectric permittivity of liquid water, PAMTRA computes the single scattering properties of liquid clouds using Mie theory (Mie, 1908). Under the Rayleigh approximation, the absorption coefficient κ_a can be written as (Evans and Stephens, 1993; Turner et al., 2016)

$$\kappa_a = \frac{6\pi\nu}{\rho_l c_0} \Im\left(\frac{\epsilon - 1}{\epsilon + 2}\right) W, \tag{2.2}$$

with the frequency ν, density of liquid water ρ_l, speed of light in vacuum ($c_0 \approx 3 \times 10^8\ m\ s^{-1}$), complex dielectric permittivity of liquid water $\epsilon = \epsilon' + i\epsilon''$, imaginary part of a complex number $\Im(\cdot)$, and cloud liquid water content within a given volume of air W. Equation (2.2) shows that the absorption by cloud liquid water droplets is proportional to the total amount of liquid water. The frequency and temperature dependence of the absorption coefficient at HAMP frequencies is shown in Fig. 2.1. The absorption coefficient increases with frequency and shows a temperature dependence at all frequencies. Therefore, errors in the cloud temperature lead to uncertainties in the radiative transfer simulation through both the Planck function and the absorption coefficient.

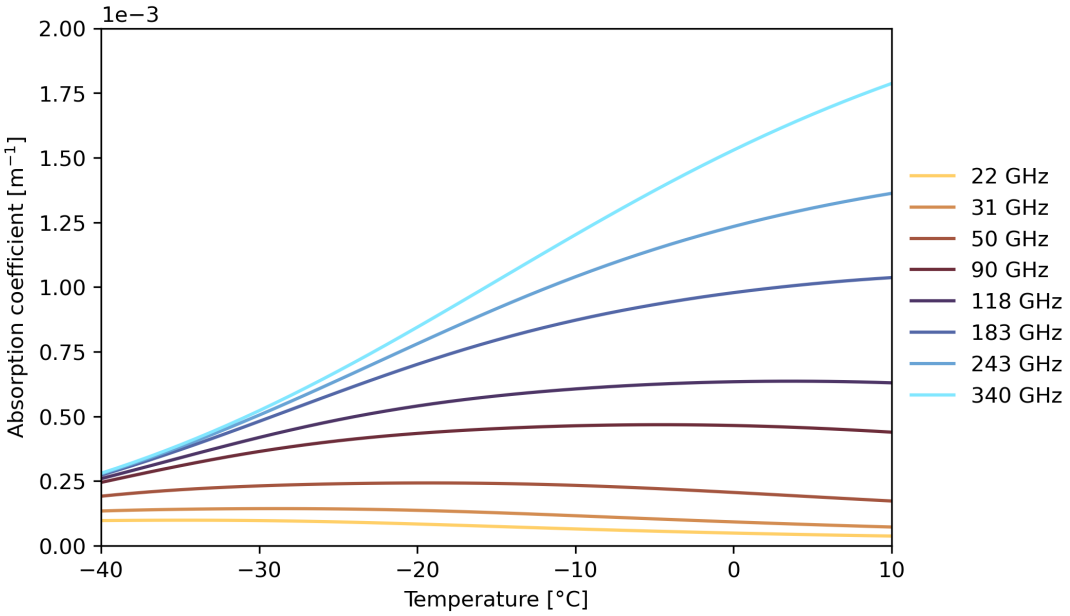

Figure 2.1: Temperature dependence of the liquid cloud absorption coefficient for a cloud liquid water content of $0.5\,\mathrm{g\,m^{-3}}$ at 22, 31, 50, 90, 118, 183, 243, and 340 GHz. The absorption coefficient is calculated with Eq. (2.2) using the liquid water dielectric permittivity parameterization by Turner et al. (2016).

2.1.4 Boundary conditions

In order to solve the radiative transfer equation, boundary conditions of the lower interface (surface) and upper interface (space) are required. While the free space is described with a fixed cosmic microwave background of 2.73 K (Fixsen, 2009), the surface is represented via an emissivity, temperature, and reflection type. Two reflection types can be selected, i.e., specular and diffuse (Lambertian) reflection (see Sect. 2.4.4). The emissivity can be extracted from a surface emissivity model or atlas. Here, we use the Tool to Estimate Sea-Surface Emissivity from Microwave to Submillimeter Waves (TESSEM^2; Prigent et al., 2017) for comparison with observations over the open ocean. TESSEM^2 parametrizes the sea surface emissivity from 10–700 GHz as a function of wind speed, sea surface temperature, and sea surface salinity based on the FAST microwave Emissivity Model (FASTEM; Liu et al., 2011).

2.2 Sea ice and snow radiative transfer

2.2.1 SMRT model

The SMRT model (Picard et al., 2018) computes the propagation of thermal radiation emitted within plane-parallel, multilayered sea ice and snow (Fig. 2.2). The uppermost layer is an atmosphere layer, and the lowest layer is a semi-infinite ocean layer where any transmitted radiation gets absorbed. Inputs to SMRT are the physical properties of the sea ice and snow layers (e.g., thickness, temperature, density, microstructure, and salinity). Then, the permittivity of the raw materials (fresh ice, air, and brine) is computed with permittivity models, and an electromagnetic model is applied to derive optical properties (effective permittivity, absorption and scattering coefficients, and phase matrix). Here, we assume that all interfaces and boundaries are flat. Thus, the reflectivity and transmissivity coefficients at intermediate layer interfaces and the boundaries (ocean and air) are computed with the Fresnel equations, based on the effective permittivity of each layer. Figure 2.3 shows the Fresnel reflectivity for radiation entering from air into nilas, first-year ice, multiyear ice, and snow. The Fresnel equations provide the only source for polarization effects, as the scattering with the microstructure of snow and sea ice is assumed to be isotropic. Finally, the vector radiative transfer equation is solved (see Eq. (2.1)) with the discrete ordinate and eigenvalue method (DORT Picard et al., 2004, 2013) with 128 discrete zenith angles (streams). SMRT neglects inter-layer interferences and coherent effects, which are mostly relevant at 1.4 GHz for homogeneous conditions (Tan et al., 2015; Leduc-Leballeur et al., 2015) or thin ice lenses (Matzler and Wegmuller,

1987).

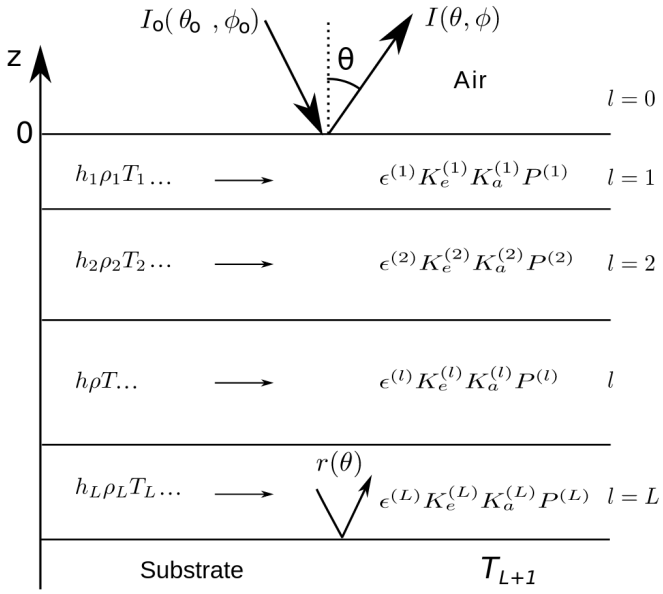

Figure 2.2: Setup of the plane-parallel, multilayered medium in SMRT. Variables denote the radiance $I(\theta, \phi)$ as a function of zenith θ and azimuth angle ϕ, reflectivity at the interface $r(\theta)$, physical inputs of each layer l (h: height, ρ: density, and T: temperature), and derived optical properties (ϵ: dielectric permittivity, K_e: extinction coefficient, K_a: absorption coefficient, P: phase matrix). Based on Fig. 1 in Picard et al. (2018).

2.2.2 Sea ice

Sea ice consists of pure ice with discrete brine pockets and air bubbles embedded within the ice matrix. Air bubbles are mostly present in multiyear ice in the freeboard layer due to flushing of brine during the summer melt (Untersteiner, 1968; Comiso, 1983). Each sea ice component (pure ice, liquid brine, and air) differs in its dielectric properties. The complex relative dielectric permittivity of air is very close to unity (Hector and Schultz, 1936) and fixed to $\epsilon = 1$ in SMRT. For pure ice, the dielectric permittivity model from Mätzler (2006, Chapter 5) is used in this thesis. The real part of the dielectric permittivity of pure ice is almost constant ($\varepsilon' \approx 3.17$) with a small temperature dependence (Fig. 2.4a). The imaginary part is generally small for pure ice ($\varepsilon'' < 0.03$) at frequencies and temperatures relevant for this thesis (Fig. 2.4c), which means that absorption by pure ice is small at microwave frequencies. For brine, the parameterization by Stogryn and Desargant (1985) is applied here, which is also a function of frequency and temperature (Fig. 2.4b,d). The much higher dielectric loss of brine compared to pure ice ($O(1000)$ below 60 GHz and $O(100)$ from 60 to 200 GHz) shows that the absorption of sea ice strongly depends on the presence of brine

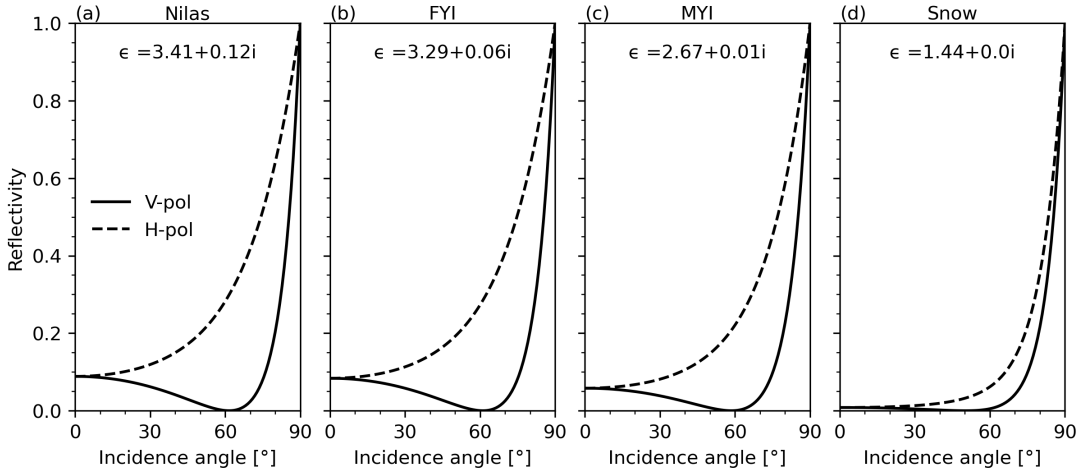

Figure 2.3: Reflectivity at horizontal (H-pol) and vertical polarization (V-pol) based on the Fresnel equations (Maezawa and Miyauchi, 2009) implemented in SMRT (Picard et al., 2018) for radiation entering from air into (a) nilas, (b) first-year ice (FYI), (c) multiyear ice (MYI), and (d) snow. The effective permittivity of each medium is computed with SMRT at 90 GHz and provided within each panel.

(Shokr, 1998). The brine volume fraction can be determined as a function of bulk salinity and temperature using the parameterizations by Cox and Weeks (1974) and Leppäranta and Terhikki (1988) as implemented in SMRT (Fig. 2.5). At a fixed bulk salinity, the brine volume fraction decreases with decreasing temperature due to the freezing of brine.

The macrophysical dielectric properties of sea ice can be approximated with dielectric mixing models from the dielectric properties of each constituent and their volume fractions. Assumptions on their shape and microstructure are needed for the application of mixing models, which introduces uncertainties in the estimated macrophysical properties (Mätzler, 2006). For sea ice and snow, the Polder–Van Santen mixing formula (Polder and van Santen, 1946) is widely used (e.g., Denoth, 1982; Matzler, 1996; Soriot et al., 2022). For spherical scatterers, the effective permittivity ϵ_{eff} of a medium consisting of two components can be computed from this relationship (Mätzler, 2006)

$$(1 - f_2)\frac{\epsilon_1 - \epsilon_{\text{eff}}}{\epsilon_1 - 2\epsilon_{\text{eff}}} + f_2\frac{\epsilon_2 - \epsilon_{\text{eff}}}{\epsilon_2 - 2\epsilon_{\text{eff}}} = 0, \tag{2.3}$$

with the permittivity of the environment phase ϵ_1, permittivity of the inclusion phase ϵ_2, and the dimensionless volume fraction of the inclusion phase f_2. For first-year ice, pure ice corresponds to the environment phase and brine pockets to the inclusion phase. For multiyear ice, which consists of pure ice, brine pockets, and air bubbles, the mixing equation is computed first for the pure ice and brine

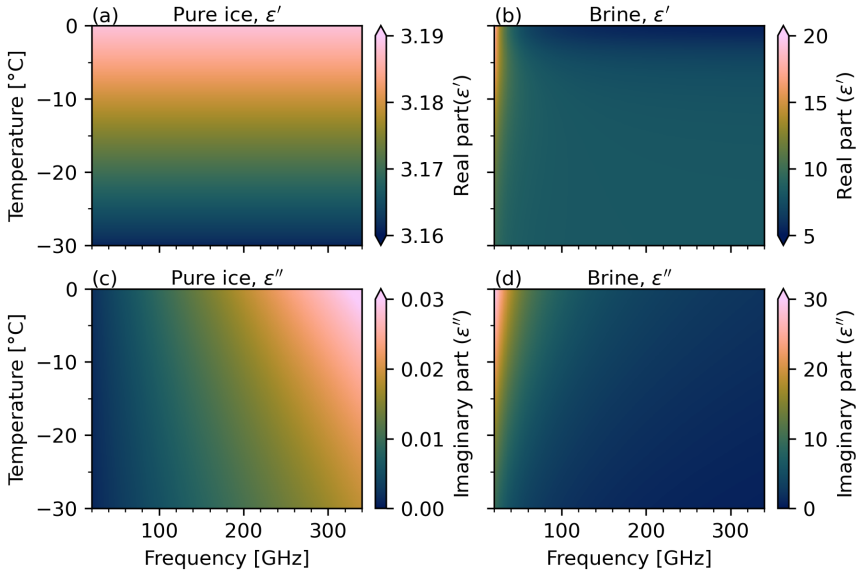

Figure 2.4: Complex relative dielectric permittivity of (a, c) pure ice (Mätzler, 2006) and (b, d) brine (Stogryn and Desargant, 1985) as a function of temperature and frequency (20 to 340 GHz). The real parts are shown in (a, b) and the imaginary parts in (c, d).

mixture, and then for the saline ice and air bubbles in SMRT. The corresponding volume fractions are the brine volume fraction (derived from temperature and salinity) and porosity (derived from temperature, salinity, and density).

2.2.3 Snow

Snow consists of air, pure ice, and potentially liquid water or brine. However, in this thesis, we only simulate dry snow and do not explicitly handle wet or saline snow. Generally, the microwave absorption of wet snow is very high even for a low liquid water content (Mätzler, 2006). For dry snow, the effective permittivity can be computed from the Polder–Van Santen mixing formula in Eq. (2.3) with air as the environment phase and pure ice as the inclusion phase (e.g., Sandells et al., 2022). The dielectric properties of dry snow are therefore mainly determined by its density or the ice volume fraction (Ulaby et al., 1986).

2.2.4 Microstructure representation

The permittivity fluctuations due to brine and air inclusions within sea ice (Vant et al., 1978) and snow grains in snowpacks lead to volume scattering of microwave radiation (Comiso, 1986). In first-year ice and nilas, the scattering is mainly caused by brine pockets (Tonboe et al., 2006), while air bubbles dominate the scattering in multiyear ice (Nghiem et al., 1995; Comiso, 1983). The size and spatial arrangement of the scatterers within the environment phase are described

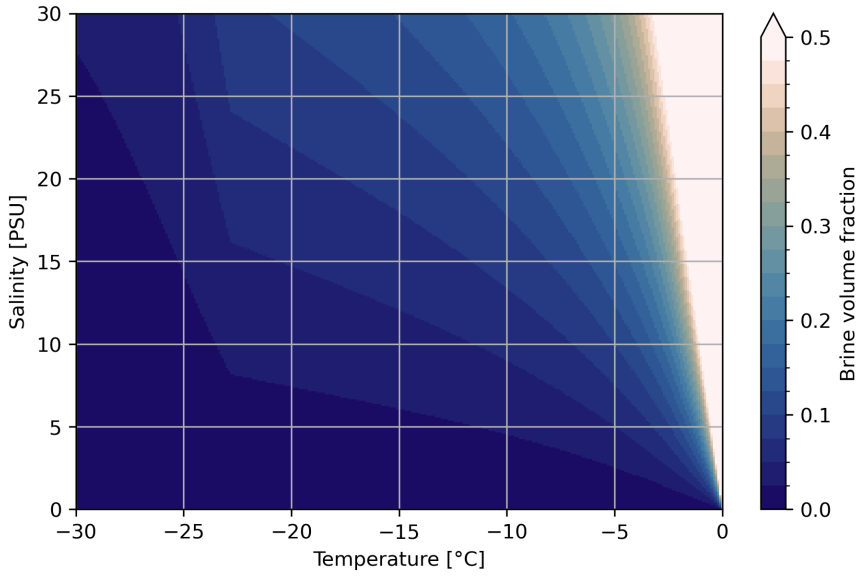

Figure 2.5: Brine volume fraction of saline ice as a function of sea ice temperature and salinity. The parameterization is based on Cox and Weeks (1974) for temperatures below −2°C and Leppäranta and Terhikki (1988) above −2°C as implemented in SMRT. The sea ice is assumed to contain no air bubbles.

by the microstructure in the form of the autocorrelation function of the indicator function. For sea ice and snow, the exponential microstructure (e.g., Kang et al., 2023; Rückert et al., 2023b) and sticky hard spheres microstructure (e.g., Soriot et al., 2022) are often used. The exponential microstructure, which is also used in MEMLS (Mätzler and Wiesmann, 1999; Tonboe et al., 2006), is described by two parameters (volume fraction and exponential correlation length), while the sticky hard spheres model requires three parameters (volume fraction, stickiness, and sphere radius) to capture more structural correlations (Picard et al., 2018). In this thesis, the exponential microstructure is applied due to its good agreement with observations over snow up to 243 GHz (Wivell et al., 2023). For simplicity, the microstructure is assumed to be isotropic, although some horizontal and vertical anisotropy is observed for old and new snow, respectively (Sandells et al., 2022; Leinss et al., 2016). The exponential autocorrelation function for isotropic materials is defined as (Picard et al., 2018; Debye et al., 1957)

$$C_{\mathrm{ex}}(r) = f_2(1-f_2)e^{\frac{-r}{\xi}}, \tag{2.4}$$

with the distance r, exponential correlation length ξ, and volume fraction of the inclusion f_2. In Fourier space, the exponential autocorrelation function writes as (Picard et al., 2018)

$$\widetilde{C}_{\mathrm{ex}}(k_{\mathrm{d}}) = \frac{8\pi\xi^3 f_2(1-f_2)}{[1+(k_{\mathrm{d}}\xi)^2]^2}, \tag{2.5}$$

with the difference of wave vectors in the effective medium in the incident and scattering directions k_d (Picard et al., 2018)

$$k_d = 2k_0\sqrt{\epsilon_\mathrm{eff}}\sin\left(\frac{\vartheta}{2}\right). \tag{2.6}$$

The scattering angle is denoted as ϑ and the wavenumber in free space as $k_0 = 2\pi\nu/c_0$.

The correlation length can be interpreted as an effective size of scatterers and is directly linked to the specific surface area within the porous medium (Mätzler, 2002). Especially for snow, the autocorrelation function and thus the correlation length show a high variability as observed from 2D or 3D binary images of the ice–air matrix from thin sections (e.g., Reber et al., 1987) or micro-computed tomography (CT) scans (e.g., Sandells et al., 2022). An example of the ice–air matrix based on micro-CT scans is shown in Fig. 2.6 for three snow types (Proksch et al., 2015a). The exponential correlation length for low-density new snow is rather low, with about 0.07 mm (Fig. 2.6a), while the correlation length is higher for larger depth hoar crystals with about 0.37 mm (Fig. 2.6c). The large difference between each sample shows the importance of snow metamorphism due to water vapor gradients and melt processes (Lehning et al., 2002) on the microstructure.

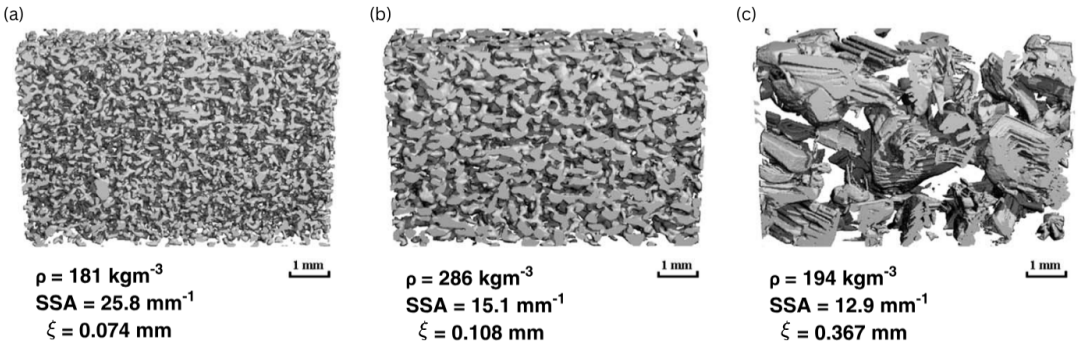

Figure 2.6: Examples of micro-CT snow structure reconstruction of (a) low-density new snow, (b) dense melt refrozen snow, and (c) medium-density depth hoar crystals. Values denote snow density (ρ), specific surface area (SSA), and exponential correlation length (ξ) derived from the micro-CT reconstruction. Adapted from Fig. 1 in Proksch et al. (2015a).

2.2.5 Improved Born approximation

The scattering coefficient, absorption coefficient, and phase function for each sea ice and snow layer are calculated from the permittivity and microstructure using electromagnetic theory. Several electromagnetic theories are available in SMRT,

such as the improved Born approximation (IBA; Mätzler, 1998), dense media radiative transfer (DMRT) based theories, and strong contrast expansion (SCE; Torquato and Kim, 2021). Picard et al. (2022) compare IBA, DMRT–quasi-crystalline approximation (QCA) Mie scattering of sticky spheres (DMRT–QMS; Liang et al., 2008; Tsang et al., 2006), and SCE for snow with the sticky hard sphere microstructure and find an agreement of the scattering coefficients up to $k_0 a \approx 1.5$, with the snow grain radius a. This corresponds to an upper bound of the radius where the theories agree of about 0.8 mm at 90 GHz and 0.2 mm at 340 GHz. Hence, the estimation of the scattering coefficient of coarse-grained snow or at high frequencies is highly uncertain and depends on the selected electromagnetic theory. Here, we apply the IBA theory, which was evaluated by Wivell et al. (2023) over snow and provides realistic emissivity spectra up to 243 GHz in agreement with in situ observations and is also often used for sea ice (e.g., Kang et al., 2023; Rückert et al., 2023b; Soriot et al., 2022; Kilic et al., 2019).

Picard et al. (2018) describes IBA based on the original work by Mätzler (1998). The phase function in the 1–2 polarization frame is given as (Picard et al., 2018; Ding et al., 2010)

$$p(\vartheta, \varphi) = f_2(1 - f_2)(\epsilon_2 - \epsilon_1)^2 Y^2(\epsilon_1, \epsilon_2) k_0^4 M(k_\mathrm{d}) \sin^2 \chi, \tag{2.7}$$

with the polarization angle χ. The mean squared field ratio $Y^2(\epsilon_1, \epsilon_2)$ for small spherical scatterers in an isotropic microstructure can be calculated from the dielectric permittivity as (Mätzler, 1998)

$$Y^2(\epsilon_1, \epsilon_2) = \left| \frac{2\epsilon_\mathrm{eff} + \epsilon_1}{2\epsilon_\mathrm{eff} + \epsilon_2} \right|^2. \tag{2.8}$$

The microstructure term $M(k_d)$ depends on the Fourier transform of the autocorrelation function $\widetilde{C}(k_d)$

$$M(k_d) = \frac{1}{4\pi} \frac{\widetilde{C}(k_d)}{f_2(1 - f_2)}. \tag{2.9}$$

In our case, $\widetilde{C}(k_d)$ corresponds to the exponential autocorrelation function from Eq. (2.5). The scattering coefficient is then determined by integrating over the phase function (Picard et al., 2018)

$$\kappa_s = \pi \int_0^\pi [p_{11}(\vartheta) + p_{22}(\vartheta)] \sin \vartheta \, \mathrm{d}\vartheta. \tag{2.10}$$

Simulated scattering coefficients of nilas, first-year ice, multiyear ice, and snow layers as a function of correlation length are presented in Fig. 2.7. The scattering coefficients increase with correlation length and cover about five orders of magnitude from fine-grained snow at 22 GHz to coarse-grained snow at 340 GHz.

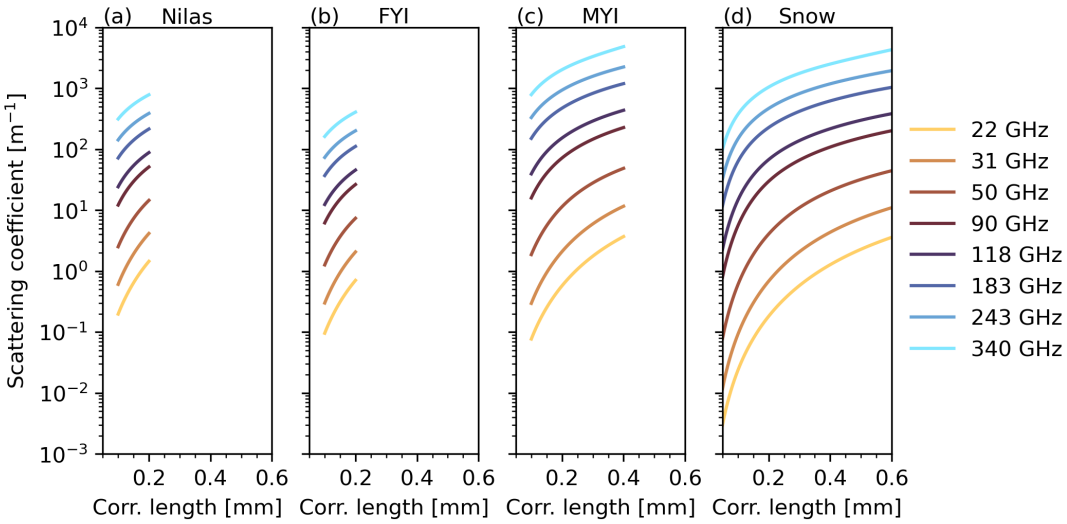

Figure 2.7: Scattering coefficients of single-layer (a) nilas, (b) first-year ice (FYI), (c) multiyear ice (MYI), and (d) dry snow as a function of correlation length derived from IBA with SMRT (Picard et al., 2018). The variability of the correlation length is set to typical values for each medium. The layers are defined with a temperature of −15°C. The density is set to 920, 920, 750, and 260 kg m^{-3} and the salinity to 14, 7, 0.5, and 0 PSU for nilas, first-year ice, multiyear ice, and snow, respectively, corresponding to the uppermost layer of each surface type in Tonboe et al. (2006).

The absorption coefficient is directly computed from the effective permittivity in IBA as

$$\kappa_a = 2k_0 \Im(\sqrt{\epsilon_{\text{eff}}}). \tag{2.11}$$

Absorption coefficients of three sea ice types (nilas, first-year ice, and multiyear ice) with a fixed salinity and dry snow are shown as a function of temperature in Fig. 2.8. The absorption coefficient is highest in the saline ice (nilas and first-year ice), and its temperature dependence is modulated by the brine volume fraction (see Fig. 2.5). Multiyear ice and snow have much lower absorption coefficients than saline ice, with slightly higher absorption in multiyear ice compared to snow.

2.3 The geophysical retrieval

The geophysical retrieval aims at inferring a geophysical state ($\mathbf{x}$) from remote sensing measurements ($\mathbf{y}$). In Chapter 5, the retrieved geophysical state corresponds to snow properties and cloud water path, and the measurements are

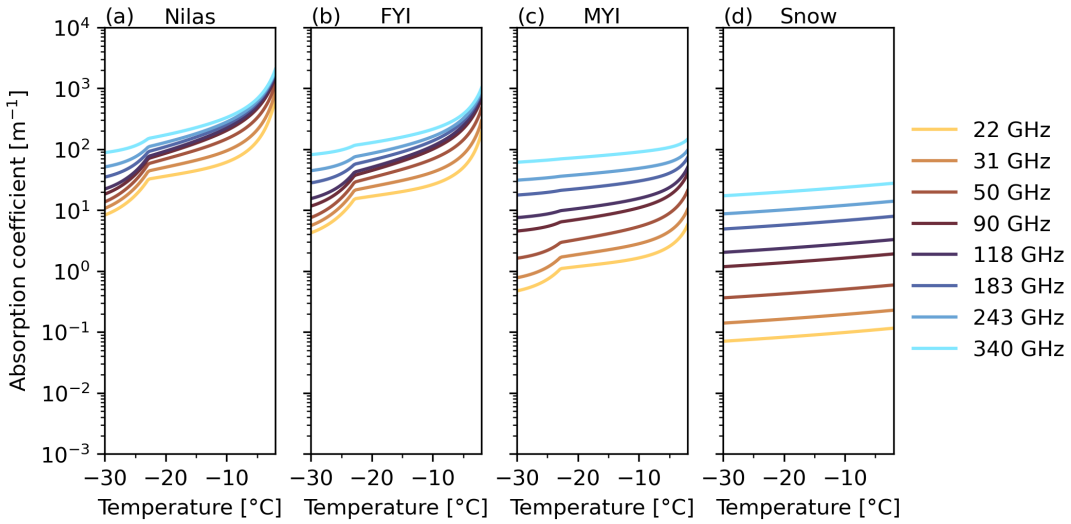

Figure 2.8: Absorption coefficients of single-layer (a) nilas, (b) first-year ice (FYI), (c) multiyear ice (MYI), and (d) dry snow as a function of temperature derived from IBA with SMRT (Picard et al., 2018). The density and salinity are set as in Fig. 2.7.

brightness temperatures at several channels from a passive microwave radiometer. As described above, the interactions of the cryosphere and atmosphere with microwave radiation can be simulated with a radiative transfer model (F)

$$F(\mathbf{x}, \mathbf{b}) = \mathbf{y}. \tag{2.12}$$

Inputs to the radiative transfer model are the state vector and model parameters ($\mathbf{b}$). The model parameters describe fixed parameters that contribute to uncertainties in the simulation (Maahn et al., 2020). Through the inversion of the generally non-linear radiative transfer model, the geophysical state can be estimated from a set of measurements. However, there exists no unique solution, as completely different geophysical states can correspond to the same measurement (Rodgers, 2000). Additionally, different measurement channels can be sensitive to the same element of the state vector, which reduces the independent information about the geophysical state contained in the measurements. These factors need to be considered to extract new information from the measurements.

There are various approaches to solving the retrieval problem. In this thesis, a physical retrieval method based on optimal estimation (Rodgers, 2000) is applied. Optimal estimation inverts the forward operator iteratively until a solution is found based on a priori knowledge of the geophysical state. The uncertainties of the a priori information, measurement, and forward model are handled during the retrieval by weighing the relative contributions of the a priori and measurement. The algorithm is based on Bayes' theorem, which provides a probabilistic

equation of the desired quantity, the posterior probability density function of the geophysical state given an observation $P(\mathbf{x}|\mathbf{y})$

$$P(\mathbf{x}|\mathbf{y}) = \frac{P(\mathbf{y}|\mathbf{x})P(\mathbf{x})}{P(\mathbf{y})}. \tag{2.13}$$

The conditional probability density function $P(\mathbf{y}|\mathbf{x})$ describes the knowledge of $\mathbf{y}$ for a given state $\mathbf{x}$, i.e., the measurement and forward model uncertainty. $P(\mathbf{x})$ is the prior distribution of the state $\mathbf{x}$, which we aim to update during the retrieval based on new information from the measurement, and $P(\mathbf{y})$ is a normalizing factor.

In order to convert the probability into quantitative estimates, optimal estimation assumes Gaussian distributions and unbiased measurement and state vectors. Hence, all distributions can be described by a mean and a covariance matrix, and an explicit expression for the a posteriori distribution is given as (Rodgers, 2000, Eq. (5.3))

$$-2\ln P(\mathbf{x}|\mathbf{y}) = (\mathbf{y} - F(\mathbf{x}))^T {\mathbf{S_e}}^{-1}(\mathbf{y} - F(\mathbf{x})) + (\mathbf{x} - \mathbf{x_a})^T {\mathbf{S_a}}^{-1}(\mathbf{x} - \mathbf{x_a}), \tag{2.14}$$

with the a priori state $\mathbf{x_a}$, a priori covariance matrix $\mathbf{S_a}$, and effective measurement uncertainty $\mathbf{S_e}$. The effective measurement uncertainty combines observation uncertainty (e.g., instrument noise) and model uncertainty

$$\mathbf{S_e} = \mathbf{S_y} + \mathbf{K_b}\mathbf{S_b}{\mathbf{K_b}}^T, \tag{2.15}$$

with the observation uncertainty $\mathbf{S_y}$, the Jacobian matrix $\mathbf{K_b} = \partial F(\mathbf{x_i}, \mathbf{b})/\partial \mathbf{b}$, and the model parameter uncertainty $\mathbf{S_b}$.

The maximum probability state is obtained by minimizing the derivative of the posterior probability density function in Eq. (2.14). The resulting cost function must be solved numerically, and here we use the Gauss–Newton method based on the software implementation by Maahn et al. (2020). The iterative updates of the state can be expressed as (Rodgers, 2000, Eq. (5.9))

$$\mathbf{x_{i+1}} = \mathbf{x_a} + ({\mathbf{S_a}}^{-1} + {\mathbf{K_i}}^T {\mathbf{S_e}}^{-1}\mathbf{K_i})^{-1}{\mathbf{K_i}}^T {\mathbf{S_e}}^{-1}[(\mathbf{y} - F(\mathbf{x_i}, \mathbf{b}) + \mathbf{K_i}(\mathbf{x_i} - \mathbf{x_a})], \tag{2.16}$$

with the Jacobian matrix $\mathbf{K_i} = \partial F(\mathbf{x_i}, \mathbf{b})/\partial \mathbf{x_i}$. The first guess is typically set to the a priori estimate (Maahn et al., 2020). The convergence criterion for the iteration is

$$(\mathbf{x_i} - \mathbf{x_{i+1}})^T {\mathbf{S_i}}^{-1}(\mathbf{x_i} - \mathbf{x_{i+1}}) \ll N, \tag{2.17}$$

where N denotes the number of retrieved parameters and $\mathbf{S_i}$ the retrieval uncer-

tainty

$$\mathbf{S_i} = (\mathbf{S_a}^{-1} + \mathbf{K_i}^T \mathbf{S_e}^{-1} \mathbf{K_i})^{-1}. \tag{2.18}$$

Hence, the iteration stops once the update of the state vector is smaller than the retrieval uncertainty. For the final iteration, Eq. (2.18) provides the a posteriori uncertainty of the retrieved parameters.

2.4 Emissivity estimation from radiometers

2.4.1 Emissivity definition

The spectral emissivity at frequency ν, polarization p (horizontal or vertical), and viewing angle θ is defined as the ratio between emitted spectral radiance (I) and the unpolarized spectral radiance of a black body $B(\nu, T)$ with temperature T (Mätzler, 2006)

$$e(\nu, p, \theta) = \frac{I(\nu, p, \theta)}{B(\nu, T)}. \tag{2.19}$$

The spectral radiance of a black body is determined by the Planck function

$$B(\nu, T) = \frac{2h\nu^3}{c^2(e^{\frac{h\nu}{k_b T}} - 1)}, \tag{2.20}$$

with the Planck constant ($h = 6.626 \times 10^{-34}\ J\ s$), the Boltzmann constant ($k_b = 1.381 \times 10^{-23}\ J\ K^{-1}$), and the speed of light in a refractive medium $c = c_0/n'$ given as ratio between the speed of light in vacuum and the real part of the complex index of refraction of the medium n' defined as $n = \sqrt{\epsilon}$. In the microwave spectrum, the dependence between spectral radiance and equivalent blackbody temperature is nearly linear as expressed by the Rayleigh–Jeans approximation ($hv/k_\mathrm{b}T \ll 1$)

$$B_\mathrm{RJ}(T) = \frac{2k_\mathrm{b}T\nu^2}{c^2}. \tag{2.21}$$

When applying this approximation to Eq. (2.19), the expression for the emissivity simplifies to

$$e(\nu, p, \theta) = \frac{T_\mathrm{b}(\nu, p, \theta)}{T}, \tag{2.22}$$

with the brightness temperature T_b. In the following, T is referred to as the surface or emitting layer temperature and denoted as T_s.

2.4.2 Surface temperature

An estimate of the surface temperature is required for the emissivity calculation. Precisely, the surface temperature denotes the weighted temperature of the layers

that contribute to the microwave radiation emitted by the sea ice and snow (e.g., Tonboe, 2010). The relative contributions of individual layers to the emitted signal are strongly linked to the physical properties of the medium and, therefore, also frequency dependent. Vertical gradients in the temperature profile, which are strongest in winter (Langlois et al., 2007), thus lead to spectrally varying emitting layer temperatures. The spectral dependence of the emitting layers is simulated with SMRT for nilas, first-year ice, and multiyear ice at nadir from 22 to 340 GHz based on idealized profiles by Tonboe et al. (2006) (Fig. 2.9). The emitting layers correspond to peaks of the temperature weighting function (Kang et al., 2025). At high frequencies, the signal is emitted only from the upper few centimeters of the nilas or snow cover. Toward lower frequencies, the radiation is emitted by layers in up to about 40 cm depth for multiyear ice. Unlike the weighting functions of oxygen sounding channels in the atmosphere (e.g., Mech et al., 2014), the shape of the sea ice and snow weighting functions changes strongly due to the highly variable sea ice and snow dielectric properties and microstructure. Hence, even if the sea ice and snow temperature profile is known from in situ data, an estimation of the emitting layer temperature requires assumptions on the emitting layer depth or weighting function (e.g., Mathew et al., 2008, 2009).

A practical solution for the emitting layer estimation is the skin temperature estimated from a thermal infrared radiometer on suborbital platforms (Thielke et al., 2022) or polar-orbiting satellites (Nielsen-Englyst et al., 2023) under clear-sky conditions. The thermal infrared emissivity is very close to unity with a small dependence on snow and ice surface properties (Hori et al., 2006). These provide a high spatial coverage to capture the horizontal temperature variations, which can be large due to leads and snow cover (Thielke et al., 2022). At high frequencies, this estimate is close to the temperature of the emitting layer near the surface (see Fig. 2.9). Using skin temperatures at lower frequencies leads to an emissivity overestimation due to the increase in temperature with depth. Spatially and temporally continuous information on the surface temperature is only available from reanalysis (Hersbach et al., 2020), which combines observations with the underlying numerical model. Observation-based all-sky surface or subsurface temperature estimates are developed from passive microwaves (Kilic et al., 2019; Kang et al., 2025), but they are not used in this thesis to avoid potential correlations with the suborbital passive microwave observations.

2.4.3 Atmospheric contribution

When estimating the emissivity from passive microwave radiometer observations in the field, there is a significant atmospheric contribution to the measured signal

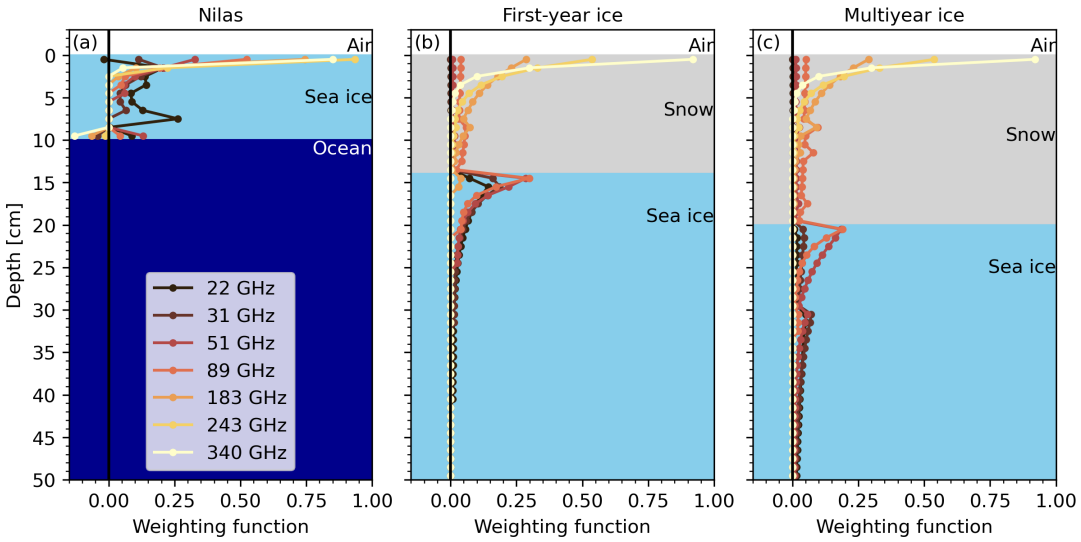

Figure 2.9: Temperature weighting functions estimated for idealized nilas, first-year ice, and multiyear ice profiles from 22 to 340 GHz at nadir. The layer properties for the profiles are taken from Tables 4.5–4.7 in Tonboe et al. (2006). As in Tonboe et al. (2006), the simulations are performed at 1 cm vertical resolution with a snow–ice interface temperature of 268.15 K, equivalent to a thermal conductivity of snow and ice of 0.3 and 2.1 $\mathrm{W\,m^{-1}\,K^{-1}}$, respectively. The ice–water and air–snow interface temperatures are set to 271.35 and 258.15 K, respectively. The weighting function is computed by perturbing the temperature of each layer by 0.1 K. The simulations are performed with the Snow Microwave Radiative Transfer (SMRT) model (Picard et al., 2018) with the setup described in Chapter 5.

(Prigent et al., 1997). Estimating the emissivity in the presence of hydrometeors typically requires a geophysical retrieval (e.g., Boukabara et al., 2011) due to the lack of accurate information on hydrometeor properties (Chapter 5). Therefore, the following discusses the clear-sky case, where the atmospheric contribution is only due to the emission and absorption by atmospheric gases. These conditions also allow simultaneous surface temperature estimates from infrared observations.

The atmospheric contributions to the measured brightness temperature are downwelling radiation reflected at the surface $T_{\mathrm{b,down}}(\infty, 0)$, upwelling radiation between the microwave radiometer height h and the surface $T_{\mathrm{b,up}}(0, h)$, and transmissivity of radiation emitted or reflected at the surface toward the instrument height $t(0, h)$. This can be expressed by the integrated radiative transfer equation with the Rayleigh–Jeans approximation for the non-scattering, plane-parallel atmosphere (Prigent et al., 1997, 1998)

$$T_{\mathrm{b}} = eT_{\mathrm{s}}t(0,h) + (1-e)T_{\mathrm{b,down}}(\infty,0)t(0,h) + T_{\mathrm{b,up}}(0,h). \tag{2.23}$$

Rearranging provides an equation for the emissivity with an atmospheric contri-

bution

$$e = \frac{T_\mathrm{b} - T_\mathrm{b,up}(0,h) - T_\mathrm{b,down}t(0,h)}{t(0,h)(T_\mathrm{s} - T_\mathrm{b,down})}. \tag{2.24}$$

In the case of a microwave radiometer close to the surface, Eq. (2.24) can be simplified to

$$e = \frac{T_\mathrm{b} - T_\mathrm{b,down}}{T_\mathrm{s} - T_\mathrm{b,down}}. \tag{2.25}$$

The downwelling atmospheric component can be directly estimated during upward scans with the microwave radiometer (NORSEX Group, 1983). Under the assumption that scattering by frozen hydrometeors is small, this approach is also applicable to cloudy conditions.

For airborne or satellite applications, Eq. (2.24) needs to be solved with appropriate estimates of the atmospheric contributions using radiative transfer simulations (Chapters 3). During field observations, dropsondes or radiosondes provide direct measurements of the thermodynamic profile of the atmosphere. However, their spatial representability, together with the measurement accuracy, needs to be considered during the emissivity estimation.

2.4.4 Surface reflection

The downwelling atmospheric radiation is anisotropic and strongly depends on the incidence angle. Therefore, the bistatic scattering coefficient, which describes how much radiation is scattered in a certain direction for a given incident direction, is required to correctly estimate the reflected sky radiation (Mätzler, 2006, Chapter 4.3.2). The bistatic scattering coefficient can have complex shapes and is generally not known. As a simplification, the surface reflection $r(\nu, p, \theta)$ is assumed to consist of a specular component $r_\mathrm{s}(\nu, p, \theta)$ and a diffuse component $r_\mathrm{d}(\nu)$. The specular component is polarized and angle-dependent, while the diffuse component is unpolarized and described by Lambertian scattering, which is independent of the angle. This leads to the equation of the upwelling radiation at the surface as a combination of specular and Lambertian contributions

$$T_\mathrm{b,surf} = e(\nu, p, \theta)T_\mathrm{s} + r_\mathrm{s}(\nu, p, \theta)T_\mathrm{b,down}(\nu, \theta) + r_\mathrm{d}T_\mathrm{b,down,d}, \tag{2.26}$$

with the diffusely scattered sky radiation $T_\mathrm{b,down,d}$ given by integrating the downwelling atmospheric radiation T_sky over the sky hemisphere

$$T_\mathrm{b,down,d} = 2\int_0^1 T_\mathrm{sky}(\mu')\mu' d\mu'. \tag{2.27}$$

An effective incidence angle is often used to approximate the Lambertian reflection. As shown by Matzler (2005), this angle varies typically between 50–60°

and tends toward 60° for low zenith opacity. With increasing zenith opacity, the effective incidence angle decreases as shown in Fig. 2.10 for a humid and dry atmosphere. Clearly, the wrong assumption on the surface reflection type would cause a large bias at nadir. However, even a fixed effective incidence angle causes biases, as can be seen in the shift at 243 GHz of the effective incidence angle from humid to dry conditions (Fig. 2.10c,g). Therefore, the most accurate approach is to perform an integration over the downwelling radiation using a combination of observations and simulations (Harlow, 2009). In general, the difference between Lambertian and specular reflection decreases if the atmosphere is very transparent, the incidence angle is near the effective Lambertian incidence angle, or the emissivity is close to unity (Mätzler, 2006, Chapter 4.3.2).

A main challenge in the Arctic is the change in surface reflection type depending on the surface properties. While the ocean reflects mostly specular, snow-covered surfaces, including sea ice, follow Lambertian scattering (Harlow, 2009; Bormann, 2022). This introduces challenges when the surface type within the radiometer footprint is unknown. Additionally, the surface reflection varies seasonally over snow surfaces (Guedj et al., 2010).

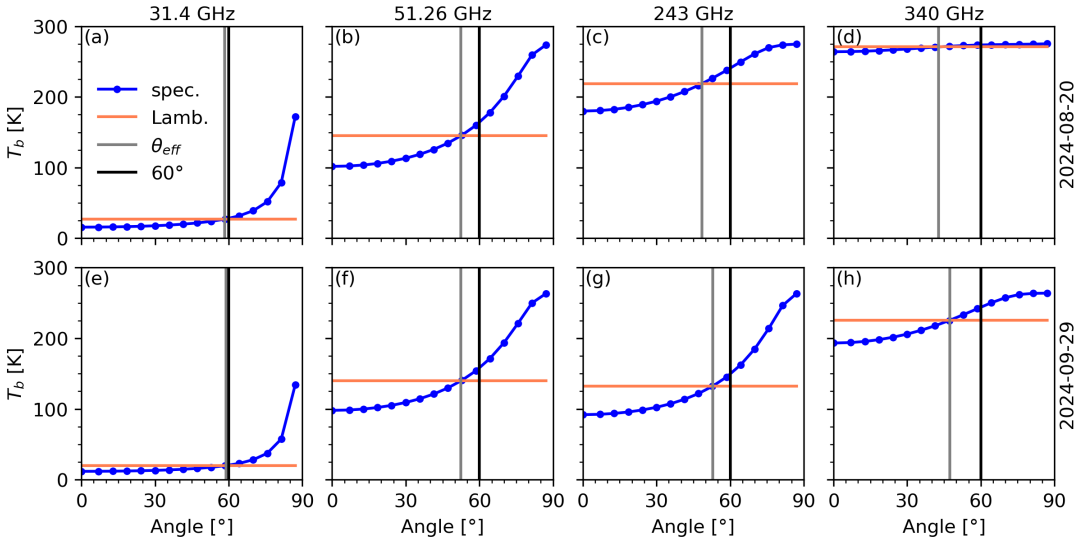

Figure 2.10: PAMTRA simulations of the reflected downwelling radiation under specular (spec.) and Lambertian (Lamb.) reflection at (a, e) 31.4, (b, f) 51.26, (c, g) 243, and (d, h) 340 GHz on 20 August (top) and 29 September 2024 (bottom) at 12 UTC. The simulations are based on retrieved temperature and humidity profiles and liquid water path (Walbröl et al., 2022) of the HATPRO microwave radiometer (Rose et al., 2005) during the VAMPIRE campaign. The liquid water path during the simulations is very low with $< 10\,\mathrm{g\,m^{-2}}$, and the integrated water vapor is $14\,\mathrm{kg\,m^{-2}}$ on 20 August and $5\,\mathrm{kg\,m^{-2}}$ on 29 September. Vertical lines indicate the effective Lambertian incidence angle as simulated with PAMTRA θ_{eff} and for the limit of zenith opacity $\tau \to 0$ (60°; Matzler, 2005).

2.5 Machine learning

2.5.1 Unsupervised clustering

Unsupervised machine learning techniques are widely applied in meteorology and remote sensing, where large amounts of unlabeled data are available from models and observations. Unlabeled means that the category of a sample is unknown due to the lack of resources for manual labeling to train a supervised classifier. A blend between unsupervised and supervised tasks is the self-supervised approach, where the model creates its own label from an augmented version of the sample (Caron et al., 2021). The categories are assigned based on the specific classification task to be solved, such as cloud pattern taxonomy (e.g., Chatterjee et al., 2023), moisture transport pathways (e.g., Mewes and Jacobi, 2019), or surface emissivity and backscatter classification (e.g., Munchak et al., 2020; Soriot et al., 2022). Here, we perform clustering of a small data set with low-dimensional samples using an unsupervised approach to objectively separate observed emissivity spectra into distinct groups (Wang et al., 2017b; Camplani et al., 2021). Distinct means that each cluster contains emissivity spectra that differ from those in other clusters. The resulting clusters can be analyzed with respect to the spatiotemporal occurrence and physical surface properties.

Here, we apply the k-means clustering algorithm (MacQueen, 1967) and related score metrics implemented in the Python package scikit-learn (Pedregosa et al., 2011). The k-means algorithm splits a data set with N samples $X = \{x_1, \ldots, x_N\}$ into K disjoint clusters $C = \{C_1, \ldots, C_K\}$ with cluster centers (centroids) $M = \{m_1, \ldots, m_K\}$. A solution is found by minimizing the within-cluster sum of squares W between each sample x_i and the cluster center m_k of the corresponding subset C_k (Likas et al., 2003)

$$W = \sum_{i=1}^{N} \sum_{k=1}^{K} I(x_i \in C_k) \|x_i - m_k\|^2. \tag{2.28}$$

The indicator function is defined as $I(X) = 1$ if X is true, and $I(X) = 0$ otherwise.

The optimal number of clusters, in which the algorithm should split the observed emissivity spectra, is unknown. Therefore, k-means is applied to a range of possible K, and three heuristics are employed to find the optimal number of clusters from the different clustering results. The methods are the elbow method (Thorndike, 1953), Calinski–Harabasz index (Calinski and Harabasz, 1974), and silhouette score (Rousseeuw, 1987), and are outlined in the following.

The elbow method is based on the change of the within-cluster sum of squares

(W) as a function of K (Thorndike, 1953). It assumes that W decreases strongly for cluster amounts less than the optimal number of clusters, and flattens when the number of clusters exceeds the optimal number of clusters.

The Calinski–Harabasz index or variance ratio criterion (VRC) is defined as (Calinski and Harabasz, 1974)

$$VRC = \frac{B/(M-1)}{W/(N-M)}, \tag{2.29}$$

with the between-cluster sum of squares (B)

$$B = \sum_{k=1}^{K} N_k \|m_k - m\|^2, \tag{2.30}$$

where N_k is the number of samples in cluster C_k, and m the mean of all samples. High values of the Calinski–Harabasz index correspond to an optimal number of clusters.

The silhouette score is the mean silhouette coefficient $s(x_i)$ over all samples N defined as (Rousseeuw, 1987)

$$s(x_i) = \frac{b(x_i) - a(x_i)}{\max[a(x_i), b(x_i)]}, \tag{2.31}$$

where $a(x_i)$ denotes the mean distance between the sample x_i to other samples within its cluster, and $b(x_i)$ the mean distance between the sample x_i to samples within the next nearest cluster. If the silhouette score is close to 1, it indicates that the sample x_i is assigned to the correct cluster. The optimal number of clusters will yield the highest silhouette score.

2.5.2 Regression

Machine learning algorithms are widely used for supervised regression tasks due to their ability to extract features from raw input through a general-purpose learning procedure (LeCun et al., 2015). During training, the model weights are optimized by mapping the inputs to the corresponding outputs. Hence, they are also suitable for emissivity estimation from satellite observations (Geer, 2024b; Kang et al., 2025). In this thesis, the microwave emissivity is estimated from input grayscale camera images obtained during VAMPIRE with the goal of detecting the link between snow cover and the microwave emissivity. To learn the underlying relationship for this narrow objective, a convolutional neural network (CNN; Lecun et al., 1998) followed by a multi-layer perceptron (MLP; Rumelhart et al., 1986) is applied. The model is implemented using the Python package Py-

Torch (Paszke et al., 2019). Details on the lightweight network architecture, loss function, and hyperparameters of the CNN and MLP are outlined in Chapter 4. The following provides an overview of the two main building blocks, the CNN and the MLP.

CNNs are designed to process data in the form of arrays, such as grayscale images, by exploiting the properties of natural signals (LeCun et al., 2015). Weights are shared throughout the image to extract objects and shapes invariant to location. Additionally, CNNs make use of the local connectivity, meaning that pixels in an image close to each other are correlated and share similar properties. This local information can be combined by pooling operations, which are essential to reduce the dimensionality and compress the information content of the image. Through the sequential operations of many layers, the local information (edges) is assembled into motifs that finally compose an object. For the application of this thesis, the object corresponds to the sea ice property relevant for the microwave emissivity.

The basic architecture of a CNN consists of a convolutional layer (convolution and activation) followed by a pooling layer (Yamashita et al., 2018). The convolutional layer performs discrete convolutions of the image using kernels that slide through the rows and columns of the image. Typically, several kernels are used, which expand the two-dimensional input to a three-dimensional feature map after the first convolutional layer. The result of the convolution is processed through an activation function. Here, we use the rectified linear unit (ReLU), defined as $f(z) = \max(z, 0)$, which learns faster than smoother functions in multi-layer neural networks (Glorot et al., 2011). The ReLU activation functions essentially mutes a node if the result of the weighted sum is negative. The pooling operations typically compute the maximum or average of a local patch of the feature map along the spatial dimension. As adjacent pooling kernels are shifted, the operation shrinks the spatial dimension of the image representation. Through several repeats of convolutional and pooling operations, the model captures an increasingly larger field of view, although individual operations only capture local information of the feature map. The compressed information on the object-level information of the image is passed to the MLP as a vector. Here, global average pooling is applied to average the spatial dimension of the CNN, which reduces the number of parameters in the MLP and makes the CNN flexible to various image sizes (Yamashita et al., 2018).

The multi-layer perceptron consists of an input layer, one or more hidden layers, and an output layer (LeCun et al., 2015). In this thesis, the input layer contains the feature vector extracted from the CNN, and the output layer maps

to the emissivity. The mapping between layers is a weighted sum

$$\mathbf{y} = \mathbf{x}\mathbf{A}^T + \mathbf{b} \tag{2.32}$$

of the input from a previous layer $\mathbf{x}$ with the 2-dimensional weights matrix $\mathbf{A}$ and a bias vector $\mathbf{b}$. The result of this computation is then passed through a non-linear activation function. As for the CNN, we use the ReLU activation function. A linear activation function is applied when mapping the output layer.

The model parameters are randomly initialized and updated iteratively during the model training. After a forward pass on a subset of the data, the prediction is compared to the corresponding target. A loss function is evaluated to quantify the distance of the prediction to the target. Through backpropagation, the gradient of each parameter with respect to the loss function is computed. Afterward, the parameters of the CNN (kernel weights) and MLP (node weights and biases) are updated based on stochastic gradient descent (Kingma and Ba, 2017). By iteratively updating the parameters for a certain number of epochs, the model predictions improve. Typically, a validation set is used to monitor overfitting by comparing its loss to the training loss for each epoch. The training is terminated once a certain convergence criterion is reached. The generalizability of the trained model can be assessed from an unseen test set.

Chapter 3

Sea ice emissivity at submillimeter waves

This study exploits airborne microwave radiometer observations over sea ice obtained during the ACLOUD and AFLUX field campaigns and collocated satellite observations. The study has been published in:

Risse, N. et al. 2024: Assessing sea ice microwave emissivity up to submillimeter waves from airborne and satellite observations, *The Cryosphere*, 18, 4137–4163, doi:10.5194/tc-18-4137-2024.

The content of this chapter has been published under the Creative Commons Attribution 4.0 License. Formatting changes were made to adopt the format of this thesis.

Detailed author contributions: Nils Risse conducted the emissivity retrieval, data analysis, and visualization and prepared the paper. Susanne Crewell, Mario Mech, and Nils Risse conceptualized the study. Susanne Crewell and Mario Mech carried out the field observations. Catherine Prigent and Gunnar Spreen provided valuable expertise in interpreting emissivity signatures. All authors reviewed and edited the paper.

Assessing sea ice microwave emissivity up to submillimeter waves from airborne and satellite observations

Nils Risse[1], Mario Mech[1], Catherine Prigent[2], Gunnar Spreen[3], and Susanne Crewell[1]

[1]Institute for Geophysics and Meteorology, University of Cologne, Cologne, Germany

[2]Laboratoire d'Études du Rayonnement et de la Matière en Astrophysique et Atmosphères, Observatoire de Paris, CNRS, Paris, France

[3]Institute of Environmental Physics, University of Bremen, Bremen, Germany

Correspondence: Nils Risse (n.risse@uni-koeln.de)

Abstract Upcoming submillimeter wave satellite missions require an improved understanding of sea ice emissivity to separate atmospheric and surface microwave signals under dry polar conditions. This work investigates hectometer-scale observations of airborne sea ice emissivity between 89 and 340 GHz, combined with high-resolution visual imagery from two Arctic airborne field campaigns that took place in summer 2017 and spring 2019 northwest of Svalbard, Norway. Using k-means clustering, we identify four distinct sea ice emissivity spectra that occur predominantly across multiyear ice, first-year ice, young ice, and nilas. Nilas features the highest emissivity, and multiyear ice features the lowest emissivity among the clusters. Each cluster exhibits similar nadir emissivity distributions from 183 to 340 GHz. To relate hectometer-scale airborne measurements to kilometer-scale satellite footprints, we quantify the reduction in the variability of airborne emissivity as footprint size increases. At 340 GHz, the emissivity interquartile range decreases by almost half when moving from the hectometer scale to a footprint of 16 km, typical of satellite instruments. Furthermore, we collocate the airborne observations with polar-orbiting satellite observations. After resampling, the absolute relative bias between airborne and satellite emissivities at similar channels lies below 3 %. Additionally, spectral variations in emissivity at nadir on the satellite scale are low, with slightly decreasing emissivity from 183 to 243 GHz, which occurs for all hectometer-scale clusters except those predominantly composed of multiyear ice. Our results will enable the development of microwave retrievals and assimilation over sea ice in current and future satellite missions, such as the Ice Cloud Imager (ICI) and EUMETSAT Polar System – Sterna (EPS–Sterna).

3.1 Introduction

Passive microwave observations from polar-orbiting satellites have continuously monitored polar regions with high spatial coverage for over 5 decades (Comiso and Hall, 2014). These observations are essential for atmosphere (e.g., Triana-Gómez et al., 2020; Perro et al., 2020), sea ice (e.g., Spreen et al., 2008; Kilic et al., 2020; Soriot et al., 2023), and joint atmosphere–sea-ice retrievals (e.g., Scarlat et al., 2020; Rückert et al., 2023b; Kang et al., 2023). Such satellite-based retrievals help us to understand the accelerated Arctic near-surface warming compared to the global mean (Rantanen et al., 2022; Wendisch et al., 2023). However, the highly variable sea ice emissions cause uncertainties in satellite retrievals and severely limit the use of surface-sensitive microwave channels in operational numerical-weather-prediction data assimilation compared to the open ocean (Lawrence et al., 2019). Therefore, current research aims to improve the assimilation of microwave observations over sea ice; for example, Bormann (2022) showed improved performance occurs when Lambertian rather than specular reflection is assumed in forward simulations.

Further spaceborne capabilities will become available through the novel Ice Cloud Imager (ICI; Buehler et al., 2007) and EUMETSAT Polar System – Sterna (EPS–Sterna; Albers et al., 2023) instruments, which will feature operational channels above 200 GHz for the first time. These channels provide higher sensitivity to small cloud ice particles than current passive microwave sensors (Buehler et al., 2012; Wang et al., 2017a; Eriksson et al., 2020). However, variable emissions from polar surfaces also significantly contribute to the atmospheric signal received at the 243 (ICI only) and 325 GHz channels due to the dry atmosphere (Wang et al., 2017b).

While there is considerable interest in expanding sea ice emissivity estimates to account for submillimeter waves, few field observations cover this frequency range. The first brightness temperature (TB) observations of sea ice at 220 GHz were obtained using an airborne cross-track scanning radiometer (Hollinger et al., 1984). However, sea ice emissivity was derived only at lower frequencies, up to 140 GHz, due to high TB noise and low atmospheric transmissivity at 220 GHz during the field study. The observations revealed similar nadir emissivities at 90 and 140 GHz, with higher emissivity over young ice (0.96) and lower emissivity over multiyear ice (0.68). Airborne observations with along-track scanning radiometers from Hewison and English (1999) provide detailed emissivity spectra for typical sea ice types and snow from 24 to 157 GHz and demonstrate the importance of volume scattering within snow at 157 GHz. Hewison et al. (2002) calculated the nadir emissivities of sea ice from 24 to 183 GHz at different de-

velopment stages, from new ice to multiyear ice, using similar instrumentation to that used in Hewison and English (1999). New-ice emissivities were highest at 89 GHz, measuring 0.95, and slightly decreased to 0.9 at 183 GHz. First-year ice emissivities decreased from 24 to 157 GHz and slightly increased from 157 to 183 GHz. This emissivity increase at higher frequencies was also found for multiyear ice. Haggerty and Curry (2001) observed first-time emissivities of up to 243 GHz at nadir at a resolution of $\sim$1 km^2. However, leads, which are typically smaller, could not be resolved. The 340 GHz channel aboard the same aircraft was insensitive to surface emission due to low atmospheric transmissivity. Airborne observations by Wang et al. (2017b) measured sea ice emissivities of up to 325 GHz, revealing high spatial variability, but the driving sea ice properties at this frequency could not be estimated.

While field studies demonstrate the high sensitivity of microwaves to sea ice and snow properties in limited regions, only global sea ice emission information allows for atmospheric retrievals from satellites. As modeling sea ice emissions is computationally expensive and requires detailed knowledge of sea ice and snow properties (Royer et al., 2017; Picard et al., 2018; Rückert et al., 2023b), which is missing on global scales, spaceborne emissivity climatologies have been developed (Wang et al., 2017b; Munchak et al., 2020). The Tool to Estimate Land Surface Emissivity from Microwave to Submillimeter Waves (TELSEM2; Wang et al., 2017b) climatology for sea ice and land surfaces extrapolates emissivities up to 700 GHz to provide first-guess emissivities for upcoming satellite missions, such as ICI. To simultaneously retrieve atmospheric, sea ice, and snow properties, radiative-transfer models of sea ice and atmosphere have been combined (Rückert et al., 2023b; Kang et al., 2023). Kang et al. (2023) additionally simulated sea ice growth to increase the temporal consistency of the retrieved sea ice and snow properties. However, sea ice radiative-transfer models might only be valid below 100 GHz. Recently, observed snow emissivities (up to 243 GHz) were successfully simulated based on realistic snow properties (Wivell et al., 2023). This result highlights the need for similar sea ice emissivity field observations that account for submillimeter waves to improve future modeling studies of sea ice. These field observations must also be related to satellite observations, which resolve the surface at a much coarser resolution.

The limitation of sea ice emissivity observations at the scale of submillimeter waves and their relevance for future satellite missions motivate our study, which is structured around two objectives. First, we aim to identify critical physical sea ice and snow properties affecting emissivity up to submillimeter wavelengths, as observed during two airborne field campaigns. We calculate the sea ice emissivity from TBs at 89 (25° incidence angle; horizontal polarization), 183, 243,

and 340 GHz (nadir) using the airborne Microwave Radar/radiometer for Arctic Clouds (MiRAC; Mech et al., 2019). Then, we characterize typical emissivity spectra with airborne visual imagery and surface temperature observations. Second, we aim to relate the observed hectometer-scale emissivity observations to the satellite scale. This includes an assessment of emissivity variability as a function of footprint size. Furthermore, we collocate MiRAC with observations from polar-orbiting satellites and analyze spectral variations in emissivity observed at satellite resolutions from 89 to 340 GHz, relevant for upcoming satellite missions (such as ICI and EPS–Sterna).

The paper is outlined as follows. Section 3.2 describes the airborne field data, microwave instruments, and auxiliary data. Section 3.3 details the emissivity calculation. Section 3.4 identifies relevant sea ice and snow properties that affect emissivity pertaining to airborne observations. Section 3.5 compares emissivity levels between airborne and satellite observations, and the study is summarized and concluded in Sect. 3.6.

3.2 Data

3.2.1 Field data

We use airborne observations from two campaigns: Arctic CLoud Observations Using airborne measurements during polar Day (ACLOUD), from 23 May to 26 June 2017 (Wendisch et al., 2019; Ehrlich et al., 2019c), and Airborne measurements of radiative and turbulent FLUXes of energy and momentum in the Arctic boundary layer (AFLUX), from 19 March to 11 April 2019 (Mech et al., 2022a). Both campaigns were conducted as part of the "Arctic Amplification: Climate Relevant Atmospheric and Surface Processes and Feedback Mechanisms" ((AC)^3) research project (Wendisch et al., 2023). The research flights (RFs) with the *Polar 5* aircraft (Wesche et al., 2016) from the Alfred Wegener Institute, Helmholtz Centre for Polar and Marine Research (AWI), covered the Fram Strait, located northwest of Svalbard, Norway (Fig. 3.1). *Polar 5* carried MiRAC (a microwave package), the KT-19 (a thermal infrared sensor), and a visual camera, as well as other instruments. Various sea ice characteristics were observed with *Polar 5* during the ACLOUD campaign (i.e., during RF23 on 25 June and RF25 on 26 June 2017) and the AFLUX campaign (i.e., during RF08 on 31 March, RF14 on 8 April, and RF15 on 11 April 2019) under clear-sky conditions and over sea ice suitable for emissivity estimation. During the two ACLOUD flights, melt ponds formed on the sea ice, and there was open water between individual ice floes. During the three AFLUX flights, snow-covered sea ice, mostly composed of multiyear

ice (Fig. 3.9), prevailed, with nilas found in refrozen leads between individual ice floes. Higher fractions of open water during the AFLUX campaign were only observed in the marginal sea ice zone of RF08. The infrared-based mean surface temperatures were near the freezing point, ranging from 0.8 to 1 °C during both ACLOUD flights, and well below the freezing point, ranging from −22 to −17 °C during the three AFLUX flights. The integrated water vapor, derived from in situ observations (see Sect. 3.2.4), was about 10 to 10.3 kg m^{-2} during the two ACLOUD flights and 1.3 to 2 kg m^{-2} during the three AFLUX flights, which indicates reduced water vapor emissions and high atmospheric transmissivity during the AFLUX campaign.

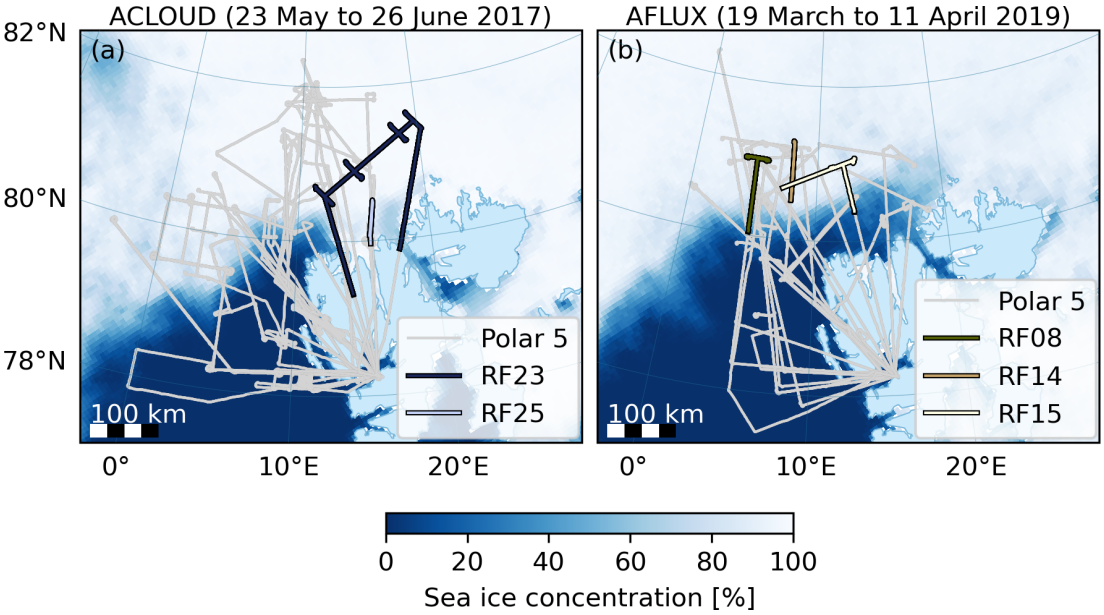

Figure 3.1: All *Polar 5* flights, clear-sky segments over sea ice, and mean sea ice concentrations (Spreen et al., 2008) during **(a)** the ACLOUD campaign, from 23 May to 26 June 2017, and **(b)** the AFLUX campaign, from 19 March to 11 April 2019.

3.2.2 Airborne microwave instruments

Polar 5 carried the MiRAC package, which includes the combined active–passive component (MiRAC-A), mounted inside a belly pod beneath the aircraft's fuselage, and the solely passive component (MiRAC-P), deployed inside the aircraft cabin (Mech et al., 2019). MiRAC-A consists of a 94 GHz cloud radar and a passive 89 GHz channel with horizontal polarization, measuring backward with a 25° incidence angle. MiRAC-P measures at six double-sideband water vapor channels (183.31 ± 0.6, ±1.5, ±2.5, ±3.5, ±5.0, and ±7.5 GHz) and two window channels (243 and 340 GHz) at nadir (see Table 3.1). Both MiRAC components measure at a temporal resolution of 1 s. We exclude MiRAC-A observations collected during

low flights, i.e., when the slant path between the instrument and the surface is less than 500 m, due to contamination resulting from back-scattered broadband noise from the cloud radar. This threshold means MiRAC-A is entirely excluded during ACLOUD RF25, where the flight altitude during clear-sky transects over sea ice ranges from 60 to 350 m. For the other four flights, the typical flight altitudes range from 60 m to 3 km, with about 80 % (15 %) of the time spent below 500 m (above 2.5 km). Furthermore, we exclude observations with aircraft roll or pitch angles above 10°. The flight distance over which MiRAC provides emissivities depends on the channel, ranging from 400 km at 89 GHz to 1,700 km at 243 GHz. For about 200 km of this distance, all MiRAC-A and MiRAC-P channels provide emissivities nearly instantaneously – i.e., the spatially matched footprint centers of MiRAC-P and the inclined MiRAC-A are less than 200 m apart.

The instrument receivers were calibrated with a two-point calibration using liquid nitrogen and an internal target at the beginning of each campaign. In addition, MiRAC-A performed gain calibrations every 15 min (and MiRAC-P performed them every 20 min) during flights using an internal target (Mech et al., 2019). After the campaign, we applied a bias correction to the 89 GHz TBs, following Konow et al. (2019); this was based on Passive and Active Microwave radiative TRAnsfer (PAMTRA; Mech et al., 2020) forward simulations and used dropsonde profiles under clear-sky conditions over the open ocean, extended by ERA5 reanalysis (Hersbach et al., 2020) to the top of the atmosphere, and a sea surface temperature analysis (UK Met Office, 2012) as inputs. The added 89 GHz TB offset for the ACLOUD (AFLUX) flights in this study is 11 (32) K and decreases linearly toward higher TBs. This high calibration offset occurred due to difficult weather conditions during the liquid-nitrogen calibration. We estimate the accuracy of the offset correction to be 2 K. For MiRAC-P, no such calibration issues occurred due to its location inside the aircraft cabin (Mech et al., 2019). The TB noise is about 0.5 K for MiRAC-A (Küchler et al., 2017) and MiRAC-P (Mech et al., 2019), indicating an upper bound of the observed TB noise of 0.2 to 0.3 K, based on a homogeneous time series during ACLOUD RF10. This random noise cancels out when averaging, but we do not consider this here as systematic effects dominate the overall emissivity uncertainty (see Sect. 3.3.2). Hence, we assume the overall TB uncertainty from bias correction and noise to be 2.5 K at 89 GHz and 0.5 K at all other frequencies. The footprint size at a 60 m s^{-1} flight velocity with a 1 s integration time is about 70×130 m^2 at 3 km flight altitude and 1×60 m^2 at 60 m flight altitude at 183 GHz, i.e., at nadir with an opening angle of 1.3° (see Table 3.1). We shift the MiRAC measurement time by 1 to 2 s (2 to 5 s) during the ACLOUD (AFLUX) campaign relative to the infrared radiometer KT-19 as determined from lagged correlations between

243 GHz TBs and KT-19 infrared TBs during the clear-sky sea ice emissivity flight segments. Note that the 243 GHz channel showed the highest correlation with the infrared TB of all MiRAC-P channels during both campaigns due to its high atmospheric transmission compared to the other MiRAC-P channels.

Table 3.1: Specifications of the passive MiRAC-A and MiRAC-P channels. H: horizontal. V: vertical.

Instrument	Channel	Frequency (GHz)	Polarization	Incidence angle (°)	Field of view (°)
MiRAC-A	1	89	H	25	0.85
MiRAC-P	1	183.31 ± 0.6	V	0	1.3
	2	183.31 ± 1.5	V	0	1.3
	3	183.31 ± 2.5	V	0	1.3
	4	183.31 ± 3.5	V	0	1.3
	5	183.31 ± 5.0	V	0	1.3
	6	183.31 ± 7.5	V	0	1.3
	7	243	H	0	1.25
	8	340	H	0	1.0

3.2.3 Satellite microwave instruments

We focus on commonly used cross-track and conical polar-orbiting scanning microwave radiometers. These include the Microwave Humidity Sounder (MHS; EUMETSAT, 2010), the Advanced Technology Microwave Sounder (ATMS; Kim et al., 2014), the Special Sensor Microwave Imager/Sounder (SSMIS; Kunkee et al., 2008), and the Advanced Microwave Scanning Radiometer 2 (AMSR2; JAXA, 2016); their platforms and specifications are summarized in Table 3.2. To ensure consistency among the sensors, we use intercalibrated Level 1C TB data (NASA Goddard Space Flight Center and GPM Intercalibration Working Group, 2022). This intercalibration corrects offsets between the constellation satellites using the well-calibrated Global Precipitation Measurement (GMP) Microwave Imager (GMI) (Hou et al., 2014), which covers up to 65° N, as a reference (Berg et al., 2016).

MHS and ATMS conduct cross-track scanning at incidence angles of up to 59 and 64°, respectively, and the SSMIS and AMSR2 scan conically at incidence angles of 53 and 55°, respectively. MHS and ATMS measure TBs with nominal vertical (QV) or nominal horizontal (QH) polarization at nadir, rotating with view angle α. These TBs are expressed as

$$T_{\mathrm{b,QV}} = T_{\mathrm{b,V}} \cos^2(\alpha) + T_{\mathrm{b,H}} \sin^2(\alpha) \tag{3.1}$$

and

$$T_{\mathrm{b,QH}} = T_{\mathrm{b,H}} \cos^2(\alpha) + T_{\mathrm{b,V}} \sin^2(\alpha), \tag{3.2}$$

respectively. We only use MHS and ATMS data with incidence angles from 0 to 30° because these angles provide observation conditions similar to those of MiRAC. Moreover, fewer footprints with higher incidence angles collocate with MiRAC, and their increased footprint sizes make comparisons more uncertain. Using this incidence angle filter for MHS and ATMS, the footprint sizes are mostly around $16 \times 16\,\mathrm{km}^2$, with the highest resolution of $3 \times 5\,\mathrm{km}^2$ provided by AMSR2. MHS aboard the NOAA-18 spacecraft only operated during the ACLOUD campaign, and the Metop-C and NOAA-20 spacecraft only operated during the AFLUX campaign. The 150 GHz channel of the SSMIS aboard the DMSP-F18 satellite was unavailable due to its failure (Berg et al., 2016).

MiRAC overlaps spectrally with MHS, ATMS, and SSMIS at 89 and 183 GHz and overlaps spectrally with AMSR2 at 89 GHz. However, MiRAC's 89 GHz channel, which measures under horizontal polarization at 25°, is not directly comparable with the satellite channels because MHS and ATMS mostly measure vertically polarized TBs near this incidence angle, and SSMIS and AMSR2 measure at higher incidence angles. Only MiRAC's 183 GHz near-nadir channel is directly comparable with near-nadir observations from MHS and ATMS.

3.2.4 Ancillary observations

The emissivity retrieval requires ancillary information on the atmospheric thermodynamic profile and surface temperature. We construct the thermodynamic profile below 3 km altitude from measurements of the aircraft's nose boom and dropsondes, and we construct the thermodynamic profile above 3 km altitude from radiosondes (Maturilli, 2020) launched at the AWIPEV station, operated jointly by the AWI and the Polar Institute Paul-Emile Victor (IPEV) in Ny-Ålesund, Svalbard, Norway (Neuber, 2003). If no dropsonde information is available over sea ice, we assume constant temperature and humidity from the lowest flight altitude of about 100 m down to the surface. The air temperature measured at these heights differs by less than 5 K from the mean surface temperature, which indicates that the profiles capture typical Arctic surface temperature inversions (e.g., Tjernström and Graversen, 2009). The uncertainties in temperature and relative humidity are ±0.2 K and ±2 % for dropsondes (Vaisala, 2010), ±0.2–0.4 K and ±3–4 % for radiosondes (Maturilli, 2020), and ±0.3 K and ±0.4 % for the nose boom (Ehrlich et al., 2019c).

The KT-19 aboard *Polar 5* provides infrared TBs integrated over the atmospheric window from 9.6 to 11.5 µm, with a 1 s resolution and an opening angle of

Table 3.2: Specifications of the MHS, ATMS, SSMIS, and AMSR2 channels used in this study. The instantaneous field of view (IFOV) from MHS and ATMS is given for nadir observations. The polarizations for MHS and ATMS are either nominal vertical (QV) at nadir, rotating with the view angle, or nominal horizontal (QH) at nadir, rotating with the view angle. The polarizations for SSMIS and AMSR2 are either horizontal (H) or vertical (V). Only 0–30° incidence angles from MHS and ATMS are used here.

Instrument	Channel	Frequency (GHz)	Polarization	Incidence angle (°)	IFOV (km^2)
MHS (Metop-A, Metop-B, Metop-C[a], NOAA-18[b], NOAA-19)	1	89	QV	0–30	16×16
	2	157	QV	0–30	16×16
	5	190.31	QV	0–30	16×16
ATMS (SNPP, NOAA-20[a])	16	88.2	QV	0–30	32×32
	17	165.5	QH	0–30	16×16
	18	183.31 ± 7	QH	0–30	16×16
SSMIS (DMSP-F16, DMSP-F17, DMSP-F18)	17	91.655	V	53	9×15
	18	91.655	H	53	9×15
	8	150	H	53	9×15
	9	183.31 ± 6.6	H	53	9×15
AMSR2 (GCOM-W1)	13	89	V	55	3×5
	14	89	H	55	3×5

[a] Satellite only operated during the AFLUX campaign. [b] MHS aboard NOAA-18 only operated during the ACLOUD campaign

2° at nadir. Hence, its opening angle is slightly larger than MiRAC's opening angles. The accuracy of the KT-19 is about ±0.5 K. The infrared TBs are converted to surface skin temperatures with an infrared emissivity of 0.995, similar to Høyer et al. (2017) and Thielke et al. (2022), which approximates the infrared emissivity of typical sea ice types and oceans with an accuracy of 0.01 to 0.02 (Hori et al., 2006). We use the KT-19 data as input for the sea ice emissivity calculation for MiRAC. We also require an accurate description of the surface temperature at the satellite footprint scale, which has higher spatial coverage than the KT-19. Therefore, we use the daily "Arctic Ocean – Sea and Ice Surface Temperature" reanalysis (Level 4) with a resolution of $0.05 \times 0.05°$ (Nielsen-Englyst et al., 2023), which matches the AMSR2 satellite footprint size (hereafter referred to as NE23). The product derives daily gap-free sea and ice surface temperatures from clear-sky thermal infrared satellite observations sensitive to the upper few millimeters of snow or ice (Warren, 1982) and passive microwave-based sea ice concentrations. A comparison between the airborne surface temperatures based on the KT-19 and the NE23 temperatures reveals biases of 4 to 6 K during the ACLOUD campaign and biases of -1 to 1 K during the AFLUX campaign (KT-19 minus NE23). During the ACLOUD campaign, the KT-19 temperatures are close to the melting point, which agrees with observed melting conditions and a snow liquid water fraction of around 15 % (Rosenburg et al., 2023). We use the nearest NE23 ice surface temperature pixel to the satellite footprint as input for the sea ice emissivity calculation for satellites. Furthermore, a downward-looking camera equipped with a fish-eye lens operating in the visible spectrum (red, green, and blue) aboard *Polar 5* provides information on sea ice characteristics every 4 to 6 s. Finally, three data products contribute surface information: daily sea ice concentration maps from the University of Bremen with a $6.25 \times 6.25\,\mathrm{km}^2$ resolution, based on AMSR2 (Spreen et al., 2008); daily wintertime multiyear ice concentration maps from the University of Bremen with a $12.5 \times 12.5\,\mathrm{km}^2$ resolution, based on AMSR2 and the Advanced Scatterometer (ASCAT; Melsheimer and Spreen, 2022); and Sentinel-2B Level 2A (L2A) visual images with a $20 \times 20\,\mathrm{m}^2$ resolution (European Space Agency, 2021). Although the multiyear ice concentration product incorporates microwave observations from AMSR2 and ASCAT that may correspond to observations collected at MiRAC frequencies, the implemented temperature and drift corrections increase independence between multiyear ice concentration and MiRAC TB.

We utilize topographic data from the Norwegian Polar Institute to exclude observations over land and near the coastline (Norwegian Polar Institute, 2014). Specifically, we exclude data within 150 m of the shoreline for MiRAC and within about one footprint radius of 2.5 km (8 km) for AMSR2 (MHS, ATMS, and SS-

MIS).

3.2.5 Collocation of MiRAC with satellites

To compare MiRAC with satellites, we require nearly simultaneous and spatially aligned observations. We achieve simultaneous observations by filtering collocations within a ±2 h window, which maximizes the number of satellite overpasses and minimizes the effects of sea ice drift. The sea ice drift during the flights is less than 1 km h^{-1}, based on data from the National Snow and Ice Data Center (NSIDC; Tschudi et al., 2020), and spatial variability exceeds temporal variability (not shown). Furthermore, we spatially align MiRAC with the nearest satellite footprints for each satellite overpass by imposing specific criteria: a footprint center distance threshold of about one footprint radius, corresponding to 2.5 km (8 km) for AMSR2 (MHS, ATMS, and SSMIS), and a minimum of 17 (50) MiRAC footprints within the AMSR2 (MHS, ATMS, or SSMIS) footprint. The latter criterion translates to a straight flight distance exceeding approximately 20 % of the satellite footprint diameter (10 % for ATMS at 89 GHz).

The number of satellite overflights during the ACLOUD (AFLUX) campaign with collocated footprints from MHS, ATMS, SSMIS, and AMSR2 is 15 (23), 0 (8), 11 (26), and 2 (9), respectively. We matched channels near 89 GHz with MiRAC-A, and channels above 100 GHz were matched with MiRAC-P. The number of satellite footprints collocated with MiRAC at 89 GHz during the ACLOUD (AFLUX) campaign is 87 (86), 0 (34), 107 (175), and 23 (159) for MHS, ATMS, SSMIS, and AMSR2, respectively. The number of satellite footprints collocated with MiRAC above 100 GHz during the ACLOUD (AFLUX) campaign is 222 (138), 0 (46), and 277 (261) for MHS, ATMS, and SSMIS, respectively. Around 70 MiRAC footprints fall within each of the satellite footprints at 89 GHz, and about 200 fall within each satellite footprint at frequencies above 100 GHz. The difference is mainly related to the higher resolution of AMSR2 at 89 GHz.

3.3 Methodology

3.3.1 Effective sea ice emissivity calculation

We directly derive effective sea ice emissivity from observed clear-sky TBs and infrared-based skin temperatures, following Prigent et al. (1997). Typically, the skin temperature differs from the temperature of the emitting sea ice or snow layer (Tonboe, 2010). The depth of the emitting layer, or penetration depth, depends on sea ice and snow properties and decreases with increasing frequency (Tonboe et al., 2006). Emissivity based on skin temperature is commonly referred

to as effective emissivity, but hereafter, we use the term "emissivity" for better readability.

Harlow (2011) compared methods for estimating emitting-layer temperature from 183 GHz observations. However, their applicability to our data is limited by the absence of simultaneous downwelling 183 GHz TB measurements and uncertainties in the atmospheric profile impacting surface temperature estimates. Other studies employ precalculated penetration depths and observed sea ice temperature profiles for specific ice types (Mathew et al., 2008, 2009), which do not apply to the diverse sea ice conditions presented here.

The emissivity calculation is based on nonscattering radiative transfer (RT), which is valid under clear-sky conditions. The TB observed at aircraft or satellite height, denoted as T_b, is given by

$$T_\mathrm{b} = T_\mathrm{s} \cdot e \cdot t + T_\mathrm{b}^{\downarrow} \cdot t \cdot (1 - e) + T_\mathrm{b}^{\uparrow}, \tag{3.3}$$

where e represents surface emissivity, T_s represents surface temperature, t represents atmospheric transmissivity in the viewing direction between the surface and the aircraft/satellite height, $T_\mathrm{b}^{\downarrow}$ represents downwelling atmospheric radiation at the surface, and $T_\mathrm{b}^{\uparrow}$ represents upwelling atmospheric radiation at the observation height. Solving Eq. (3.3) for the surface emissivity yields

$$e = \frac{T_\mathrm{b} - T_\mathrm{b}^{\uparrow} - T_\mathrm{b}^{\downarrow} \cdot t}{(T_\mathrm{s} - T_\mathrm{b}^{\downarrow}) \cdot t}. \tag{3.4}$$

Equation (3.4) can be solved using two RT simulations with $e = 0$ and $e = 1$ (Mathew et al., 2008). The solution is expressed as

$$e = \frac{T_\mathrm{b} - T_\mathrm{b}(e = 0)}{T_\mathrm{b}(e = 1) - T_\mathrm{b}(e = 0)}. \tag{3.5}$$

We perform RT simulations for the *Polar 5* or satellite height using PAMTRA. In PAMTRA, we select the Rosenkranz (1998) gas absorption with modifications for water vapor continuum absorption (Turner et al., 2009). We simulate specular and Lambertian reflections separately.

Satellite-based emissivity studies typically limit the emissivity calculation to channels with high atmospheric transmissivity. Using aircraft, we can increase transmissivity by flying at low altitudes. However, in addition to transmissivity, the contrast between surface temperature and atmospheric downwelling TB dominates the surface sensitivity, i.e., the sensitivity of the observed TB to emissivity changes. This can be seen when calculating the partial derivative from Eq. (3.3),

given as follows:

$$\frac{\partial T_\mathrm{b}}{\partial e} = (T_\mathrm{s} - T_\mathrm{b}^{\downarrow}) \cdot t = T_\mathrm{b}(e = 1) - T_\mathrm{b}(e = 0). \tag{3.6}$$

This term corresponds to the denominator in Eq. (3.5) and should be maximized to avoid noisy emissivity estimates. We identify 40 K as a reasonable threshold below which emissivity noise exceeds typical signatures of sea ice. Observed mean surface sensitivities during the AFLUX campaign are 200 K (50 K) at 89 GHz (340 GHz). Only observations obtained at 183 and 340 GHz during the ACLOUD campaign fall below the surface sensitivity threshold and are excluded to avoid highly uncertain emissivity estimates.

3.3.2 Emissivity uncertainty estimation

We estimate the emissivity uncertainty by propagating errors from TB (see Sect. 3.2.2), air temperature, relative humidity, and surface temperature. The assumed uncertainties for air temperature and relative humidity are ±2 K and ±5 %, respectively. These assumed uncertainties are higher than the dropsonde and radiosonde uncertainties to account for representability errors along the flight path. The assumed uncertainty in surface temperature is ±3 K during the ACLOUD campaign and ±8 K during the AFLUX campaign. The surface temperature uncertainty pertaining to the ACLOUD campaign mainly accounts for errors in infrared emissivity and KT-19 measurement uncertainty. The higher uncertainty in surface temperature during the AFLUX campaign, compared to the ACLOUD campaign, accounts for the spread between surface skin temperature and emitting-layer temperature, which can deviate by up to 10 K at 89 GHz over multiyear ice due to insulating snow (Tonboe, 2010). During the ACLOUD campaign, we expect mostly isothermal sea ice due to surface melt (Perovich et al., 1997). The uncertainty estimation is performed only on aircraft data, not on satellite observations, because the MiRAC channels already include most satellite channels. A notably higher emissivity uncertainty occurs for satellites operating near 183 GHz than for MiRAC, due to the higher atmospheric contributions.

3.3.3 Surface reflection model

The surface reflection model affects the direction from which downwelling atmospheric radiation is reflected at the surface. Typically, the surface is approximated as either purely specular or Lambertian. Across specular surfaces, the incidence angle matches the reflection angle, whereas Lambertian surfaces exhibit isotropic and unpolarized reflection. High sensitivity to the assumed surface reflection type

occurs at nadir, where MiRAC conducts measurements, and low sensitivity occurs at incidence angles between 50 to 60°, where imagers like SSMIS and AMSR2 conduct measurements (Matzler, 2005; Karbou and Prigent, 2005).

Guedj et al. (2010) presented a method for constraining the surface reflection model at 50 GHz sounding channels by combining TB measurements with an emissivity retrieval. They calculated the emissivity at a wing channel of the absorption line to simulate an adjacent inner channel, finding Lambertian reflection across Antarctica in winter and seasonal variations in specular contributions. Here, we adapt the method to 183 GHz MiRAC observations collected during the three AFLUX flights by following three steps. First, we calculate emissivities at 183.31 ± 7.5 GHz under both specular and Lambertian reflection. Second, we use the emissivities derived at 183.31 ± 7.5 GHz to simulate TBs at 183.31 ± 5 GHz with PAMTRA, taking the respective surface reflection into account. Third, we compare the simulation with the observed TB at 183.31 ± 5 GHz. The bias distribution is closest to zero under the Lambertian assumption (Fig. 3.2). Despite the relatively high uncertainty near the water vapor absorption line, the results confirm Lambertian behavior of sea ice at 183 GHz, consistent with findings by Harlow (2011) and Bormann (2022).

In the following, we only present the emissivities calculated using Lambertian surface reflection from aircraft and satellites, based on findings collected at 183 GHz. Hence, we assume similar surface reflection behavior at 89, 243, and 340 GHz. Additionally, we assume that the reflection type identified during the AFLUX campaign also applies to ACLOUD observations, where 183 GHz surface emissivity data are lacking. However, at 89 GHz, it is well known that sea ice exhibits a distinct polarization signature (NORSEX Group, 1983), indicating a specular contribution to the reflection. While we are still able to reproduce polarization signatures from satellites operating at an incidence angle close to 50° (Matzler, 2005), the specular contribution modifies the magnitude of the simulated 25° reflected downwelling atmospheric TB. For MiRAC observations at 89 GHz, fully specular emissivities exceed fully Lambertian emissivities by about 6 % to 2 % during the ACLOUD campaign and by 3 % to 1 % during the AFLUX campaign when Lambertian emissivities range from 0.6 to 0.8. This emissivity uncertainty is comparable to or lower than the uncertainty due to the surface temperature assumption since sea ice is not fully specular at 89 GHz (Bormann, 2022).

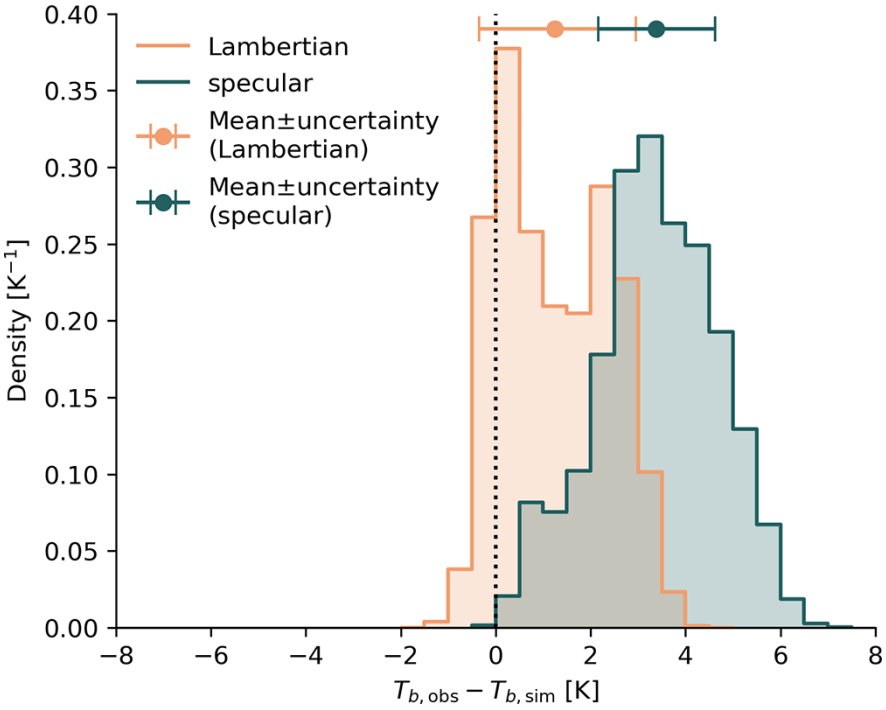

Figure 3.2: Histogram and mean of the difference between observed and simulated 183.31 ± 5 GHz TBs ($T_{b,obs}$ and $T_{b,sim}$, respectively), employing 183.31 ± 7.5 GHz emissivities under Lambertian and specular surface reflection during the AFLUX campaign. The TB bin width is 0.5 K.

3.4 Airborne observations

3.4.1 Case study

In this section, we first illustrate the available airborne observations collected along an 11 km transect during AFLUX RF08 on 31 March 2019 (Fig. 3.3). Satellite observations indicate that ∼75 % of the ice within the area is multiyear ice (Fig. 3.9). The sea ice types along the transect are distinguishable in airborne visual-camera observations (Fig. 3.3a–d) and Sentinel-2B imagery (Fig. 3.3e). We observe predominantly snow-covered sea ice from 0 to 7 km. Notably, surface structural variations from 3 to 4 km suggest the presence of young ice, defined as the transition stage between nilas and first-year ice (WMO, 2014) that is sometimes formed within leads among thicker multiyear ice. Progressing from 7 to 11 km, we encounter refrozen leads with nilas attached to individual snow-covered ice floes. The observed surface temperatures reflect the changing sea ice and snow properties, with almost constant temperatures of −24 °C over snow-covered sea ice and up to −18 °C over nilas. The TBs vary significantly with ranges of 76, 47, 48, and 30 K at 89, 183.31 ± 7.5, 243, and 340 GHz, respectively, and exceed the 6 K surface temperature range. This high variability demonstrates the importance of surface emissivity variations in the observed TB.

The difference between the minimum and maximum sea ice emissivity decreases as frequency increases, with values of 0.35, 0.27, 0.24, and 0.21 at 89, 183.31 ± 7.5, 243, and 340 GHz, respectively. The higher emissivity variability at 89 GHz compared to the other frequencies likely relates to its horizontal polarization at a 25° incidence angle. Previous studies have shown that horizontal polarization exhibits higher sea ice emissivity variability at 89 GHz than vertical polarization does at an incidence angle of 53° (e.g., Shokr et al., 2009). This is related to the enhanced sensitivity to sea ice and snow properties with horizontal polarization. Similar effects likely occur at a 25° incidence angle. Furthermore, horizontal polarization at 89 GHz results in emissivities that are up to 0.05 lower compared to nadir, depending on the sea ice type, as shown in past airborne observations at varying incidence angles (Hewison and English, 1999). This partly explains the low emissivity at 89 GHz observed here compared to that from the other nadir-viewing channels.

Despite the implications of incidence angle and polarization differences on spectral features, this transect showcases typical sea ice emission signatures. Over nilas from 7 to 11 km, sea ice emissivity increases across all channels, with values ranging from 0.9 to 1. Hewison and English (1999) and Hewison et al. (2002) observed similar emissivities at 89 and 183 GHz over bare ice under the same observing geometry as MiRAC. Sea ice emissivity over multiyear ice within the first 7 km is lower than that over nilas at all frequencies. The snow-covered and refrozen leads from 3 to 4 km only cause higher emissivities at 89 GHz, likely due to the higher sensitivity of the horizontal polarization at this channel to sea ice and snow properties. Observations of multiyear ice at nadir in Hewison et al. (2002) are comparable to multiyear ice observations along this transect. The 243 GHz nadir emissivity is close to the mean emissivity of 0.84 at 220 GHz, observed by Haggerty and Curry (2001). The alignment of MiRAC emissivity features with past sea ice emissivity studies provides confidence in the 243 GHz emissivity resolved at the hectometer scale. Moreover, the high similarity between 243 and 340 GHz emissivities shows that MiRAC provides submillimeter sea ice emissivities with a clear dependence on distinct sea ice types for the first time.

The ±8 K surface temperature uncertainty causes the highest emissivity uncertainty for all channels (not shown). The uncertainty magnitude varies highly between the channels. The lowest uncertainty range occurs at 89 and 243 GHz, while the highest range occurs at 183.31 ± 2.5 GHz, which is the channel closest to the 183.31 GHz water vapor absorption line, exceeding the 40 K surface sensitivity threshold. In the following, we only show the 183.31 ± 7.5 GHz channel due to its higher surface sensitivity and similar emissivity compared to the inner 183 GHz channels (Fig. 3.3j). The measured emissivity difference between mul-

tiyear ice and nilas exceeds the emissivity uncertainty at all frequencies, while no significant variations occur in the first 7 km at 340 GHz. Overall, this case study demonstrates the relevance of sensitivity tests in interpreting the retrieved emissivities to distinguish emissivity features arising from uncertainties inherent to the assumptions of the emissivity calculation, caused by unknown subsurface temperatures and uncertain atmospheric thermodynamic profiles.

3.4.2 TB and emissivity variability

In the following, we analyze the distributions of TB and emissivity observed during all clear-sky flights over sea ice during the ACLOUD and AFLUX campaigns (Fig. 3.4). The histograms corresponding to 89 GHz and 183–340 GHz include different samples due to the exclusion of low flight altitudes at 89 GHz, which introduces a potential inconsistency (Table 3.3). Therefore, we compared these histograms with those from instantaneous measurements in which all channels sample the same sea ice, and we found no changes in the shape of the histograms that exceed the estimated emissivity uncertainties (not shown). Hence, we present all available observations here. The TB variability during the AFLUX campaign exceeds that during the ACLOUD campaign at all frequencies (Fig. 3.4a–d). The ACLOUD TBs at 183, 243, and 340 GHz show low variability and higher values, attributed to the increased atmospheric water vapor and surface temperature. Two distinct peaks occur at 89 and 243 GHz during the AFLUX campaign. These peaks become even more pronounced in the emissivity distributions, ranging from around 0.7 to 0.85 and from 0.9 to 1, respectively (Fig. 3.4e–h). These emissivity ranges correspond to those pertaining to multiyear ice and nilas in the AFLUX RF08 case (see Sect. 3.4.1). The histograms derived for 243 GHz are broader than the 220 GHz emissivities reported by Haggerty and Curry (2001) due to MiRAC's higher resolution, which captures previously unresolved leads. MiRAC's 340 GHz emissivity distribution follows a similar shape to the 183 and 243 GHz channels. The broader emissivity distribution at 340 GHz could be related to the higher emissivity uncertainty of 9 % compared to the emissivity uncertainty at 183 GHz (6 %) and 243 GHz (5 %) during the AFLUX campaign (Table 3.3). The apparent shape difference of the 89 GHz distribution and the 2-fold higher interquartile range (Table 3.3) indicate that this horizontally polarized and 25° inclined channel is more sensitive to sea ice and snow properties than the other channels at higher frequencies. The 89 GHz distribution is narrower during the ACLOUD campaign than during the AFLUX campaign in the presence of melting sea ice, which agrees with findings from Haggerty and Curry (2001). Lower emissivities during the ACLOUD campaign, indicated by the two lower peaks around 0.65,

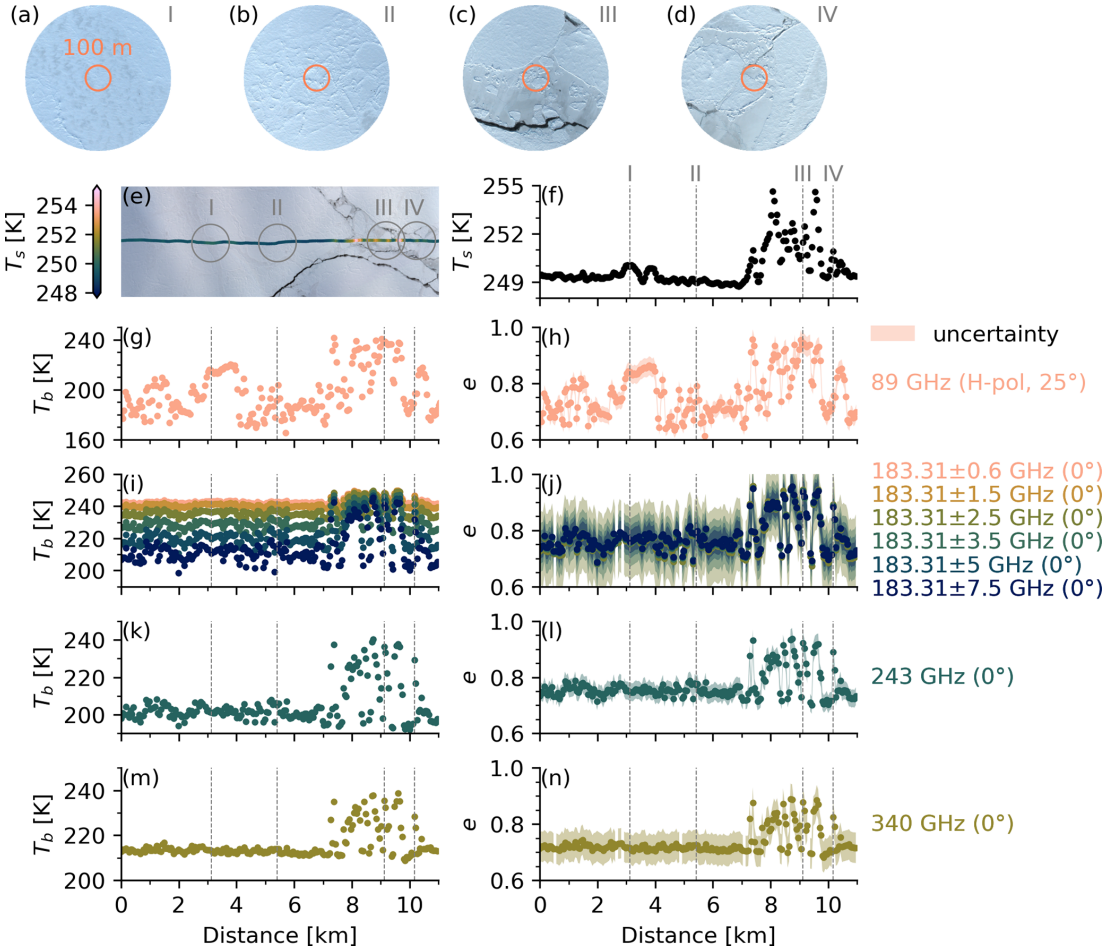

Figure 3.3: Observations collected along an 11 km transect at 81.01° N, 4.28–4.91° E (about 100 km north of the sea ice edge) during AFLUX RF08 (31 March 2019). *Polar 5* flew westward (right to left in this figure) at an altitude of 540 m for about 4 min, starting at 11:39 UTC. **(a–d)** Fish-eye lens images with a 100 m diameter nadir reference circle obtained at **(a)** 11:42:16 UTC, **(b)** 11:41:32 UTC, **(c)** 11:40:20 UTC, and **(d)** 11:40:00 UTC. **(e)** Sentinel-2B L2A natural-color image obtained at 14:37 UTC, showing the flight track, surface skin temperature from the KT-19, and the location of the airborne imagery. **(f)** Surface skin temperature from the KT-19. **(g, i, k, m)** TB at all MiRAC channels. **(h, j, l, n)** Emissivity and uncertainty from MiRAC's surface-sensitive channels, i.e., except the two inner 183 GHz channels in this case. The Sentinel-2B image was shifted northward by 2.5 km to correct for sea ice drift. H-pol: horizontal polarization

correspond to regions with lower sea ice concentrations. These emissivities should be treated with care due to the specular contributions of the sea surface.

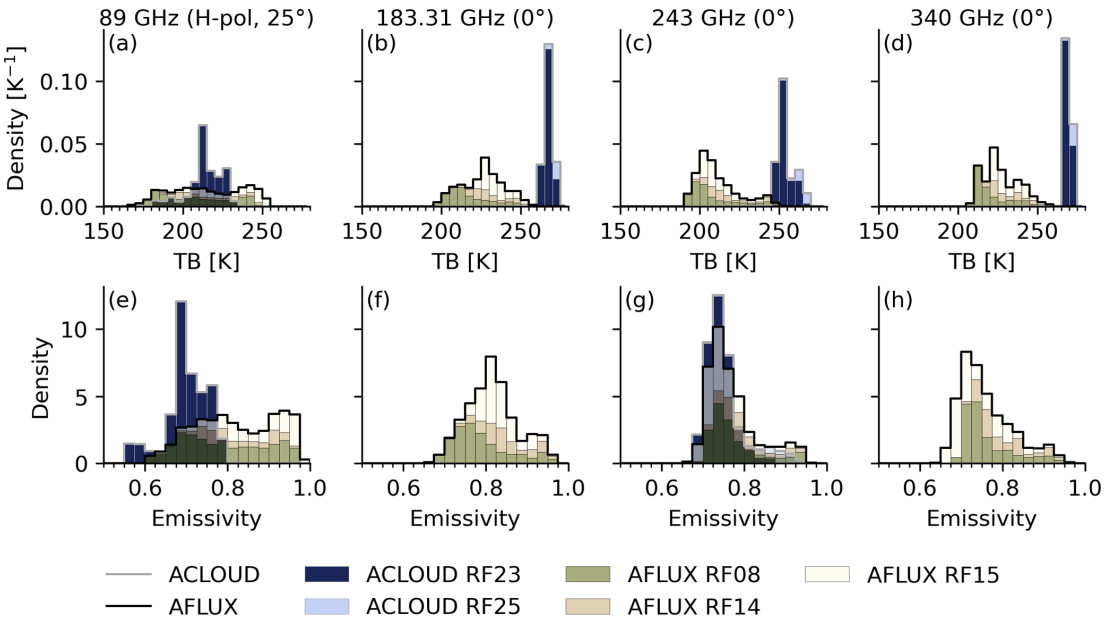

Figure 3.4: Histograms of **(a–d)** TB and **(e–h)** emissivity at **(a, e)** 89, **(b, f)** 183, **(c, g)** 243, and **(d, h)** 340 GHz during the ACLOUD and AFLUX campaigns. The TB bin width is 5 K, and the emissivity bin width is 0.025. The observations at 183 and 340 GHz collected during the ACLOUD campaign fall below the surface sensitivity threshold and are therefore excluded from panels **(f)** and **(h)**. The histograms for 183, 243, and 340 GHz contain more samples than the 89 GHz histogram (see Table 3.3).

3.4.3 Influence of sea ice and snow properties

In this section, we aim to relate the observed sea ice emissivity variability to sea ice and snow properties visible in fish-eye lens images and surface skin temperature. Previous airborne studies have classified sea ice based on airborne imagery or visual inspection and calculated emissivity spectra for each sea ice type (e.g., Hewison and English, 1999). However, this approach requires sea ice classification at a high temporal resolution. Therefore, we use k-means clustering to extract distinct emissivity spectra – a similar approach to that seen in previous sea ice and snow emissivity studies (Wang et al., 2017b; Wivell et al., 2023). First, we normalize the data by subtracting the mean emissivity and dividing the result by the standard deviation at each channel to ensure equal channel weighting. Then, we cluster the normalized emissivity spectra across all four MiRAC frequencies using k-means to identify distinct sea ice emissivity spectra.

The crucial hyperparameter for k-means clustering is the total number of clusters. Therefore, we analyze three heuristics – distortion (Thorndike, 1953),

Table 3.3: Sea ice emissivity at MiRAC frequencies during individual flights and across all flights from the ACLOUD and AFLUX campaigns. Values include the sample count (Cnt.), median (Mdn.), interquartile range (IQR), and relative uncertainty averaged over all samples (Unc.). The sample counts for 183, 243, and 340 GHz are constant, except for the ACLOUD flights, where emissivities measured at 183 and 340 GHz are not available.

Campaign (RF)	89 GHz				183 GHz				243 GHz			340 GHz		
	Cnt.	Mdn.	IQR	Unc. (%)	Cnt.	Mdn.	IQR	Unc. (%)	Mdn.	IQR	Unc. (%)	Mdn.	IQR	Unc. (%)
ACLOUD (RF23)	3431	0.7	0.06	2	15 152				0.74	0.04	8			
ACLOUD (RF25)					1595				0.87	0.06	5			
AFLUX (RF08)	1955	0.78	0.17	4	4632	0.77	0.08	5	0.75	0.07	4	0.74	0.07	7
AFLUX (RF14)	638	0.81	0.15	4	2358	0.83	0.07	6	0.79	0.06	4	0.78	0.08	8
AFLUX (RF15)	1097	0.88	0.14	4	4662	0.82	0.05	6	0.73	0.05	5	0.71	0.09	10
ACLOUD	3431	0.7	0.06	2	16 747				0.74	0.04	8			
AFLUX	3690	0.81	0.17	4	11 652	0.81	0.08	6	0.75	0.07	5	0.74	0.08	9

the Calinski–Harabasz index (Calinski and Harabasz, 1974), and silhouette score (Rousseeuw, 1987) – and yield an optimal cluster number of four (Appendix 3.B). However, not all clusters separate clearly due to transitional stages and inhomogeneous sea ice properties within MiRAC's footprint (Fig. 3.10b). Fish-eye images for all samples underline the high diversity in sea ice and snow properties (Fig. 3.11).

The occurrence of each cluster varies between the flights. Cluster 1 (C1) occurs more often than the other clusters (appearing in 52 % of cases during RF08), while C2 is predominant during RF14 (accounting for 68 % of occurrences), and C3 is observed in 48 % of instances during RF15. C4 occurs about 20 % of the time during RF08 and RF14, and it occurs 8 % of the time during RF15. It is unclear whether these changes are due to sea ice drift or temporal changes in ice properties, given the coarse temporal resolution and potential bias resulting from the flight pattern.

Each cluster exhibits distinct emissivity features (Figs. 3.5a and 3.12). The lowest emissivity prevails in C1, and the highest is found in C4. C1 occurs over snow-covered sea ice (Fig. 3.5c), which might be classified as multiyear ice and predominates during the AFLUX flights (Fig. 3.9). This also corresponds to the lower skin temperature of 250 K for this cluster compared to the other clusters (Fig. 3.5b). Few open leads are present within C1 as water shows a spectral signature similar to that of this cluster. C4 occurs over nilas in refrozen leads (Fig. 3.5c). This aligns with the generally warmer skin temperature observed in this cluster compared to in the other clusters (Fig. 3.5b). C4 is distinct from the other three clusters at 183, 243, and 340 GHz. C2 emissivities fall between those of C1 and C4 at all frequencies. This cluster occurs over various surface types, but it predominantly occurs over ice with visual properties of first-year ice. C3 emissivities are close to those of C4 at 89 GHz and close to those of C1 at 243 and 340 GHz. This cluster occurs over young ice that has more snow cover than the sea ice in C4. Hence, scattering within the upper snow layer could explain the lower emissivity at 243 and 340 GHz in C3 than in C4. However, the emissivity is lower than in C2, where snow is also present, which indicates the importance of other factors, such as snow density and grain size.

The evaluation of airborne emissivities reveals (1) low differences in the median emissivity and interquartile range at 183, 243, and 340 GHz; (2) higher emissivities over nilas compared to those over multiyear ice at all frequencies; and (3) four distinct emissivity spectra. The similarity between 243 and 340 GHz implies a lower spectral variation in sea ice emissivity in the submillimeter wave range. However, the emissivity variability at both frequencies is still notable and depends on the sea ice type, with the highest contrast observed between multiyear

ice and nilas.

3.5 Comparison with satellites

3.5.1 Spatial variability at a subfootprint scale

Airborne and satellite observations resolve sea ice emissivity on different spatial scales. Hectometer-scale airborne observations resolve most leads, while kilometer-scale satellite observations partially smooth out these structures. Figure 3.6a shows a *Polar 5* transect during AFLUX RF08, covering a 5 km lead mainly composed of nilas. MiRAC's 89 GHz emissivity exhibits a pronounced increase from multiyear or first-year ice to nilas, followed by a sharp decrease over a short section of open water. Consequently, emissivity clusters shift from C1 over multiyear or first-year ice to C4 over younger sea ice. The 5 km AMSR2 footprints partially resolve the lead, with higher emissivities observed over nilas, whereas the $16 \times 16\,\mathrm{km}^2$ MHS footprints cannot fully capture it. This example underscores the significance of subfootprint-scale emissivity variations over spatially heterogeneous sea ice.

Next, we examine how emissivity varies with footprint size from 0.1 to 20 km for all airborne observations. We calculate the larger-scale emissivity from the mean airborne surface temperature and emission for each footprint size interval. The interquartile range of the emissivity decreases rapidly with increasing footprint size during the ACLOUD and AFLUX campaigns at all frequencies (Fig. 3.6b). For example, the variability in 100 m footprints at 340 GHz during the AFLUX campaign decreases by 42 % (65 %) when the footprint size corresponds to $5{\times}5\,\mathrm{km}^2$ ($16 \times 16\,\mathrm{km}^2$). The smallest decrease occurs at 89 GHz during the ACLOUD campaign, with a decrease of 21 % (20 %) when the footprint size reaches $5 \times 5\,\mathrm{km}^2$ ($16{\times}16\,\mathrm{km}^2$). Hence, a larger satellite footprint averages out small-scale emissivity variations.

3.5.2 Channel intercomparison

Before integrating MiRAC data with all satellite observations to study spectral variations of up to 340 GHz on a satellite scale, we must ensure that our collocation approach reproduces satellite observations at similar frequencies and observing geometries. The near-nadir (0–30°) 157 GHz MHS and 165.5 GHz ATMS channels are comparable to MiRAC's 183 GHz channel at nadir. We compare these satellite channels rather than the 190.31 and 183.31 ± 7 GHz channels due to their higher surface sensitivity and lower uncertainty, even though spectral emissivity gradients might occur (e.g., Hewison et al., 2002). Other channel or

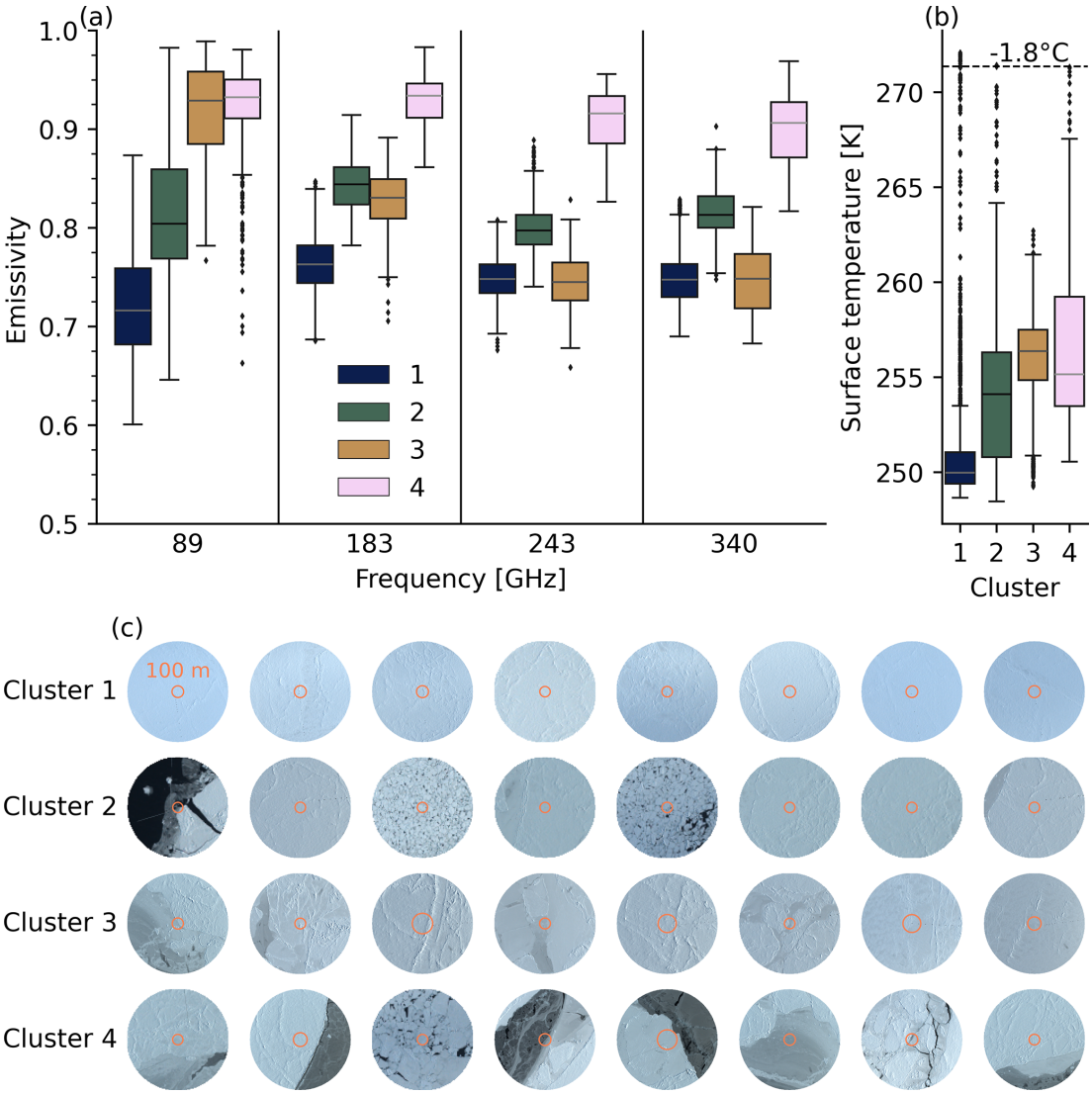

Figure 3.5: Comparison of sea ice emissivity and surface temperature across k-means clusters. **(a)** Tukey boxplot depicting the distribution of sea ice emissivity at MiRAC frequencies within each k-means cluster. **(b)** Tukey boxplot showing the distribution of surface temperature within each k-means cluster. **(c)** Fish-eye lens images representing the k-means cluster centroids, i.e., for emissivity samples similar to the mean cluster emissivity, with a 100 m diameter nadir reference circle (see Fig. 3.11 for all images). It should be noted that the actual footprint might not lie within the indicated region due to the aircraft attitude causing MiRAC-P to point off-nadir by a few degrees and potential temporal shifts between the camera and MiRAC.

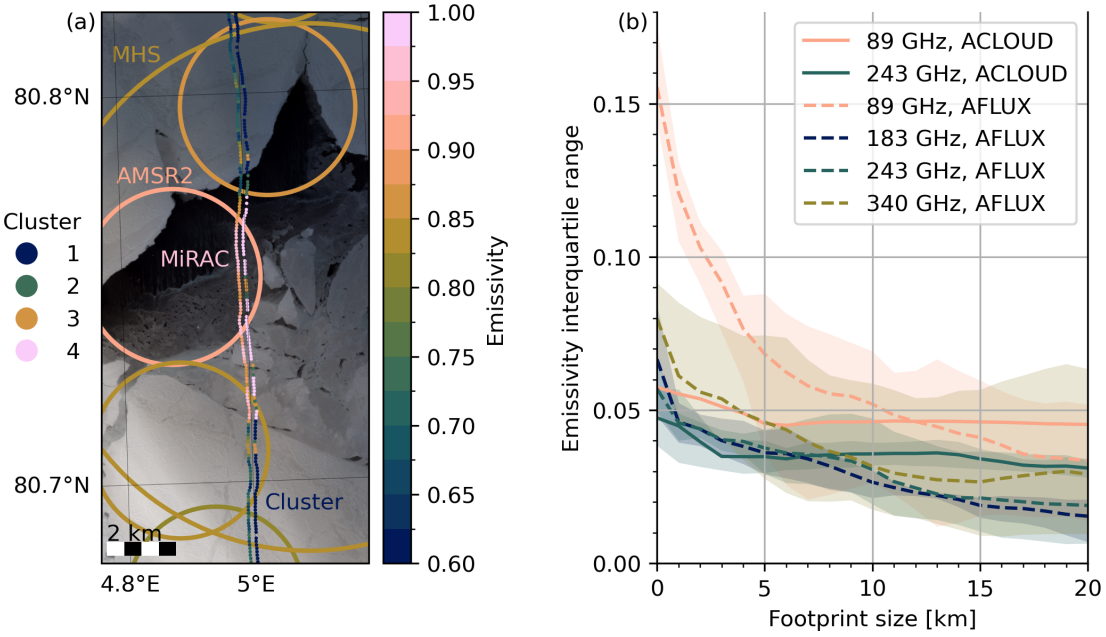

Figure 3.6: **(a)** Sea ice emissivity at 89 GHz from MiRAC (10:32 to 10:37 UTC), AMSR2 (11:02 UTC), and MHS onboard Metop-B (11:38 UTC) during AFLUX RF08 on 31 March 2019. The MiRAC emissivity cluster is displayed 100 m east of the emissivity. The actual MiRAC footprints lie between the emissivity and emissivity cluster locations. The background shows a Sentinel-2B L2A natural-color image that was obtained at 14:37 UTC and shifted 4 km northward to correct for sea ice drift. **(b)** The emissivity interquartile range as a function of footprint size from 0.1 to 20 km for all flights and channels. The spread represents the minimum and maximum interquartile ranges for each campaign.

instrument combinations differ in terms of incidence angle or polarization, making footprint-level comparisons less meaningful.

Figure 3.7 illustrates the resampling process, which transitions from MiRAC's high-resolution emissivity to the satellite footprints. It also shows the corresponding satellite emissivity and the differences for all AFLUX flights. Notably, MiRAC reveals hectometer-scale emissivity features, such as leads, which are not captured by MHS and ATMS due to their $16 \times 16\,\mathrm{km}^2$ footprint. This high hectometer-scale variability consistently occurs within each satellite footprint (right column in Fig. 3.7) and diminishes after resampling to the satellite footprint scale. The limited spatial coverage of MiRAC causes deviations from MHS and ATMS as MiRAC only captures a narrow strip of the satellite footprint (e.g., during AFLUX RF08 near 80.4° N, 5° E; Fig. 3.7a), resulting in the highest emissivity bias (Fig. 3.7d). However, the collocation method is robust in most cases and yields MiRAC emissivities that are representative of the $16 \times 16\,\mathrm{km}^2$ satellite footprints. Moreover, the assessment of relative bias, calculated by subtracting the MiRAC emissivity from MHS or ATMS emissivity and dividing the result by the MiRAC emissivity, yields insights into the consistency of MiRAC observations from satellites (Tables 3.4 and 3.5). This relative bias of $-3\,\%$ to $1\,\%$ falls well within MiRAC's $6\,\%$ uncertainty range at 183 GHz (see Table 3.3). The correlation between MiRAC and MHS or ATMS ranges from 0.4 to 0.6 and reflects the partial footprint overlap, reducing the representation of MiRAC for each satellite footprint. In summary, the comparison with MHS and ATMS provides confidence in the accuracy of our airborne-emissivity estimates and the reliability of converting from hectometer to satellite footprint scales. Hence, we can apply the same approach to other MiRAC channels at frequencies up to 340 GHz.

3.5.3 Spectral variations

In this section, we collocate MiRAC with MHS, ATMS, SSMIS, and AMSR2 to analyze spectral variations in sea ice emissivity from 88 to 340 GHz as well as angular and polarization effects. We group all collocated emissivities by frequency into the following categories: 88–92, 150–165 (only for satellites), 176–190, 243, and 340 GHz. The MiRAC observations are averaged to align with the collocated footprints of each satellite instrument, ensuring equivalent spatial sampling (see Sect. 3.2.5).

The channel-dependent emissivity variability observed on a satellite scale during the ACLOUD and AFLUX campaigns reveals distinct features related to spectral, angular, and polarization differences (Fig. 3.8). Low spectral differences during the ACLOUD campaign occur near nadir from 89 to 243 GHz (MHS and

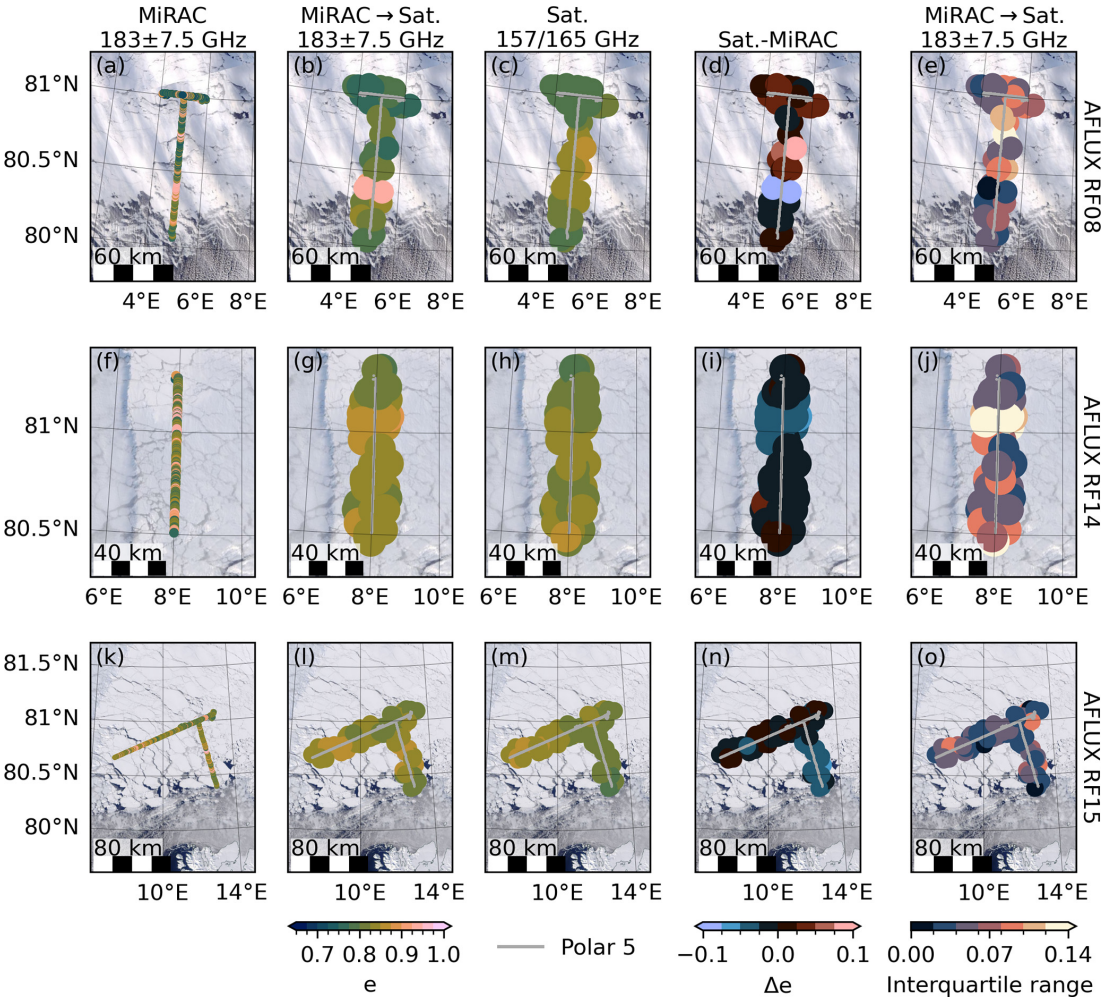

Figure 3.7: Comparison of emissivity from nadir 183 GHz MiRAC observations and near-nadir (0–30°) 157 GHz MHS and 165.5 GHz ATMS observations collected along the *Polar 5* flight track during AFLUX RF08, RF14, and RF15 (rows). **(a, f, k)** MiRAC emissivity at the original resolution. **(b, g, l)** MiRAC emissivity resampled to satellite (Sat.) footprints. **(c, h, m)** Satellite emissivity. **(d, i, n)** Emissivity difference between MiRAC and the satellites (satellite emissivity minus MiRAC emissivity). **(e, j, o)** MiRAC emissivity interquartile range within the satellite footprint. No 183 GHz observations from MiRAC were available during the ACLOUD campaign. The background images are composites of MODIS onboard Terra from the same day (NASA Worldview). All footprints are approximated as circles. MiRAC's footprints are enlarged to a 5 km diameter. The satellite footprint size corresponds to the footprint size at nadir.

Table 3.4: Comparison of collocated emissivity from nadir 183 GHz MiRAC observations and near-nadir (0–30°) 157 GHz MHS observations collected during the three AFLUX flights. Values include the number of collocated satellite footprints (Count); median; interquartile range (IQR); relative bias (Rel. bias), i.e., MHS emissivity minus MiRAC emissivity divided by MiRAC emissivity; relative root-mean-square deviation (Rel. RMSD), normalized by MiRAC emissivity; and Pearson's correlation coefficient (Corr.).

Campaign (RF)	Count	Median		IQR		Rel. bias (%)	Rel. RMSD (%)	Corr.
		MiRAC	MHS	MiRAC	MHS			
AFLUX (RF08)	36	0.79	0.81	0.04	0.04	1	5	0.56
AFLUX (RF14)	34	0.84	0.83	0.02	0.02	−1	2	0.48
AFLUX (RF15)	68	0.83	0.82	0.02	0.02	−1	2	0.5

Table 3.5: Comparison of collocated emissivity from nadir 183 GHz MiRAC observations and near-nadir (0–30°) 165.5 GHz ATMS observations collected during the three AFLUX flights. The columns are identical to those in Table 3.4.

Campaign (RF)	Count	Median		IQR		Rel. bias (%)	Rel. RMSD (%)	Corr.
		MiRAC	ATMS	MiRAC	ATMS			
AFLUX (RF08)	18	0.81	0.81	0.04	0.04	1	4	0.63
AFLUX (RF14)	13	0.84	0.82	0.03	0.01	−3	4	0.58
AFLUX (RF15)	15	0.83	0.82	0.02	0.01	−1	3	0.42

MiRAC) and at vertical polarization from 91 to 150 GHz (SSMIS; Fig. 3.8a). The higher satellite emissivity can be attributed to the underestimation of the NE23 skin temperature compared to that of the KT-19. As expected, the 89 GHz emissivity shows a polarization signal of about 0.1. This indicates a specular contribution to surface reflection and an underestimation of emissivity in the case of purely Lambertian reflection at 89 GHz for MiRAC (see Sect. 3.3.3). Combining both polarizations from SSMIS or AMSR2 with quasi-vertical polarization, following Eq. (3.1), reduces the absolute emissivity difference, meaning it falls within the 0–30° emissivity range of MHS. Furthermore, the horizontally polarized 89 GHz channel of MiRAC is closer to the horizontally polarized channels of SSMIS and AMSR2. Spectral differences observed during the AFLUX campaign exceed those observed during the ACLOUD campaign, which might be due to contrasting sea ice properties (i.e., melting conditions during the ACLOUD campaign versus much colder and dryer sea ice and snow during the AFLUX campaign; Fig. 3.8b). The near-nadir emissivity remains constant from 89 to 183 GHz but decreases near frequencies of 243 and 340 GHz. No significant difference in spectral emissivity can be detected in the 165 to 183 GHz frequency range, where all satellites fall within MiRAC's 6 % uncertainty (see Table 3.3)). The decrease around 243 GHz exceeds the 243 GHz emissivity uncertainty. The AFLUX emissivities show a lower polarization difference at 89 GHz compared to the ACLOUD emissivities, which can be attributed to the lower amount of open water between ice floes during the AFLUX campaign. The emissivity of the 89 GHz MiRAC channel lies between the horizontally polarized AMSR2 and SSMIS channels and the near-nadir MHS and ATMS channels.

Different instruments show similar emissivity distributions at similar channels. For example, the three MHS and ATMS channels exhibit nearly identical distributions during the AFLUX campaign (see Fig. 3.8b). Additionally, the polarized 89 GHz channels of the SSMIS and AMSR2 show good agreement. However, during the ACLOUD campaign, emissivity differences between AMSR2 and SSMIS are noted for the vertically polarized channel, primarily due to the low number of collocated AMSR2 footprints compared to MiRAC footprints. For the AFLUX campaign, where the footprint counts of SSMIS and AMSR2 are comparable, AMSR2 shows higher variability as it has a smaller footprint than SSMIS.

Furthermore, MiRAC distributions align with MHS and ATMS distributions near nadir. The increased emissivity variability in MiRAC's 25° inclined 89 GHz channel, compared to that of MHS and ATMS, may be explained by its horizontal polarization. When comparing the vertically and horizontally polarized SSMIS and AMSR2 channels, horizontal polarization exhibits higher variability, consistent with findings from experiments by Shokr et al. (2009).

The consistent outcomes from spaceborne and airborne observations unveil a first-time representation of sea ice emissivity variability from 89 to 340 GHz. As detected by MiRAC, hectometer-scale emissivity variations smooth out when observed from a satellite perspective. Our analysis shows a potential decline in emissivity from 183 to 243 GHz under cold and dry conditions during the AFLUX campaign. This spectral pattern occurs within airborne emissivity clusters – i.e., within C3 (young ice) and, to some extent, within C2 (first-year ice) and C4 (nilas) – but is notably absent in C1 (multiyear ice) and prevails after being resampled onto a satellite scale. These cluster differences underscore the importance of spatial distributions among sea ice types.

3.6 Conclusions

The upcoming launches of ICI and EPS–Sterna, featuring novel frequencies above 200 GHz, and AMSR3, exhibiting a novel AMSR2-like resolution at 183 GHz, require an improved understanding of sea ice emissivity to distinguish atmospheric and surface microwave signals under dry polar conditions (Wang et al., 2017b). However, few field observations have measured sea ice emissivity at such high frequencies using a hectometer-scale resolution. Therefore, we analyzed sea ice emissivity variations observed with the MiRAC microwave radiometer during two airborne field campaigns – the ACLOUD campaign (summer 2017) and the AFLUX campaign (spring 2019). The flights analyzed in this study covered about 1700 km of distance. Moreover, 7000 samples were collected at 89 GHz (25° incidence angle; horizontal polarization), 28 000 samples were collected at 243 GHz (nadir), and 11 000 samples were collected at 183 and 340 GHz (nadir).

Our first objective was to identify critical physical sea ice and snow properties affecting emissivity up to submillimeter wavelengths. Sea ice emissivity exhibits high variability, ranging from about 0.65 to 1, with the lowest emissivities observed at 89 GHz. The 89 GHz distribution showed higher variability than the nadir channels due to its inclination and horizontal polarization. MiRAC resolves sea ice emissivity features that align with sea ice and snow properties identified from visual imagery. Four emissivity spectra from 89 to 340 GHz could be identified through k-means clustering. These spectra predominantly correspond to multiyear ice, first-year ice, young ice, and nilas. However, the emissivity variability for each cluster is significant due to variations in snow or sea ice microphysical properties and mixed types within the radiometer footprint. The lowest emissivity is observed over multiyear ice, and the highest emissivity is found over nilas, consistent with previous studies conducted at 89 and 183 GHz (NORSEX Group, 1983; Hewison and English, 1999; Hewison et al., 2002).

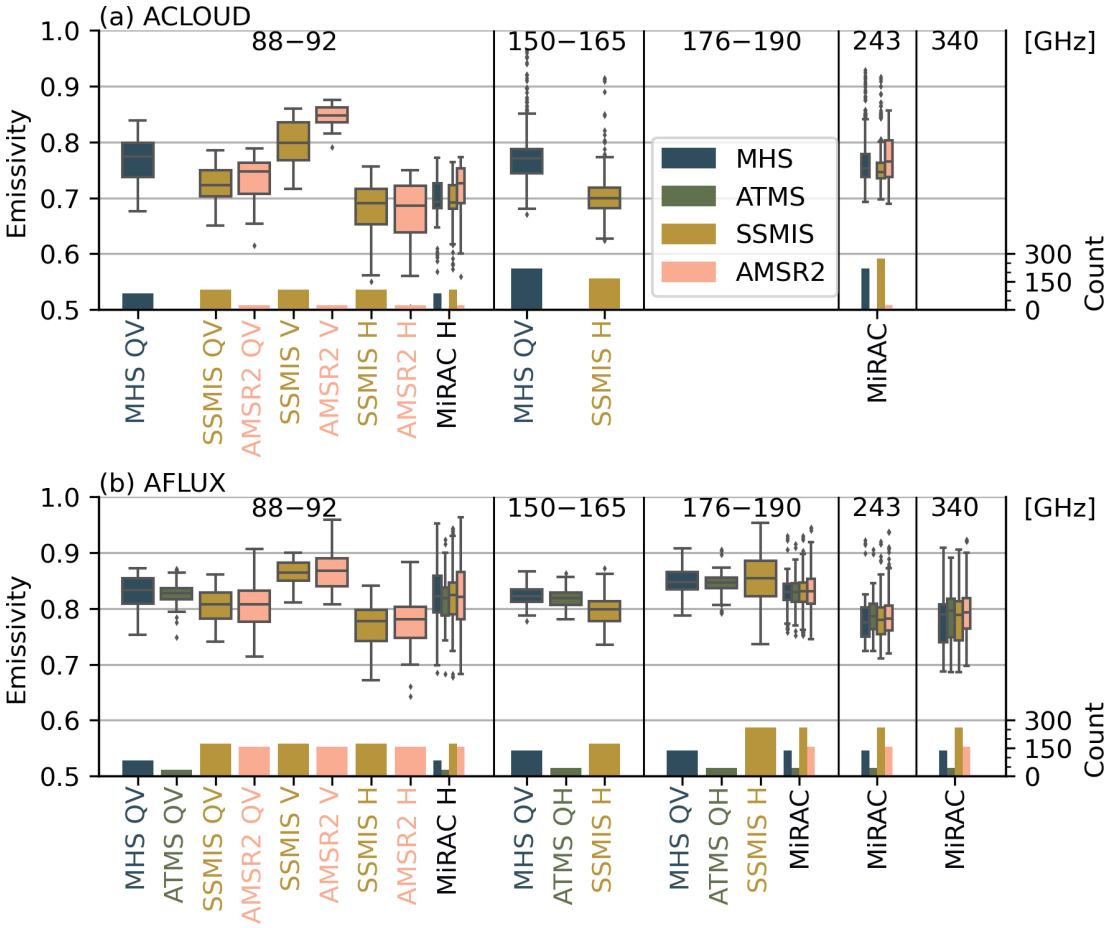

Figure 3.8: Tukey boxplots of collocated emissivity observed during **(a)** the ACLOUD campaign and **(b)** the AFLUX campaign for the frequency ranges 88–92, 150–165, 176–190, 243, and 340 GHz, derived from MHS (0 to 30°), ATMS (0 to 30°), SSMIS (53°), AMSR2 (55°), and MiRAC (25° at 89 GHz and 0° at 183, 243, and 340 GHz). The secondary axis denotes the count of the collocated footprints. Quasi-vertical SSMIS QV and AMSR2 QV polarizations are characterized by dominant contributions of 64 % and 67 %, respectively, from horizontal polarization. The 88–92 GHz satellite footprint count might be lower than the satellite footprint count at frequencies above 150 GHz because satellite footprints are excluded if the nearest MiRAC channel exhibits no emissivity. Note that no ATMS overpass occurred during the ACLOUD campaign.

Our second objective was to relate the observed hectometer-scale emissivity observations to the satellite scale. We collocated MiRAC with MHS, ATMS, SSMIS, and AMSR2 for this purpose. Satellite instruments do not resolve hectometer-scale sea ice emissivity variations observed by MiRAC due to their larger footprints. By averaging the airborne observations, we estimated the decrease in the emissivity interquartile range as footprint size increases. The reduction in the interquartile range is most significant during the AFLUX campaign, when leads induce significant hectometer-scale emissivity variations. For example, the emissivity interquartile range decreases by almost half from the hectometer scale to a footprint of $16 \times 16\,\mathrm{km}^2$, typical of microwave satellite instruments. We find high agreement between MHS, ATMS, and MiRAC emissivities near 183 GHz. During the AFLUX campaign, emissivity decreases significantly from 183 to 243 GHz, while it remains almost constant during the ACLOUD campaign. The estimates provided here may represent the emissivities that future satellites, such as ICI and EPS–Sterna, will observe.

The study's implications are as follows:

- The first implication involves hectometer-scale frequency dependency. The 183, 243, and 340 GHz channels exhibit similar hectometer-scale sea ice emissivity variations at nadir, regardless of the sea ice type (e.g., multiyear ice and nilas). This finding is crucial for the development of airborne retrieval methods.

- The second concerns spatial and temporal representation. At the satellite footprint scale, hectometer-scale sea ice emissivity variations average out, which facilitates sea ice emissivity parameterization. However, these variations become more relevant for higher-resolution channels, such as AMSR2.

- The third pertains to emissivity frequency extrapolation. The relatively low spectral variation in emissivity at the satellite scale from 89 to 340 GHz at nadir supports using a first-order approximation of constant emissivities over sea ice within existing parameterizations, such as TELSEM2 (Wang et al., 2017b). Accounting for spatial and temporal emissivity variations appears to be more relevant than focusing on spectral gradients.

This study has several limitations:

- The first limitation concerns channel intercomparison. The 25° inclination and horizontal polarization of the 89 GHz channel may affect comparisons with the 183–340 GHz nadir-viewing channels by increasing the channel's variability and lowering its emissivity compared to an 89 GHz nadir-viewing channel. Quantification of this effect might be possible by analyzing the

airborne HALO–(AC)^3 campaign conducted in spring 2022 (Wendisch et al., 2021).

- Another limitation involves surface temperature assumption. Using the surface skin temperature rather than the emitting-layer temperature imposes a frequency-dependent bias on emissivity measurements collected during the AFLUX campaign.

- Sea ice and snow properties pose another limitation. The aerial images provide only a broad perspective on sea ice and snow properties and have limitations in providing vertical profiles of sea ice microphysics, such as density, grain size, or salinity.

- Spatial resolution is also a limiting factor. MiRAC's hectometer scale may not resolve smaller sea ice features, such as ridges or melt ponds, which could influence emissivity.

- There are also spatial and temporal limitations. Field observations are limited in space (approximately 100 km) and time (5 d), potentially restricting the generalizability of findings across polar regions.

Three primary challenges persist when it comes to comprehending sea ice emissivity variations to advance atmospheric and surface retrievals over sea ice. First, the relatively unexplored emissivity dependence on polarization and incidence angles, especially at frequencies above 200 GHz, demands comprehensive investigation. Potential solutions include utilizing shipborne or airborne observations with scanning radiometers. Second, the high uncertainty due to atmospheric emissions that mask spectral features of emissivity, particularly at 340 GHz and over the more reflective multiyear ice, requires simultaneous measurements of near-surface downwelling atmospheric TB for emissivity calculations. Third, observed emissivity spectra must be combined with in situ measurements of sea ice and snow microphysics to advance radiative-transfer modeling. In summary, addressing these challenges will help bridge remaining knowledge gaps in sea ice microwave emissivity and will have implications for current and upcoming satellite missions. Future work will need to focus on separating sea ice and atmospheric signals under all-sky conditions.

Appendix

3.A Multiyear ice concentration maps

We include maps illustrating multiyear ice concentration to offer additional context for the three AFLUX flights (Fig. 3.9). The multiyear ice concentration is mainly around 50 %, with higher concentrations in the northern parts of the RF08 and RF14 flight tracks. The case study transect observed during RF08 falls within a pixel corresponding to ∼75 % multiyear ice concentration (Fig. 3.9a).

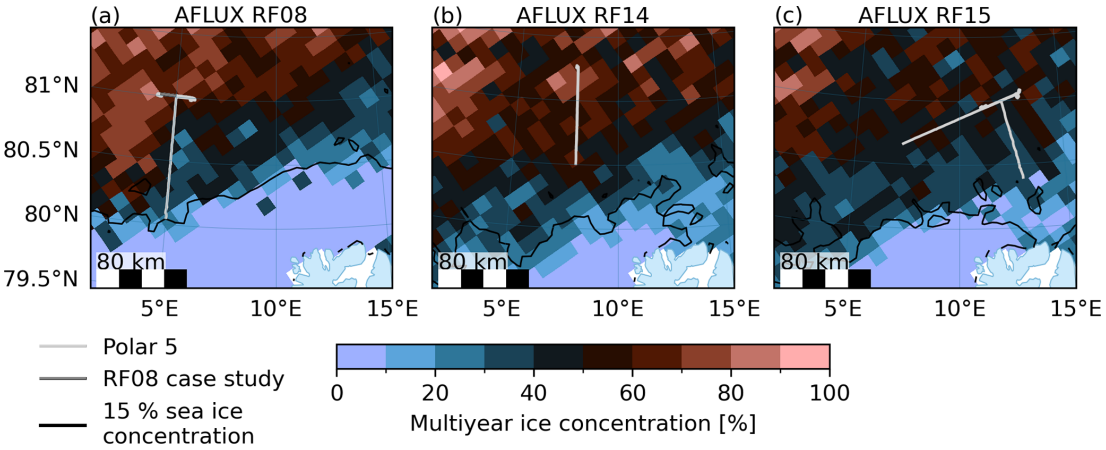

Figure 3.9: Maps illustrating the *Polar 5* flight track; the sea ice edge, indicated by the 15 % sea ice concentration isoline (Spreen et al., 2008); and multiyear ice concentration (Melsheimer and Spreen, 2022) during **(a)** AFLUX RF08 (including the case study transect), **(b)** RF14, and **(c)** RF15.

3.B Optimal number of k-means emissivity clusters

The k-means algorithm assigns a cluster to each normalized emissivity spectrum across the four MiRAC frequencies. Normalization involves subtracting the mean and scaling the emissivity of each channel to include unit variance, which ensures equal weighting between the four channels. However, the absolute number of clusters (k) is unknown and needs to be defined objectively. Therefore, we evaluate three metrics for cluster sizes ranging from 2–10 to identify the optimal k value (Fig. 3.10a). The distortion represents the sum of squared distances from all samples to their assigned cluster centroids (Thorndike, 1953). The distortion ideally follows an elbow-shaped curve, exhibiting a decrease until the optimal k value is reached and constant distortion for higher k values. The distortion curve for the emissivity samples flattens slightly after a k value of 4. The

Calinski–Harabasz index determines the ratio of between-cluster dispersion to within-cluster dispersion, i.e., the ratio of separation to cohesion (Calinski and Harabasz, 1974). Higher Calinski–Harabasz index values correspond to optimal clustering with well-separated and dense clusters. The index peaks at a k value of 4 and decreases for both higher and lower values (Fig. 3.10a). The silhouette score represents the mean silhouette coefficient, which measures the similarity of a sample to its cluster compared to other clusters (Rousseeuw, 1987). Silhouette coefficients of 1 (-1) indicate correct (wrong) class assignment. On average, the silhouette score is 0.37 for 2–10 clusters. The silhouette score is highest for two clusters and shows a secondary peak at four clusters. All three metrics indicate that the emissivity spectra can be optimally divided into four clusters. The two-dimensional principal component analysis compression (Hotelling, 1933) shows the four identified emissivity clusters (Fig. 3.10b). Overall, the emissivity clusters are well separated, with gradual transitions occurring due to mixed types within the radiometer's footprint or transitional stages of the sea ice. Fish-eye lens images resolve these mixed types and transitional stages (Fig. 3.11).

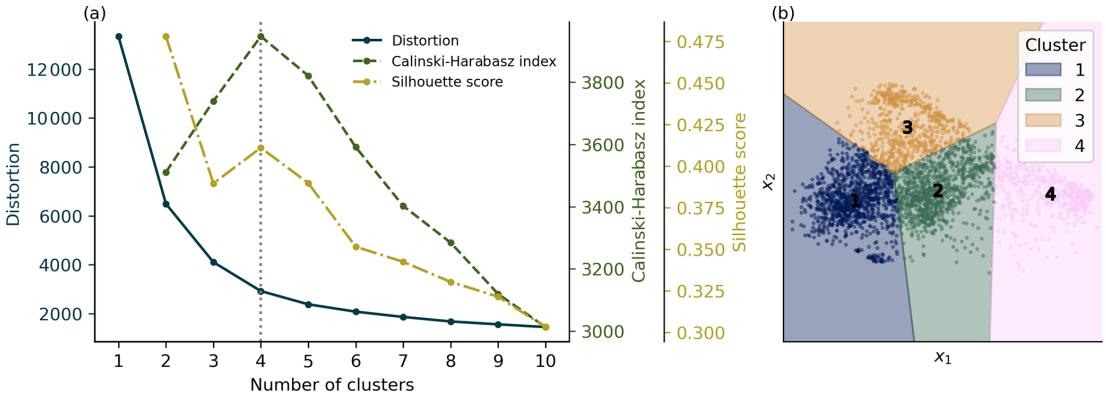

Figure 3.10: **(a)** The k-means clustering metrics – distortion, the Calinski–Harabasz index, and silhouette score – plotted as functions of the number of clusters. **(b)** Clustered emissivity spectra projected along the first two principal components (x_1, x_2) using k-means. The k-means cluster boundaries are approximated in a Voronoi diagram based on the cluster centroid projections. The cluster numbers are shown at the centroid positions.

3.C Sea ice emissivity spectra

We provide a figure of the MiRAC sea ice emissivity spectra and the k-means cluster centroids (Fig. 3.12).

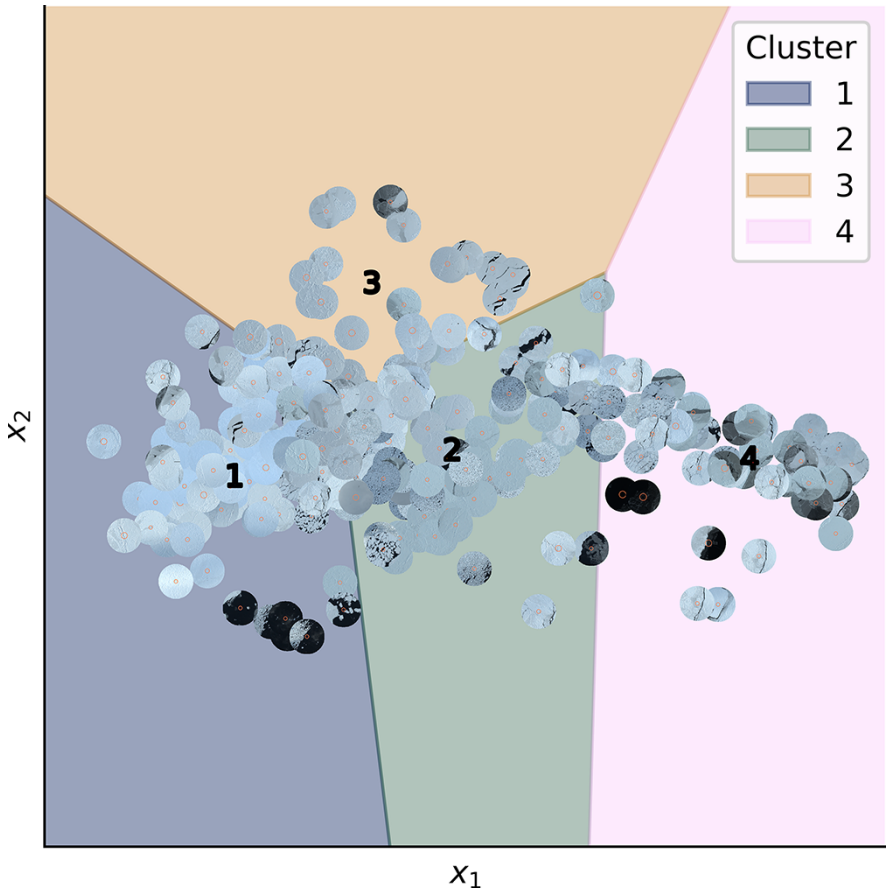

Figure 3.11: Fish-eye lens images corresponding to the emissivity samples shown in Fig. 3.10b. The k-means cluster boundaries are approximated in a Voronoi diagram based on the cluster centroid projections onto the first two principal components (x_1, x_2). The cluster numbers are shown at the centroid positions.

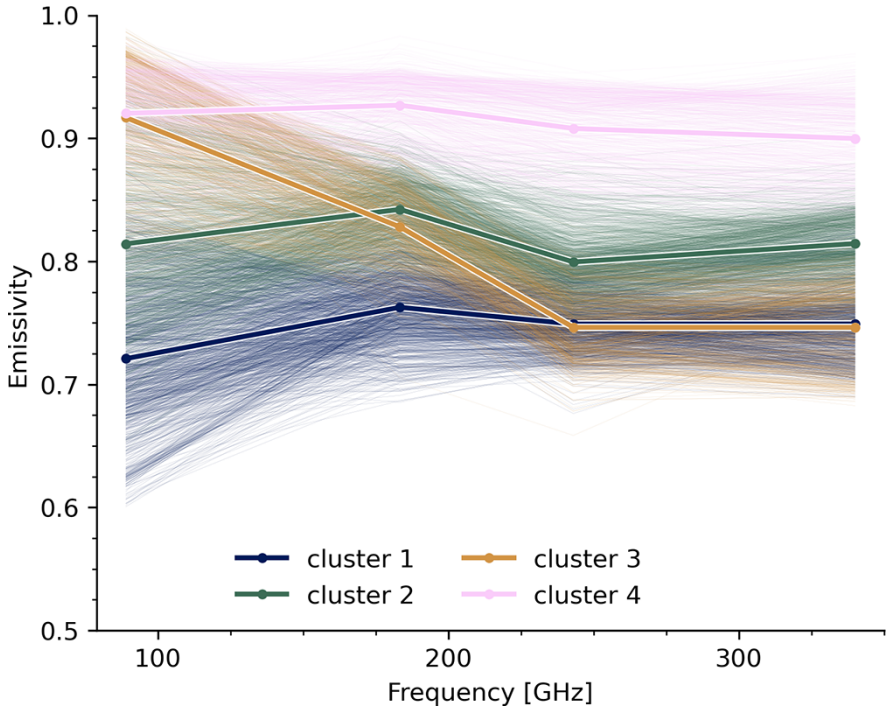

Figure 3.12: MiRAC sea ice emissivity spectra and k-means cluster centroids. Note that the 89 GHz channel measures horizontal polarization at an incidence angle of 25°, while the 183, 243, and 340 GHz channels measure it at nadir.

Code and data availability

The code for this study and a usage example of the published emissivity data are available on Zenodo at doi:10.5281/zenodo.11535477 (Risse, 2024). The MiRAC emissivity data are available on PANGAEA at doi:10.1594/PANGAEA.965569 (Risse et al., 2024a). MiRAC-A measurements collected during the ACLOUD campaign were obtained from doi:10.1594/PANGAEA.899565 (Kliesch and Mech, 2019), and those collected during the AFLUX campaign were obtained from doi:10.1594/PANGAEA.944506 (Mech et al., 2022b). MiRAC-P measurements collected during the ACLOUD campaign were obtained from doi:10.1594/PANGAEA.944070 (Mech et al., 2022c), and those collected during the AFLUX campaign were obtained from doi:10.1594/PANGAEA.944057 (Mech et al., 2022d). Camera images taken during the AFLUX campaign were obtained from doi:10.1594/PANGAEA.901024 (Jäkel and Ehrlich, 2019). KT-19 measurements collected during the ACLOUD campaign were obtained from doi:10.1594/PANGAEA.900442 (Stapf et al., 2019), and those collected during the AFLUX campaign were obtained from doi:10.1594/PANGAEA.932020 (Stapf et al., 2021). Dropsonde measurements collected during the ACLOUD campaign were obtained from doi:10.1594/PANGAEA.900204 (Ehrlich et al., 2019a), and those collected during the AFLUX campaign were obtained from doi:10.1594/PANGAEA.922004 (Becker et al., 2020). Nose boom measurements collected during the ACLOUD campaign were obtained from doi:10.1594/PANGAEA.902849 (Hartmann et al., 2019), and those collected during the AFLUX campaign were obtained from doi:10.1594/PANGAEA.945844 (Lüpkes et al., 2022). Aircraft position and orientation were obtained from the "ac3airborne" intake catalog (Mech et al., 2022e). Radiosoundings from Ny-Ålesund were obtained from doi:10.1594/PANGAEA.914973 (Maturilli, 2020). The sea–land mask for Svalbard was obtained from the Kartdata Svalbard 1 : 100 000 (S100 Kartdata)/Map Data of the Norwegian Polar Institute at doi:10.21334/npolar.2014.645336c7 (Norwegian Polar Institute, 2014). The L1C TB data for SSMIS on DMSP-F16 were obtained from doi:10.5067/GPM/SSMIS/F16/1C/07 (Berg, 2021a). The L1C TB data for SSMIS on DMSP-F17 were obtained from doi:10.5067/GPM/SSMIS/F17/1C/07 (Berg, 2021b). The L1C TB data for SSMIS on DMSP-F18 were obtained from doi:10.5067/GPM/SSMIS/F18/1C/07 (Berg, 2021c). The L1C TB data for AMSR2 on GCOM-W1 were obtained from doi:10.5067/GPM/AMSR2/GCOMW1/1C/07 (Berg, 2022a). The L1C TB data for MHS on Metop-A were obtained from doi:10.5067/GPM/MHS/METOPA/1C/07 (Berg, 2022b). The L1C TB data for MHS on Metop-B were obtained from doi:10.5067/GPM/MHS/METOPB/1C/07 (Berg, 2022c). The L1C TB data for MHS on Metop-C were obtained from doi:10.5067/GPM/M

HS/METOPC/1C/07 (Berg, 2022d). The L1C TB data for MHS on NOAA-18 were obtained from doi:10.5067/GPM/MHS/NOAA18/1C/07 (Berg, 2022e). The L1C TB data for MHS on NOAA-19 were obtained from doi:10.5067/GPM/MHS/NOAA19/1C/07 (Berg, 2022f). The L1C TB data for ATMS on SNPP were obtained from doi:10.5067/GPM/ATMS/NPP/1C/07 (Berg, 2022g). The L1C TB data for ATMS on NOAA-20 were obtained from doi:10.5067/GPM/ATMS/NOAA20/1C/07 (Berg, 2022h). The NE23 Level-4 "Arctic Ocean – Sea and Ice Surface Temperature" data were obtained from doi:10.48670/moi-00123 (Copernicus Marine Service, 2024; Nielsen-Englyst et al., 2023). The AMSR2 sea ice concentration data from the University of Bremen were retrieved from `https://data.seaice.uni-bremen.de/` (last access: 8 September 2024, Spreen et al., 2008). The AMSR2 and ASCAT multiyear ice concentration data from the University of Bremen were retrieved from `https://data.seaice.uni-bremen.de/MultiYearIce/MYIuserguide.pdf` (Melsheimer and Spreen, 2022). Sentinel-2B L2A images were obtained from the Copernicus Data Space Ecosystem doi:10.5270/S2_-znk9xsj (European Space Agency, 2021). Images from MODIS onboard Terra were retrieved from the NASA Worldview application at `https://worldview.earthdata.nasa.gov` (NASA ESDIS, 2024). Satellite bandpass information was obtained from the EUMETSAT Numerical Weather Prediction Satellite Application Facility at `https://nwp-saf.eumetsat.int/site/software/rttov/download/coefficients/spectral-response-functions/` (NWP SAF, 2024). Sea ice drift data were retrieved from the NASA National Snow and Ice Data Center Distributed Active Archive Center at doi:10.5067/INAWUWO7QH7B (Tschudi et al., 2019).

Author contributions

NR conducted the emissivity retrieval, data analysis, and visualization and prepared the paper. SC, MM, and NR conceptualized the study. SC and MM carried out the field observations. CP and GS provided valuable expertise in interpreting emissivity signatures. All authors reviewed and edited the paper.

Acknowledgements

We gratefully acknowledge the funding from the German Research Foundation (Deutsche Forschungsgemeinschaft; DFG) as part of the Transregional Collaborative Research Center SFB/TRR 172 "Arctic Amplification: Climate Relevant Atmospheric and Surface Processes and Feedback Mechanisms" ((AC)^3) research project (grant no. 268020496). We sincerely thank the Alfred Wegener Institute for providing and operating the *Polar 5* aircraft, and we extend our sin-

cere appreciation to the dedicated crew and technicians who supported its missions. We acknowledge the use of imagery from the NASA Worldview application (https://worldview.earthdata.nasa.gov, last access: 8 September 2024), part of the NASA Earth Science Data and Information System (ESDIS). Furthermore, we acknowledge the freely available Python packages, including (but not limited to) "NumPy" (Harris et al., 2020), "pandas" (McKinney, 2010), "Xarray" (Hoyer and Hamman, 2017), "SciPy" (Virtanen et al., 2020), "GDAL" (Warmerdam, 2008), "Matplotlib" (Hunter, 2007), "seaborn" (Waskom, 2021), "cartopy" (UK Met Office, 2023), and "scikit-learn" (Pedregosa et al., 2011). We sincerely appreciate Fabio Crameri for providing scientific colormaps via an open repository, enhancing the visual quality of this work (Crameri, 2018). We acknowledge the use of OpenAI's language models, including GPT-3.5 (Generative Pre-trained Transformer 3.5) via ChatGPT and GPT-4 via GitHub Copilot, in preparing and refining written content and code, respectively.

Chapter 4

Microwave signature of snow accumulation

This study analyses the sea ice microwave emissivity during autumn freeze-up with a focus on new ice formation and snow accumulation from 22 to 243 GHz in the Central Arctic using observations from the VAMPIRE experiment during R/V *Polarstern* expedition PS144. The study is currently in preparation for submission:

Risse, N. et al. 2025: Microwave signature of new ice formation and snow accumulation on newly formed sea ice: New insights at 183 and 243 GHz from the ship-based VAMPIRE experiment, in preparation.

Detailed author contributions: Nils Risse conducted the emissivity retrieval, data analysis, data visualization, and prepared the manuscript. Nils Risse conceptualized the study with support from Susanne Crewell, Mario Mech, and Catherine Prigent. All authors reviewed and edited the manuscript.

Microwave signature of new ice formation and snow accumulation on newly formed sea ice: New insights at 183 and 243 GHz from the ship-based VAMPIRE experiment

Nils Risse[1], Mario Mech[1], Catherine Prigent[2], and Susanne Crewell[1]
[1]Institute for Geophysics and Meteorology, University of Cologne, Cologne, Germany
[2]Laboratoire d'Instrumentation et de Recherche en Astrophysique, Observatoire de Paris, CNRS, Paris, France
Correspondence: Nils Risse (n.risse@uni-koeln.de)

Abstract The spaceborne passive microwave capabilities recently expanded beyond 200 GHz, providing new information on atmospheric and surface properties. However, the properties and processes that modify the spectral, angular, and polarization dependence of sea ice and snow emissivity at frequencies above 200 GHz are not fully understood. Moreover, it is unclear how well surface microwave emission models represent the observed sea ice emissivity at high frequencies. Here, we use data from the VAMPIRE experiment conducted during R/V *Polarstern* expedition PS144 from August to October 2024. The microwave radiometers HATPRO (22–58 GHz) and MiRAC-P (183–340 GHz) performed regular scans of the upwelling radiation from the surface (35–65°) and downwelling radiation from the sky with collocated thermal infrared and visual surface cameras. A statistical analysis of the observed emissivity spectra during ship transit is performed with a focus on the emissivity evolution during new ice formation and snow accumulation on newly formed ice after surface freeze onset. New ice formation shows highly correlated emissivity at all frequencies from the open water signature and saturates at a high emissivity (0.95). Snow accumulation leads to a reduction of the emissivity due to scattering at 183.31±7.5 and 243 GHz to about 0.6, while the emissivity at 23.84, 31.4, and 51.26 GHz remains almost unchanged. A regression model was developed with visual grayscale images as input to predict the emissivity at 243 GHz, which confirmed the importance of snow cover in the emissivity reduction. Based on the observed variability, we perform Monte-Carlo SMRT simulations and sensitivity tests of bare and snow-covered nilas. Snow density, correlation length, and thickness dominate the signal at 183.31±7.5 and 243 GHz as suggested from observations. Moreover, the simulated emissivity of bare and snow-covered sea ice matches the observations when considering biases due to the emitting layer temperature and surface reflection assumptions. The results of this study are useful for coupled satellite data assimilation and atmospheric and surface retrievals over sea ice above 200 GHz.

4.1 Introduction

Passive microwave observations from polar-orbiting satellites contain information on various sea ice and snow properties (Sandven et al., 2023) and their long-term changes (e.g. Stroeve et al., 2014) in the Arctic. With the launch of novel instruments with channels above 200 GHz that improve remote sensing of cloud ice (Buehler et al., 2007; May et al., 2024) and supercooled liquid water (Camplani et al., 2024b), new spectral capabilities of sea ice and snow remote sensing are also available from partly surface-sensitive channels under cold and dry Arctic conditions. Examples are the TROPICS-01 Pathfinder (204.8 GHz), Arctic Weather Satellite or EPS-Sterna constellation (325±6.6 GHz), Microwave Sounder (229 GHz), and Ice Cloud Imager (243 and 325±9.5 GHz). Understanding the underlying properties and processes that modify the sea ice and snow emissivity and its spectral, angular, and polarization dependence is highly relevant for data assimilation within numerical weather prediction models (De Rosnay et al., 2022). Uncertainties in the modeling of the surface emissivity and its temporal changes currently limit the use of microwave observations for numerical weather prediction (Lawrence et al., 2019).

A fast temporal change of the sea ice emissivity occurs from summer to autumn. The end of summer melt is initiated by radiative energy flux changes due to decreased downwelling shortwave radiation, increased surface albedo, and decreased downwelling longwave radiation (Persson, 2012). This leads to the surface freeze onset and the formation of new sea ice in between the multiyear ice, defined as sea ice that survived summer melt. At the same time, the precipitation phase transitions from a rain-dominated regime to predominantly snowfall (Ebell et al., 2025), which accumulates on the sea ice. The transition in surface properties during the surface melt and surface freeze onset can be detected from satellite passive microwave observations (Drinkwater and Xiang Liu, 2000; Drobot and Anderson, 2001; Wang et al., 2011; Markus et al., 2009; Bliss et al., 2017) and allows for the derivation of changes in the timing of the surface freeze onset (Stroeve et al., 2014). In summer, the microwave emissivity of sea ice and snow is high due to the high liquid water content. Once the surface begins to freeze, the emissivity decreases and is dominated by scattering within the upper sea ice layers and snow (Gogineni et al., 1992), and allows for retrievals of multiyear and first-year ice concentration (Melsheimer et al., 2023). New sea ice in between older ice exhibits a high emissivity (Hewison and English, 1999). The brine volume, especially at the surface, and ice temperature influence the microwave emissivity of new ice at 6, 19, and 37 GHz as found from surface-based observations (Hwang et al., 2008) and the polarization ratio at 37 GHz is used for ice thickness retrievals (Cavalieri,

1994; Martin et al., 2004). Thin snow thickness can be observed with higher frequencies around 85 GHz (Comiso et al., 2003). This was also found by Hwang et al. (2008) over thin ice, while lower frequencies are not sensitive to the shallow snow cover, except for saline snow.

Several ship expeditions were conducted with microwave radiometers pointing at the sea ice during stations or transit through the sea ice. The earliest was the Norwegian Remote Sensing Experiment (NORSEX) in September and October 1979 with frequencies between 4.9 and 94 GHz (NORSEX Group, 1983; Matzler et al., 1984), followed by the Marginal Ice Zone Experiment (MIZEX) in June and July 1983 and 1984 (Onstott et al., 1987; Tucker et al., 1991). Grenfell (1992) conducted the Coordinated Eastern Arctic Experiment (CEAREX) with traverse observations during the initial stages of freeze-up from 11 to 16 September 1988. In October 2003, Hwang et al. (2008) performed measurements of thin newly formed sea ice combining ship-based microwave radiometers and in situ sampling in the Beaufort Sea and Amundsen Gulf at 19, 37, and 85 GHz for incidence angles from 30 to 70°. Surface-based microwave radiometer observations on a multiyear ice floe with extensive in situ observations were conducted during the Multidisciplinary drifting Observatory for the Study of Arctic Climate (MOSAiC) expedition (Nicolaus et al., 2022), providing new insights into rain-on-snow events (Stroeve et al., 2022). The Water Vapor, Cloud Liquid Water, and Surface Emissivity over the Arctic Marginal Ice Zone in Summer (WALSEMA) project carried out microwave observations onboard R/V *Polarstern* in July and August 2022 in the Fram Strait with frequencies between 22.24 and 243 GHz during the melt season (Rückert et al., 2025). Measurements from 89 to 340 GHz were also conducted during two airborne campaigns, ACLOUD (Wendisch et al., 2019) and AFLUX (Mech et al., 2022a). These showed on average flat emissivity spectra from 89 to 340 GHz, but also emissivity spectra over snow-covered young ice with a high emissivity at 89 GHz and low emissivity at 243 and 340 GHz (Risse et al., 2024b). However, there is a gap in describing the sea ice emissivity change at frequencies above 200 GHz from highly emissive newly formed bare ice to snow-covered first-year ice and in evaluating microwave emission models at high frequencies over sea ice.

In this work, we analyze the temporal evolution of sea ice microwave emissivity from 22.24 to 51.26 GHz and 183.31±7.5 to 243 GHz using quasi-continuous ship-based passive microwave, thermal infrared, and visual camera observations in the Central Arctic from August to October 2024. Two microwave radiometers were mounted on the railing of R/V *Polarstern* and performed surface scans with incidence angles between 35 and 65°. Based on this data, we aim to (1) analyze the spectral and angular emissivity variability during summer melt and autumn

freeze-up, (2) understand microwave emissivity changes after surface freeze onset from new ice formation to ice growth and snowpack formation, and (3) assess its representation in the Snow Microwave Radiative Transfer (SMRT) model (Picard et al., 2018).

This paper is structured as follows. Section 4.2 provides an overview of the VAMPIRE experiment and the data. The emissivity estimation and radiative transfer simulations are presented in Sect. 4.3. The results are presented in Sect. 4.4. Section 4.5 summarizes and concludes the study.

4.2 Data

4.2.1 VAMPIRE experiment

The Water Vapor, Mixed-Phase Clouds, and Sea Ice Emissivity over the Central Arctic Ocean (VAMPIRE) experiment was conducted during Research Vessel (R/V) *Polarstern* cruise PS144 from 9 August to 13 October 2024 (Rabe and Geibert, 2025). The ship traveled within the sea ice between 84 and 90° N for 52 days from 14 August to 4 October (Fig. 4.1). Hence, the VAMPIRE experiment captured processes during the transition phase from polar day to polar night, such as new ice formation and snow accumulation. The new ice that formed within leads is predominantly sampled during transit, while ten ice stations were performed on multiyear ice floes. Here, we analyze observations during transit, defined as ship velocity above $0.5\,\mathrm{m\,s^{-1}}$, which provide a large amount of quasi-random regular samples over diverse sea ice and snow conditions. Observations at low ship velocity are used to visualize homogeneous emissivity scans only.

August was dominated by surface melt conditions with intermittent freezing events, which caused refreezing of melt ponds and formation of patches with new ice (Fig. 4.2a). After 2 September, air temperatures remained below the freezing point of salt water until the end of the expedition with 3-hourly mean surface and air temperature minima of 257 K. Based on this, we divide the ship trajectory into a melting period and a continuous freezing period with a surface freeze onset on 2 September, which is within climatological estimates for the region (Markus et al., 2009; Stroeve et al., 2014).

The precipitation events during both time periods are depicted in Fig. 4.2b. While rain and mixed-phase precipitation occurred before the surface freeze onset, several snowfall events led to the development of a snowpack on the multiyear and newly formed sea ice. These snowfall observations along the ship trajectory agree qualitatively with in situ snow depth measurements. While no snow was observed during the three ice stations from 16 August to 2 September, snow was

observed for all ice stations thereafter (5 to 25 September) with a snow depth mostly between 5–10 cm (Rabe and Geibert, 2025, Table 6.6). Thus, the snow accumulation on multiyear ice happens during a single episode after surface freeze onset. The continuous formation of new ice in leads after surface freeze onset and regular snowfall leads to a high variability in snow cover along the ship track. Based on visual camera imagery, the first snow patches on young ice occurred on 10 September.

The instrumentation of the VAMPIRE experiment is an extension of the WALSEMA experiment during R/V *Polarstern* cruise PS131 (Rückert et al., 2025). Several instruments were installed on the ship, including 22–58 and 183–340 GHz microwave radiometers, W- and G-band cloud radars, thermal infrared and visual surface cameras, a disdrometer, an ultrasonic anemometer, and a sky camera (Rabe and Geibert, 2025, Fig. 6.22 and 6.23). Further meteorological data are collected by the German Weather Service (DWD). Radiosondes were launched by DWD and the VAMPIRE project, mostly three times per day (Rabe and Geibert, 2025, Fig. 6.24), and in situ sea ice and snow sampling was performed during ten ice stations.

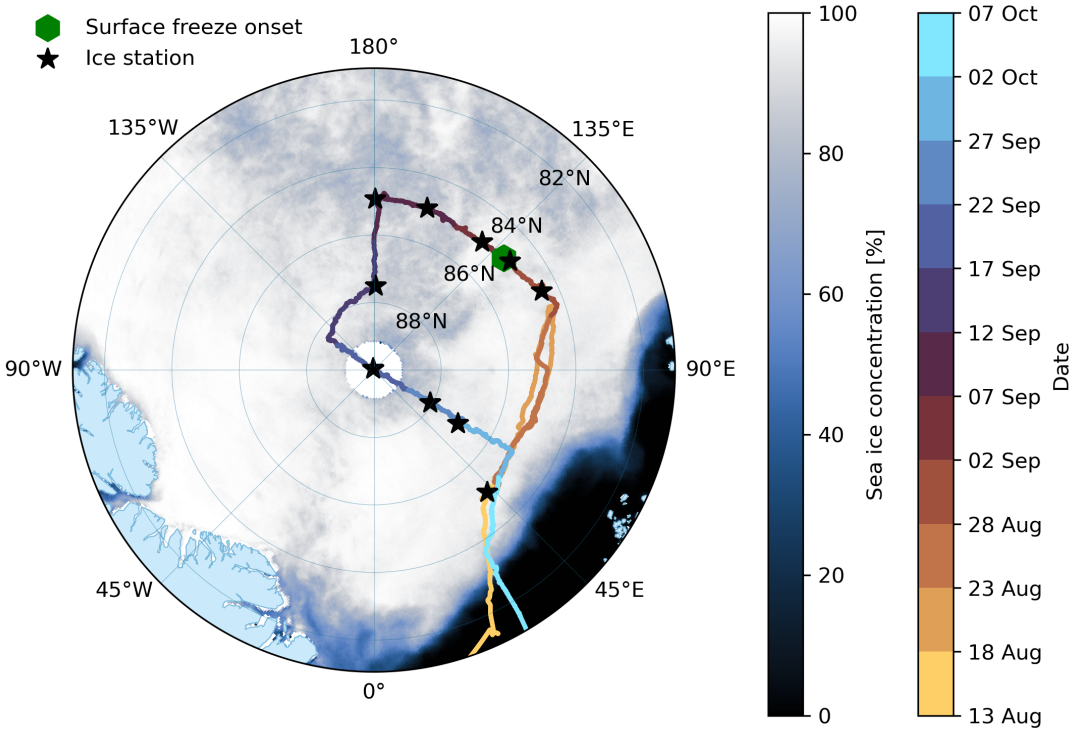

Figure 4.1: Track of R/V *Polarstern* and the mean sea ice concentration (Spreen et al., 2008) from 14 August to 4 October as shading. The position during surface freeze onset on 2 September and ice stations are indicated along the ship trajectory. Note that the sea ice concentration product is not available north of about 89° N.

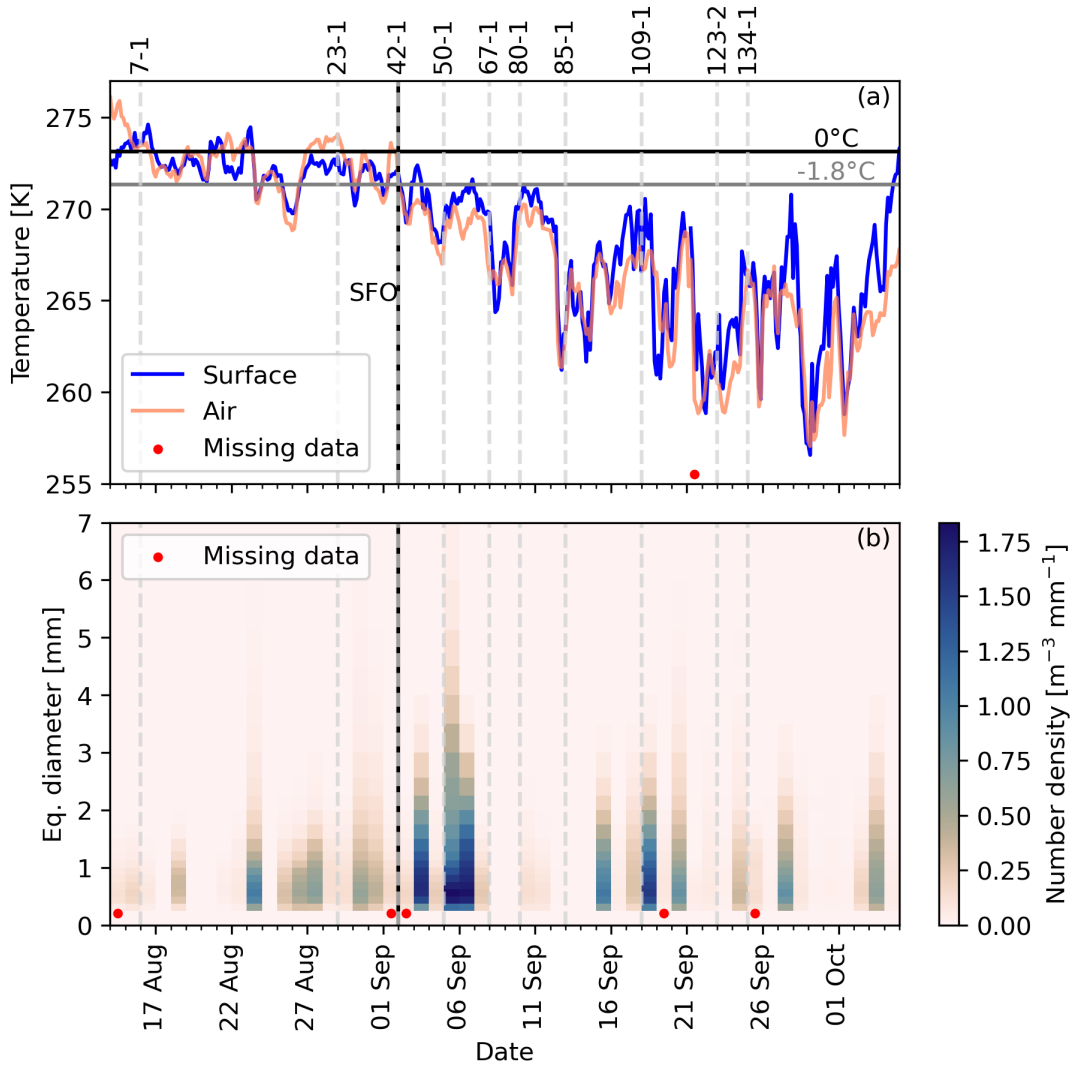

Figure 4.2: Meteorological and surface conditions from 14 August to 4 October with dates of the surface freeze onset (SFO) and ice stations. (a) 3-hourly mean surface temperature from the thermal infrared camera and 3-hourly mean air temperature at about 40 m above sea level. (b) Daily mean number density of the equivalent diameter measured by the disdrometer. The missing data flag indicates days with less than 75 % of thermal infrared camera or disdrometer data.

4.2.2 Microwave radiometers

The microwave radiometers Humidity and Temperature Profiler (HATPRO; Rose et al., 2005) and Microwave Radar/radiometer for Arctic Clouds - Passive (MiRAC-P; Mech et al., 2019) are mounted on the railing in the forward part of the ship about 21 m above sea level. HATPRO measures at seven channels between 22.24 and 31.4 GHz, and seven channels between 51.26 and 58 GHz (Table 4.1). MiRAC-P measures at six channels along the 183.31 GHz water vapor absorption line with the outermost double side-band channel at 183.31±7.5 GHz and two channels at 243 and 340 GHz. The 340 GHz channel is not considered in this analysis due to high receiver noise throughout the expedition and thus very noisy emissivity estimates. All channels measure mixed polarization that changes with scan or incidence angle (θ). Note that the polarization is opposite to the WALSEMA campaign. The relative contributions of vertical and horizontal polarization to the brightness temperature (TB) at quasi-vertical polarization (QV) $T_{\mathrm{b,QV}}$ can be computed with

$$T_{\mathrm{b,QV}} = T_{\mathrm{b,V}} \cos^2(\theta) + T_{\mathrm{b,H}} \sin^2(\theta), \tag{4.1}$$

and for quasi-horizontal polarization (QH) with

$$T_{\mathrm{b,QH}} = T_{\mathrm{b,H}} \cos^2(\theta) + T_{\mathrm{b,V}} \sin^2(\theta). \tag{4.2}$$

The relative contributions of vertical (horizontal) polarization to the QV (QH) channel at 35, 45, 53, 55, and 65° are 67, 50, 36, 33, and 18 %, respectively. Thus, the measured radiation is mixed equally between horizontal and vertical polarization at an incidence angle of 45°. The same relationships as in Eq. (4.1) and (4.2) also hold for the emissivity under unpolarized downwelling TB.

Both microwave radiometers measured continuously in the sea ice with short interruptions on 27 August and 11 September (Rabe and Geibert, 2025, Fig. 6.24). Synchronized adjustments of the internal mirror of each instrument allowed frequent automated scans of the upwelling TB from the surface and the downwelling TB from the atmosphere. Four scan types are performed: surface scans at 35–65° and corresponding sky views (A), zenith scan (B), surface scan at 53° and corresponding sky view (C), and boundary layer scans (D; Table 4.2). The scan types are combined to a scan pattern of about 30 min duration in the following order: A-B-C-B-C-D-B (Fig. 4.13). The frequent switch between the scan types ensures regular sampling along the ship trajectory, and regular restarts at 00 and 30 min of each hour ensure synchronization of both instruments. Here, we use all surface scans and match them with the sky views averaged over 15 min intervals,

excluding sky views near the horizon (94.2–104.4°). We can assume that the sky views are representative of the time where surface scans were measured, due to the low ship velocity and temporal proximity of the surface scans and slanted sky views (Fig. 4.13). To reduce the influence of ship motion on the scans, we filter data where the ship roll or pitch angles (recorded by ship sensors) are larger than ±2.5° from both the upwelling and downwelling TB scans. About 750,000 upwelling TB samples are available at 53° incidence angle, and 35,000 each at 35, 45, 55, and 65° incidence angle during transit within the sea ice. This corresponds to about 8 d of continuous sampling at 53° and 12 h at each of the other four incidence angles. Despite the short sampling time compared to the cruise duration, the regular sampling of the upwelling TB captures large-scale features present in collocated Advanced Microwave Scanning Radiometer 2 (AMSR2) data (see Appendix 4.B). Moreover, the comparison with AMSR2 highlights the capability of the small footprint size to separate sea ice types and leads.

Absolute calibrations with liquid nitrogen were performed after instrument installation, before the cruise start, and during the cruise on 11 September. Additionally, the instruments perform an internal gain calibration for 10 s at the beginning of each zenith scan. To further validate the observations, we compare them with forward simulations of 13 radiosondes launched during clear-sky conditions between 25 August and 1 October using the Passive and Active Microwave radiative TRAnsfer (PAMTRA) model (Mech et al., 2020). Potential contamination due to fog is excluded using ceilometer measurements by DWD. The agreement is very good for HATPRO channels with mean biases between -0.5 and 2 K at zenith. For MiRAC-P channels, a larger mean bias occurs for zenith scans at 183.31±7.5, 243, and 340 GHz with -2, -4, and 3 K, respectively. As the bias changes smoothly with incidence angle, we assume that the bias originates from the radiative transfer simulation. The other MiRAC-P channels show a much lower mean bias between 0 and 1.5 K at zenith. The biases of HATPRO and MiRAC-P are stable before and after the absolute calibration on 11 September, which provides confidence in the measurement accuracy.

4.2.3 Surface cameras

A thermal infrared (FLIR A315) and visual camera (GoPro HERO11) are installed next to the microwave radiometers at an incidence angle of about 53° to provide surface skin temperature data and daytime information on the surface conditions. The thermal infrared camera records TB images at 7.5–13 µm with 1 s temporal resolution and a field of view of 25°×18.8° resolved by 320×240 pixels. The accuracy of the recorded temperature data is ±2 K in the observed tempera-

Table 4.1: Frequency, polarization (Pol.), and footprint size of the HATPRO and MiRAC-P channels during VAMPIRE. The footprint size corresponds to an incidence angle of 53° (Rückert et al., 2025). QH: quasi-horizontal. QV: quasi-vertical.

Instrument	Frequency (GHz)	Pol.	Footprint (m^2)
HATPRO	22.24, 23.04, 23.84, 25.44, 26.24, 27.84, 31.4	QV	4.0×2.4–3.6×2.2
	51.26, 52.28, 53.86, 54.94, 56.66, 57.3, 58.0	QH	2.7×1.6–2.4×1.4
MiRAC-P	$183.31 \pm 0.6; 1.5; 2.5; 3.5; 5.0; 7.5$	QV	1.4×0.8
	243	QH	1.4×0.8
	340	QH	1.1×0.7

Table 4.2: Sky angles, surface angles, and duration per angle for the four scan types. An angle of 180° corresponds to zenith and 0° to nadir.

Scan	Sky angles [°]	Surface angles [°]	Duration per angle [s]
A	115, 125, 135, 145	35, 45, 55, 65	15
B	180		360 (270[a])
C	127	53	2×15 (sky), 155[b], 175[c] (surface)
D	180, 120, 109.2, 104.4, 101.4, 98.4, 96.6, 95.4, 94.8, 94.2		10

[a]Duration of the final scan within a 30 min scan pattern. [b]HATPRO. [c]MiRAC-P

ture range. The camera is actively heated to avoid condensation on the lens. As the camera's range of covered incidence angles (44–62°) is slightly smaller than the microwave radiometer scans (35–65°), we use the mean temperature of the camera image for the emissivity calculation at all angles. Typically, the conversion of thermal infrared TB is performed under the assumption of an infrared emissivity. Here, we directly perform a correction based on in situ skin temperature measurements during the ten ice stations, which revealed a consistent bias of 3.5 K in the FLIR data for in situ temperature ranges of 260–273 K.

The visual camera records high-resolution images with a temporal resolution of 2 s. As the color ratio of the images adjusts to ambient light, we derive grayscale images as the mean of all channels. Its large field of view covers all incidence angles of the microwave radiometer. Here, we use crops with a size of 384×384 pixels that cover the surface viewed by the different scan positions. The crops are not corrected for the camera viewing geometry. The global radiation (G) observations from DWD are used to remove images with sun glint ($G \geq 40\,\mathrm{W\,m^{-2}}$) and dark images ($G \leq 3\,\mathrm{W\,m^{-2}}$). Images with condensation on the lens are filtered manually. The lenses of both cameras were cleaned regularly during the expedition.

4.2.4 Ancillary data

We use temperature profiles, absolute humidity profiles, and liquid water path retrieved from HATPRO zenith observations (Walbröl et al., 2022). These profiles are averaged to 15 min and used as input to PAMTRA. Moreover, we use pressure values from radiosondes launched during the expedition for the radiative transfer simulation. The temperature and relative humidity profiles from the radiosondes are used under clear-sky conditions for the analysis of the microwave radiometer measurement accuracy based on PAMTRA simulations.

Data from the OTT Parsivel disdrometer is used for qualitative information on the precipitation intensity and type, especially snowfall after surface freeze onset. However, these observations are only of limited use and not necessarily related to the accumulated snowfall on the sea ice. To get information on the general presence of accumulated snow, we use the in situ samples in the microwave radiometer footprint provided in Rabe and Geibert (2025).

The DWD also provides standard meteorological data. Air temperature data are used to identify the surface freeze onset and for qualitative comparison with the thermal infrared skin temperature. Additionally, we use global radiation data for quality control of the visual camera images. We also use sea ice concentration data from the University of Bremen to provide context on the sea ice in the

Central Arctic (Spreen et al., 2008). Intercalibrated Level 1C TB data (NASA Goddard Space Flight Center and GPM Intercalibration Working Group, 2022) from AMSR2 (JAXA, 2016) at 23.8 GHz along the ship trajectory are used to analyze the representability of the ship measurements for the large-scale satellite TB variability during transit.

4.3 Methods

4.3.1 Surface emissivity estimation

The emissivity calculation from the ship is based on the non-scattering radiative transfer equation (Prigent et al., 1997)

$$T_b = e \cdot T_s \cdot t(0,h) + (1-e) \cdot T_{b,down}(\infty,0) \cdot t(0,h) + T_{b,up}(0,h), \tag{4.3}$$

with the measured upwelling brightness temperature T_b, emissivity e, surface temperature T_s, transmissivity between the surface and instrument height $t(0,h)$, downwelling TB at the surface $T_{b,down}(\infty,0)$, and upwelling TB of the atmosphere between the surface and the microwave radiometer $T_{b,up}(0,h)$. We assume that the effect of scattering by frozen hydrometeors above the ship can be neglected. As the instrument is close to the surface at an altitude of 21 m, we can also assume that the upwelling TB is negligible ($T_{b,up}(0,h) \approx 0\,\mathrm{K}$) and the transmissivity close to unity ($t(0,h) \approx 1$) at window channels and channels at the wing of absorption lines. This leads to the simplified version of the radiative transfer equation at the surface

$$T_b = e \cdot T_s + (1-e) \cdot T_{b,down}(\infty,0). \tag{4.4}$$

Moreover, we can assume that the measured downwelling TB at the instrument height is similar to the downwelling TB at the surface ($T_{b,down}(\infty,0) \approx T_{b,down}(\infty,h)$). Hence, we can estimate the emissivity directly from the surface temperature and observed microwave TB following

$$e = \frac{T_b - T_{b,down}(\infty,h)}{T_s - T_{b,down}(\infty,h)}. \tag{4.5}$$

We estimate the emissivity under both specular and Lambertian reflection of the downwelling TB. For specular reflection, the downwelling TB is taken directly from the corresponding angle from the sky view. For Lambertian reflection, an integration over the entire hemisphere is needed. Similar to airborne observations by Harlow (2009), we only measure the downwelling TB at a few angles during the sky view and need additional information to account for contributions from angles

not measured by the microwave radiometers. Therefore, we simulate the downwelling TB with PAMTRA every 15 min (see Sect. 4.3.3). Channel-dependent biases are corrected using all available sky views between 0–71° incidence angle for each 15 min time window. Any measurement where the bias or residual error is larger than the channel (and angle) dependent 95th percentile is excluded from the analysis to automatically filter for poor simulations of the downwelling TB or observations. The residual mean absolute error between simulation and observation varies with channel and angle, but is mostly below 2 K.

Several factors contribute to the emissivity uncertainty. Here, we use Gaussian error propagation to estimate the uncertainty of the emissivity calculation at the surface as described in Rückert et al. (2025). The error estimation considers uncertainties from the upwelling TB, downwelling TB, and surface skin temperature. The error of the observed upwelling TB is estimated as 1.5 K, which represents the microwave radiometer measurement uncertainty. The error of the observed downwelling TB is a combination of the radiometer noise (1.5 K) and also takes into account the representativeness of the downwelling TB for the surface scan. For specular reflection, this representativeness is given as the standard deviation of the downwelling TB for the given angle. For Lambertian reflection, this uncertainty is computed as the root mean squared error (RMSE) of the residual between the surface scan and the bias-corrected downwelling TB simulation. The surface temperature uncertainty consists of instrument noise, which is assumed to be 1 K based on comparison with in-situ measurements, and the standard deviation of temperatures within the image. We discard any data with an emissivity uncertainty larger than 0.1, except for the case study in Fig. 4.4. This threshold includes all observations from 22.24 to 51.26 GHz, 16–75 % of observations at 183.31±7.5 GHz, and 70–90 % of observations at 243 GHz. The lowest number of observations is available under specular reflection at an incidence angle of 65° at the high frequencies. Uncertainties due to fog between the instrument and the surface are assumed to be negligible for the statistical analysis.

In addition to random errors, there are potentially large biases due to the difference between skin temperature and emitting layer temperature. While the difference is small at high frequencies due to the small penetration depth (Tonboe et al., 2006), larger biases occur at low frequencies. To assess the impact of a warm emitting layer temperature on the emissivity, we also derive the emissivity with a temperature of $\max(271K, T_s)$. The minimum temperature value is based on the bulk temperature of multiyear ice during ice stations (Rabe and Geibert, 2025, Table 6.6). These emissivity estimates are used for comparison with SMRT simulations only.

The surface reflection type varies seasonally (Guedj et al., 2010), spectrally,

and between surface types, i.e., open water and snow-covered sea ice. While the difference between specular and Lambertian reflection is small at channels with low zenith opacity (Matzler, 2005), the biases cannot be neglected from 51.26 to 243 GHz. Lambertian reflection was found to be more accurate than specular reflection over snow-covered surfaces at high frequencies (Harlow, 2009). Therefore, we primarily analyze Lambertian emissivity.

Changes of the sea ice and snow by the ship through breaking or flooding strongly impact the microwave emissivity compared to pristine conditions. The largest effect is expected at the 35° angle, which scans at a distance of about 12 m to the vessel (42 m at 65°). However, as intense disturbances are rare and partly similar to natural sea ice processes, they are assumed to be negligible during the statistical analysis.

4.3.2 Image–emissivity regression

Visual images contain high-level information on sea ice and snow properties through brightness differences, shapes, and structures. These are usually used to classify the sea ice and snow into categories, such as open water, melt ponds, dark nilas, white nilas, snow cover, ridges, first-year ice, and multiyear ice. Several studies have shown that these high-level categories translate into distinct microwave emission signals (e.g., NORSEX Group, 1983; Hewison and English, 1999) and explain substantial parts of the variability. For example, the difference between snow-covered multiyear ice and nilas can be easily detected from camera images, and they also show distinct microwave emission spectra. Emissivity variability within a given sea ice or snow type is dominated by low-level features, such as snow and sea ice microstructure, salinity, density, and thickness, which are not resolved by visual images. However, the importance of high-level information motivates the development of an unbiased and automated information extraction method from visual images.

As we are only interested in features relevant to microwave emission, we extract the information with the objective of explaining the observed microwave TB. Hence, the model solves an image–emissivity regression problem, transforming grayscale visual images (384×384 pixels) to microwave TB. For model training and evaluation, we use about 12,500 collocated visual and microwave samples over newly formed sea ice after surface freeze onset. Newly formed sea ice is defined as scans where the 51.26 GHz emissivity exceeds its 65th percentile ($e = 0.91$). This represents a simpler task than predicting the entire emissivity variability, including surface melt. The output of the network is the surface emissivity under Lambertian reflection at 243 GHz and 53° incidence angle. Details on the training

and network architecture can be found in Appendix 4.C.1 and 4.C.2, respectively.

4.3.3 Atmospheric radiative transfer simulations

Atmospheric radiative transfer simulations are performed with the PAMTRA model (Mech et al., 2020). From the simulations, we extract the downwelling TB at the surface, and the transmissivity and upwelling TB from the surface to the top of the atmosphere. Inputs are the temperature profile, humidity profile, and liquid water path retrieved from the HATPRO zenith scans, averaged to 15 min intervals. The pressure values for the retrieval height levels are interpolated from the radiosonde observations. The liquid water path is distributed with a homogeneous cloud water content from 0–4 km height and simulated with a cloud droplet diameter of 20 µm. Supercooled liquid water emission is estimated following Turner et al. (2016). Absorption by atmospheric cases is modeled using Rosenkranz (1998) with water vapor continuum absorption modifications (Turner et al., 2009). Frozen hydrometeors are not included in the simulations. Atmospheric transmissivity and upwelling TB are only used at 23.84 GHz, where scattering by frozen hydrometeors can be neglected.

4.3.4 Sea ice and snow radiative transfer simulations

Radiative transfer simulations of the sea ice and snow are performed with SMRT (Picard et al., 2018). The simulations are compared statistically with the observations and are used to study the impact of snow properties on the emissivity at high frequencies. Here, we perform simulations of bare and snow-covered sea ice above a semi-infinite ocean layer with the layer properties listed in Table 4.3. The sea ice and snow layers are defined to represent newly formed sea ice in leads with a snow cover with small and medium-sized grains. The snow cover is dry and contains no brine in all simulations. This is a simplification as snow frequently merges with the surface brine of new sea ice (Ehn et al., 2007). Scattering is assumed to occur in the sea ice due to brine pockets only, typical for first-year ice. The microstructure is represented by the exponential autocorrelation function (Wiesmann et al., 1998) with the improved Born approximation as electromagnetic theory (Mätzler, 1998; Mätzler and Wiesmann, 1999). The radiative transfer is solved with the discrete ordinate and eigenvalue radiative transfer solver (Picard et al., 2013). The permittivity of the sea ice is calculated with the Polder–van Santen mixing formula (Polder and van Santen, 1946), assuming spherical brine inclusions.

Two types of simulations are performed. First, the base profile (Table 4.3) is simulated while varying a single parameter between the minimum and maximum

values. These simulations provide insights into the impact of snow thickness, density, and correlation length on the emissivity. Second, random Monte-Carlo simulations with uniformly distributed parameters between the minimum and maximum values are conducted, i.e., density, correlation length, thickness, and temperature of the snow, and correlation length, thickness, temperature, and salinity of the sea ice. In total, 5000 random profiles are simulated, out of which 75 % contain a snow cover. While it would be possible to simulate the observed distribution of surface temperatures, we vary it uniformly as well for simplicity. As will be shown later, mainly the ice temperature is important, which is not directly observed in the presence of snow. The Monte-Carlo simulations are used for comparison with the observed variability.

The emissivity is calculated from the simulated TB following Wiesmann and Mätzler (1999). This calculation considers the emitting layer temperature instead of the surface skin temperature as used for the observations. We simulate the frequencies of HATPRO, MiRAC-P, and intermediate frequencies at 89, 118, and 165 GHz. For direct comparison with HATPRO and MiRAC-P observations, we mix the vertically and horizontally polarized emissivity equivalent to Eq. (4.1) and (4.2) as measured by the different channels.

Table 4.3: Snow and sea ice layer parameters as input for SMRT simulations. Values indicate the base profile used for snow sensitivity tests (Base), and minimum (Min.) and maximum (Max.) values of the uniform distribution for the Monte-Carlo simulations.

Layer	Parameter	Symbol	Unit	Base	Min.	Max.
Snow	Density	ρ_{snow}	$\mathrm{kg\,m^{-3}}$	225	100	350
	Corr. length	ξ_{snow}	mm	0.1	0.05	0.25
	Thickness	h_{snow}	cm	5	0	10
	Temperature	T_{snow}	°C	-5	-15	-2
Sea ice	Corr. length	ξ_{ice}	mm	0.15	0.1	0.2
	Thickness	h_{ice}	cm	10	0.5	10
	Temperature	T_{ice}	°C	-5	-15	-2
	Salinity	S_{ice}	psu	15	1	40

4.4 Results

4.4.1 Observed sea ice emissivity

Temporal evolution

The temporal variability of the surface microwave emissivity measured along the ship track is dominated by the local conditions. For example, a high variability in the observed emissivity occurs even within a single day (Fig. 4.3). At the same time, large-scale forcings modify the measured emissivity time series. The dominant large-scale forcing is the surface freeze onset on 2 September, after which the occurrence of open water and its emissivity signature along the ship track decreases, e.g., at 23.84 GHz (< 0.5) and 51.26 GHz (< 0.6) (Fig. 4.3a,b). A similar regime shift occurs at 243 GHz after the surface freeze onset. Low emissivity values occur more frequently, especially from mid-September onward after the ship passed the North Pole (Fig. 4.3c). In general, the surface emissivity changes gradually after the surface freeze onset. This might be related to the formation and thickening of new ice and snow accumulation. However, new ice forms continuously along the ship track in newly formed leads, as will be shown in the following case.

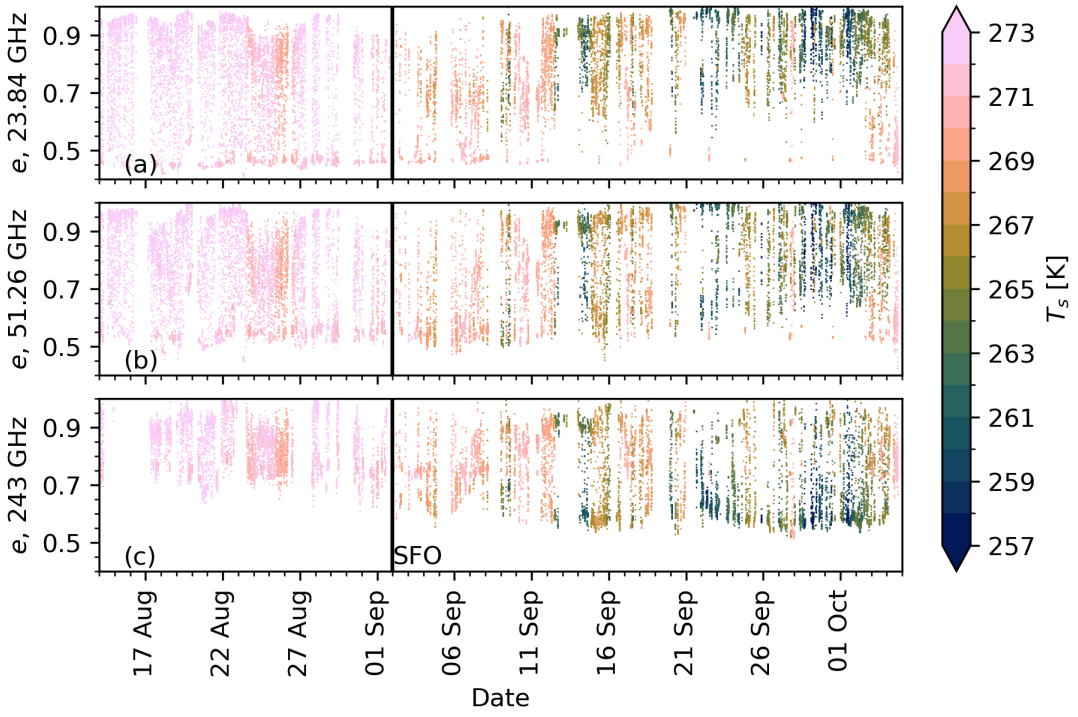

Figure 4.3: Time series of the Lambertian emissivity during transit at (a) 23.84, (b) 51.26, and (c) 243 GHz at an incidence angle of 45° with the surface temperature from the thermal infrared camera as shading. SFO: surface freeze onset.

After analyzing the large-scale emissivity variability, we provide an example

of a small-scale time series from the 53° scan with a duration of about 3 min (Fig. 4.4). This case shows various sea ice types, including dark nilas with high skin temperature, young ice with a brighter surface, and older sea ice with more heterogeneity toward the end of the surface scan. The change in ice types corresponds to changes in the emissivity regime. For example, the dark nilas lead to an emissivity reduction at 23.84 to 51.26 GHz compared to the high emissivity of the thicker young ice. Over the multiyear ice toward the end of the surface scan, the low frequencies show a high variability and the lowest emissivity of about 0.6 at 51.26 GHz. The emissivity at 183.31±7.5 and 243 GHz reduces over the young ice that is observed around 15:50 UTC, while the emissivity from 23.84 to 51.26 GHz remains high. From visual images, the ice appears to be partly snow-covered. This shows that the measurements resolve small-scale details in the surface properties. In Sect. 4.4.1, we will analyze all observations statistically to identify the persistence of these features along the ship trajectory.

Emissivity distribution

In the following, we present specular and Lambertian emissivity distributions at 23.84, 31.4, 51.26, 183.31±7.5, and 243 GHz for incidence angles between 35 and 65° (Fig. 4.5). The good match between the ocean emissivity computed with the Tool to Estimate Sea-Surface Emissivity from Microwaves to sub-Millimeter waves (TESSEM^2; Prigent et al., 2017) implemented in PAMTRA and the ocean peak in the specular emissivity histograms allows filtering of ocean surfaces from the Lambertian histogram using 23.84 to 31.4 GHz observations. Therefore, MiRAC-P scans are not shown in the Lambertian distribution if they are not synchronized with HATPRO. Larger differences in the ocean emissivity occur at 51.26 GHz for the 35 and 45° angles, and at 183.31±7.5 GHz for the 65° angle. While the difference at 183.31±7.5 GHz can be explained by reduced surface sensitivity, the higher observed emissivity at 51.26 GHz could be explained by the formation of foam and waves near the ship.

The Lambertian emissivity distribution changes with frequency and becomes increasingly bimodal from 23.84 to 243 GHz at 45°. The three channels from 23.84 to 51.26 GHz peak at an emissivity around 0.95, and measure emissivities as low as 0.5. Generally, low emissivities occur more frequently with increasing frequency from 23.84 to 51.26 GHz. This is expected due to the increased scattering with decreasing wavelength due to air pockets in the upper part of the multiyear ice and large snow grains in the surface scattering layer. At 183.31±7.5 and 243 GHz, two separated peaks emerge with maxima around 0.6 and 0.9. The peak at 0.9 is broader than the peak at 0.6, and both are well separated at 243 GHz.

The emissivity distributions change with angle (and polarization) at each

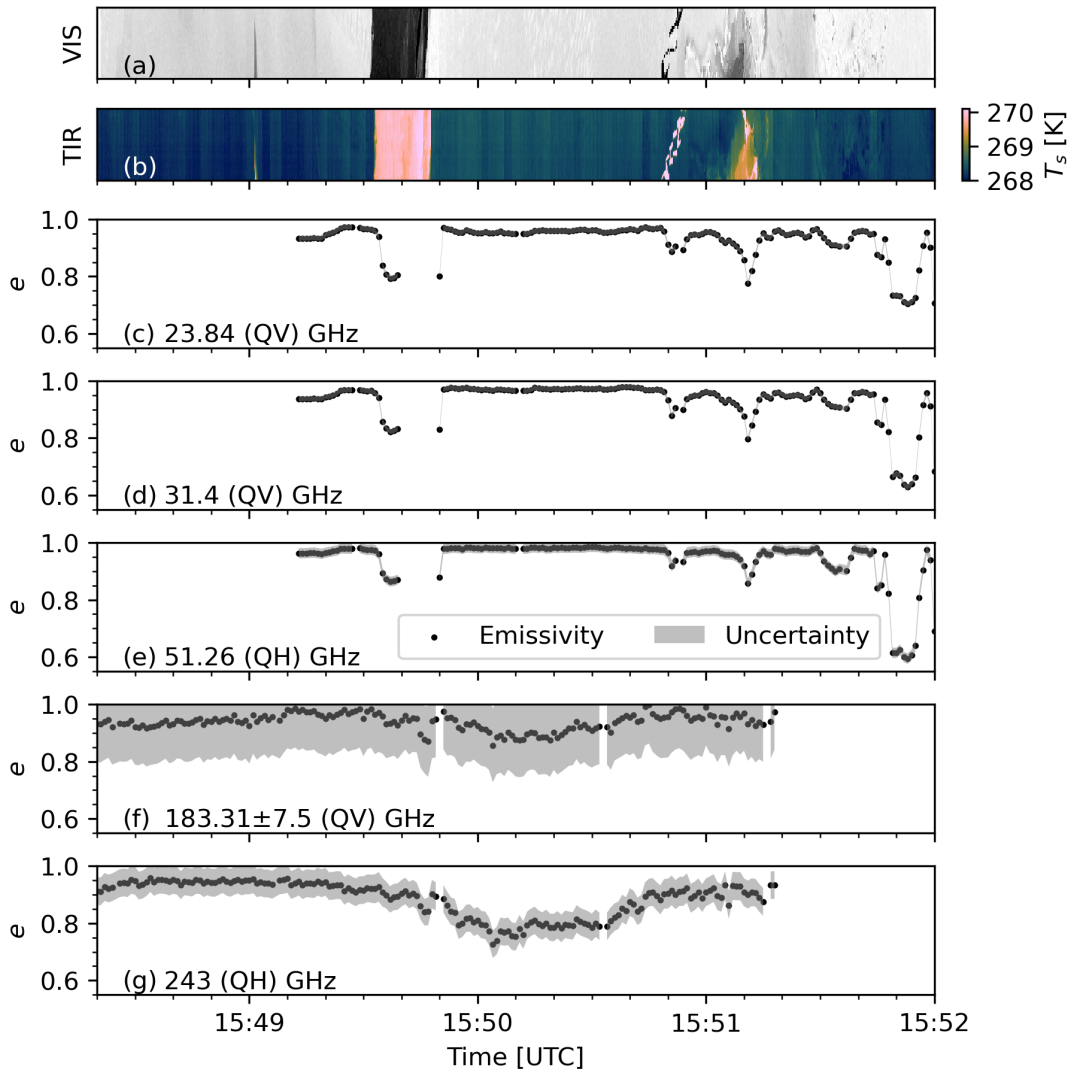

Figure 4.4: Case study of small-scale emissivity variability at an incidence angle of 53° along an 800 m transect from 15:48:20 to 15:52:00 UTC on 20 September. (a) Visual (VIS) camera image stripes, (b) thermal infrared (TIR) camera image stripes, and Lambertian emissivity at (c) 23.84, (d) 31.4, (e) 51.26, (f) 183.31±7.5 GHz, and (g) 243 GHz. Vertical stripes are extracted near the center of each camera image.

channel. This indicates that not all surfaces are Lambertian reflectors. In general, the three QV channels show decreasing emissivity with increasing incidence angle due to the larger contribution of horizontal polarization. Similarly, the two QH channels slightly increase with incidence angle or remain constant. Apart from shifts of the distributions, their shape changes notably between 35 and 65°. The most notable change in the emissivity distribution shape occurs at 243 GHz. At 35°, the emissivity follows a uniform distribution with values between 0.6 and 0.95. As the incidence angle increases, two separate peaks emerge and are almost entirely separated at 65°. Additionally, the low-emissivity peak shifts from 0.6 to 0.55, which is not observed for the low-emissivity peak at 51.26 GHz for the same polarization. These potential angular and polarization dependencies introduce non-Lambertian contributions to the reflected downwelling radiation, which are not considered in the emissivity calculation. However, the angular consistency over sea ice appears more stable when using Lambertian reflection compared to specular reflection for high incidence angles.

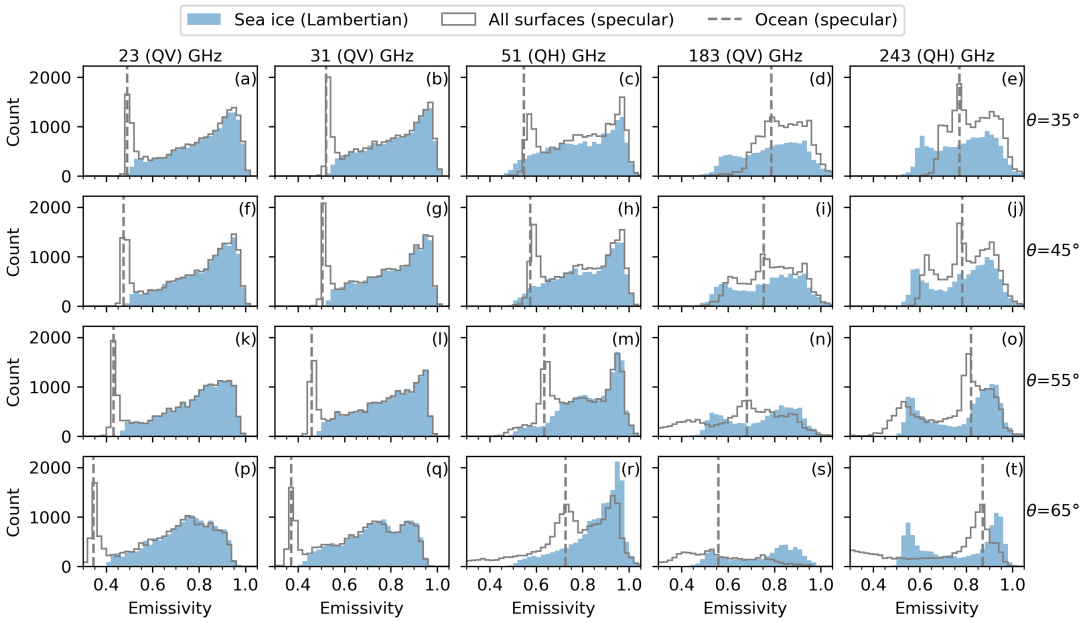

Figure 4.5: Histograms of the Lambertian emissivity over sea ice and specular emissivity over all surfaces at 23.84, 31.4, 51.26, 183.31±7.5, and 243 GHz (columns) for incidence angles of 35, 45, 55, and 65° (rows). Emissivity spectra are defined as sea ice if the specular emissivity deviates from the water emissivity spectrum calculated with TESSEM^2 (Prigent et al., 2017) by more than 0.05 at any of the seven channels from 22.24 to 31.4 GHz.

Spectral variability

In the following, we present the spectral and angular co-variability at 23.84, 51.26, and 243 GHz to relate the emissivity distribution shifts to surface properties.

Figure 4.6 compares the emissivity co-variability at these channels before and after surface freeze onset on 2 September. The distinct patterns before and after surface freeze onset can be linked to sea ice and atmospheric processes.

Before surface freeze onset, the relationship of both frequencies is almost linear at 35 and 45° with a low emissivity mode over open water and melt ponds and a high emissivity mode over melting sea ice (Fig. 4.6i,j) and potentially refrozen melt ponds. The emission signatures of melting sea ice and melt ponds are also described by Gogineni et al. (1992) at lower frequencies. The high emissivity over melting sea ice is used to detect the melt and freeze onset from satellite observations (e.g., Markus et al., 2009). Intermittent refreezing events, e.g., from 24 to 26 August (Fig. 4.3), explain the emissivity values between 0.6 and 0.9, which are almost constant with incidence angle compared to the open water signature. At 65° incidence angle, the lowest emissivity occurs over sea ice, which also corresponds to a higher 23.84 GHz emissivity compared to open water. The dry surface scattering layer on the multiyear ice reduces the emissivity at all frequencies. However, the high heterogeneity of its microstructure and thickness of the refrozen layer likely explains the large variability of emissivity values (Gogineni et al., 1992).

After surface freeze onset, snow accumulation and new ice formation alter the spectral emissivity co-variability, which broadly splits into three distinct branches. The upper branch is comparable to the water and melting sea ice or refrozen melt pond signature before surface freeze onset. However, the high emissivity mode is caused by newly formed sea ice, such as nilas (Fig. 4.6l). This also agrees with several previous studies that found high emissivity over newly formed sea ice (Hewison and English, 1999; Hwang et al., 2008; Risse et al., 2024b). Earlier stages of sea ice formation, such as dark nilas (Fig. 4.6k), show a reduced emissivity in between both ends of this branch. The high correlation of both frequencies at all angles along this branch indicates that the same physical properties influence the emissivity, i.e., temperature, salinity, and thickness. This generalizes the patterns presented for the case study in Fig. 4.4.

The second branch is characterized by a high emissivity at 51.26 GHz between around 0.95 and a variable emissivity between 0.55 and 0.95 at 243 GHz. Corresponding visual images along this branch indicate the presence of accumulated snow redistributed by wind on level sea ice (Fig. 4.6m,n). This indicates that snow accumulation and corresponding scattering at 243 GHz could explain the reduction in emissivity along this branch. At 51.26 GHz, fresh snow with rather small grain size is expected to scatter much less, which explains the constant emissivity. However, we are limited in interpreting this signal as thin layers of wet snow or snow-ice cannot be easily identified on visual imagery. Nevertheless,

we hypothesize that this branch is a continuation of the new ice formation process as snow accumulates. The absence of frequent deviations from this pattern might relate to the lack of snow accumulation before the ice reaches a thickness where the microwave emissivity saturates at the upper limit. Also, a similar emissivity spectrum was observed in the frequency range from 89 to 340 GHz in spring at nadir (Risse et al., 2024b, Fig. 5), but the airborne data were insufficient in identifying the continuous evolution of the sea ice emissivity.

The third branch shows almost flat emissivity at 243 GHz of 0.6 and variable emissivity at 51.26 GHz between 0.5 and 0.9. The mode separates well from the open water emissivity at higher incidence angles. Corresponding images indicate snow-covered sea ice with deformations (Fig. 4.6o,p). The low emissivity at 51.26 GHz indicates multiyear ice, similar to the signature of intermittent refreezing events before surface freeze onset. The accumulation of fresh snow on multiyear ice likely explains the emissivity reduction at 243 GHz compared to before surface freeze onset. Interestingly, the emissivity at 23.84 and 51.26 GHz reaches lower values compared to before surface freeze onset. This might be explained by further drying of the upper ice layer or changes in the multiyear ice properties along the ship trajectory.

In the following, we will focus on the second branch, which likely shows the impact of snow accumulation on newly formed sea ice. As we can find visual structures in the images that correspond to the reduction in 243 GHz emissivity from region 4 to 6 (Fig. 4.6l–n) and during the case study (Fig. 4.4a), we now test this hypothesis using the image–emissivity regression model.

4.4.2 Image–emissivity regression skill

The model's skill on the test set provides an indication of the information content of the images to predict the microwave emissivity. Here, we assess the skill in reproducing the observed TB, which is minimized by the loss function, and the emissivity. The predicted TB correlates with the observed TB (0.84), while the correlation is lower for the emissivity (0.67) (Table 4.4). The RMSE is about 9 K for the TB and 0.11 for the emissivity. Figure 4.7 compares the predicted and observed TB and emissivity. Clearly, the model is able to extract information from the images for the sea ice emissivity prediction. There are certain clusters that align close to the 1:1 line. This indicates that spatial structures, such as sea ice and snow shapes, are extracted from the image. However, intermediate emissivity of 0.7 to 0.8 is not well predicted by the model, although they are well-represented in the training data.

In the following, we analyze images of the test set grouped into four cate-

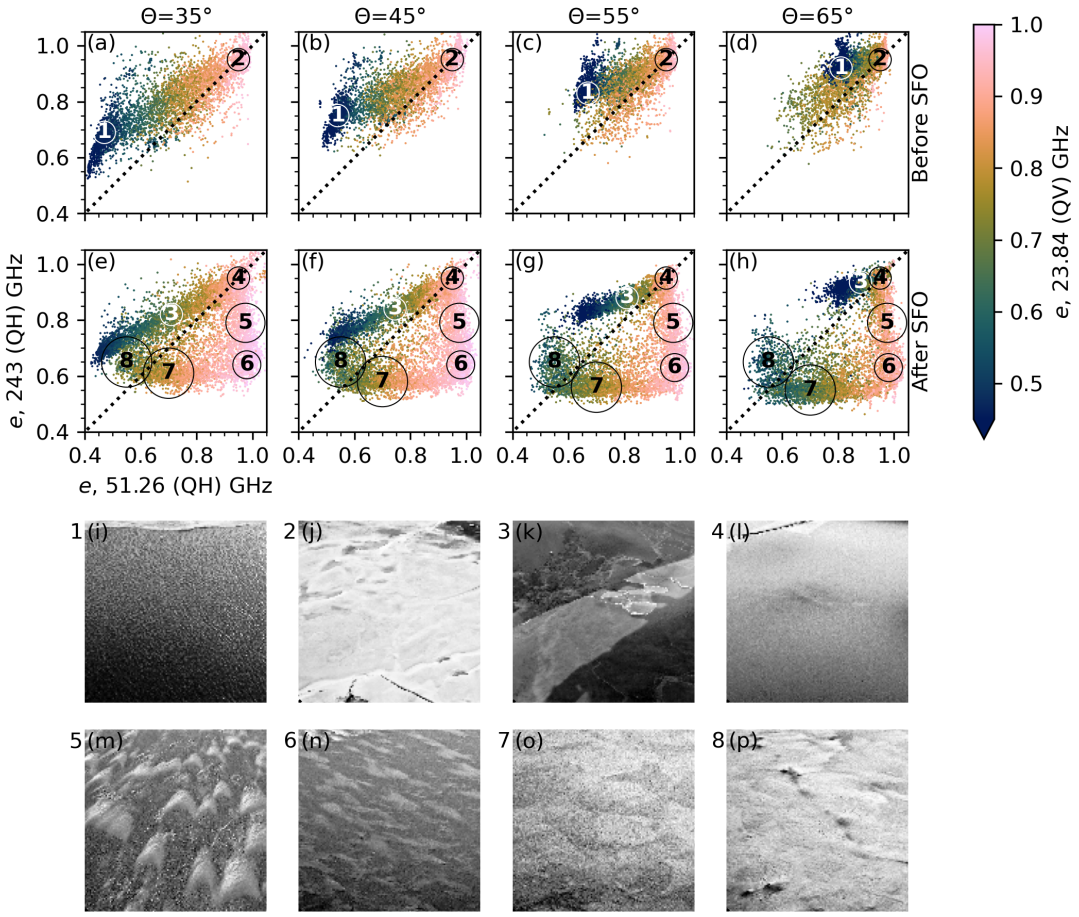

Figure 4.6: Scatter plot of the Lambertian surface emissivity at 51.26 and 243 GHz with shading indicating the emissivity at 23.84 GHz at incidence angles from 35 to 65° (a-d) before and (e-h) after surface freeze onset (SFO) on 2 September. Panels (a–h) show observations during transit. (i–p) Visual images during stationary and homogeneous observations where 90 % of the observed emissivity is within the corresponding circle (1–8). Note that the polarization mixing is different at 23.83 GHz (QV) compared to 51.26 and 243 GHz (QH) except for 45° incidence angle.

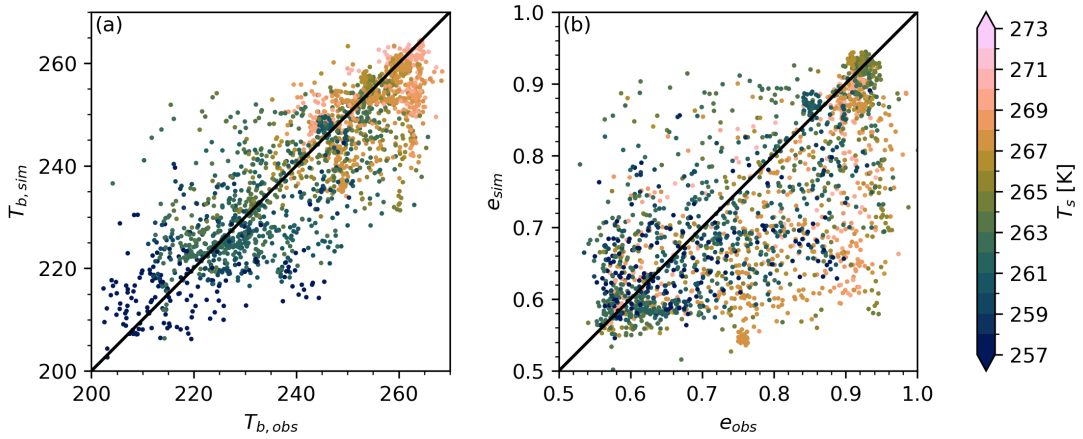

Figure 4.7: Comparison between the observation and image–emissivity regression model prediction for the test data. Panels show the (a) TB and (b) emissivity at 243 GHz at an incidence angle of 53°. Shading indicates the observed surface temperature.

gories of model skill to identify the sea ice and snow properties that determine the emissivity (Fig. 4.8). The first category corresponds to accurate predictions of surfaces with a high emissivity. These images show nilas without snow cover and diverse structures (Fig. 4.8a–f). These images are also generally darker than other images (not shown). The second category represents accurate predictions of sea ice with a low emissivity. Corresponding images show various snow structures and a high variability of shapes. For some images, the snow cover appears closed, whereas for other images, the snow appears redistributed by wind. The third category corresponds to images where the emissivity is underestimated by the model. These images also show some snow structures and are more heterogeneous compared to the images of the first category. The fourth category represents overestimation in emissivity. All images show heterogeneous conditions that might be challenging as the model assigns a single emissivity for the entire image. Generally, the images show that snow appears as the main feature that determines the emissivity reduction, while snow microstructure, density, and thickness lead to larger uncertainties in the prediction.

4.4.3 SMRT simulations

Parameter importance

After identifying snow as a key parameter related to the reduction in microwave emissivity at 243 GHz, we test this behavior using the Monte-Carlo SMRT simulations with uniform sea ice and snow parameter distributions across HATPRO and MiRAC-P frequencies. As a measure of parameter importance, we use the

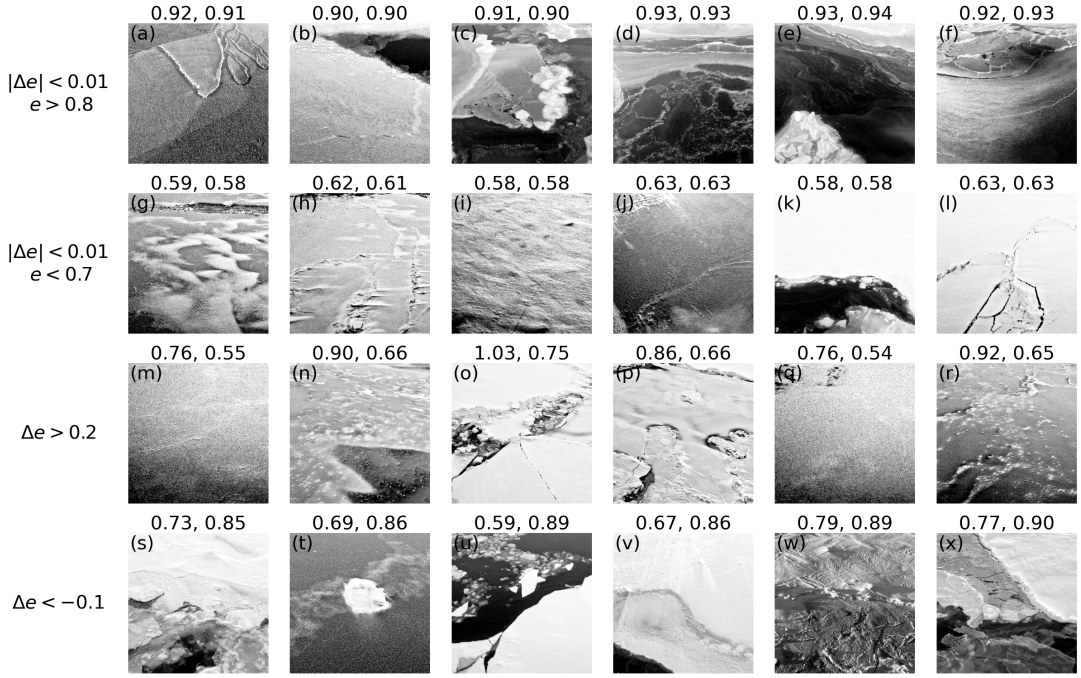

Figure 4.8: Random camera images of the test data grouped into four categories of emissivity prediction skill ($\Delta e = e_{obs} - e_{sim}$). (a–f) Accurate emissivity prediction ($|\Delta e| < 0.01$) and high observed emissivity ($e > 0.8$), (g–l) accurate emissivity prediction and low observed emissivity ($e < 0.7$), (m–r) emissivity underestimation ($\Delta e > 0.2$), and (s–x) emissivity overestimation ($\Delta e < -0.1$). Indicated values indicate the observed and predicted emissivity for each image. The image brightness is rescaled to improve the visualization of snow structures.

correlation between each parameter and the emissivity at an incidence angle of 55°. The results are split into bare and snow-covered ice, and horizontal and vertical polarization (Fig. 4.9).

In the absence of snow cover, the sea ice temperature and salinity are the most important parameters at all frequencies and both polarizations (Fig. 4.9a,b). The temperature and salinity determine the volume fraction of brine inclusions and thus the permittivity of the saline ice. The sea ice salinity dependence is used for satellite retrievals of thin ice thickness as these parameters are inversely correlated (Naoki et al., 2008). Sea ice thickness also directly affects the emissivity, especially at low frequencies. However, this dependence saturates already for an ice thickness of about 3 cm (not shown). The emissivity is almost insensitive to the correlation length of brine inclusions. Generally, the emissivity variability is higher at horizontal polarization than at vertical polarization (not shown).

For snow-covered sea ice, the influence of ice parameters decreases compared to bare ice from 89 to 340 GHz under vertical polarization and from 118 to 340 GHz under horizontal polarization (Fig. 4.9c,d). Snow density, correlation length, and thickness dominate the simulated emissivity variability, while snow temperature is less important. At horizontal polarization, snow density correlates with the emissivity across the entire frequency range. As expected from the scattering process, increases in correlation length and snow thickness reduce the emissivity. The dependence on snow density follows a more complex spectral shape due to nonlinearities, likely related to the dielectric contrast at the snow–ice interface. The highest sensitivity to snow thickness occurs from 90 to 200 GHz, but this sensitivity also depends on the simulated snow thickness distribution (Sect. 4.4.3). While the low-frequency channels are typically used for snow depth retrievals over sea ice (Sandven et al., 2023), this dependence is not simulated here due to the rather small snow correlation length (grain size) and snow thickness provided to SMRT. Overall, the high influence of snow at 243 GHz from the SMRT simulations aligns with the moderate skill of the image–emissivity regression model applied to ship observations.

Influence of snow properties

This section analyzes the emissivity from SMRT simulations of the base sea ice and snow profile (Table 4.3) as a function of snow thickness, density, and correlation length. The simulations are shown for HATPRO and MiRAC-P frequencies and additionally at 89, 118, and 165 GHz (Fig. 4.10).

The vertically polarized emissivity reduction with increasing snow thickness is largest at high frequencies and saturates for a snow thickness of about 2 cm at 340 GHz and 4 cm at 243 GHz (Fig. 4.10a). No reduction in the vertically polar-

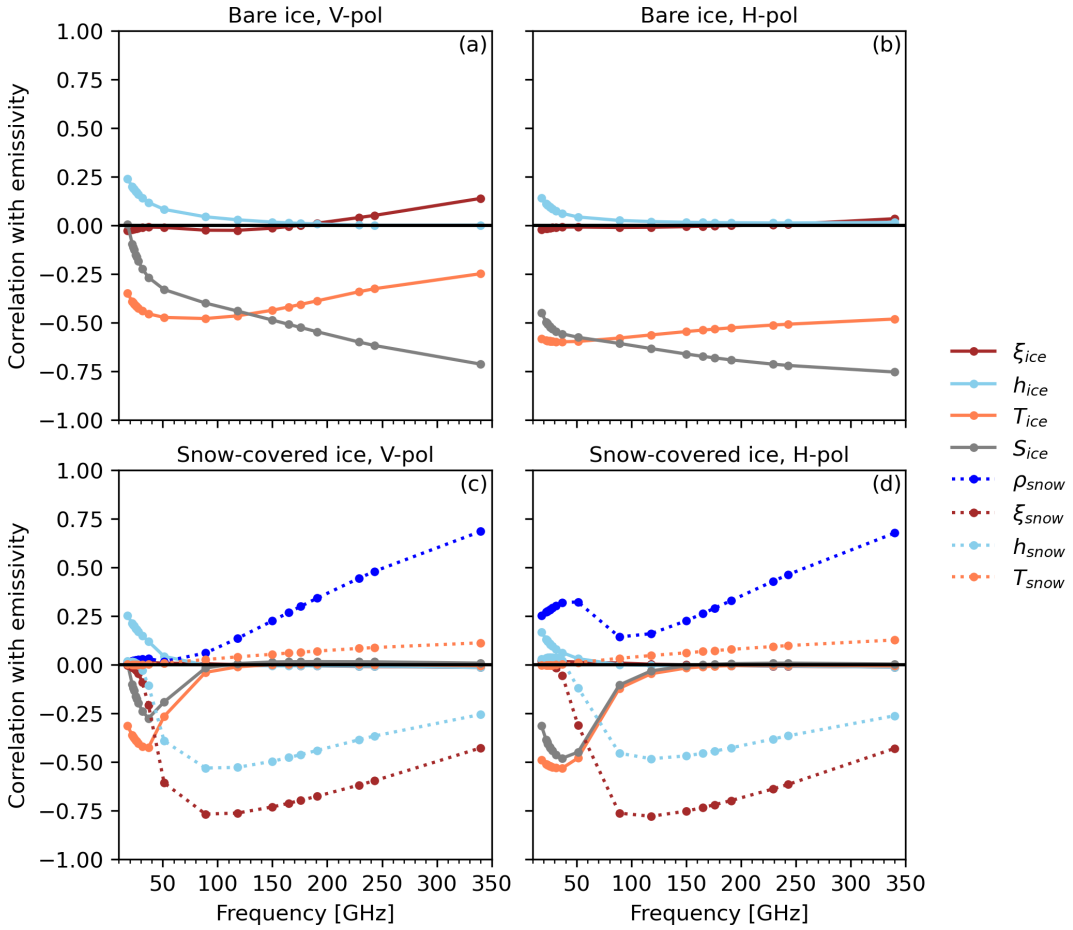

Figure 4.9: Correlation between emissivity and surface parameters for (a, b) bare ice and (c, d) snow-covered ice based on Monte-Carlo SMRT simulations at an incidence angle of 55°. The correlation is shown for (a, c) vertical polarization (V-pol) and (b, d) horizontal polarization (H-pol). The range of simulated values and parameter names of each symbol is provided in Table 4.3.

ized emissivity occurs at frequencies below 89 GHz due to the limited scattering for the simulated correlation length. However, the polarization difference slightly reduces with increasing snow thickness at 51 GHz by about 0.025. At high frequencies, reductions in the polarization difference of about 0.075 are simulated as the snow thickness increases.

Increases in the snow density generally lead to an increase in the vertically polarized emissivity at high frequencies, while the lower frequencies show a lower sensitivity and a slight non-linear relationship (e.g., 118 GHz). As shown from the Monte-Carlo simulations, the horizontal polarization changes with snow density also at low frequencies, affecting the emissivity polarization difference (Fig. 4.10e). While the polarization difference increases at high frequencies with increasing density, it decreases at low frequencies.

The change of vertically polarized emissivity with correlation length is directly linked to the scattering in the snowpack. Saturation occurs at 340 GHz for a correlation length of about 0.15 mm and at 243 GHz near 0.2 mm. Additionally, the emissivity spectrum reaches its minimum at 340 GHz for correlation lengths below 0.1 mm, while the minimum occurs at 165 GHz for a correlation length of 0.25 mm. The polarization difference is less sensitive to correlation length compared to the snow thickness and density, especially at high frequencies.

The simulations from 23 to 90 GHz qualitatively agree with the spectral and polarization signatures observed at 19, 37, and 85 GHz from ship observations over bare and snow-covered new ice (Hwang et al., 2008). At high frequencies, the results of these sensitivity tests align with the observation of an initially high emissivity over bare new sea ice and a reduction in emissivity at high frequencies due to snow accumulation on the newly formed sea ice (Fig. 4.6). Moreover, the simulations suggest that the emissivity difference between the 183.31±7.5 and 243 GHz is non-linear and largest for shallow snow thickness (1–3 cm) with a low density ($< 250\,\mathrm{kg\,m^{-3}}$) and low correlation length (< 0.12 mm). Also, a change in the spectral emissivity gradient at high frequencies might be expected, e.g., between 183.31±7.5 and 243 GHz, for low emissivity (high snow thickness, high density, and high correlation length). This simulated behavior at high frequencies will be compared statistically with the observations in the next section.

Comparison with observations

After analyzing the sensitivity of the emissivity from SMRT simulations to snow and sea ice parameters, we compare the Monte-Carlo simulations with the statistical sampling of Lambertian emissivity along the ship track. The focus of the comparison is new ice formation and the snow accumulation signature on newly formed sea ice after surface freeze onset. However, due to the challenge of filter-

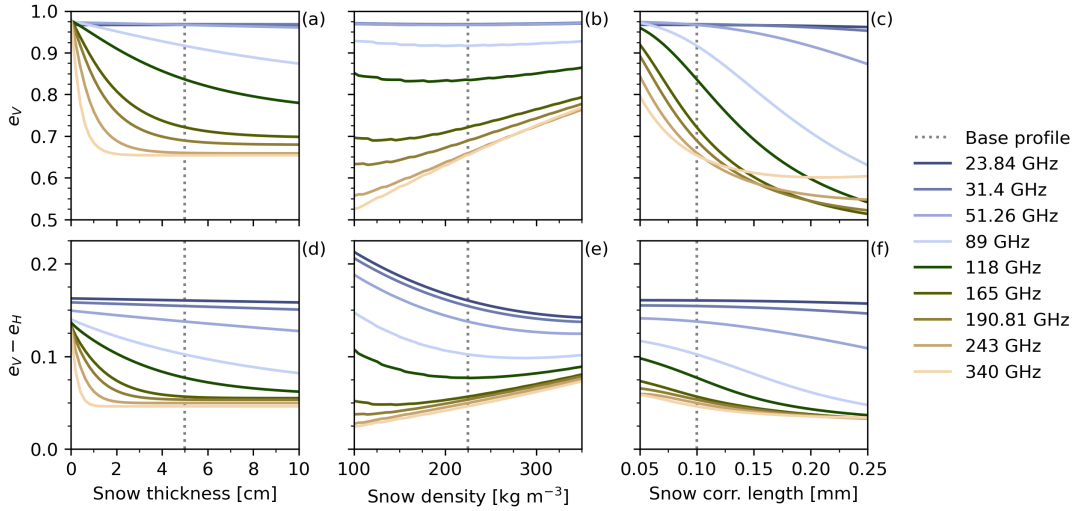

Figure 4.10: Idealized SMRT simulations of (a–c) vertically polarized emissivity (e_V) and (d–f) emissivity polarization difference ($e_V - e_H$) from 23 to 340 GHz at an incidence angle of 55° as a function of (a, d) snow thickness, (b, e) snow density, and (c, f) snow correlation length. The sea ice and snow parameters of the base profile are listed in Table 4.3.

ing the surface type, we include all observations for the comparison and apply the physical interpretation of the three main branches found in Fig. 4.6. The spectral, angular (35 to 65°), and polarization dependence at three channel pairs is analyzed: 31.4 and 183.31±7.5 GHz (QV-pol), 51.26 and 243 GHz (QH-pol; see Fig. 4.6e–h), and 183.31±7.5 and 243 GHz (QV-pol and QH-pol).

Figure 4.11 shows the simulated and observed co-variability for each of the channel pairs and observed incidence angles. The observed variability is well represented by the simulations for all frequency pairs and angles. The main difference is the absence of the third branch with low emissivities at 31.4 and 51.26 GHz as no multiyear ice and surface scattering layers with large snow grains (high correlation length) near the snow–ice interface are simulated. Parts of the third branch are visible in the 51.26 and 243 GHz co-variability for snow with a high thickness and correlation length.

A clear difference between simulation and observation can be found at 31.4 and 51.26 GHz, where the observed emissivity is higher by about 0.05 to 0.1, especially when the emissivity at 183.31±7.5 and 243 GHz is low. This can be attributed to the bias of the emissivity calculation from observations using the skin temperature, which is typically colder than the emitting layer temperature.

The signature of thin and bare new ice is clearly visible in the simulations as a thin upper branch with low simulated variability. However, the observations show much higher variability in this region. While the difference is partly related to inhomogeneities within the footprint, it might also be explained by variations

in the shape of brine inclusions, vertical gradients, and brine films on the surface of the ice not represented in the single-layer simulations. However, the agreement with observations is remarkable, especially at the QH frequency pair (Fig. 4.11e–h). A larger difference occurs for the QV frequency pair, which disappears when assuming specular reflection, as will be shown later.

The snow-covered sea ice corresponds to the second branch visible in the QV and QH polarization pairs. Similar to the observations, the emissivity decreases at 183.31±7.5 and 243 GHz while it remains almost constant at 31.4 and 51.26 GHz. Whether such a signature was also observed will be shown later when considering uncertainties in the observations due to the surface reflection and emitting layer temperature. The sensitivity experiments with different snow properties suggest an earlier reduction in the 243 GHz emissivity compared to 183.31±7.5 GHz during snow accumulation. The same feature is also visible in the simulations and observations at all four angles (Fig. 4.11i–l). Very low emissivity values at 243 GHz in the simulations were not observed along the trajectory. These relate to potentially unrealistic snow with a high thickness (> 5 cm), low density ($200\,\mathrm{kg\,m^{-3}}$) and high correlation length (> 0.2 mm).

To analyze the impact of the assumptions on surface reflection type and emitting layer temperature during the emissivity calculation, we visualize the overlap of SMRT simulations with three different emissivity estimates (Fig. 4.12). These are specular reflection, Lambertian reflection (as in Fig. 4.11), and a mixture of specular reflection at 31.4 and 51.26 GHz and Lambertian reflection at 183.31±7.5 and 243 GHz. Additionally, the mixture uses a minimum surface temperature of 271 K to account for the difference between emitting layer temperature and skin temperature at low frequencies. This analysis can be summarized by three main findings. First, the simulated emissivity of bare ice is best represented under specular reflection. This is based on the result that only specular emissivity matches most bare ice simulations, with the exception at 65° for the 31.4 and 183.31±7.5 GHz pair, potentially due to larger uncertainty at 183.31±7.5 GHz and emissivity variability at 31.4 GHz. Second, only Lambertian emissivity matches the snow-covered sea ice at 183.31±7.5 and 243 GHz, with the exception of very low simulated emissivities corresponding to unrealistic snow conditions. Third, accounting for the warmer emitting layer temperature at 31.4 and 51.26 GHz and specular contributions improves the agreement with the simulations. This effect is most evident at the 51.26 and 243 GHz channel pair (Fig. 4.12e–h).

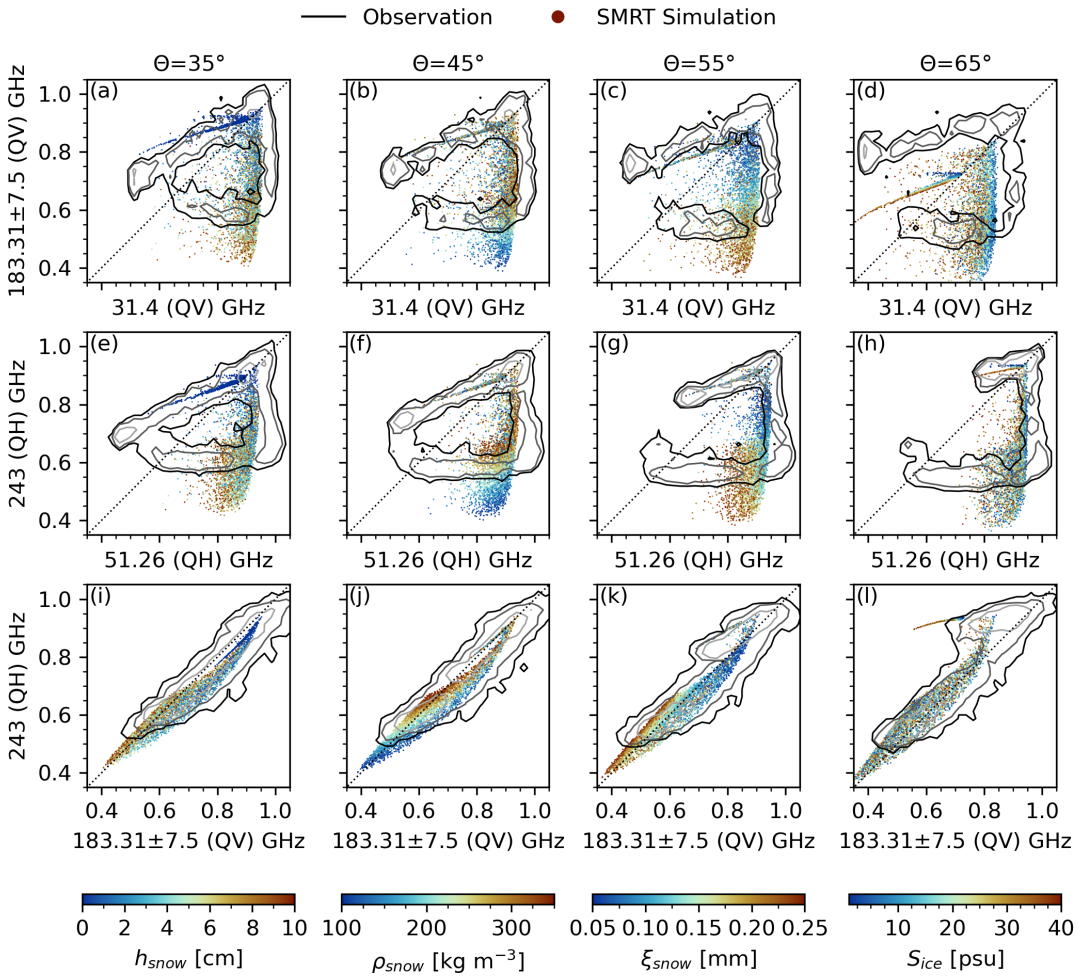

Figure 4.11: Comparison of the emissivity co-variability between observations after surface freeze onset and Monte-Carlo SMRT simulations at (a–d) 31.4 and 183.31±7.5 GHz (both QV-pol), (e–h) 51.26 and 243 GHz (both QH-pol), and (i–l) 183.31±7.5 (QV-pol) and 243 GHz (QH-pol) at incidence angles from 35 to 65°. Contours of the observed Lambertian emissivity correspond to the 94th, 96th, and 98th percentiles of the distribution density at a bin width of 0.025.

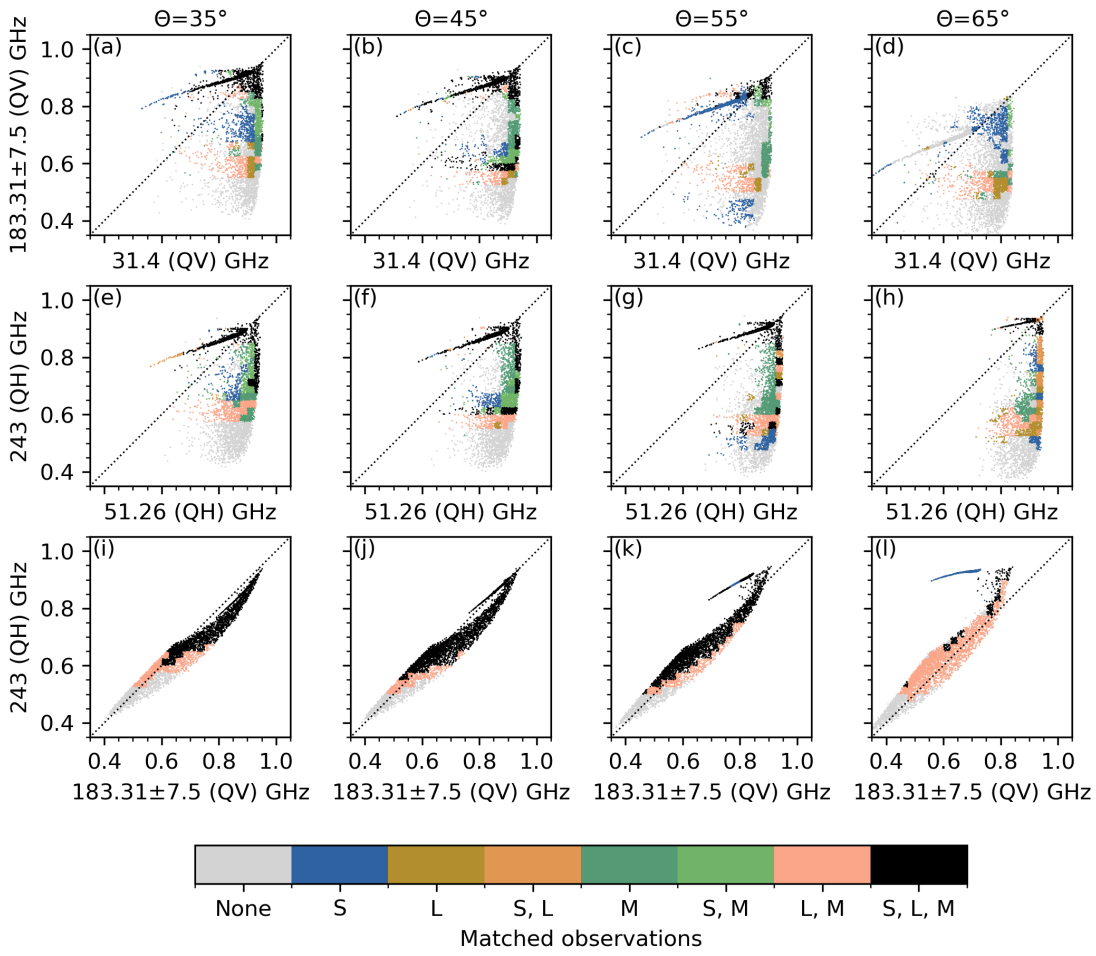

Figure 4.12: Emissivity co-variability from Monte-Carlo SMRT simulations at (a–d) 31.4 and 183.31±7.5 GHz (both QV-pol), (e–h) 51.26 and 243 GHz (both QH-pol), and (i–l) 183.31±7.5 (QV-pol) and 243 GHz (QH-pol) at incidence angles from 35 to 65° as in Fig. 4.11. Shading indicates the overlap with the observed emissivity calculated from specular reflection (S), Lambertian reflection (L), and specular reflection at 31.4 and 51.26 GHz with a surface temperature ≥271 K and Lambertian reflection at 183.31±7.5 and 243 GHz with the surface temperature from thermal infrared (M). A simulation overlaps with the observation if it lies within the contour of the 94th percentile of the observed distribution density at a bin width of 0.025.

4.5 Conclusions

Satellite passive microwave capabilities are expanding beyond 200 GHz and provide novel spectral information on snow and sea ice emission in polar regions. Especially, the Ice Cloud Imager (ICI) will provide dual-polarized information on the surface at 243 GHz, which contains notable surface emission of Arctic sea ice and snow. Simulating these emission signatures is essential for coupled data assimilation (De Rosnay et al., 2022) and satellite retrievals of ice cloud properties (May et al., 2024) and snowfall (Camplani et al., 2024a). In this study, we analyzed quasi-continuous observations of sea ice and snow microwave emissivity from two passive microwave radiometers onboard the R/V *Polarstern* during the PS144 expedition to the Central Arctic from August to October 2024 (VAMPIRE experiment). The microwave radiometers HATPRO and MiRAC-P were mounted on the ship's railing and scanned the surface at incidence angles between 35 and 65° between 22.24 and 58 GHz and 183.31±7.5 to 340 GHz. These observations were collocated with visual and thermal infrared cameras that provide additional information on the surface characteristics. The objectives of this work were to (1) analyze the spectral and angular emissivity variability during summer melt and autumn freeze-up, (2) understand microwave emissivity changes after surface freeze onset from new ice formation to ice growth and snowpack formation, and (3) assess its representation in the Snow Microwave Radiative Transfer (SMRT) model (Picard et al., 2018).

The analysis of spectral and angular emissivity variability before and after surface freeze onset could be explained by various processes. Before surface freeze onset, the signature was dominated by open water, open and refrozen melt ponds, and melting and refrozen multiyear sea ice. While the open water signature exhibits angular variability as expected, the angular variability of the refrozen multiyear ice was much smaller. After surface freeze onset, the emissivity co-variability between low and high frequency channels could be divided into three main branches. The first branch connects the open water and bare nilas signatures. Both the low and high frequency channels are highly correlated along this branch and saturate at a high emissivity. Subsequent snow accumulation on the newly formed sea ice leads to a reduction of the emissivity at 183.31±7.5 and 243 GHz, while emissivity remains high from 22.24 to 51.26 GHz (second branch). The third branch corresponds to multiyear ice and is connected to the lower emissivity end of the second branch. While the high frequency channels are saturated by the newly accumulated snow, the low frequencies vary due to multiyear ice properties at the snow–ice interface, such as refrozen melt ponds, surface scattering layer, and air inclusions.

The emissivity changes at 243 GHz of the second branch after surface freeze onset relate to snow accumulation on newly formed ice. A small image–emissivity regression model was used to predict the microwave emissivity at 243 GHz at an incidence angle of 53° from collocated grayscale images of the visual camera for this branch. The moderate skill of the model showed that high-level features visible in the images, such as snow presence and structure, partly explain the emissivity reduction at 243 GHz. Based on idealized SMRT simulations, it was further found that the high frequencies already saturate for a snow thickness of a few centimeters. Additionally, variations in snow density and correlation length cause a high variability of the emissivity, which explains the limitations of the simple image-based regression model.

The comparison of Monte-Carlo SMRT simulations showed that SMRT reproduces the angular, spectral, and polarization dependence of bare and snow-covered nilas after surface freeze onset when considering uncertainties in the observations due to emitting layer temperature and surface reflection. Moreover, the observed emissivity-dependent spectral gradients from 183.31±7.5 to 243 GHz in the observations can be reproduced with realistic parameter combinations by SMRT at all incidence angles.

Limitations of this study are the convolution of spatial and temporal changes of sea ice properties along the ship trajectory. Moreover, the analysis is limited due to the large gap of observed frequencies between 51.26 and 183.31±7.5 GHz, which misses the gradual transitions of snow accumulation that are simulated by SMRT at 89, 118, and 165 GHz. Finally, the impact of saline snow at the snow–ice interface of young sea ice is not considered in the simulations.

The results imply improved monitoring of sea ice and snow properties with observations at 243 GHz and along the 325.15 GHz water vapor absorption line from satellites, such as the Ice Cloud Imager. Moreover, the extended spectral information is expected to improve the emissivity estimates at 183.31±7.5 GHz, as the emissivity at both frequencies varies almost linearly over snow-covered surfaces. This might improve the temperature and humidity profiling from the Metop-SG satellites. Finally, SMRT could be useful in a coupled data assimilation context and for atmospheric satellite retrievals, even at high frequencies, ideally considering surface heterogeneity (open water, leads, snow-covered sea ice) within the satellite footprint.

There are several ways for future work regarding the analysis of field observations, radiative transfer evaluation, and satellite observations. This includes the analysis of the emissivity variability over multiyear sea ice and its relation to physical properties observed during ice stations of the VAMPIRE experiment. This will also provide input data for a more detailed SMRT evaluation similar to

Wivell et al. (2023) over snow. Additionally, satellite observations above 200 GHz will be used to assess whether the features observed during the VAMPIRE experiment also occur on pan-Arctic scales on satellite footprint scales during new ice formation.

Appendix

4.A Radiometer scan positions

We attach an overview of the radiometer scan positions. Figure 4.13 shows the order of scans and the number of observations during the scan interval of 30 min.

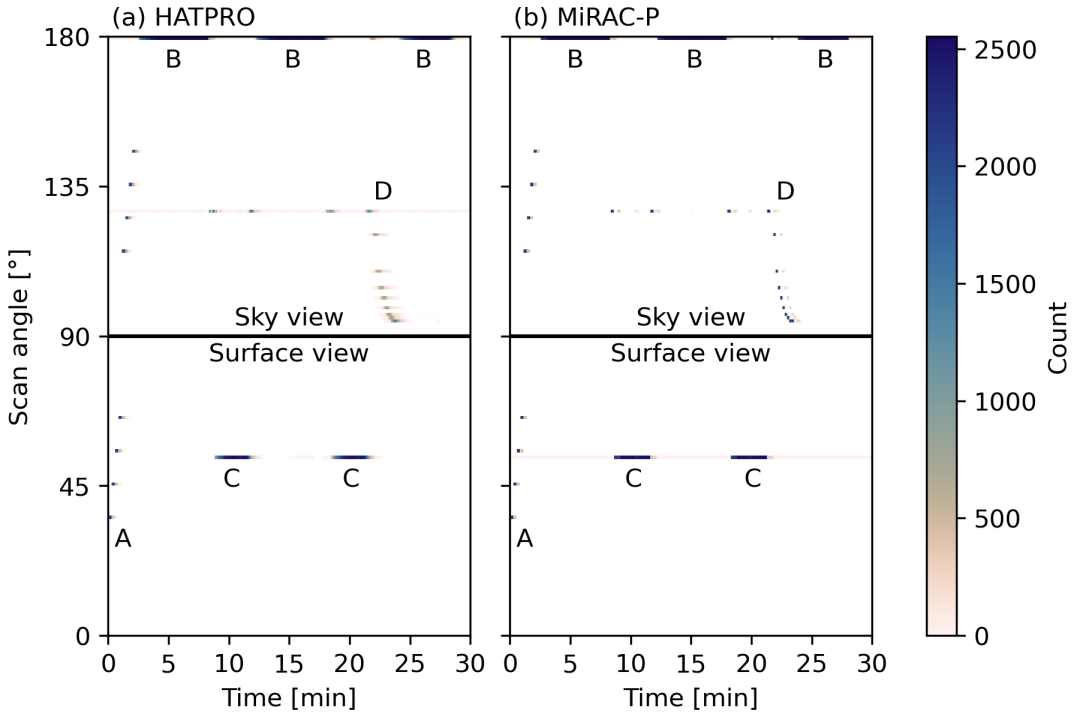

Figure 4.13: Overview of the scan pattern with a duration of 30 min for (a) HATPRO and (b) MiRAC-P. Shading provides the observation count per degree and second while the ship was within the sea ice. Capital letters indicate the surface scan at 35–65° and corresponding sky view (A), zenith scan (B), surface scan at 53° and corresponding sky view (C), and boundary layer scan (D).

4.B Collocation with AMSR2

The microwave radiometers on the ship observe the upwelling TB on a scale of a few meters in close proximity to the research vessel. To assess, whether these observations capture the large-scale variability measured from satellites, we

match HATPRO scans at 53° incidence angle with AMSR2 at 23.8 GHz with a maximum temporal offset of ±4 h and maximum distance to the AMSR2 footprint center of 10.5 km. The observations can be compared directly when applying QV polarization mixing to AMSR2 following Eq. (4.1) and scaling the HATPRO TB measurements at the surface $T_{b,surf}$ to the corresponding satellite TB $T_{b,sat}$ based on the simulated atmospheric transmissivity t and upwelling TB $T_{b,up}$ along the slant path

$$T_{b,sat} = T_{b,surf} * t + T_{b,up}. \tag{4.6}$$

The atmospheric contribution at 23.8 GHz for an incidence angle of 52.8° is low during the entire expedition, with 25th and 75th percentiles of 0.82 and 0.9 for the transmissivity, and 26 and 48 K for the upwelling TB, respectively. Hence, surface emissivity variations are dominating the TB variability measured by AMSR2.

Figure 4.14 shows the time series of HATPRO and AMSR2 from 14 August to 4 October and a histogram of the TB difference. Despite the notable small-scale variability resolved by HATPRO, the observations averaged over the satellite footprint mostly agree with the AMSR2 observations. The distribution is centered near 0 K, with a skewness toward a TB underestimation. Based on the time series, this is mostly attributed to open water patches in late August and early September. From mid to end September, the ship measurements tend to overestimate the TB, likely due to new ice formation in leads. Several features are captured by HATPRO, such as the TB (and emissivity) reduction from 24 to 26 August, which is linked to colder air and surface temperatures and potential refreezing of the sea ice surface (Fig. 4.2a). Based on this overall good agreement, the small-scale observations during transit periods provide detailed insights into the emissivity variability at HATPRO and MiRAC-P frequencies relevant at satellite scales.

4.C Image–emissivity regression model

4.C.1 Training objective

The training objective of this model is to reproduce the observed upwelling TB corresponding to the input image. Rather than training the model on potentially noisy emissivity estimates, we use the radiative transfer equation to convert the predicted emissivity to an upwelling TB using Eq. (4.4). Then, the loss is computed as the mean absolute error between the simulated and observed TB

$$L = \frac{1}{N} \sum_{i}^{N} |T_{b,obs} - T_{b,sim}|. \tag{4.7}$$

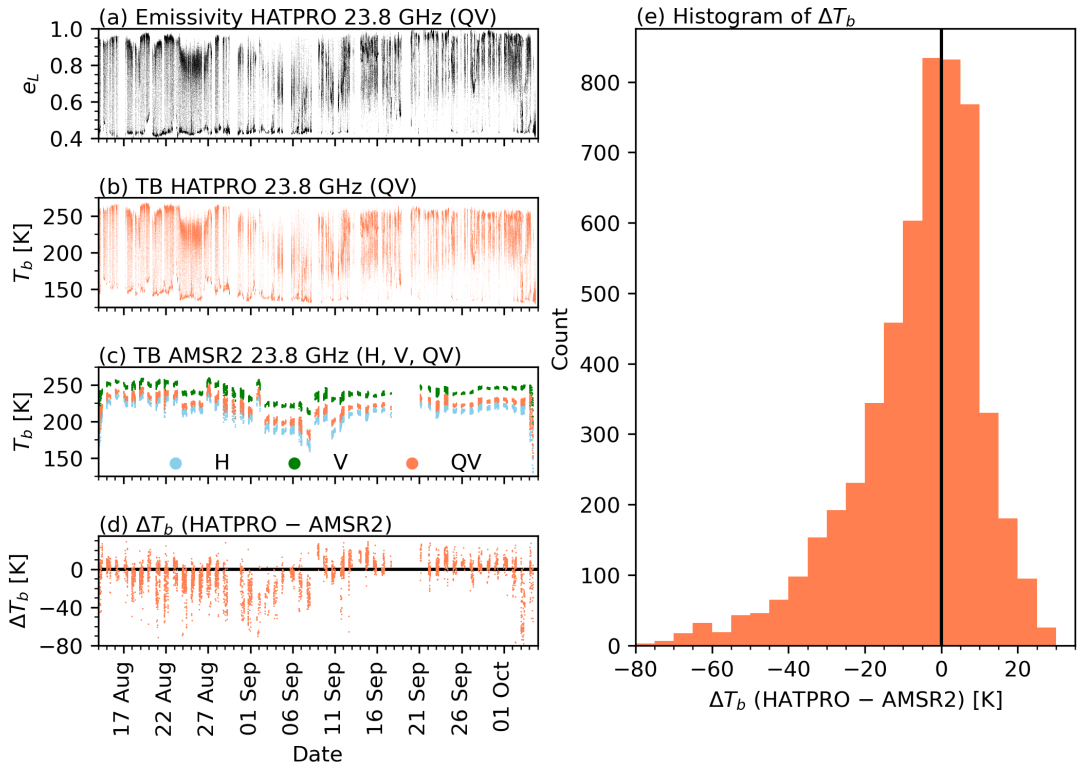

Figure 4.14: Comparison between HATPRO and collocated AMSR2 observations along the ship trajectory at 23.8 GHz. (a) Lambertian emissivity from HATPRO, (b) TB from HATPRO, (c) TB from AMSR2, (d) difference between HATPRO resampled to the AMSR2 footprint with atmospheric correction and collocated AMSR2 observations, and (e) histogram of the difference between HATPRO and AMSR2.

The emissivity distribution of the data is adjusted to ensure balanced targets. Samples are randomly dropped from the two most frequent emissivity intervals with a bin width of 0.1 until their count matches the third most frequent emissivity interval. All other intervals with a lower count remain unchanged. Also, data is thinned to ensure a distance of at least 4 m between consecutive time steps based on the ship's velocity. The network is trained on 60 % of the data, while the remaining data is left for validation (20%) and testing (20%). The split is performed using non-overlapping temporal blocks of length 400. This split ensures that each subset captures the temporal evolution during VAMPIRE and reduces temporal and spatial correlation between the three data sets. The batch size during training is set to 64, the learning rate is 0.001, and training is stopped after 200 epochs. The Adam optimizer is used to update the model parameters (Kingma and Ba, 2017).

Data augmentation is performed on all network inputs and parameters included in the loss function to reduce the risk of overfitting and inform the model about underlying data uncertainty. Augmentations for the grayscale image are random horizontal flips, random crops of 288×288 pixels, random brightness offsets, and random noise. Random noise is applied to the upwelling TB and downwelling TB (1.5 K). Additionally, the uncertainty of the Lambertian downwelling TB is added as random noise to the downwelling TB. Moreover, noise is applied to the thermal infrared temperature (1 K).

4.C.2 Network architecture

The network consists of a convolutional neural network (CNN; Lecun et al., 1998) as encoder and a multi-layer perception (MLP; Rumelhart et al., 1986) as decoder (Fig. 4.15). The encoder extracts features from the grayscale image input, which are provided to the decoder for emissivity prediction. The predicted raw emissivity is then converted to a physical emissivity using the sigmoid function to bound it into the range $0 \leq e \leq 1$. The CNN consists of three convolutional layers with 4, 8, and 12 channels, and a kernel size of 3, padding of 1, dilation of 2, and a stride of 2. Each convolution is followed by batch normalization, Rectified Linear Unit (ReLU) activation function, and maximum pooling with a kernel size and stride of 2. After the three convolutions, an averaging over the spatial dimension is performed to get a 1-dimensional feature vector z. This vector of length 12 is the input to the MLP. The MLP consists of 2 hidden layers with five neurons each and a ReLU activation function. A linear activation function is applied to the output layer. The total number of parameters is about 1,200, which is about 10 % of the number of training samples. We also trained networks

based on the mean image brightness and the distribution of brightness for the image. While the mean brightness did not provide skillful predictions, the network trained on 12 percentiles of the cumulative density function of image brightness provided similar performance to the CNN-based architecture. This indicates that the variability of brightness within the image contains useful information.

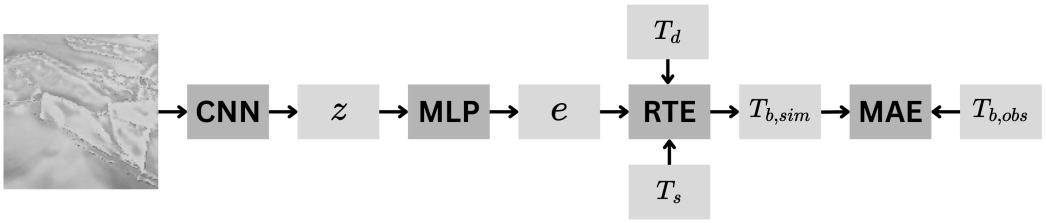

Figure 4.15: Architecture of the image–emissivity regression model. Variables denote the feature vector z, emissivity e, downwelling TB T_d, surface temperature T_s, simulated upwelling TB $T_{b,sim}$, and observed upwelling TB $T_{b,obs}$. CNN: convolutional neural network; MLP: multi-layer perceptron; RTE: radiative transfer equation; MAE: mean absolute error.

4.C.3 Prediction skill

The following table summarizes the model skill for predicting the upwelling TB and surface emissivity at 243 GHz for the training, validation, and test sets (Table 4.4). All metrics are similar between the three data sets, which indicates that the model generalizes well. The model slightly underestimates the TB by about 2 K and the emissivity by 0.05. The RMSE of the TB is about 9 K and 0.11 for the emissivity, which is larger than the measurement uncertainty at 243 GHz. This is likely related to the limited information content of the images for the microwave signature and the treatment of images as spatially homogeneous in microwave emissivity by the network. The correlation of the prediction in TB space is higher (0.84) than in emissivity space (0.67) (see also Fig. 4.7). This can be explained by the use of the TB in the loss function, which puts a reduced weight on emissivity estimates with a low surface sensitivity.

Table 4.4: Model skill in predicting the upwelling TB and sea ice emissivity measured at 243 GHz at an incidence angle of 53° for the training, validation, and test set. Note that the emissivity is predicted by the model, and the TB departure is minimized during model training. The three metrics are bias (observation minus prediction), root mean squared error (RMSE), and correlation coefficient (Corr.).

Data set	Bias		RMSE		Corr.	
	T_b [K]	e	T_b [K]	e	T_b [K]	e
Training	3	0.06	9.2	0.12	0.84	0.61
Validation	2.3	0.04	9.1	0.11	0.83	0.7
Test	2.1	0.05	8.9	0.11	0.84	0.67

Chapter 5

Sea ice–atmosphere retrieval

This study develops a sea ice–atmosphere retrieval to estimate cloud liquid water path over sea ice from airborne microwave radiometer observations during the HALO–$(\mathcal{AC})^3$ field campaign. The study has been submitted to Atmospheric Measurement Techniques and is currently under review:

Risse, N. et al. 2025: Cloud liquid water path detectability and retrieval accuracy from airborne passive microwave observations over Arctic sea ice, *EGUsphere [preprint]*, doi:10.5194/egusphere-2025-3311, submitted on 9 July 2025.

The content of this chapter has been published under the Creative Commons Attribution 4.0 License. Formatting changes were made to adopt the format of this thesis.

Detailed author contributions: Nils Risse conducted the retrieval, data analysis, and visualization, and prepared the manuscript. Susanne Crewell, Mario Mech, Catherine Prigent, and Nils Risse conceptualized the study. Susanne Crewell, Mario Mech, and Nils Risse carried out the field observations. Joshua J. Müller derived the VELOX surface classification within the radiometer footprint. All authors reviewed and edited the manuscript.

Cloud liquid water path detectability and retrieval accuracy from airborne passive microwave observations over Arctic sea ice

Nils Risse[1], Mario Mech[1], Catherine Prigent[2], Joshua J. Müller[3], and Susanne Crewell[1]

[1]Institute for Geophysics and Meteorology, University of Cologne, Cologne, Germany

[2]Laboratoire d'Instrumentation et de Recherche en Astrophysique, Observatoire de Paris, CNRS, Paris, France

[3]Leipzig Institute for Meteorology, University of Leipzig, Leipzig, Germany

Correspondence: Nils Risse (n.risse@uni-koeln.de)

Abstract Clouds are critical in the Arctic's water balance and energy budget. Especially, the cloud liquid water path (CLWP) modifies the cloud radiative properties and affects the surface energy balance. Spaceborne microwave radiometers provide a high sensitivity to CLWP at pan-Arctic scales, but extracting this information over sea ice requires separation of surface and cloud emission. Here, we assess CLWP detectability and retrieval accuracy over sea ice from a physical optimal estimation retrieval applied to airborne passive microwave observations during the HALO–$(\mathcal{AC})^3$ campaign. Reference data on surface temperature, young ice fraction, hydrometeor occurrence, and cloud liquid layers are available from collocated airborne instruments. The retrieval estimates CLWP and five surface parameters by inverting a forward operator consisting of the Snow Microwave Radiative Transfer (SMRT) and Passive and Active Microwave radiative TRAnsfer (PAMTRA) models. We find a consistent representation of sea ice and snow emission from 22–183 GHz under clear-sky conditions in both observation and state space. The CLWP detectability, defined as the 95th percentile of retrieved CLWP under clear-sky conditions, is about $50\,\mathrm{g\,m^{-2}}$ in the Central Arctic and increases towards the marginal ice zone up to $350\,\mathrm{g\,m^{-2}}$. The CLWP retrieval accuracy increases with increasing CLWP, with a relative root mean squared error below 50 % for CLWP above $100\,\mathrm{g\,m^{-2}}$. Retrieval uncertainties occur due to ambiguities between cloud liquid water emission and scattering in the snowpack and emission by newly formed sea ice. We further analyze the impact of surface melt and a rain-on-snow event associated with the warm air intrusion on the surface parameters. Finally, we show CLWP distributions along the flight track for all HAMP observations in comparison to ERA5 for different cloud regimes. The retrieval algorithm enhances the understanding of Arctic clouds and allows for an improved use of passive microwave satellite data in polar regions.

5.1 Introduction

The Arctic is warming at a faster rate than the global average in recent decades (Rantanen et al., 2022). Clouds play a critical role as a feedback mechanism in the amplified warming in the Arctic (Tan et al., 2021). Cloud liquid water modifies the cloud radiative effect (Shupe and Intrieri, 2004; Ebell et al., 2020) with implications for the surface energy budget (Sledd et al., 2025). Additionally, cloud liquid water plays a critical role in precipitation formation processes, such as efficient ice crystal growth through riming (Maherndl et al., 2024). Passive microwave radiometers allow for a quantification of the cloud liquid water path (CLWP), defined as the columnar integral of cloud liquid water content, by observing the temperature-dependent microwave emission of liquid droplets (Kneifel et al., 2014; Turner et al., 2016). This emission of liquid droplets increases with frequency, and retrievals typically use observations at window channels in the range from 19 to 90 GHz (Greenwald et al., 1993; Crewell and Löhnert, 2003). Over sea ice, high-quality CLWP estimates are provided from ship-based microwave radiometers (Westwater et al., 2001; Walbröl et al., 2022). Operational satellite CLWP products are currently not available over sea ice due to the variable emission and polarization of the sea ice and snow. For example, the Multisensor Advanced Climatology of Liquid Water Path (MAC-LWP; Elsaesser et al., 2017; O'Dell et al., 2008) is limited to ice-free ocean, and the Microwave integrated Retrieval System (MiRS; Boukabara et al., 2011) provides estimates over ice-free ocean and land only. First estimates of the CLWP retrieval accuracy from passive microwaves are presented by Haggerty et al. (2002) using airborne microwave observations and collocated in situ data. Their results show a high accuracy for CLWP above $100\,\mathrm{g\,m^{-2}}$ and poor accuracy for CLWP below $50\,\mathrm{g\,m^{-2}}$. Generally, the CLWP uncertainty increases with increasing surface emissivity due to the decreasing contrast between the liquid cloud emission and the surface (Prigent et al., 2003). Hence, airborne or satellite retrievals of atmospheric properties require an accurate representation of the surface emissivity and its polarization.

Several methods were developed to describe the emissivity of sea ice and snow-covered surfaces. Emissivity atlases derived from long-term satellite observations under clear-sky with collocated surface temperature data provide robust first-guess emissivities and their variability (Prigent et al., 1997; Wang et al., 2017b). However, as the emissivity variability over sea ice can be very high, the long-term mean might deviate largely from the actual emissivity (Perro et al., 2020). To better capture this emissivity variability, dynamic emissivity modeling approaches are developed in a data assimilation context (e.g., Di Tomaso et al., 2013). This approach computes the emissivity at window channels and extrapolates to neigh-

boring sounding channels in the same field-of-view, but is limited to clear-sky conditions. A novel machine learning approach by Geer (2024a) addresses the need for better sea ice emissivity modeling in a numerical weather prediction context over sea ice (Lawrence et al., 2019). The approach exploits long-term observations to learn a compact representation of relevant sea ice and snow microphysical properties and their empirical transformation to an emissivity. While machine learning provides a computationally efficient approach, interpreting the underlying geophysical parameters is challenging. Physical snow and sea ice radiative transfer modeling approaches directly compute the emission from plane parallel sea ice and snow layers and their properties, such as density, grain size, salinity, temperature, thickness, and microstructure (Tonboe et al., 2006). The Arctic-wide retrieval by Rückert et al. (2023b) validated with observations from the Multidisciplinary drifting Observatory for the Study of Arctic Climate (MOSAiC) expedition provides simultaneous atmospheric and sea ice properties from an optimal estimation retrieval framework. While their retrieval used a fixed assumption on the snow and ice layering, Kang et al. (2023) explored the coupling of a sea ice and snow radiative transfer model with a thermodynamic sea ice and snow evolution model to better capture snow metamorphism and temporal variations in snow layering. This approach could be useful in a coupled land-atmosphere assimilation of surface-sensitive microwave channels (Hirahara et al., 2020). Yet, we lack a detailed assessment of the CLWP detectability and retrieval accuracy from passive microwave observations over sea ice.

To study the CLWP signal over sea ice, we develop an optimal estimation sea ice–atmosphere retrieval specifically for airborne passive microwave observations from 22–183 GHz at nadir. The underlying forward operator simulates the brightness temperature (T_b) at flight altitude from a loose coupling of the Snow Microwave Radiative Transfer (SMRT; Picard et al., 2018) model with the Passive and Active Microwave radiative TRAnsfer (PAMTRA; Mech et al., 2020) tool via the spectral surface emissivity and effective temperature. This physical modeling approach allows a simultaneous retrieval of snow layer properties (correlation length and thickness), snow and sea ice temperature, and CLWP, under non-heavy cloud ice and snow conditions, since frozen water path is not retrieved. We apply the retrieval to the airborne Microwave Package (HAMP; Mech et al., 2014) radiometer onboard the *High Altitude and Long Range Research Aircraft* (*HALO*) during the HALO–$(\mathcal{AC})^3$ field campaign carried out in spring 2022 in the Fram Strait and Central Arctic. *HALO's* cloud observatory suite (Stevens et al., 2019) with coincident cloud radar, lidar, and infrared observations provides a unique opportunity for passive microwave retrieval evaluation (Jacob et al., 2019). We aim to (1) assess the representation of sea ice and snow

microwave emission by the forward model, (2) estimate the CLWP detectability and retrieval accuracy, and (3) analyze the spatial variability of CLWP over sea ice during HALO–$(\mathcal{AC})^3$.

The paper is structured as follows. Section 5.2 provides an overview of the airborne field data and auxiliary satellite and reanalysis data. Section 5.3 describes the sea ice–atmosphere retrieval and the forward operator. Section 5.4 details the clear-sky evaluation (first objective), CLWP detectability, and CLWP retrieval accuracy (second objective). Section 5.5 addresses the third objective by presenting the retrieval application to two case studies, a rain-on-snow event, and comparing the CLWP from HAMP with ERA5. The study is summarized and concluded in Sect. 5.6.

5.2 Data

5.2.1 HALO–$(\mathcal{AC})^3$ field campaign

The multi-platform field campaign HALO–$(\mathcal{AC})^3$ included 17 flights with the research aircraft *HALO* between 11 March and 12 April 2022 over sea ice in the Fram Strait and Central Arctic (Wendisch et al., 2024; Ehrlich et al., 2024). Thus, *HALO* captured diverse sea ice conditions from young ice near the sea ice edge to perennial sea ice north of Greenland. Here, we include all observations over at least 90 % sea ice concentration (Spreen et al., 2008) with a distance of more than 15 km to coasts (Fig. 5.1). Due to the coarser spatial resolution of the sea ice product compared to the airborne observations, few open water pixels remain in the airborne data.

The meteorological conditions during HALO–$(\mathcal{AC})^3$ were dominated by warm air intrusions from 11–20 March 2022 and colder northerly winds from 21 March 2022 until the end of the campaign (Walbröl et al., 2024). The warm air intrusions caused rainfall on sea ice up to about 83° N (see Fig. 10 in Walbröl et al., 2024), which *HALO* captured on three consecutive days (11–13 March 2022).

The cloud observatory configuration of *HALO* includes a microwave radiometer, cloud radar, lidar, thermal infrared radiometer, thermal infrared spectral imager, and solar spectral imager. In addition, 85 dropsonde launches over sea ice provide vertical profiles of air temperature, humidity, and wind between flight altitude and the surface (George et al., 2024). This dropsonde data was partly assimilated into the European Centre for Medium-Range Weather Forecasts (ECMWF) Integrated Forecasting System (IFS). Details on the *HALO* instrumentation and dropsonde assimilation can be found in Ehrlich et al. (2024). An example of the microwave radiometer, radar, and lidar observations is provided in Fig. 5.2 for

a 550 km southbound transect. The following sections describe the instruments and products of the cloud observatory configuration and ancillary products.

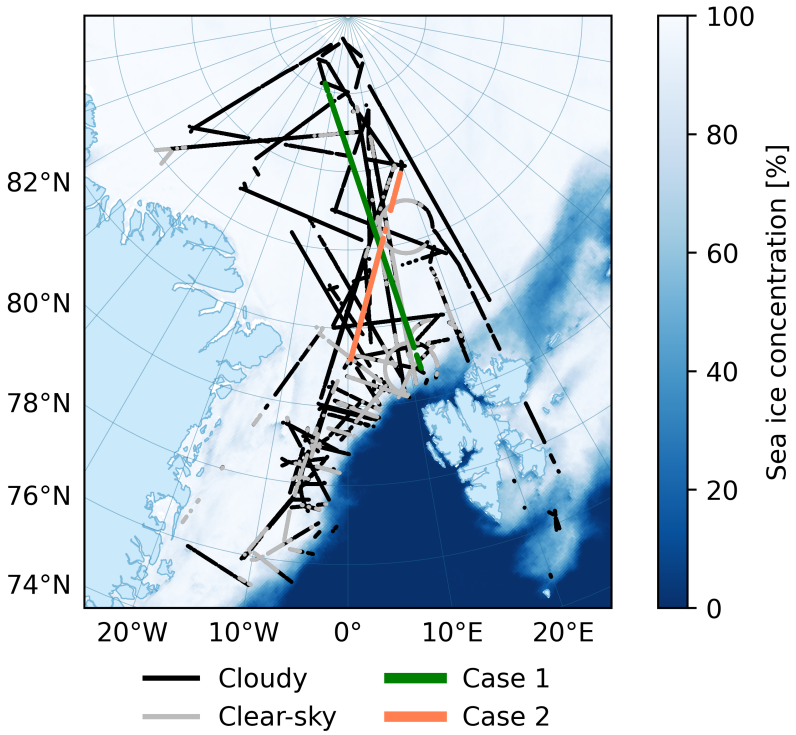

Figure 5.1: Map of the *HALO* flight track and mean sea ice concentration (Spreen et al., 2008). Only positions where the retrieval was applied are shown.

5.2.2 Microwave radiometer

The HAMP radiometer measures at 25 channels in the frequency range from 22.24 to 183.31±7.5 GHz (Mech et al., 2014). Six channels each are located along the 22.24 GHz water vapor absorption line and around the 183.31 GHz water vapor absorption line, seven channels are located along the 50–60 GHz oxygen absorption complex, four channels are located around the 118.75 GHz oxygen absorption line, and two channels are located within atmospheric windows at 31.4 and 90 GHz. HAMP points nadir and samples with a temporal resolution of 1 s. The footprint sizes range from about 0.7 to 1.4 km at typical *HALO* flight altitude and speed (Table 5.1). The data was corrected for biases using dropsondes over open ocean (Dorff et al., 2024). Here, we use an updated version of the bias correction. Measurement gaps that were filled by temporal interpolation in the published data are discarded, and we removed any observations where aircraft roll or pitch exceed ±6°. Moreover, we exclude about 19 % of the observations due to potentially high scattering by frozen hydrometeors or surface melt. In total, about 85,000 HAMP samples are available over sea ice along a flight distance of

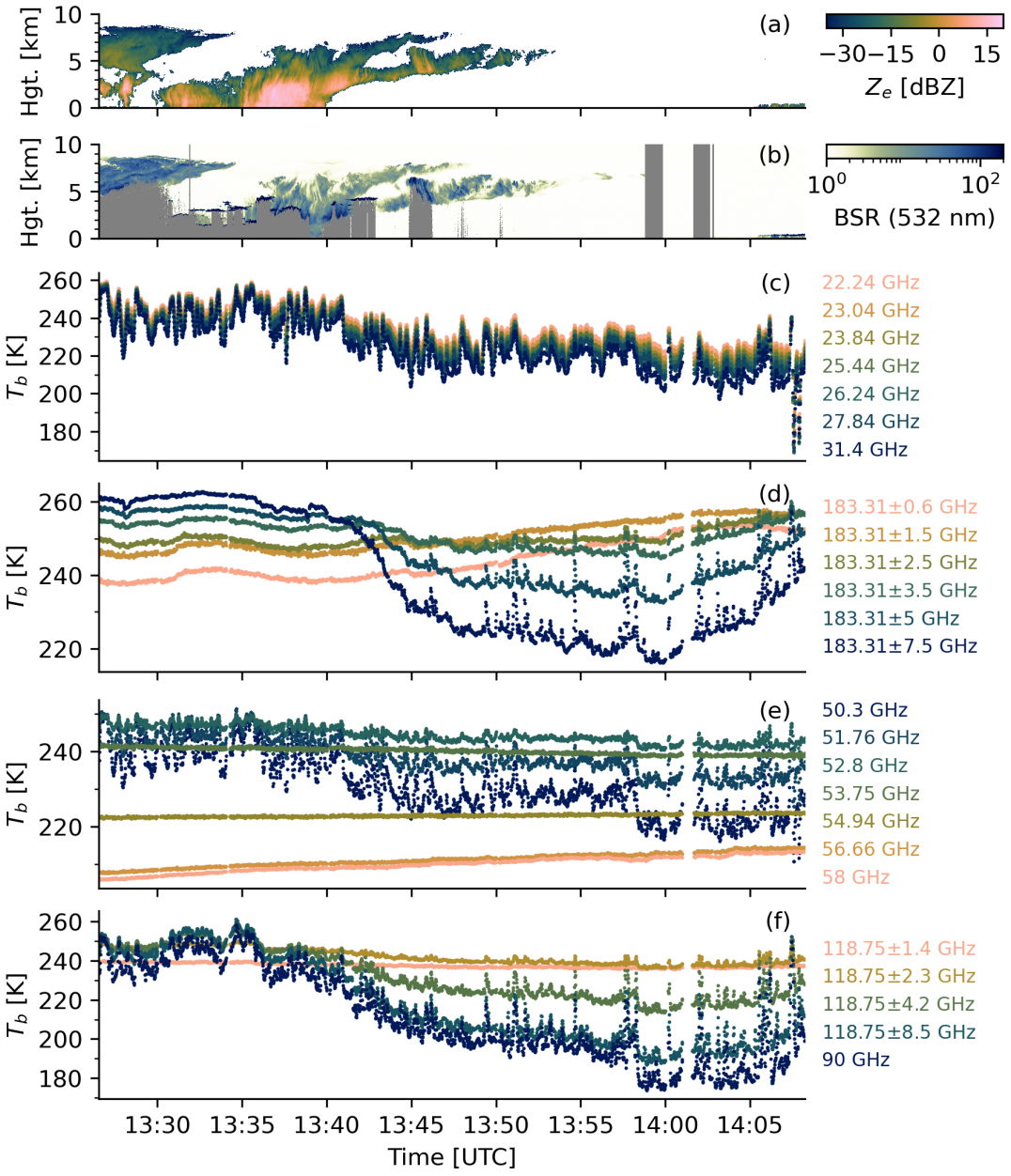

Figure 5.2: Radar, lidar, and microwave radiometer observations during a 550 km southbound transect over sea ice on 14 March 2022 (case 2 in Fig. 5.1). (a) Radar reflectivity, (b) lidar backscatter ratio, (c) T_b from 22 to 31 GHz, (d) T_b around 183.31 GHz, (e) T_b from 50 to 58 GHz, and (f) T_b at 90 and around 118.75 GHz. Missing/flagged data is shown in gray.

20,000 km between -55–27° E and 74.8–89.4° N, out of which about 14 % (12,200) were clear-sky as identified from the radar–lidar cloud mask with available thermal infrared data.

Most weighting functions of HAMP peak at the surface under cold and dry Arctic conditions. Thus, the T_b varies due to changes in surface emission along the flight track with a high correlation between neighboring surface-sensitive channels (Fig. 5.2c–f). Therefore, we only use six HAMP channels for the retrieval: 22.24, 31.4, 50.3, 90, 118.75±8.5, and 183.31±7.5 GHz. This includes channels typically used for ground-based and satellite CLWP retrievals, with the highest sensitivity at 90 and 118.75±8.5 GHz. Moreover, these channels fully exploit HAMP's spectral range for surface characterization.

Table 5.1: Beam width, noise equivalent differential temperature (NeDT), and footprint size of HAMP channels. The footprint size is calculated for a flight velocity of 300 m s^{-1} and 12 km flight altitude.

Channels	Frequency range [GHz]	Beam width [°]	NeDT [K]	Footprint size [km^2]
1–7	22.24–31.4	5	0.1	1.1×1.4
8-14	50.3–58	3.5	0.2	0.7×1
15	90	3.3	0.25	0.7×1
16–19	110.25–127.25	3.3	0.6	0.7×1
20–25	175.81–190.81	2.7	0.6	0.6×0.9

5.2.3 Radar–lidar cloud mask

The cloud radar and lidar onboard *HALO* provide reference data on the occurrence of hydrometeors in the field of view of HAMP. Especially, the lidar is highly sensitive to liquid cloud layers. Both instruments and derived products are described below.

The HAMP cloud radar operates in the Ka-band at 35.5 GHz with a temporal resolution of 1 s and vertical resolution of 30 m (Ewald et al., 2019). The sensitivity of the HAMP radar is about -30 dBZ (Konow et al., 2019). Here, we use the radar reflectivity product aligned temporally with the passive microwave radiometer observations and filtered for ground clutter in the lowest about 100 m (Dorff et al., 2024). Hence, shallow fog layers cannot be detected by the radar. Compared to the microwave radiometer, the radar's footprint size is rather narrow, with about 130 m (Mech et al., 2014).

Backscatter lidar and water vapor differential absorption lidar profiles were measured by the airborne demonstrator for the WAter vapor Lidar Experiment in Space (WALES; Wirth et al., 2009). Here, we use the backscatter ratio (BSR)

and depolarization ratio at 532 nm, which are available with a vertical resolution of 15 m and a temporal resolution of 1 s (Wirth and Groß, 2024). We exclude all data with a non-zero quality flag and below 50 m above the surface.

The radar observation is defined as cloudy if the radar reflectivity of any bin exceeds -40 dBZ. Similarly, we apply a backscatter ratio threshold of 4 to the lidar column. We define a scene as cloudy if either the radar or the lidar observations fulfill their cloud mask criterion. Both thresholds reduce the impact of thin ice clouds on the thermal infrared radiometer measurements.

In addition to the hydrometeor detection, we need to identify scenes with potential impact of scattering by frozen hydrometeors, which is relevant at HAMP frequencies above 90 GHz (Bennartz and Bauer, 2003). Here, we use a maximum radar reflectivity threshold of 5 dBZ at any height level in the radar column, which corresponds to a snowfall rate of about 0.05 to 0.5 mm h^{-1} depending on the ice particle habit and size distribution (Kneifel et al., 2011).

Further, we build a detection method for liquid cloud layers based on the lidar backscatter ratio and depolarization ratio. Cloud regions dominated by liquid water exhibit a high backscatter and near-zero depolarization ratio (Shupe, 2007; De Boer et al., 2009; Luke et al., 2010). Several threshold-based methods are developed for liquid classification from both parameters (Kalesse-Los et al., 2022), and here we subjectively define a similar thresholding method from the examination of WALES statistics of both parameters for HALO–$(\mathcal{AC})^3$. We define a region as liquid-dominated if the depolarization ratio is below 0.1 and the backscatter ratio is above 50. Typically, only the uppermost liquid layer can be detected from airborne lidars, and we define the uppermost bin of liquid-dominated regions as liquid layer top height (h_l). To account for attenuation of the lidar beam by large amounts of frozen hydrometeors, we classify columns that did not satisfy the liquid water criterion as potentially liquid clouds if the radar hydrometeor fraction in the lowest 5 km exceeds 50 %.

5.2.4 Radiation data

The thermal infrared radiometer KT-19 provides T_b in the atmospheric window from 9.6–11.5 µm (Schäfer et al., 2022). The T_b accuracy of KT-19 is about 0.5 K. The instrument points nadir with a beam width of 2.3°, which is comparable to the HAMP radiometer channels. The sampling frequency of 20 Hz is averaged to 1 Hz to match the HAMP radiometer sampling. We convert the clear-sky infrared T_b to surface skin temperature under the assumption of an infrared emissivity of 0.995 (Høyer et al., 2017; Thielke et al., 2022). Remaining atmospheric effects in the atmospheric window are considered to be negligible. This data is used as a

data source for the development of the microwave-only retrieval.

The Video airbornE Longwave Observations within siX channels (VELOX) camera provides two-dimensional thermal infrared T_b in the atmospheric window from 8.65–12 µm (Schäfer et al., 2022). The data are available at a temporal resolution of 1 s (Schäfer et al., 2023a). Here, we use the 10.74±0.39 µm channel (band 3) for qualitative information on spatial surface temperature features. From each image, we extract the cross-track scan at nadir. This data is used as a visualization during case studies.

The VELOX-based clear-sky surface classification product groups each pixel into four surface types, i.e., open water, sea ice water mixture, thin sea ice, and snow-covered sea ice (Müller et al., 2025). The classification exploits spatial skin temperature variations of sea ice, snow, and open water with a spatial resolution of about $10\times10\,\mathrm{m}^2$. We derive the thin sea ice area fraction within the microwave radiometer footprint from the high-resolution pixel-based classification. The accuracy of the thin sea ice classification, defined as the ratio of correct to total predictions, is approximately 70 % (Müller et al., 2025). We use this data for retrieval evaluation under clear-sky conditions.

The spectrometer of the Munich Aerosol Cloud Scanner (specMACS) measures two-dimensional fields of reflected spectral radiances from 0.4–2.5 µm (Ewald et al., 2016; Weber et al., 2024a). SpecMACS points nadir with a field of view of about 35° and a temporal resolution of 30 Hz. Since the visible bands were not available during HALO–$(\mathcal{AC})^3$, we use the 1 µm near infrared radiance for qualitative information on clouds and surface conditions. This data is used as a visualization during case studies.

5.2.5 Ancillary products

The ERA5 reanalysis provides hourly air temperature, pressure, and specific humidity on 137 model levels, and skin temperature, 2 m air temperature, and total column liquid water on surface levels at a spatial resolution of 31 km resampled to 0.25×0.25° (Hersbach et al., 2020). Here, we use data from the ERA5 grid cells that are nearest in space and time to the *HALO* flight track. The data is used as input for the retrieval and, in the case of the total column liquid water, for comparison with the CLWP retrieved from HAMP. The 2 m air temperature is used to filter potential surface melt, which occurred during parts of the warm air intrusion over sea ice. Here, we use a 2 m air temperature threshold of -1 °C.

Daily sea ice concentration maps from the University of Bremen with a 6.25× 6.25 km^2 resolution based on Advanced Microwave Scanning Radiometer - 2 (AMSR2) 89 GHz observations (Spreen et al., 2008) are used to filter for observations

over sea ice. To include data close to the north pole not covered by the AMSR2 swath, we assume sea ice concentrations are above 90 % in this area. Based on this data, we define the sea ice edge as the 50 % sea ice concentration contour and the Central Arctic as a region with a distance of at least 200 km from the sea ice edge.

We use Level 1C T_b data from channel 17 of the Special Sensor Microwave Imager/Sounder (SSMIS; Kunkee et al., 2008) onboard the DMSP-F16 satellite to get qualitative information on the spatial T_b variability around the *HALO* track (NASA Goddard Space Flight Center and GPM Intercalibration Working Group, 2022). Channel 17 of SSMIS measures vertically polarized T_b at 91 GHz under an incidence angle of 53° with a footprint size of $9 \times 15\,\mathrm{km}^2$.

5.3 Sea ice–atmosphere retrieval

5.3.1 Retrieval overview

For a coupled sea ice–atmosphere retrieval using a physical forward operator, we need to solve the radiative transfer of both the cryosphere and the atmosphere. Unfortunately, no model exists that simultaneously solves the radiative transfer equations of both spheres. Therefore, previous work on sea ice–atmosphere retrievals performed a loose coupling between the sea ice and snow radiative transfer model and radiative transfer model for the atmosphere via T_b or emissivity and emitting layer temperature (e.g., Kang et al., 2023; Sandells et al., 2024). Here, we follow the same approach and loosely couple the radiative transfer models SMRT (Picard et al., 2018) for the surface and PAMTRA (Mech et al., 2020) for the atmosphere. Both models are called sequentially, and the surface radiative properties are provided to PAMTRA as frequency-dependent emissivity and emitting layer temperature. This workflow is depicted in Fig. 5.3a and relevant input parameters are listed in Table 5.2.

Using optimal estimation (Rodgers, 2000), we retrieve six state parameters from the HAMP observations, considering observation, forward model, and a priori uncertainties. The retrieved state parameters are CLWP and five surface parameters: wind slab correlation length, depth hoar correlation length, wind slab thickness, snow–ice interface temperature, and air–snow interface temperature. The selection of these state parameters is based mainly on two criteria. First, there should be high sensitivity to state parameter variations within the parameter uncertainty range at HAMP frequencies based on SMRT–PAMTRA simulations. Second, ambiguities in the radiometric sensitivity between state parameters should be minimized to ensure stable retrieval convergence, i.e., cor-

relations between columns of the Jacobian should be low. Note that CLWP is the only atmospheric parameter that gets retrieved. The selection of snow parameters is also motivated by Wivell et al. (2023), who found that varying wind slab correlation length, depth hoar correlation length, and wind slab thickness reproduces observed tundra snow emissivity spectra from 89 to 243 GHz.

The main challenge for the retrieval is the lack of ground truth on the surface characteristics along the flight track. Therefore, we define two retrievals, hereafter referred to as retrieval 1 (R1; Fig. 5.3b) and retrieval 2 (R2; Fig. 5.3c). R1 is only applied to clear-sky and retrieves four surface parameters using wind slab and depth hoar correlation length a priori from the literature and an a priori guess of the wind slab thickness. Additionally, the air–snow interface is taken from KT-19, and CLWP is fixed to $0\,\mathrm{g\,m^{-2}}$. The retrieved distribution for all clear-sky samples (mean and standard deviation) of wind slab correlation length, depth hoar correlation length, and wind slab thickness is then used as a priori for the microwave-only retrieval R2 for both clear-sky and cloudy conditions to remove potential biases of the a priori values in R1. The clear-sky data used for the calibration covers most parts of the *HALO* study area and is therefore likely representative for cloudy scenes (Fig. 5.1).

5.3.2 Optimal estimation

During the optimal estimation retrieval, the state vector $\vec{x}$ is iteratively updated until an optimal solution is found. Here, we use a priori as a first guess. The updated state

$$\vec{x_{i+1}} = \vec{x_a} + \mathbf{S_i}\mathbf{K_i}^T\mathbf{S_e}^{-1}[(\vec{y} - F(\vec{x_i}, \vec{b}) + \mathbf{K_i}(\vec{x_i} - \vec{x_a})] \tag{5.1}$$

is computed from the observation $\vec{y}$ (HAMP T_b), effective measurement uncertainty $\mathbf{S_e}$, a priori state $\vec{x_a}$, forward operator F, forward model parameters $\vec{b}$, Jacobian matrix $\mathbf{K_i}$ of the forward operator $F(\vec{x_i}, \vec{b})$, and retrieval uncertainty $\mathbf{S_i}$. The effective measurement uncertainty combines observation and model uncertainty, i.e.,

$$\mathbf{S_e} = \mathbf{S_y} + \mathbf{K_b}\mathbf{S_b}\mathbf{K_b}^T, \tag{5.2}$$

with the observation uncertainty $\mathbf{S_y}$, the Jacobian matrix for model parameters $\mathbf{K_b}$ (computed during each iteration), and the model parameter uncertainty $\mathbf{S_b}$. We choose an uncorrelated observation uncertainty of 1.5 K from 22 to 118 GHz and 2 K at 183 GHz. Table 5.2 lists the mean and uncertainty of the model parameters (wind slab density, depth hoar density, depth hoar thickness, and specularity).

The retrieval uncertainty is given as

$$\mathbf{S_i} = (\mathbf{S_a}^{-1} + \mathbf{K_i}^T \mathbf{S_e}^{-1} \mathbf{K_i})^{-1}, \tag{5.3}$$

with the a priori covariance matrix $\mathbf{S_a}$. The optimal solution and its a posteriori uncertainty are found if the condition

$$(\vec{x_i} - \vec{x_{i+1}})^T \mathbf{S_i}^{-1} (\vec{x_i} - \vec{x_{i+1}}) < \frac{N}{10} \tag{5.4}$$

is met within six iterations. The retrieval algorithm assumes that the parameters follow a Gaussian distribution. While this is valid for most parameters, the CLWP may differ from a Gaussian distribution. A logarithmic transformation of CLWP similar to Boukabara et al. (2011) will be applied in the future.

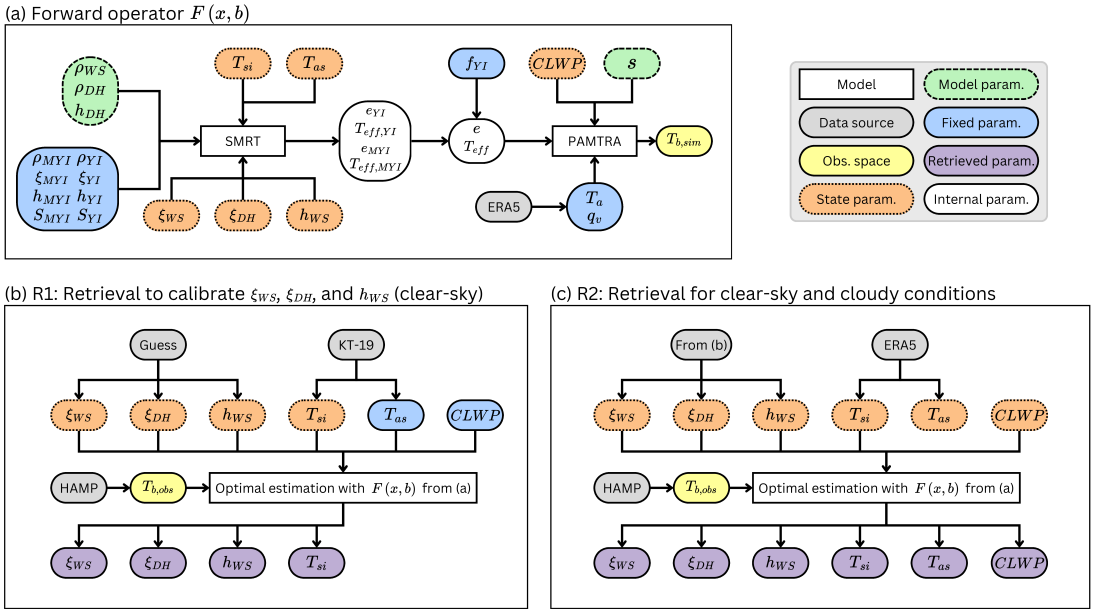

Figure 5.3: Flow diagrams of the (a) SMRT–PAMTRA forward operator ($F(x,b)$) coupled via emissivity (e) and effective temperature (T_{eff}), (b) clear-sky retrieval to calibrate snow parameters (R1), and (c) retrieval for clear-sky and cloudy conditions (R2). The parameter labeling of the forward operator in (a) corresponds to the retrieval for clear-sky and cloudy conditions in (c) (the air–snow interface temperature (T_{as}) and cloud liquid water path ($CLWP$) are fixed parameters in (b)). Note that the surface is characterized by fractions of young ice (YI) and multiyear ice (MYI), such that $f_{YI} + f_{MYI} = 1$. Parameter names of each symbol are listed in Table 5.2.

5.3.3 Sea ice radiative transfer

The sea ice radiative transfer is solved with SMRT (Picard et al., 2018). SMRT simulates the microwave emission and scattering of horizontal and plane-parallel

Table 5.2: State, model, and fixed parameters of the retrieval with references. The mean value of the state parameters denotes the a priori mean, while they denote the value used during the forward simulation for the model and fixed parameters. ERA5 or KT-19 mean values are derived from spatially and temporally collocated data. The standard deviation (Std.) denotes the diagonal of the a priori or model parameter covariance matrices. The minimum (Min.) and maximum (Max.) values indicate parameter limits.

Type	Parameter	Symbol	Unit	Mean	Std.	Min.	Max.	Reference
State	Cloud liquid water path	$CLWP$	$\mathrm{g\,m^{-2}}$	0^b	150	0	1000	
	Wind slab corr. length	ξ_{WS}	mm	0.13 0.12^a	0.05 0.03^a	0.05	0.25	Rückert et al. (2023b)
	Depth hoar corr. length	ξ_{DH}	mm	0.22 0.34^a	0.1 0.09^a	0.1	0.6	Rückert et al. (2023b)
	Wind slab thickness	h_{WS}	cm	13 12^a	5 3^a	3	40	
	Snow–ice interface temp.	T_{si}	K	KT-19 ERA5	3	243.15	271.15	Schäfer et al. (2024) Hersbach et al. (2020)
	Air–snow interface temp.	T_{as}	K	KT-19^b ERA5	3	233.15	273.14	Schäfer et al. (2024) Hersbach et al. (2020)
Model	Wind slab density	ρ_{WS}	$\mathrm{kg\,m^{-3}}$	350	30	150	450	King et al. (2020)
	Depth hoar density	ρ_{DH}	$\mathrm{kg\,m^{-3}}$	200	30	100	400	Domine et al. (2007)
	Depth hoar thickness	h_{DH}	cm	15	3	3	40	
	Specularity	s	-	0	0.25	0	1	Guedj et al. (2010)
Fixed	Young ice fraction	f_{YI}	-	0				
	Air temperature	T_a	K	ERA5				Hersbach et al. (2020)
	Specific humidity	q_v	$\mathrm{kg\,kg^{-1}}$	ERA5				Hersbach et al. (2020)
	Multiyear ice density	ρ_{MYI}	$\mathrm{kg\,m^{-3}}$	850				Timco and Frederking (1996)
	Young ice density	ρ_{YI}	$\mathrm{kg\,m^{-3}}$	915				Timco and Frederking (1996)
	Multiyear ice corr. length	ξ_{MYI}	mm	0.28				Rostosky et al. (2020)
	Young ice corr. length	ξ_{YI}	mm	0.15				Rostosky et al. (2020)
	Multiyear ice thickness	h_{MYI}	cm	150				
	Young ice thickness	h_{YI}	cm	30				
	Multiyear ice salinity	S_{MYI}	psu	1.2				Cox and Weeks (1974)
	Young ice salinity	S_{YI}	psu	30				

[a] Determined from the clear-sky retrieval (Fig. 5.3b). [b] Fixed during the clear-sky retrieval (Fig. 5.3b)

snow and sea ice layers. We assume that the snow consists of a mixture of ice and air without any liquid water or brine. Although liquid water likely occurred in the snowpack during parts of HALO–$(\mathcal{AC})^3$, a CLWP retrieval would be very uncertain over the highly emissive wet snow (Prigent et al., 2003; Vuyovich et al., 2017). The sea ice is characterized either as first-year or multiyear ice in SMRT. First-year ice comprises pure ice with brine inclusions, and multiyear ice comprises pure ice with brine and air inclusions. Below the sea ice, we add a semi-infinite ocean layer.

The propagation and scattering of microwave radiation in sea ice and snow depend on the snow and ice microstructure (Mätzler, 2002). Here, we use the exponential autocorrelation function as microstructure representation for both snow and sea ice, which is a function of the correlation length (Wiesmann et al., 1998). We select the improved Born approximation as electromagnetic theory to compute the scattering coefficient, which was shown to reproduce observed T_b over snow from 5–243 GHz (Vargel et al., 2020; Sandells et al., 2022, 2024), and the discrete ordinate and eigenvalue radiative transfer solver (Picard et al., 2013). The permittivity of multiyear ice is calculated with the Polder–Van Santen mixing formulas. Spherical inclusions are assumed for brine in first-year ice and air bubbles in multiyear ice.

As we lack detailed sea ice and snow layer properties along the *HALO* flight track, we define two simplified sea ice types: snow-covered sea ice and bare young sea ice. The snow-covered sea ice comprises multiyear sea ice covered with a two-layer snowpack. Snow-covered first-year ice is not defined explicitly due to the limited sensitivity of frequencies above 18 GHz to the sea ice type with constant snow parameters based on SMRT (Soriot et al., 2022). The two-layer snow consists of a depth hoar and a wind slab layer, commonly observed in the Arctic (Merkouriadi et al., 2017; King et al., 2020). Wind slab typically consists of rounded snow grains, and its density is higher than the density of the underlying depth hoar. We do not retrieve the snow density, due to the limited sensitivity at the low HAMP frequencies and similar sensitivity to correlation length at high frequencies (Wivell et al., 2023). The snow thickness is set to 38 cm a priori typical for the study region in spring (Warren et al., 1999) with a depth hoar fraction of about 40 % similar to field observations (King et al., 2020). The young sea ice is simulated as bare first-year sea ice, typically present in refrozen leads that are resolved by high-resolution aircraft observations and have a higher emissivity and surface temperature than surrounding sea ice (e.g., Hewison and English, 1999; Risse et al., 2024b). Note that the young sea ice fraction is included in the forward operator for sensitivity tests only and not retrieved due to poor retrieval regulation when the influence of snow parameters decreases with increasing young ice

fraction and the lack of accurate a priori data under cloudy conditions. Since the sea ice type and its physical properties do not notably impact the T_b at HAMP frequencies (Soriot et al., 2022), we can define a single-layer sea ice with fixed thickness, density, correlation length, and salinity (Table 5.2).

The sea ice and snow layer temperatures are linearly interpolated between the air–snow and snow–ice interface temperatures. An exception is the multiyear sea ice layer, where the snow–ice interface temperature is used as layer temperature, because the radiation emanates mostly from the upper part of the sea ice. Details on the a priori estimation are provided in Appendix 5.B.

The emissivity (e) for each sea ice type (young ice or multiyear ice) is calculated using SMRT simulations of the upwelling brightness temperature ($T_{\mathrm{b,up}}$) with and without atmospheric downwelling brightness temperature ($T_{\mathrm{b,down}}$) following Wiesmann and Mätzler (1999), i.e.,

$$e = 1 - \frac{T_{\mathrm{b,up}}(T_{\mathrm{b,down}} = 100\,\mathrm{K}) - T_{\mathrm{b,up}}(T_{\mathrm{b,down}} = 0\,\mathrm{K})}{100\,\mathrm{K}}. \tag{5.5}$$

Then, the emitting layer or effective temperature (T_{eff}) is calculated as

$$T_{\mathrm{eff}} = \frac{T_{\mathrm{b,up}}(T_{\mathrm{b,down}} = 0\,\mathrm{K})}{e}. \tag{5.6}$$

The emissivity and effective temperature of the two sea ice types are combined using the young ice fraction. To reduce computational cost, we simulate e and T_{eff} only for the center frequencies of each channel and interpolate linearly to all HAMP band passes.

5.3.4 Atmospheric radiative transfer

The atmospheric radiative transfer is simulated with PAMTRA (Mech et al., 2020). PAMTRA computes the nadir T_b at the six HAMP channels for the flight altitude of *HALO*, considering the atmospheric and surface contributions. For the surface, we provide PAMTRA with the frequency-dependent emissivity and effective temperature simulated with SMRT. The Lambertian and specular contributions to surface reflection are weighted by specularity (s), where $s = 0$ ($s = 1$) corresponds to a fully Lambertian (specular) surface. The specularity parameter is set to 0 as found for winter over snow (Guedj et al., 2010; Harlow and Essery, 2012), with an uncertainty accounting for 25 % specular contribution. Atmospheric profiles are used from ERA5 and not adjusted during the retrieval (Appendix 5.A). The gas absorption model by Rosenkranz (1998) is used with modifications of the water vapor continuum absorption (Turner et al., 2009).

The a priori CLWP is set to $0\,\mathrm{g\,m^{-2}}$ with a standard deviation of $150\,\mathrm{g\,m^{-2}}$.

Although CLWP is available from ERA5, we keep the retrieval simple and always assume cloud-free conditions a priori. Negative CLWP values are set to $0\,\mathrm{g\,m^{-2}}$ before calling the forward operator. The CLWP is distributed with a homogeneous cloud liquid water content between the surface and 4 km height where the air temperature is above -38 °C and simulated using a monodisperse size distribution of 20 µm diameter. Both assumptions are considered to have a minimal impact on the simulated T_b (Crewell et al., 2009; Ebell et al., 2017). The emission of supercooled liquid water is derived following the model by Turner et al. (2016). Rain is not included in the forward simulations because we also do not consider associated wetting of the snowpack in our SMRT setup.

Cloud ice is not included in the simulation due to the low scattering at HAMP frequencies up to 183 GHz (e.g., Buehler et al., 2007). However, high amounts of larger snow particles lead to notable scattering from 90 to 183 GHz. For example, we observed T_b depressions up to 10 K at 183±7.5 GHz during parts of the warm air intrusion over sea ice during HALO–$(\mathcal{AC})^3$. However, since we remove these cases based on the radar reflectivity threshold, we assume that the remaining snow scattering can be neglected. Adding snow water path is in principle possible, but for simplicity, we focus on the cloud liquid water signal in this work.

5.3.5 Synthetic retrieval setup

The synthetic retrieval allows for the quantification of the CLWP retrieval accuracy and the identification of parameter ambiguities. The observation for the synthetic retrieval consists of realistic forward simulations of a known state rather than real observations. To create realistic forward simulations that resemble natural variability, we randomly generate state and model parameters using the a priori and model parameter covariance matrices. No noise is added to the synthetic forward simulations, but it is part of the effective measurement uncertainty of the retrieval. The synthetic database is built from random samples of HAMP observation positions and respective state, model, and fixed parameters to represent HALO–$(\mathcal{AC})^3$ conditions. The mean ERA5 integrated water vapor of the database is $5\,\mathrm{kg\,m^{-2}}$ with a standard deviation of $3\,\mathrm{kg\,m^{-2}}$, and the mean ERA5 skin temperature is -14 °C with a standard deviation of 8 K. For the CLWP accuracy assessment, we sample CLWP uniformly from 0–500 $\mathrm{g\,m^{-2}}$ and run 5000 simulations. For the identification of parameter ambiguities (2000 simulations), all parameters are sampled from Gaussian distributions truncated by the parameter limits (Table 5.2).

5.4 Retrieval evaluation

5.4.1 Clear-sky evaluation

Observation space

A comparison between the HAMP observation and simulations under clear-sky conditions (12,250 samples) provides an indication of whether the SMRT–PAMTRA forward operator represents real sea ice and snow conditions. In the following, we present T_b departure statistics of the a priori and optimal states for the retrievals R1 and R2 (Fig. 5.4). To ensure equal sampling, we analyze 81 % of the clear-sky observations where both R1 and R2 converge. Generally, R1 shows a slightly higher convergence rate with 90 % than R2 (87 %), which is expected due to the higher number of state parameters in R2.

The departures of the optimal solution improve notably and are much narrower than the a priori for both R1 and R2, especially from 22–118 GHz. The highest difference between the R1 and R2 distributions occurs at 90 and 118 GHz. While R1 tends to underestimate the T_b, R2 slightly overestimates the T_b in some cases by up to 10 K. Still, both distributions align well with the effective measurement uncertainty despite the increase in state parameters from four to six from R1 to R2. The highest bias in R2 occurs at 22 GHz with -3 K, but the effect on the CLWP retrieval is expected to be small. The biases of the other channels are much smaller (-0.6–1.5 K). This indicates a substantial improvement compared to the a priori with biases between -11 K at 22 GHz and 2 K at 118 GHz. A T_b bias correction could be performed at a later stage, but is not included here. The root mean squared error of the R2 retrieval varies between 2–4 K and lies close to the effective measurement uncertainty. Also, the correlations between observed and simulated T_b of the optimal solution are very high from 31–118 GHz with 0.9–0.93. Hence, this clear-sky evaluation shows that the retrieval finds a state that closely matches the observations, which provides the basis for the retrieval application to synthetic and cloudy observations.

State space

Encouraged by the good match of the retrieval with HAMP in observation space, we now analyze the corresponding retrieved state parameters (Fig. 5.5). The mean and standard deviation of the retrieved states in R1 for all clear-sky observations lie mostly close to the a priori mean and standard deviation. The largest difference occurs for the mean depth hoar correlation length, which increases by about 1.2σ (a priori uncertainty) from the a priori to the optimal state. This increase might be related to snow metamorphism throughout the winter, which

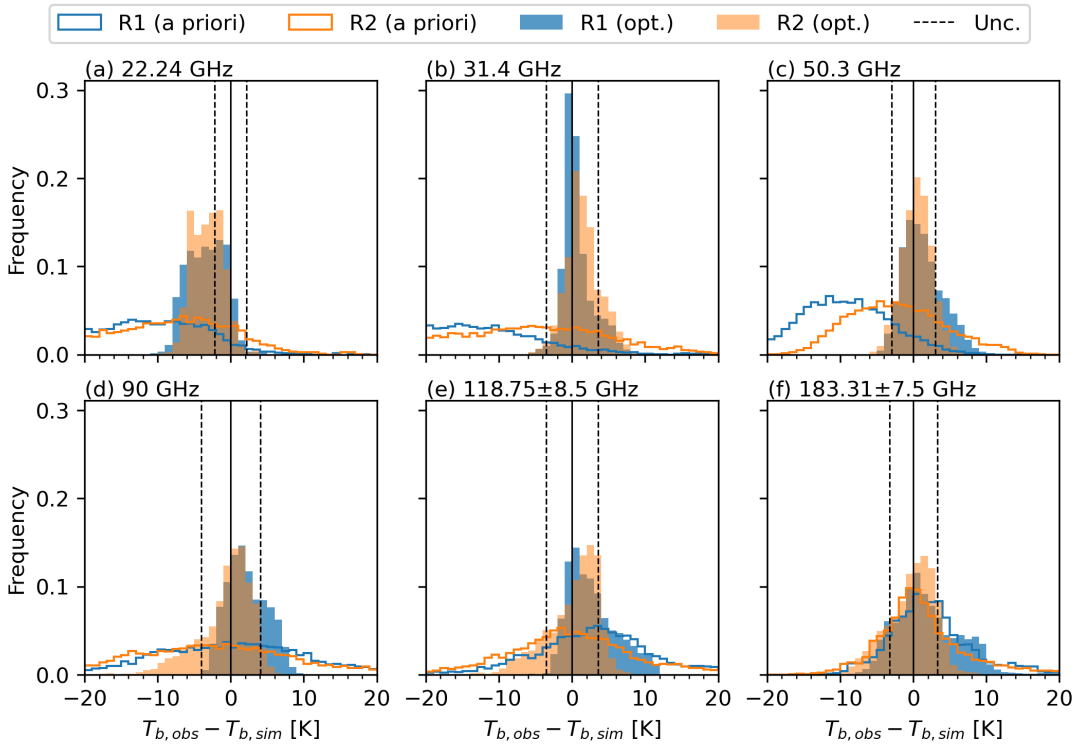

Figure 5.4: Histograms of the T_b departure between clear-sky observations and forward simulations of the a priori and optimal (opt.) states retrieved with R1 and R2. Panels show the (a) 22, (b) 31, (c) 50, (d) 90, (e) 118, and (f) 183 GHz channels. Note that only times where both retrievals converge are shown (81 % of the data). Unc.: Effective measurement uncertainty.

increased depth hoar grain size and microwave scattering in this layer. This increase in a priori depth hoar correlation length explains the differences in the a priori T_b bias between R1 and R2 (Fig. 5.4). The changes in the wind slab correlation length (-0.2σ) and wind slab thickness (0.2σ) are much smaller. The retrieved variability of the wind slab correlation length is lower than the value from the literature. For the snow–ice interface temperature, a relatively large negative deviation can be seen. This might be related to the observed negative bias of the a priori at low frequencies in Fig. 5.4 and might originate from the assumed relationship in Eq. (5.7) or a misrepresentation of sea ice and snow layering. An assessment of the spatial consistency of these parameters is presented during the retrieval application in Sect. 5.5.

The distributions of the optimal parameters from the R2 retrieval shift slightly compared to the R1 retrieval, but differences are overall small (Fig. 5.5). This shows that the retrieved state is not very sensitive to the a priori mean, which is important for the poorly constrained snow parameters. Compared to R1, the R2 retrieval also derives the air–snow interface temperature, as this information will not be available under cloudy conditions. The retrieved temperature centers well around the ERA5-based a priori estimate, indicating that the ERA5 skin temperature is a suitable a priori choice. The root mean squared error between the retrieved air–snow interface temperature and the skin temperature from KT-19 is 2.8 K, which is similar to the ERA5-based a priori (3.1 K; not shown). For CLWP, which is also retrieved by R2 and should ideally be zero under clear-sky identified from the radar–lidar cloud mask, the root mean squared error is 112 g m^{-2} (Fig. 5.5f). Generally, the state distributions are realistic despite some deviations in the snow–ice interface temperature, which affect the low-frequency HAMP channels. Thus, we conclude that the retrieval with the SMRT–PAMTRA forward operator provides a generalized representation of the sea ice and snow layer properties for a CLWP retrieval.

5.4.2 Cloud liquid water path detectability

This section analyses the CLWP detectability of the HAMP retrieval from clear-sky observations. During clear-sky conditions, the retrieved CLWP should ideally be close to 0 g m^{-2}. Hence, we can define the CLWP detectability as the 95th percentile of retrieved CLWP under clear-sky (Fig. 5.6a). For all observations, about 95 % of the retrieved CLWP are below 306 g m^{-2}. We identify a distinct spatial pattern in the Central Arctic, where this detectability improves a lot down to 45 g m^{-2}. This decrease with increasing distance to the ice edge is shown in Fig. 5.6b. Between 150–200 km, the detectability decreases from

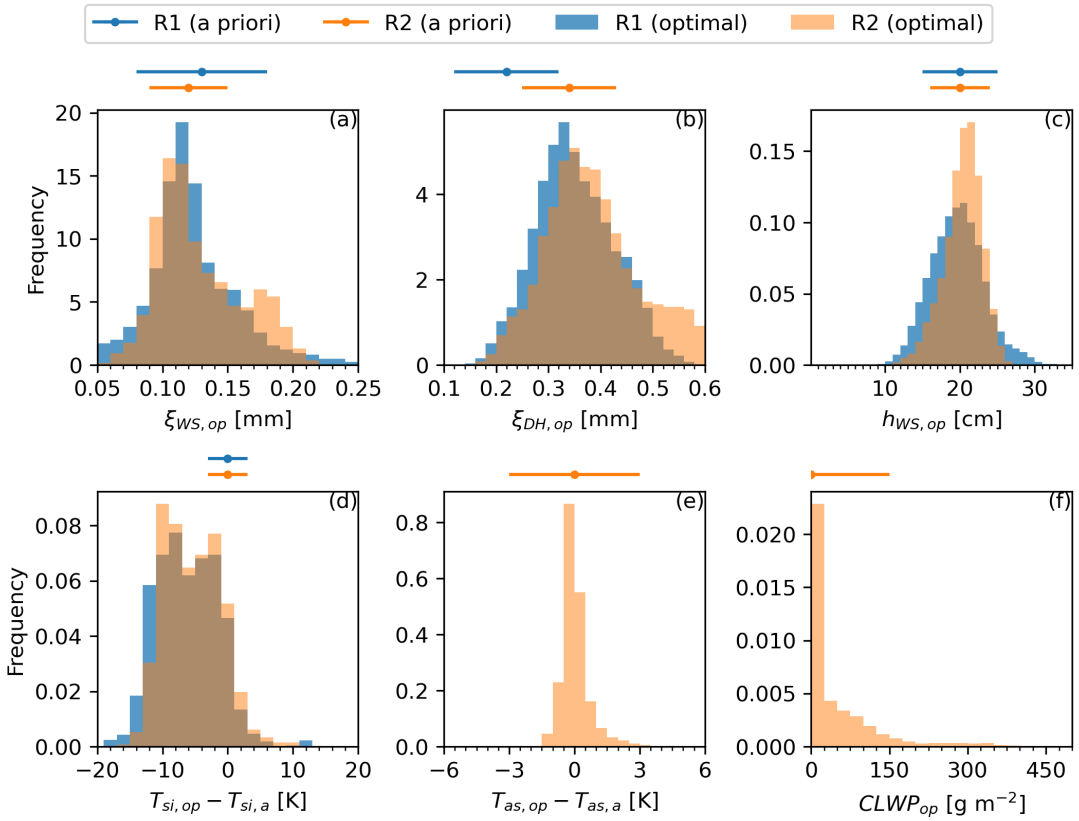

Figure 5.5: Histograms of the retrieved parameters from the retrievals R1 and R2 during clear-sky observations corresponding to Fig. 5.4. The a priori mean and uncertainty are shown above each panel. Panels show the (a) wind slab correlation length, (b) depth hoar correlation length, (c) wind slab thickness, (d) snow–ice interface temperature minus a priori, (e) air–snow interface temperature minus a priori (R2 only), and (f) cloud liquid water path (R2 only). Note that only times where both retrievals converge are shown (81 % of the data).

300 to below 100 g m^{-2} and remains low for further distances to the ice edge. The infrared-based analysis by Müller et al. (2025) shows a consistent decrease of refrozen leads with distance to the ice edge. These leads and their respective high microwave emissivity and skin temperature are correlated with false CLWP detections (Fig. 5.6c). The high false detection for low thin ice fraction likely corresponds to thicker young ice, potentially with a snow cover, and a skin temperature comparable to surrounding sea ice. A similar T_b response between CLWP and increased bare ice fraction can also be simulated with SMRT and PAMTRA (Fig. 5.6d). Overall, the clear-sky retrieval evaluation shows that the retrieval detects CLWP above 50 g m^{-2} at higher distances from the ice edge and can thus be applied to cloudy scenes.

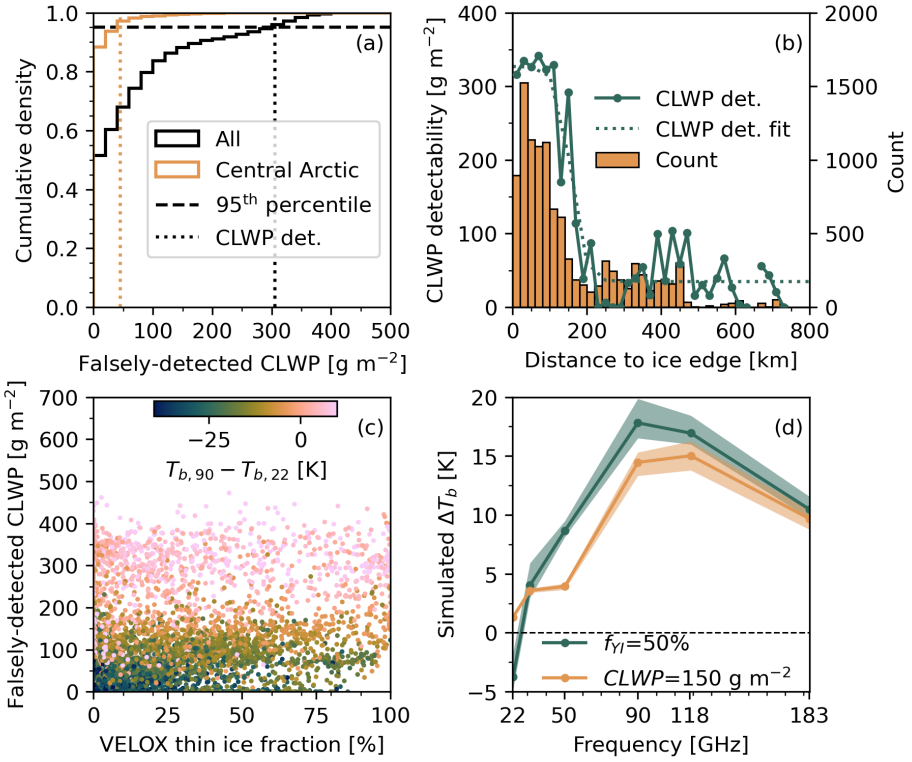

Figure 5.6: Assessment of cloud liquid water path (CLWP) detectability and falsely-detected CLWP. (a) Cumulative density of retrieved CLWP for all and Central Arctic clear-sky samples with the corresponding detectability estimated from the 95th percentile. (b) CLWP detectability and sigmoidal fit as a function of distance to sea ice edge. (c) Scatter plot between thin ice fraction derived from the thermal infrared spectral imager and falsely-detected CLWP with T_b difference between 90 and 22 GHz as shading. (d) Simulated brightness temperature difference (ΔT_b) between the a priori state and modified a priori states with increased f_{YI} (from 0 to 50 %) and CLWP (from 0 to 150 g m^{-2}) for all clear-sky samples. Shading indicates the 25–75 percentile range of ΔT_b for both sensitivity tests.

5.4.3 Cloud liquid water path accuracy

In Sect. 5.4.1, we proved that the forward operator and adjustment of the state parameters closely match with clear-sky HAMP observations. In the following, we analyze the CLWP retrieval skill based on synthetic retrieval experiments (Fig. 5.7). Generally, the retrieval is able to reproduce the real CLWP, but with a high relative uncertainty of about 125 % for CLWP below 50 g m^{-2} and growing underestimation toward high CLWP values. The high relative uncertainty of more than 100 % for low CLWP indicates the challenge in identifying thin or low-level clouds over sea ice (Turner et al., 2007). The RMSE of the synthetic experiment for low CLWP conditions can be compared with the clear-sky retrieval (Fig. 5.7b). At larger distances from the sea ice edge toward the Central Arctic, the clear-sky RMSE is about 30 g m^{-2}, which is comparable to the RMSE estimated from the sensitivity test for low CLWP conditions. The growing bias toward high CLWP values can likely be explained by the retrieval starting with cloud-free conditions a priori. As the CLWP exceeds multiples of its uncertainty, a growing fraction of the cloud liquid signal influences the retrieval of snow parameters with similar Jacobians, particularly the wind slab correlation length (Appendix 5.C).

The uncertainty estimated from the synthetic experiments holds for all conditions that meet the forward model assumptions. Mainly, the occurrence of leads, open water, wet snow, and deviations from the simple two-layer snow assumptions increases the CLWP uncertainty and leads to biases. However, the synthetic experiments provide the only way to assess the retrieval skill due to the lack of independent CLWP data. The good performance under clear-sky conditions provides confidence that the estimated skill closely represents real conditions. While some improvements might be expected with an improved CLWP a priori information, such as ERA5, we keep the clear-sky a priori assumption for simplicity.

We also performed sensitivity tests with two additional dual oxygen channel pairs (51.76, 52.8, 118±4.2, and 118±2.3 GHz; not shown). The lower surface sensitivity and differential water vapor emission signal were shown to provide additional information on precipitation, especially over land (Bauer and Mugnai, 2003; Bauer et al., 2005). However, the synthetic experiments did not yield an improvement in CLWP retrieval accuracy in relation to the additional computational cost. Furthermore, we increased the number of channels starting with the lower three channels (22–50 GHz) and found the highest improvement in accuracy when adding the 90 GHz channel. However, we use the entire frequency range during the retrieval to provide a broad spectral range for the surface characterization.

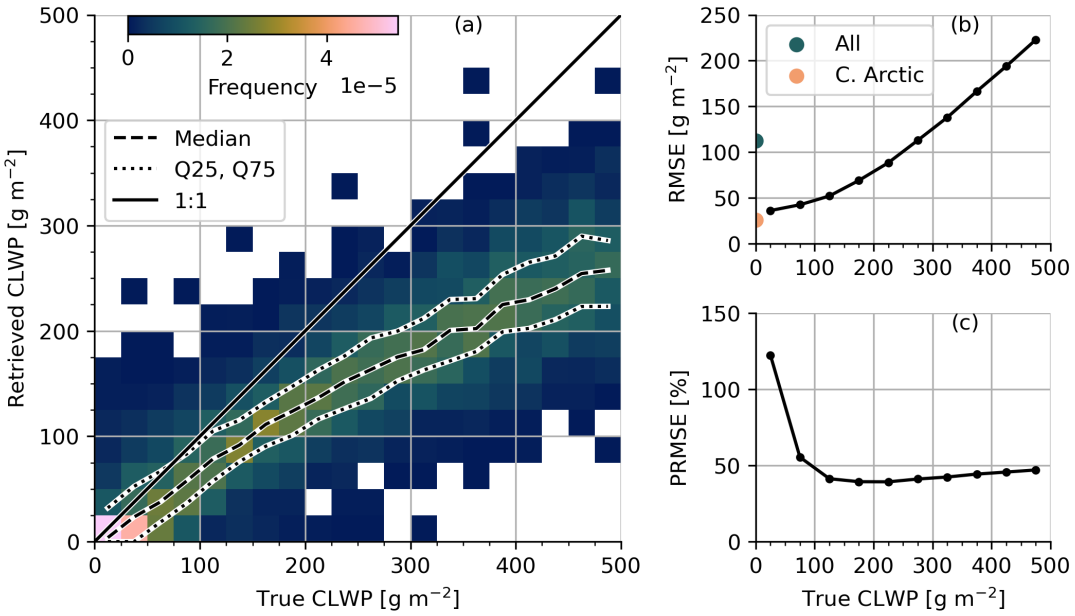

Figure 5.7: Cloud liquid water path (CLWP) retrieval skill based on synthetic experiments. (a) Joint histogram of the true CLWP used in the forward simulation and the retrieved CLWP, with median, 25th (Q25), and 75th percentiles (Q75). (b) Root mean squared error (RMSE) as a function of true CLWP from the synthetic experiments and clear-sky observations split into all and Central Arctic (C. Arctic) observations. (c) RMSE normalized by the true CLWP (PRMSE) as a function of true CLWP.

5.5 Retrieval application

5.5.1 Case 1: Stratocumulus (12 April 2022)

In this section, we present the HAMP retrieval for an overflight of about 800 km across a stratocumulus field over sea ice from the ice edge toward the north pole on 12 April 2022 (Fig. 5.8; case 1 in Fig. 5.1). About 92 % of the retrievals converged, which is slightly above the convergence rate of 85 % for all flights. The near and thermal infrared images indicate refrozen leads in the initial 150 km until the stratocumulus and a cirrus layer dominate the images (Fig. 5.8a1–b1). The cloud top height is stable with about 300–400 m along the 250 km cross section captured by *HALO* (Fig. 5.8b2). The radar reflectivity signal of the cloud is rather weak with few low-reflectivity streaks (Fig. 5.8a2).

The observed HAMP T_b generally decreases toward the north, with a breakpoint around 400 km at 22, 31, and 50 GHz (Fig. 5.8c1-h1). This large-scale gradient might be related to a transition in the snow and sea ice regime toward the Central Arctic with predominantly perennial sea ice, apart from surface cooling. Small-scale features at a scale below 25 km indicate snow and sea ice variations at floe scales and the presence of refrozen leads, which likely cause the

high 90, 118, and 183 GHz T_b peaks. The retrieval is able to find a matching T_b for most conditions, which represents this small and large scale T_b variability not represented by the a priori. An exception is the section from 450–600 km with differences of about 5–10 K, especially at 90, 118, and 183 GHz.

While no distinct cloud emission signature can be identified from the observed T_b time series, the retrieval finds CLWP from 0–400 km and 650–850 km. Very high and short CLWP peaks coincide with leads due to the similar Jacobians of lead fraction and CLWP (see Fig. 5.6d). The broader CLWP plateau from 150–400 km might be linked to actual cloud liquid presence in the stratocumulus field. However, most CLWP values are below the CLWP detectability. The CLWP signal at the end of the segment does not align with an observed liquid layer in the lidar. The other state parameters follow the small and large scale T_b features discussed earlier. Notably, the depth hoar correlation length increases around 400 km, which could be linked to more multiyear ice toward the north. Interestingly, the wind slab correlation length does not follow the same pattern and increases around 600 km.

Overall, this case study demonstrates that the retrieval finds a state space, which matches the observations under cloudy and clear-sky conditions along a long flight segment from the sea ice edge to the Central Arctic (81–88° N). However, the retrieval does not clearly identify the CLWP signature of the low-level stratocumulus field, likely due to its CLWP being below the CLWP detectability threshold, and falsely retrieves CLWP in areas without liquid cloud layers.

5.5.2 Case 2: Warm air intrusion (14 March 2022)

After analyzing the HAMP retrieval for a stratocumulus cloud with low CLWP, we now present a second case during a crossing from north to south of the warm air intrusion on 14 March 2022 (Fig. 5.9; case 2 in Fig. 5.1). Almost all of the retrievals converged along this transect (99 %). The radar shows the cloud and precipitation structure with snowfall occurring from 25–175 km. The lidar signal shows liquid top heights from 2–4 km within the precipitating system. Lower clouds occur toward the end of the segment. These clouds can also be seen in the near-infrared images. The thermal infrared images indicate increased fraction and size of leads with warmer skin temperature than the surrounding sea ice toward the end of the segment, around 550 km.

The observed HAMP T_b decreases toward the end of the segment at all frequencies, which is partly linked to the decrease in atmospheric water vapor and temperature as *HALO* leaves the warm air intrusion center. This gradient is also reflected by the a priori T_b. However, the T_b decreases well below the a priori

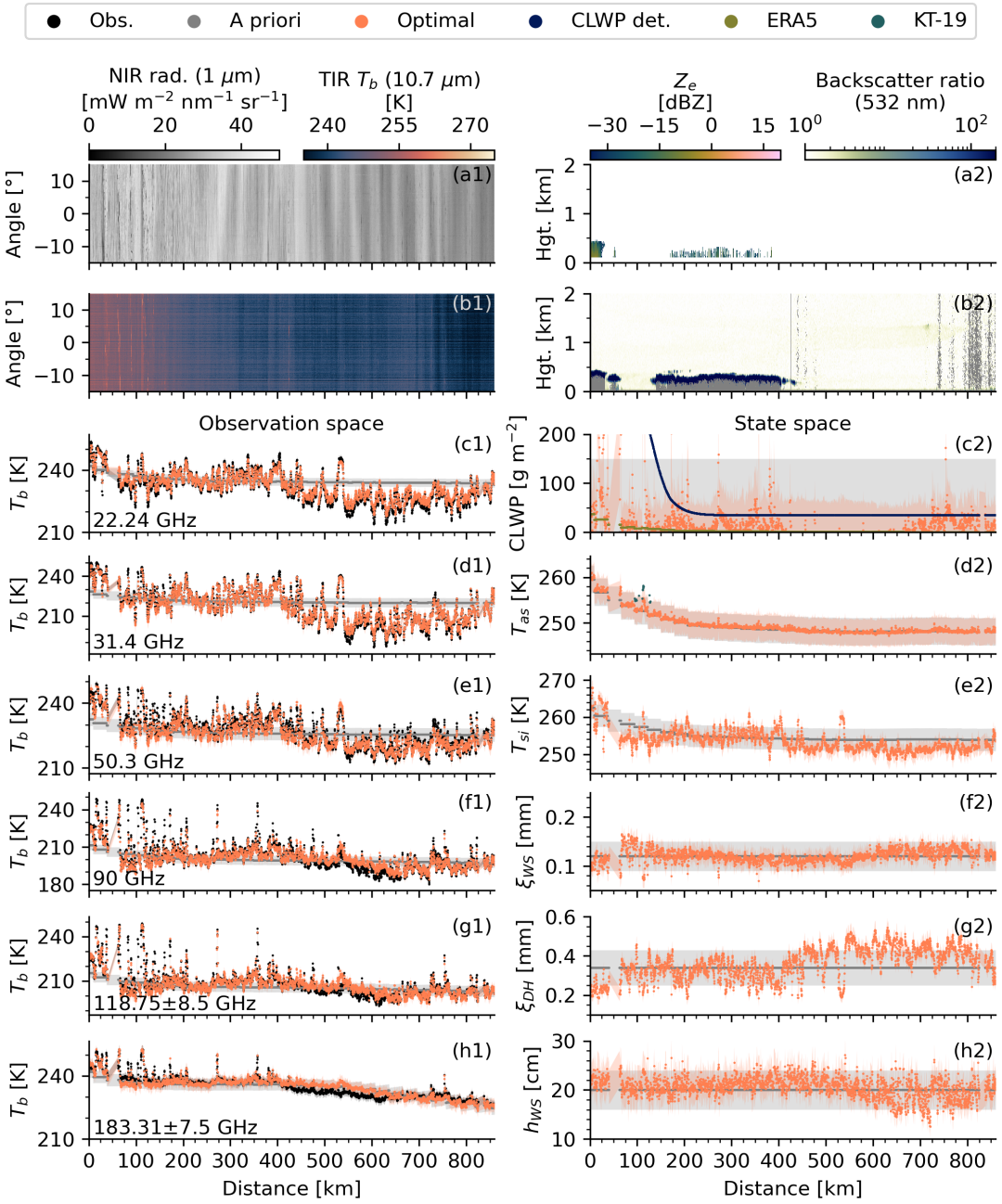

Figure 5.8: HAMP observation and retrieval for a northbound flight segment above a stratocumulus field on 12 April 2022 (case 1 in Fig. 5.1). (a1) Near infrared radiance, (a2) radar reflectivity, (b1) thermal infrared T_b, and (b2) backscatter ratio. (c1-h1) Observation space: Observed, a priori, and optimal T_b at (c1) 22, (d1) 31, (e1) 50, (f1) 90, (g1) 118, and (h1) 183 GHz. (c2-h2) State space: A priori and optimal (c2) cloud liquid water path from HAMP with ERA5 cloud liquid water path and HAMP cloud liquid water path detectability (CLWP det.), (d2) air–snow interface temperature with KT-19 skin temperature under clear-sky, (e2) snow–ice interface temperature, (f2) wind slab correlation length, (g2) depth hoar correlation length, and (h2) wind slab thickness. Note that the CLWP detectability exceeds the axis limit from 0–100 km.

at all frequencies with sharp boundaries at about 200 and 425 km. Similar to the stratocumulus case in Fig. 5.8, the observations and the simulated optimal state align well on both small and large spatial scales. Larger differences between the observations and retrieved state occur between 250–450 km. Moreover, the simulation overestimates the observed 22 GHz T_b from 200 km until the end of the segment.

The retrieval adds CLWP for regions where the lidar also identifies liquid layers with up to 300 g m^{-2} from 0–225 km. This region corresponds to the cloudy region at the core of the warm air intrusion and is partly excluded from the retrieval due to potential scattering by frozen hydrometeors that are not considered in the radiative transfer. The decrease in CLWP also aligns with the transition from liquid to non-liquid layers in the lidar backscatter ratio. Also, ERA5 data contains clouds with CLWP up to about 75 g m^{-2}, although a comparison is challenging due to the larger size of the model grid compared to the HAMP footprint. The retrieved CLWP toward the end of the segment is likely associated with the low-level clouds and false detections from refrozen leads, which formed in response to the warm air intrusion.

The air–snow interface temperature aligns well with the KT-19 skin temperature with absolute differences mostly below 2 K. The snow–ice interface temperature drops to very low values at about 200 km, corresponding to the 22 GHz T_b decrease. A similar trend can be found for the wind slab and depth hoar correlation lengths, which increase toward the end of the segment at about 425 km. The wind slab correlation length is very low within the precipitating system, likely due to the ambiguity with the CLWP signal (see Appendix 5.C). Overall, the liquid cloud signal during the warm air intrusion is well represented by the retrieval.

5.5.3 Rain-on-snow event (12–14 March 2022)

Sea ice parameters retrieved during the warm air intrusion on 14 March 2022 partly lie outside of the expected parameter range. This flight covered an area affected by surface melt and rain on 13 March 2022 and subsequent refreezing. It is well known that rain-on-snow (ROS) events and associated surface glazing strongly influence the sea ice microwave signature from ground-based (Stroeve et al., 2022) and satellite observations (Voss et al., 2003; Rückert et al., 2023a). In the following, we present the evolution of the state parameters during three consecutive flights from 12 to 14 March 2022, covering the conditions before, during, and after the ROS event (Fig. 5.10). The 91 GHz V-pol imagery captured by SSMIS onboard DMSP-F16 close to the *HALO* overpasses shows an increase in T_b by several tens of Kelvins from 12 to 13 March 2022. After the ROS event

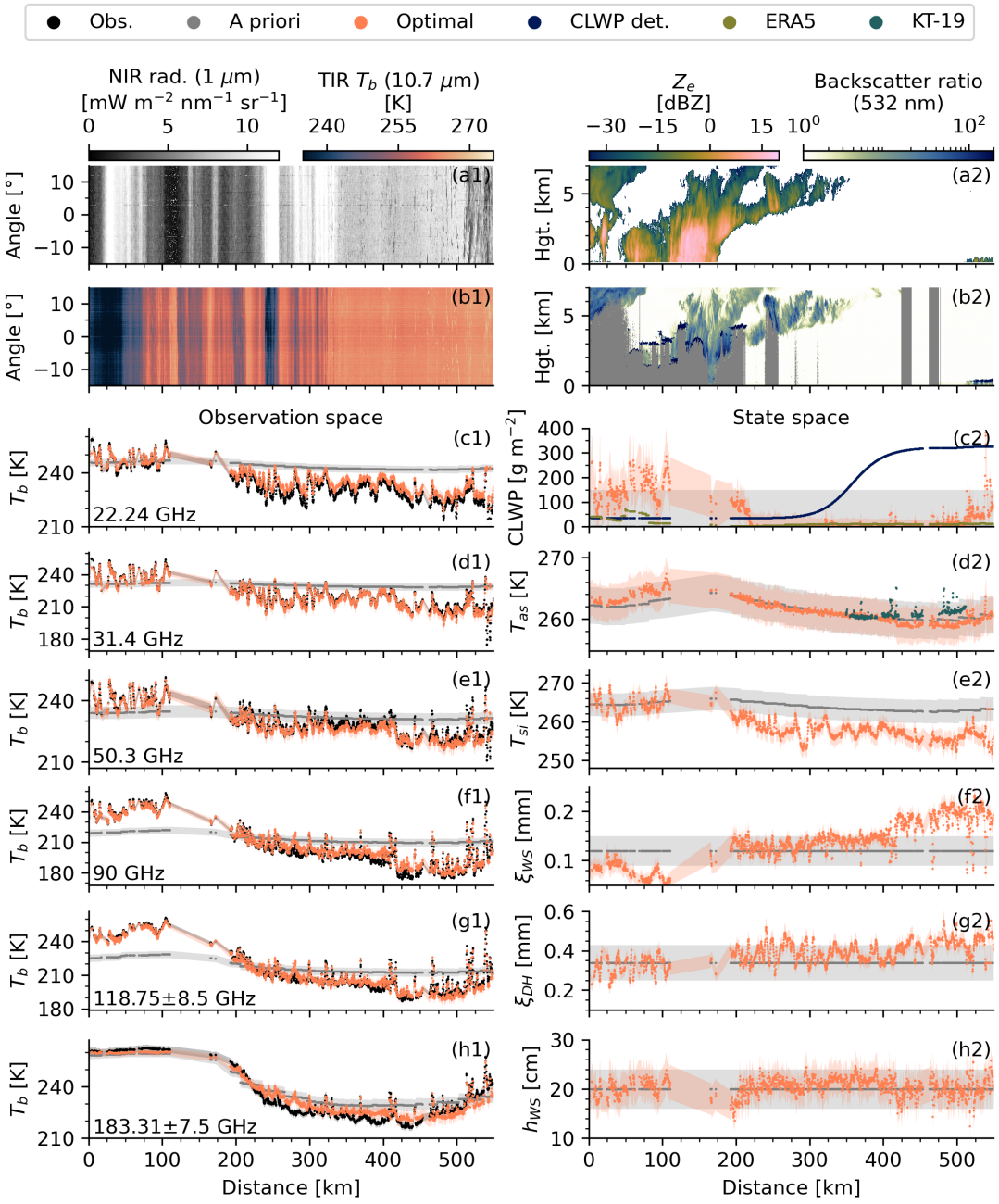

Figure 5.9: HAMP observation and retrieval for a southbound flight segment during the warm air intrusion on 14 March 2022 (case 2 in Fig. 5.1). Panels as in Fig. 5.8.

on 14 March 2022, the T_b decreases far below the condition observed prior to the ROS event (Fig. 5.10a3), and remains low for a couple of weeks until April 2022 (not shown).

The HAMP retrieval on 12 March lies near the a priori values and converges 87 % of the time. The only outlier is an open water patch near the ice edge at 80° N, which corresponds to very low T_b that causes artificial sharp gradients in the retrieved snow–ice interface temperature and depth hoar correlation length. The cloudy region south of 82° N visible in radar and lidar is captured by the retrieval. The retrieved CLWP reaches mostly values between 200 and 300 $\mathrm{g\,m^{-2}}$, which aligns with liquid layer top heights of 4–5 km detected by the lidar.

On 13 March, a clearly visible bright band at 1 km height in the radar reflectivity profile likely indicates melting snow and associated rainfall on the sea ice. Therefore, the retrieval is invalid for most parts of this segment and masked out by the 2 m air temperature and radar reflectivity flags. The northern part of the bright band is not flagged at about 83° N, but the HAMP retrieval does not converge in this area (Fig. 5.10a2). The area not affected by the ROS event (north of 83° N) mostly lies close to the a priori. A notable increase in the depth hoar correlation length north of 86° N might be related to the higher fraction of perennial sea ice.

After the ROS event, the HAMP retrieval converged for most observations (99 %) on 14 March (see Sect. 5.5.2). While sea ice parameters in the northern region lie close to the a priori, they deviate from the expected range in the low-T_b region south of 84.5° N (Fig. 5.10a3). This is slightly farther north than the observed melting layer in the radar at 83° N and could be explained by the northward transport of warm and moist air masses between the flights and potential rain or surface melt up to 84.5° N. Especially the wind slab correlation length and the snow–ice interface temperature lie far from the a priori and the conditions observed before the ROS event on 12 March. Potential reasons for the altered sea ice emissivity could be the formation of ice lenses after the freeze-up at the surface. Ice lenses are weakly scattering and lower the microwave emissivity through the dielectric contrasts between adjacent layers of different densities. Additionally, newly accumulated snow on top of the ice lens could amplify the T_b reduction. Interestingly, a secondary increase in the wind slab correlation length occurs as *HALO* approaches the T_b minimum of the SSMIS swath around 82.5° N. Near and thermal infrared images do not show apparent surface patterns that correlate with this microwave signature (not shown). Thus, we assume that spatial variations of snowpack changes (ice lens, fresh snow) contribute.

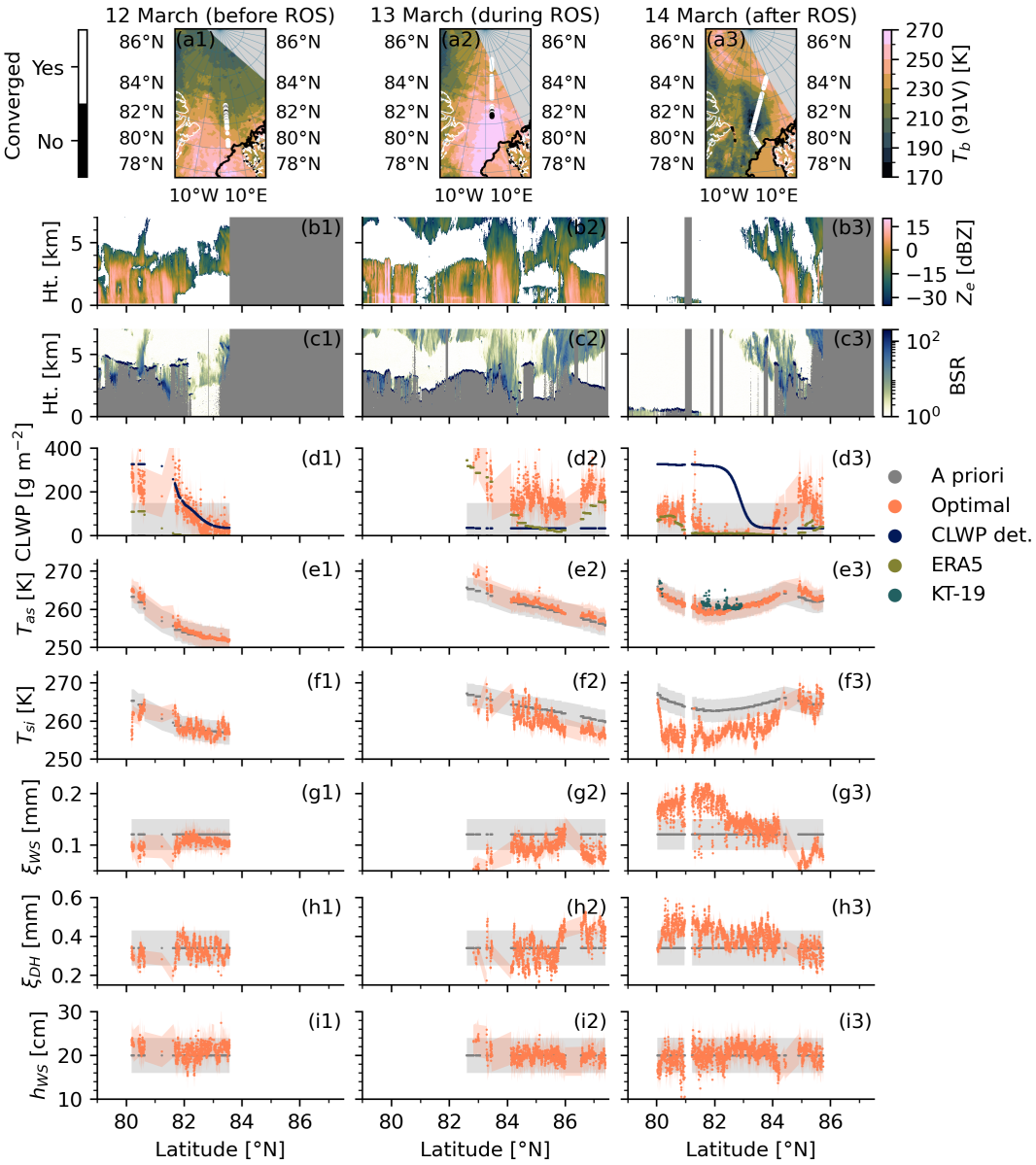

Figure 5.10: HAMP retrieval and satellite observations before the rain-on-snow (ROS) event (12 March 2022, column 1), during the ROS event (13 March 2022, column 2), and after the ROS event (14 March 2022, column 3). (a1–a3) 91 GHz V-pol T_b from SSMIS onboard DMSP-F16 at about (a1) 13:30 UTC, (a2) 15:00 UTC, and (a3) 14:45 UTC, 15 % sea ice concentration contour, and meridional *HALO* flight tracks with retrieval convergence mask as shading from (a1) 13:56–15:42 UTC, (a2) 13:43–15:30 UTC, and (a3) 13:26–16:45 UTC. Note that *HALO* flew a zonal segment during the turn in (a3), not shown here. Panels below the maps show *HALO* observations and retrieval parameters (a priori and optimal) as a function of latitude: (b1–b3) Radar reflectivity, (c1–c3) backscatter ratio (BSR), (d1–d3) cloud liquid water path from HAMP with ERA5 cloud liquid water path and HAMP cloud liquid water path detectability (CLWP det.), (e1–e3) air–snow interface temperature with KT-19 skin temperature under clear-sky, (f1–f3) snow–ice interface temperature, (g1–g3) wind slab correlation length, (h1–h3) depth hoar correlation length, and (i1–i3) wind slab thickness.

5.5.4 CLWP variability during HALO–$(\mathcal{AC})^3$

In this section, we exploit the collocated radar–lidar cloud remote sensing data from *HALO* to assess CLWP distributions for different cloud types (Fig. 5.11). In total, 85 % of HAMP retrievals converge during the entire campaign, which is similar to the clear-sky convergence rate (87 %). The CLWP distributions of HAMP shift gradually toward higher values with increasing liquid top height determined from the lidar (Fig. 5.11a). The low liquid top class predominantly shows CLWP below 25 g m^{-2} and the high liquid top class shows a broad peak from 100–200 g m^{-2}. During the absence of a liquid layer, the CLWP follows the clear-sky distributions (Fig. 5.5f) with a considerable amount of falsely detected CLWP likely related to refrozen leads. To exclude these cases, we filter for the Central Arctic where fewer leads are expected (Fig. 5.11c). The no liquid class remains mostly below 50 g m^{-2}, which aligns with the lower CLWP detectability threshold found in this region. Most CLWP values above 100 g m^{-2} align with observations with liquid top heights between 1–5 km. In the 50–100 g m^{-2} range, the 0.5–1 km liquid top heights become more frequent.

The distributions from ERA5 follow a similar shape as the HAMP distributions for all observations (Fig. 5.11b) and the Central Arctic (Fig. 5.11d). A notable difference for all cases is the higher number of extremes derived from HAMP, which likely relates to the small footprint size of HAMP with 1 km compared to a spatial resolution of 31 km of ERA5. Moreover, potential false detection over leads could cause artificial CLWP peaks. Both CLWP distributions peak at 125–150 g m^{-2} when a liquid layer was detected by the lidar. For the distribution in the Central Arctic, both HAMP and ERA5 show CLWP up to 175 g m^{-2} and a few extremes above 200 g m^{-2} mostly linked to high liquid tops.

The analysis of CLWP distributions for HAMP and ERA5 indicates agreement in both the shape and magnitude of CLWP. However, the relatively high uncertainty of the HAMP retrieval and the negative bias found for high CLWP from synthetic experiments should be considered when evaluating ERA5 CLWP.

5.6 Conclusions

Passive microwave observations provide high spatial and temporal coverage in the Arctic onboard polar orbiting satellites, but their use remains limited due to the variable sea ice and snow emission. Here, we exploited nadir-viewing passive microwave observations (22–183 GHz) and collocated active cloud remote sensing data for diverse cloud and sea ice conditions captured with the *HALO* aircraft during the Arctic spring HALO–$(\mathcal{AC})^3$ campaign (Wendisch et al., 2024).

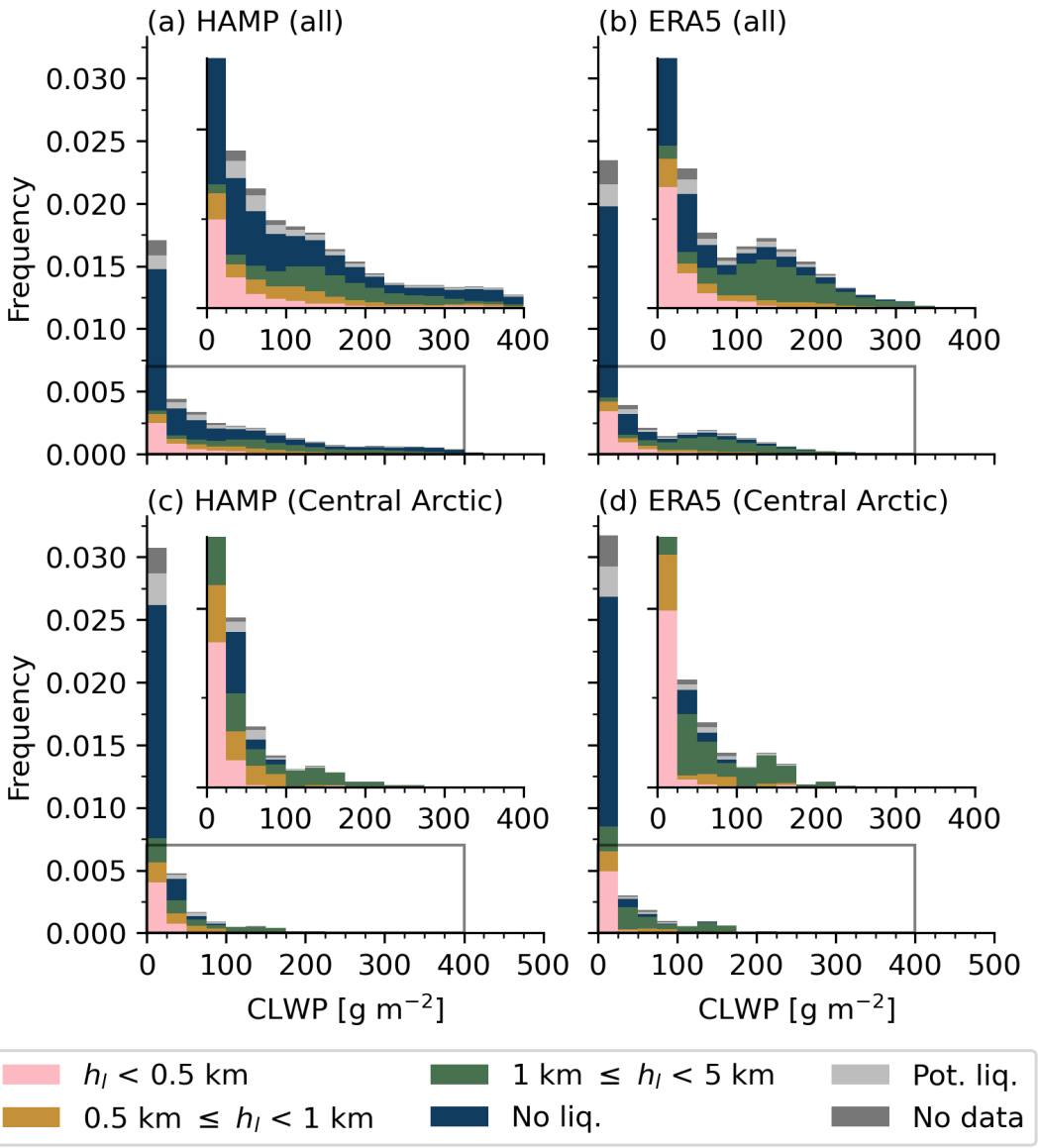

Figure 5.11: Cloud liquid water path histogram along the HALO flight track from (a, c) HAMP and (b, d) ERA5. (a, b) All observations and (c, d) observations in the Central Arctic. Shading classifies observations based on liquid top height (h_l), no liquid (No liq.), potential liquid (Pot. liq.), and missing lidar data. The inset region is denoted by the gray rectangle. Note that ERA5 is only shown for times where the HAMP retrieval converged.

We developed a physical sea ice–atmosphere optimal estimation retrieval algorithm with the loosely coupled SMRT (Picard et al., 2018) and PAMTRA (Mech et al., 2020) radiative transfer models for the HAMP microwave radiometer channels. The algorithm retrieves three snow layer parameters (wind slab correlation length, depth hoar correlation length, and wind slab thickness), the air–snow and snow–ice interface temperatures, and CLWP. The combination of this passive microwave retrieval with *HALO's* cloud observatory instrument suite, which is typically not available for passive microwave observations from satellites, provides a unique opportunity to (1) assess the representation of sea ice and snow microwave emission by the forward model, (2) estimate the CLWP detectability and retrieval accuracy, and (3) analyze the spatial variability of CLWP over sea ice during HALO–$(\mathcal{AC})^3$.

The optimal estimation retrieval found a geophysical state consistent with HAMP clear-sky observations identified by the collocated radar–lidar cloud mask with a convergence rate of 87 %. The T_b departure of the optimal solution strongly improved compared to the a priori, which assumed no spatial variability of the three snow properties. Moreover, the distributions of all snow parameters lie within the expected range.

The CLWP detectability was assessed from the clear-sky performance. We find a detectability threshold of $50\,\mathrm{g\,m^{-2}}$ in the Central Arctic, which increases towards the marginal ice zone up to $350\,\mathrm{g\,m^{-2}}$. The detectability near the marginal ice zone can be potentially improved with additional information on lead or young ice fraction. From SMRT–PAMTRA simulations, we found that a young ice fraction of 50 % causes a similar T_b signature as $150\,\mathrm{g\,m^{-2}}$ CLWP. The CLWP retrieval accuracy was derived from synthetic retrieval experiments. The relative root mean squared error of CLWP decreased from above 100 % for CLWP below $50\,\mathrm{g\,m^{-2}}$ to below 50 % above $100\,\mathrm{g\,m^{-2}}$. The identified bias for higher CLWP values can be explained by the parameter ambiguity between CLWP and wind slab correlation length.

The retrieval was applied to a stratocumulus case and a warm air intrusion case. While the CLWP of the stratocumulus case was mostly near the detectability threshold and not clearly matching with the liquid layer visible in the lidar observations, the higher CLWP of the warm air intrusion event aligned well with the lidar. The simultaneously derived surface parameters for the stratocumulus case follow realistic spatial gradients with increased snow correlation length and thus increased scattering from the ice edge toward the north pole. A statistical comparison of CLWP for all flights between HAMP and ERA5 found generally a similar CLWP shape and increasing CLWP for increasing liquid top height.

This work implies that SMRT could be useful in a coupled sea ice–atmosphere

data assimilation system using a priori data from a thermodynamic sea ice and snow evolution model. This approach would benefit from the high sensitivity of passive microwave observations to snow emissivity changes due to atmospheric processes, such as rain, snowfall, and near-surface air temperature. For example, the warm air intrusion in March 2022 and the associated surface melt and rain-on-snow event altered the emissivity within a few hours due to increased liquid water fraction within the snowpack, and the subsequent refreezing and potential ice lens formation altered the T_b signature for several weeks compared to conditions prior the warm air intrusion.

There are several limitations of this study, apart from the limited seasonal and spatial generalization of field observations. First, no independent quantitative reference observations of the state variables exist at scale, especially under cloudy conditions and regarding snow microstructure. The second limitation involves the simplified two-layer snowpack without fresh surface snow from accumulating snow or ice lenses from melt-freeze cycles, which both impact the emissivity at frequencies sensitive to CLWP (e.g., Sandells et al., 2024). The difficulty of simulating these scattering signatures with our two-layer snow setup might partly explain the non-convergence rate of 13 % under clear-sky conditions.

A way for future work to advance the use of passive microwave observations in the Arctic lies in exploiting the influence of atmospheric events on surface emission, such as rain-on-snow, and the integration of more observation geometries from microwave imagers and sounders. This would not only increase the temporal resolution, which is crucial during extreme events like warm air intrusions, but also ensure spectral, angular, and polarization consistency of the radiative transfer simulations. Especially the angular and polarization dependence over sea ice requires validation of SMRT, e.g., using ship observations (Rabe and Geibert, 2025; Rückert et al., 2025), and could provide additional information benefit for integrated sea ice–atmosphere retrievals.

Appendix

5.A Atmospheric profiles

The approach of fixed atmospheric temperature and specific humidity profiles differs from sea ice–atmosphere retrievals that derive temperature profiles (Kang et al., 2023) or integrated water vapor (IWV) (Rückert et al., 2023b) based on climatological mean a priori data. The collocated instantaneous ERA5 data provide accurate IWV when compared to dropsondes launched over sea ice with a root mean squared error (RMSE) of 0.25 $\mathrm{kg\,m^{-2}}$ and percentage RMSE (PRMSE)

of 9 %, without notable improvement for assimilated dropsondes. Similarly low RMSE between ERA5 and dropsondes over sea ice are found for profiles of temperature (0.5 K above 1 km height and up to 2 K below 1 km height) and relative humidity (10–15 %) (see Fig. 3 in Walbröl et al., 2024). To assess the impact of ERA5 IWV uncertainty at HAMP frequencies, we conduct a sensitivity test by increasing IWV by 10 %. This test results in maximum T_b changes of up to 2 K at 183±7.5 GHz for IWV ranges of 2 to 4 kg m^{-2} and 1.5 K at 118±8.5 GHz for IWV ranges of 8 to 13 kg m^{-2} (not shown). These relatively moderate sensitivities support our use of fixed atmospheric profiles.

5.B A priori interface temperatures

The snow–ice interface temperature (T_{si}) a priori is computed by a simple linear scaling between the air–snow interface temperature a priori (T_{as}) and the water temperature ($T_w = 271.35K$) with a manually determined scaling factor ($a = 0.25$), chosen from sensitivity tests, as

$$T_{si} = T_{as} + a \cdot (T_w - T_{as}). \tag{5.7}$$

The ERA5-based air–snow interface temperature a priori used in R2 is derived from ERA5 skin temperature ($T_{s,ERA5}$) with an empirical correction to remove biases with respect to the KT-19 skin temperature. We derive the following empirical relationship from clear-sky HALO–$(\mathcal{AC})^3$ data:

$$T_{as} = 0.94 \cdot T_{s,ERA5} + 11\,\mathrm{K}. \tag{5.8}$$

5.C Parameter ambiguities

In the following, we analyze parameter ambiguities between the six retrieved state parameters and the four fixed model parameters from synthetic retrievals. The ambiguities are quantified from correlations between the normalized residuals derived for the state parameters as

$$r_{x,i} = \frac{x_{op,i} - x_{true,i}}{\sqrt{S_{a,ii}}}, \tag{5.9}$$

with the retrieved state x_{op} and state used for the synthetic observation x_{true}. The same equation is adapted to the model parameters, which are fixed during

the retrieval, i.e,

$$r_{b,i} = \frac{b_i - b_{true,i}}{\sqrt{S_{b,ii}}}, \tag{5.10}$$

where b_{true} denotes the model parameter used for the synthetic observation. Correlations between two model parameters are neglected here as they are not directly relevant for the retrieval performance.

In total, 14 out of 39 parameter combinations show correlations larger than ±0.1, and five of the relationships include CLWP (Fig. 5.12). The highest correlation is found between CLWP and wind slab correlation length (0.67). This indicates that scattering in the wind slab layer partly compensates the spectral cloud emission signature and vice versa. This is consistent with similar Jacobians, which indicates that both parameters affect the simulated T_b in a similar way (not shown). Also, the posterior covariance matrix shows a high correlation of 0.8 between CLWP and wind slab correlation length. Negative correlations are found between CLWP and air–snow interface temperature (-0.21) and wind slab density (-0.18). Minor relationships occur between CLWP and the specularity parameter and snow–ice interface temperature. The lower correlation with these parameters can be related to the larger differences in the Jacobian matrix. Correlations between other parameters are also found, notably between depth hoar correlation length and depth hoar thickness (-0.63) and snow–ice interface temperature (0.51). Overall, the pronounced ambiguity between CLWP and wind slab correlation length suggests that HAMP observations can only partly separate both signals over sea ice from real observations.

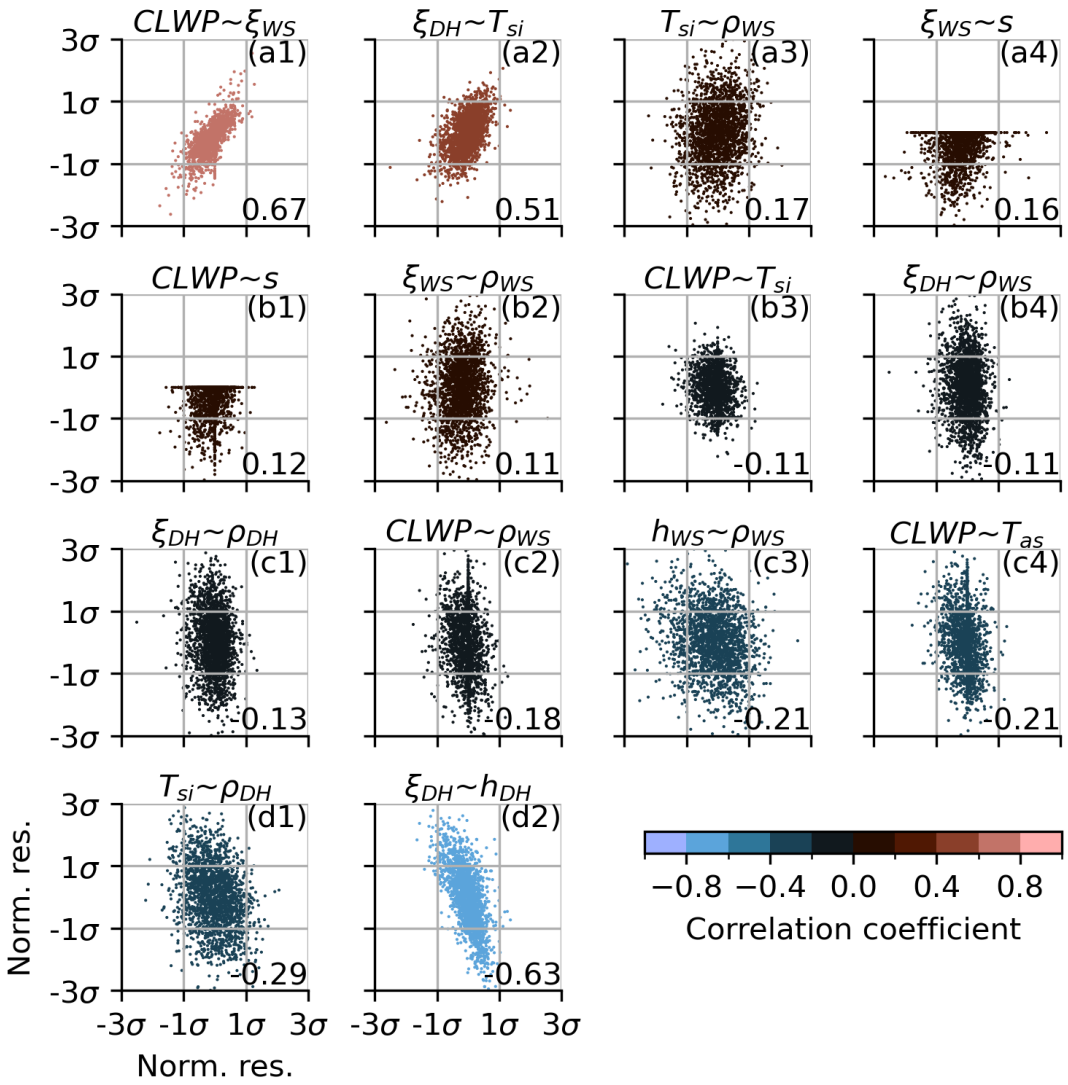

Figure 5.12: Correlations between normalized parameter residuals from the synthetic retrieval experiment. The parameter combinations are sorted from positive to negative correlations, and the first (second) parameter is shown on the horizontal (vertical) axis. Note that parameter combinations with correlations within ±0.1 are not shown and that no positive residuals occur for the specularity model parameter. Parameter names of each symbol are listed in Table 5.2.

Code and data availability

The code for this study is available on Zenodo at https://doi.org/10.5281/zenodo.15849617 (Risse, 2025b). The optimal estimation retrieval inputs and outputs are available on Zenodo at https://doi.org/10.5281/zenodo.15848709 (Risse, 2025a). The version of PAMTRA with an emissivity vector extension corresponds to commit fb71f43 (last access: 21 November 2024), pulled from https://github.com/nrisse/pamtra/commit/fb71f43 (Mech et al., 2020). The version of SMRT corresponds to commit 6f7dadc (last access: 29 October 2024), pulled from https://github.com/smrt-model/smrt/commit/6f7dadc (Picard et al., 2018). The version of pyOptimalEstimation corresponds to commit 1eb4f26 (last access: 22 November 2024), pulled from https://github.com/maahn/pyOptimalEstimation/commit/1eb4f26 (Maahn et al., 2020). HAMP measurements were obtained from https://doi.org/10.1594/PANGAEA.974108 (Dorff et al., 2024), and the updated version of the bias correction used here will be made available soon. WALES measurements were obtained from https://doi.org/10.1594/PANGAEA.967086 (Wirth and Groß, 2024). KT-19 measurements were obtained from https://doi.org/10.1594/PANGAEA.967378 (Schäfer et al., 2024). VELOX measurements were obtained from https://doi.org/10.1594/PANGAEA.963382 (Schäfer et al., 2023b). SpecMACS measurements were obtained from https://doi.org/10.1594/PANGAEA.966992 (Weber et al., 2024b). Dropsonde measurements were obtained from https://doi.pangaea.de/10.1594/PANGAEA.968900 (George et al., 2024). The VELOX surface classification data is currently accessible upon request and will be made publicly available on PANGAEA (Müller et al., 2025). Aircraft position and orientation were obtained from the "ac3airborne" intake catalog (Mech et al., 2022e). The sea ice concentration data from the University of Bremen were obtained from https://data.seaice.uni-bremen.de (last access: 30 April 2025, Spreen et al., 2008). The ERA5 reanalysis data on model levels were obtained from https://doi.org/10.24381/cds.143582cf (last access: 28 June 2025, Hersbach et al., 2017). The ERA5 reanalysis data on single levels were obtained from https://doi.org/10.24381/cds.adbb2d47 (last access: 28 June 2025, Hersbach et al., 2023). The Level 1C TB data for SSMIS on DMSP-F16 were obtained from https://doi.org/10.5067/GPM/SSMIS/F16/1C/07 (Berg, 2021b).

Author contributions

NR conducted the retrieval, data analysis, and visualization, and prepared the manuscript. SC, MM, CP, and NR conceptualized the study. SC, MM, and NR carried out the field observations. JM derived the VELOX surface classification

within the radiometer footprint. All authors reviewed and edited the manuscript.

Acknowledgements

We gratefully acknowledge the funding by the German Research Foundation [Deutsche Forschungsgemeinschaft (DFG)] of the Transregional Collaborative Research Center SFB/TRR 172 "Arctic Amplification: Climate Relevant Atmospheric and Surface Processes, and Feedback Mechanisms ($\mathcal{AC}$)^3" (Project-ID 268020496). The authors are grateful to the AWI for providing and operating the two Polar 5 and Polar 6 aircraft. We thank the crews and the technicians of the three research aircraft for excellent technical and logistical support. The generous funding of the flight hours for the Polar 5 and Polar 6 aircraft by AWI and for HALO by the DFG, Max-Planck-Institut für Meteorologie (MPI-M), and Deutsches Zentrum für Luft- und Raumfahrt (DLR) is greatly appreciated. We are further thankful for the funding provided by DFG within the framework of Priority Program (SPP 1294) to promote research with HALO (grant no. 316646266). We would like to thank Ghislain Picard for his support on the SMRT simulation setup. Furthermore, we acknowledge the freely available Python packages, including but not limited to numpy (Harris et al., 2020), pandas (McKinney, 2010), xarray (Hoyer and Hamman, 2017), and scipy (Virtanen et al., 2020) for data analysis, and matplotlib (Hunter, 2007), seaborn (Waskom, 2021), and cartopy (UK Met Office, 2023) for visualization. We sincerely appreciate Fabio Crameri for providing scientific colormaps via an open repository, enhancing the visual quality of this work (Crameri, 2018). We acknowledge the use of large language models by OpenAI via GitHub Copilot for code generation assistance during the development of the retrieval and analysis.

Chapter 6

Conclusions and outlook

6.1 Conclusions

Passive microwave observations in the Arctic capture physical properties of both the sea ice and clouds, which are essential components of the Arctic climate system. This dissertation aims to improve the use of high-frequency passive microwave observations from polar-orbiting satellites over sea ice. Unique airborne and ship-based observations were analyzed from the ACLOUD, AFLUX, HALO–$(\mathcal{AC})^3$, and VAMPIRE campaigns. The field observations provided insights into the spatial variability of sea ice emissivity at high frequencies within satellite footprints (Chapter 3). Parts of these sea ice emissivity variations could be attributed to atmospheric processes (Chapter 4). The observations were also compared with sea ice and snow radiative transfer simulations during new ice formation and snow accumulation. The radiative transfer model is inverted in a newly developed sea ice–atmosphere optimal estimation retrieval, which allows for cloud liquid water path estimation over sea ice from airborne observations (Chapter 5). To assess the retrieval capabilities, extensive evaluation is performed with reference data from collocated cloud radar and lidar instruments. To address the objectives of this work, four research questions were formulated. The contributions of the three studies are summarized below.

RQ1: How does sea ice emissivity vary spatially within satellite footprints, and how is this reflected in the spectral variability at the satellite scale toward submillimeter wavelengths?

The sea ice emissivity is highly variable on small spatial scales that are typically averaged out at the satellite scale. The spatial variability of the sea ice emissivity

within satellite footprints was quantified from *Polar 5* observations during the ACLOUD and AFLUX field campaigns up to 340 GHz (Chapter 3). The spectral emissivity variability at satellite scale toward submillimeter wavelengths was quantified by resampling the airborne observations to the footprints of current satellite sensors.

The field observations spatially resolve the surface emissivity with a footprint size of about 100 m. The change in emissivity variability with increasing footprint size up to 20 km was estimated. As expected, a reduction of the emissivity variability occurs with increasing footprint size. The reduction is larger during the AFLUX campaign than during the ACLOUD campaign, due to the melting conditions during ACLOUD. During AFLUX, the 340 GHz emissivity variability across all flights decreases by about half from the hectometer resolution of the aircraft to a typical satellite footprint with a diameter of 16 km. A relevant small-scale feature is the newly formed sea ice in leads between larger ice floes. This newly formed sea ice has a higher emissivity than the adjacent older sea ice, likely due to the absence of scattering from snow on the sea ice. The results further showed that AMSR2 is able to resolve more small-scale features at 5 km footprint size at 89 GHz.

The collocation of MiRAC observations with MHS, ATMS, SSMIS, and AMSR2 provides insights into the spectral emissivity variability that can be expected above 200 GHz from satellites. Differences are found between the spectral variability from ACLOUD and AFLUX, with an emissivity reduction during AFLUX from 183 to 243 GHz and constant emissivity during ACLOUD. From the airborne observations, a similar co-variability occurs at 183, 243, and 340 GHz with a small spectral emissivity gradient from 89 to 340 GHz. In general, the spatial and temporal variability might be larger than the spectral differences in this frequency range at satellite scales.

RQ2: Which atmospheric processes influence sea ice emissivity toward high frequencies?

Atmospheric processes influence the sea ice emissivity at high frequencies through precipitation and the melt–freeze cycle. The field observations analyzed in Chapter 4 quantify the effects of the surface freeze onset, snow accumulation, and new ice formation. The retrieval in Chapter 5 captured the sea ice emissivity change after a rain-on-snow that occurred during a warm air intrusion in March 2022.

The impact of snowfall on the emissivity could be quantified from the quasi-continuous statistical observations during the VAMPIRE expedition onboard R/V *Polarstern* before and after surface freeze onset. The newly accumulated

snow reduces the emissivity at the high frequencies to an almost constant level over multiyear ice. The continuous formation of new ice with varying snow thickness provided evidence that snow accumulation causes the emissivity reduction of young ice from about 0.95 to 0.6 at high frequencies. The signature of snowfall is only visible at 183 and 243 GHz and not at lower frequencies (22 to 51 GHz). A machine learning regression model that predicts the microwave emissivity at 243 GHz from visual images confirmed the role of snow formations. The model could predict the emissivity with a root mean squared error of 0.11 and a correlation to the observation of 0.67.

The findings from VAMPIRE also match emissivity spectra observed in spring 2019 during AFLUX at nadir from 89 to 340 GHz (Chapter 3). However, not enough samples were collected to establish the role of snow cover in the evolution from nilas with a high emissivity from 89 to 340 GHz to young ice with a high emissivity at 89 GHz and low emissivity at high frequencies. The observed emissivity variability at high frequencies over snow-covered sea ice is high and attributed to snow correlation length and density variations based on Snow Microwave Radiative Transfer (SMRT; Picard et al., 2018) simulations. The influence of snow thickness saturates once snow thickness exceeds a few centimeters at 243 GHz. Another impact of the snow accumulation on the microwave signature of bare ice at high frequencies is a potential change in surface reflection type from specular to more diffuse reflection.

The impact of a rain-on-snow event in March 2022 during a warm air intrusion on the sea ice emissivity before and after the event was studied. Before the event, satellite observations show rather homogeneous conditions in the Fram Strait and toward the Central Arctic. During the rain event, the brightness temperature reached high values at all frequencies, likely due to the increased liquid water content in the snowpack (e.g., Stroeve et al., 2022). Refreezing after the rain-on-snow event likely led to the formation of an ice lens in the snow pack, which reduced the emissivity for several weeks compared to conditions before the event. The impact was seen from 22 to 183 GHz with a sharp transition to regions that were likely unaffected by the rain or surface melt conditions (see Fig. 5.10).

New ice formation can also be viewed as a link between the atmosphere and the surface once air temperatures reach sub-freezing. The VAMPIRE observations provided detailed insights into the relation of the emissivity at low and high frequencies for newly forming sea ice. The emissivity changes almost linearly between the open water and nilas signature and with a high correlation from 22 to 243 GHz. This likely relates to salinity variations and the low penetration depth over saline ice.

RQ3: How representative are sea ice and snow radiative transfer simulations at high frequencies?

Simulations with the SMRT model for various snow and sea ice properties indicate a good agreement with observations. The statistical comparison in Chapter 4 for VAMPIRE observations showed that both bare and snow-covered young sea ice could be simulated by SMRT up to 243 GHz. Additionally, the implementation of SMRT in the forward operator in Chapter 5 shows consistency with observations during HALO–$(\mathcal{AC})^3$ at 118 and 183 GHz.

To provide an SMRT evaluation that accounts for the natural variability of sea ice and snow parameters, we chose a Monte-Carlo approach, where all parameters are varied uniformly within a realistic range. We compare the simulated and observed variability and assess the overlap with observations in the emissivity space. The statistical comparison of the spectral, angular, and polarization variability between observations and simulations indicates a good agreement from 183 to 243 GHz. However, in order to match simulations and observations at low frequencies, it was required to account for the surface reflection type and penetration depth during the emissivity calculation from observations. At high frequencies, the skin temperature from thermal infrared observations was used directly due to their lower penetration depth. While Wivell et al. (2023) could show that SMRT simulations agree well with in situ observations over tundra snow, the VAMPIRE observations showed for the first time that SMRT also produces realistic emissivity spectra at high frequencies over newly formed bare and snow-covered sea ice.

The representativeness of SMRT from 22 to 183 GHz can also be assessed from the sea ice–atmosphere retrieval applied to HAMP observations during HALO–$(\mathcal{AC})^3$ under clear-sky conditions. A consistent geophysical state was found by adjusting the parameters of a two-layer snowpack, i.e., wind slab correlation length, depth hoar correlation length, and wind slab thickness, within the expected variability. About 90 % of observations converged for the clear-sky retrieval (R1), and the difference between observation and simulation at 118 and 183 GHz improved from the a priori to the optimal solution. Residuals can be explained by parameters that were not adjusted, such as snow density and depth hoar thickness. Moreover, several surfaces cannot be represented by a simple two-layer snowpack on multiyear ice, such as potential ice lens formation after the rain-on-snow event at the beginning of the campaign and snow-covered young sea ice. In general, the clear-sky retrievals showed that SMRT provides realistic emissivity at high frequencies over larger areas in the Fram Strait and Central Arctic during most conditions.

RQ4: How accurately can we retrieve cloud liquid water path from passive microwave observations over sea ice?

The cloud liquid water path detectability and retrieval accuracy are quantified in Chapter 5 using the sea ice–atmosphere optimal estimation retrieval applied to HAMP observations during HALO–$(\mathcal{AC})^3$. The cloud liquid water path detectability is estimated under clear-sky conditions, and the retrieval accuracy is determined using synthetic retrieval experiments.

The HAMP observations during HALO–$(\mathcal{AC})^3$ allow for cloud liquid water path retrieval evaluation with ancillary airborne observations, which provide collocated information on hydrometeor occurrence and liquid layers down to 100 m above the surface. First, the a priori snow parameters are adjusted to match the observations under clear-sky conditions. Then, the cloud liquid water path and air–snow interface parameters are added to the state vector. From clear-sky observations, the cloud liquid water path detectability, defined as the 95th percentile of retrieved cloud liquid water path (CLWP) under clear-sky conditions, is estimated. It was found to increase from the Central Arctic ($50\,\mathrm{g\,m^{-2}}$) to the marginal ice zone ($350\,\mathrm{g\,m^{-2}}$). The main reason for the false detection of CLWP is young sea ice in leads, which occur more frequently near the ice edge. The spectral signature of a high emissivity at high frequencies is similar to the CLWP signature. To estimate the retrieval accuracy in the absence of a CLWP ground truth, synthetic retrieval experiments were performed based on forward simulations of a known CLWP. Generally, the accuracy increases with increasing CLWP, with a relative root mean squared error below 50 % for CLWP above $100\,\mathrm{g\,m^{-2}}$. This highlights the challenge of detecting clouds with a low CLWP. Despite the limitations, the application to a stratocumulus and warm air intrusion case demonstrates the qualitative agreement with liquid layers detected by the lidar. Moreover, the CLWP distribution from HAMP agrees with ERA5 along the flight track and shows the expected trend of higher CLWP for higher liquid layer top heights.

Several factors limit the performance of the CLWP derived from the sea ice–atmosphere retrieval. First, the a priori assumptions on the sea ice and snow can differ largely from the actual conditions due to atmospheric events, as found for the warm air intrusion case. Second, retrievals under conditions with rain-on-snow events that add liquid water into the snowpack or a high young ice fraction mask any additional CLWP emission. Third, there is an ambiguous signal of scattering in the uppermost snow layer (wind slab) and CLWP emission at 90 and 118 GHz as found from synthetic retrieval experiments. Frequencies from 22 to 50 GHz, which are less sensitive to CLWP, are also less sensitive to the

scattering signal of the wind slab snow layer.

6.2 Outlook

6.2.1 Future field campaigns

The planned field campaign Clouds over Complex Environment (COMPEX) in spring 2026 will further expand the sampling of clouds and sea ice from the ACLOUD and AFLUX campaigns. With new high-frequency satellite missions in polar orbit, such as the Arctic Weather Satellite (AWS) and EPS-SG Microwave Sounder (MWS), satellite observations can be related to the high-resolution airborne observations at 243 and 340 GHz. In spring, AWS will receive a significant surface contribution at 325 GHz. This allows for further study of the impact of small-scale sea ice emissivity variation on the satellite footprint and how it varies during the campaign. Also, potential scattering by ice clouds above the aircraft could be studied, using the known surface contributions below the cloud measured by the aircraft. This could help evaluate the AWS products over sea ice depending on the underlying surface conditions.

Microwave radiometers for continuously scanning sky and surface radiation during the R/V *Polarstern* expeditions PS131 (WALSEMA; Rückert et al., 2025) and PS144 (VAMPIRE; Chapter 4) proved successful for understanding the emission signature of sea ice and snow and for evaluating radiative transfer simulations with SMRT. Recently, similar measurements were performed during the R/V *Polarstern* expedition PS149 from July to September 2025 (VAMPIRE 2; Nicolaus, 2025). These observations can provide further insights into the microwave signature of melting sea ice and the effects of surface refreezing, similar to the observations during WALSEMA and VAMPIRE. This design could be continued in upcoming expeditions as it combines the need for high-quality observations of the atmospheric thermodynamic profiles, integrated water vapor, and clouds (Walbröl et al., 2022) and surface microwave emission to improve the long-term characterization of sea ice and the atmosphere from satellites. Moreover, in situ sampling over diverse sea ice types within the radiometer footprint can be used for validation of radiative transfer models. The setup requires low maintenance, suitable for long-term and recurring monitoring.

6.2.2 Statistical emissivity modeling

Physical sea ice and snow radiative transfer models require detailed inputs on the sea ice and snow from climatology, field observations, or numerical models, which are difficult to obtain globally at high quality. Moreover, in order to solve the

radiative transfer, several assumptions are needed, such as horizontal homogeneity, scattering, and dielectric mixing, which might lead to deviations from the radiative signature in observations. Therefore, emissivity models based on neural networks provide a promising opportunity for emissivity estimation by replacing (parts of) the physical radiative transfer model. While field observations are generally not suitable for the development of robust statistical models applicable on global scales, they provide valuable independent data on the emissivity for a given time and location for the evaluation of large-scale satellite-based emissivity models.

Additionally, emissivity models based on neural networks can be used to systematically learn from large amounts of field data with the goal of better understanding the observed emissivity variability. This was demonstrated for collocated visual camera and passive microwave observations at 243 GHz using R/V *Polarstern* VAMPIRE observations (Chapter 4). The approach could be extended to all expeditions (PS131, PS144, and PS149) and observed sea ice and snow conditions, rather than only bare and snow-covered nilas after surface freeze onset. A suitable method is the extraction of low-dimensional feature vectors or clusters from the images using self-supervision (Caron et al., 2021) to compress the sea ice and snow structures of the image. Such frameworks are established in various applications for unlabeled data, such as sky camera (Fabel et al., 2022) and satellite images (Chatterjee et al., 2024). In a first step, it can be tested whether the resulting feature vectors or clusters explain the observed microwave emissivity variability, similar to the regression approach used here, by replacing the CNN with the feature vector or cluster. Furthermore, physical radiative transfer models can be applied to reproduce the observed microwave signature for certain clusters of images based on assumptions about the sea ice and snow properties. This can provide statistically robust insights into the importance of small-scale surface features captured by the camera, such as ridges, refrozen melt ponds, and snow formations, on the observed spectral, angular, and polarization dependence.

6.2.3 Physical retrieval extensions

The physical retrieval could be extended by including frozen water path and integrated water vapor into the state vector, and refining specular contributions and polarization signals for inclined observations. These changes would allow an application to high-frequency channels up to 340 GHz and inclined 89 GHz observations available during field campaigns (ACLOUD, AFLUX, and COMPEX). The inclusion of frozen hydrometeors can be evaluated using collocated cloud radar and lidar observations. This can provide insights into the added informa-

tion from submillimeter channels similar to those onboard AWS and ICI over sea ice. Potential challenges are the positioning of liquid layers within the cloud, which could mask the scattering signal (Camplani et al., 2024b). Accounting for variations in integrated water vapor, e.g., by scaling the background humidity profile, might be necessary at 340 GHz and when using more water vapor channels. An improvement in lower tropospheric humidity retrieval might be expected from additional channels in the 243 GHz window and along the 325 GHz water vapor absorption line compared to observations up to 183 GHz. The 243 GHz channel provides information on the emissivity at the neighboring sounding channels as observed during VAMPIRE and AFLUX that could be used for the water vapor retrieval. This additional information could be tested using *Polar 5* observations over sea ice and using dropsondes as reference data. An application to field campaigns up to 340 GHz under clear-sky conditions could further allow refinement of the snow layers near the surface defined in SMRT to match the diverse emissivity spectra observed during AFLUX and VAMPIRE. For example, a third snow layer might be needed to better capture spectral gradients (Wivell et al., 2023). Also, it could be tested if bare ice and snow-covered young ice area fractions should be retrieved for *Polar 5* observations near the marginal ice zone to capture mixtures of the three emissivity branches observed during VAMPIRE. Simulating off-nadir observations (VAMPIRE, MiRAC-A) requires a refined treatment of specular contributions from the surface at high frequencies in PAMTRA to simulate the observed polarization signals and angular dependence. Reproducing the signal measured during VAMPIRE accurately could also improve cloud liquid water path retrievals from space by additionally observing the absorption of polarized and emission of unpolarized radiation of liquid cloud droplets, and polarization signal of frozen hydrometeors (Xie et al., 2015). As the suggested extensions might increase CLWP detectability and retrieval accuracy, the retrieval could be used for evaluating ERA5 and high-resolution ICON simulations over sea ice (Schemann and Ebell, 2020) as shown in Mech et al. (2019) over open ocean. A general drawback of the physical approach is the rather slow radiative transfer simulation, which could be solved by generating a retrieval database from forward simulations and a statistical inversion, or replacing SMRT with a machine learning emulator that retains physical consistency.

6.2.4 Retrieval application to satellites

Application to satellites helps to understand the long-term trends and spatiotemporal consistency of surface and atmospheric parameters. The sea ice state could be derived from observations with different frequencies, incidence angles, and

polarizations. Also, findings from the VAMPIRE expedition that highlight the importance of snow accumulation on newly formed sea ice could be studied further with pan-Arctic satellite observations. Inclusion of both cross-track and conical scanners could be tested. Validation with visual, thermal infrared, and cloud radar and lidar observations (EarthCARE) could be performed for collocated footprints. Also, the microwave radiometer, atmospheric sounding, and cloud radar observations from field observations can be used for satellite retrieval evaluation. Another promising extension is the addition of surface backscatter, which is measured by WIVERN (Illingworth et al., 2018) together with the cloud radar and passive radiometer signal. This could potentially improve both the characterization of sea ice and snow, as well as cloud liquid water path, compared to solely passive observations. So far, limited information is available on the relation between the surface backscatter and surface emissivity in W-band that could allow improved use of the radiometer signal. Also, the representation of small-scale variability from satellites will improve with the CIMR mission from 1.4 to 36 GHz, with potential benefit at higher frequencies through high-resolution sea ice concentration, type, and thickness estimates.

6.2.5 Coupled data assimilation

Coupled Earth system models simulate the thermodynamic and dynamic interactions between the ocean, cryosphere, and atmosphere, and predict their spatiotemporal evolution. In a 1-dimensional standalone retrieval as applied in Chapter 5, the temporal and spatial consistency is unconstrained, which imposes an inherent limitation of the retrieval. Coupled data assimilation uses the coupled model trajectory as background information for the assimilation of observations (De Rosnay et al., 2022). The coupled model should capture the long-term evolution of snowpacks, such as snow accumulation, layering, sea ice growth, and metamorphism due to water vapor gradients. Additionally, fast processes need to be captured, such as snow and sea ice temperature profile changes, increases of liquid water content during rain-on-snow events, refreezing, and lead formation. This physical information can be simulated with a coupled forward operator, such as SMRT and PAMTRA used in this thesis. In this work, it could be shown that such coupled forward operators are generally suitable for the application in data assimilation of passive microwave observations at high frequencies by employing simple static a priori information. Further work is needed to represent the physical interactions between the sea ice and snow and atmospheric processes in numerical models to capture the highly diverse microwave emissivity signatures of Arctic sea ice. Moreover, sensor synergies between thermal infrared, passive mi-

crowave, and conventional systems can be fully exploited during the assimilation process. Field observations, such as those collected during the $(\mathcal{AC})^3$ project, will play a key role in defining the needs for such an advanced coupled data assimilation system in polar regions to further advance the assimilation of low-peaking microwave sounding and window channels and improve the long-term monitoring of polar regions.

Bibliography

Aires, F., Paul, M., Prigent, C., Rommen, B., and Bouvet, M.: Measure and exploitation of multisensor and multiwavelength synergy for remote sensing: 2. Application to the retrieval of atmospheric temperature and water vapor from MetOp, Journal of Geophysical Research, 116, D02 302, doi:10.1029/2010JD014702, 2011.

Albers, R., Emrich, A., and Murk, A.: Antenna Design for the Arctic Weather Satellite Microwave Sounder, IEEE Open Journal of Antennas and Propagation, 4, 686–694, doi:10.1109/OJAP.2023.3295390, 2023.

Arduini, G., Balsamo, G., Dutra, E., Day, J. J., Sandu, I., Boussetta, S., and Haiden, T.: Impact of a Multi-Layer Snow Scheme on Near-Surface Weather Forecasts, Journal of Advances in Modeling Earth Systems, 11, 4687–4710, doi:10.1029/2019MS001725, 2019.

Balsamo, G., Beljaars, A., Scipal, K., Viterbo, P., Van Den Hurk, B., Hirschi, M., and Betts, A. K.: A Revised Hydrology for the ECMWF Model: Verification from Field Site to Terrestrial Water Storage and Impact in the Integrated Forecast System, Journal of Hydrometeorology, 10, 623–643, doi:10.1175/2008JHM1068.1, 2009.

Balsamo, G., Albergel, C., Beljaars, A., Boussetta, S., Brun, E., Cloke, H., Dee, D., Dutra, E., Muñoz-Sabater, J., Pappenberger, F., De Rosnay, P., Stockdale, T., and Vitart, F.: ERA-Interim/Land: a global land surface reanalysis data set, Hydrology and Earth System Sciences, 19, 389–407, doi:10.5194/hess-19-389-2015, 2015.

Barre, H. M. J. P., Duesmann, B., and Kerr, Y. H.: SMOS: The Mission and the System, IEEE Transactions on Geoscience and Remote Sensing, 46, 587–593, doi:10.1109/TGRS.2008.916264, 2008.

Bartsch, A., Bergstedt, H., Pointner, G., Muri, X., Rautiainen, K., Leppänen, L., Joly, K., Sokolov, A., Orekhov, P., Ehrich, D., and Soininen, E. M.: Towards

long-term records of rain-on-snow events across the Arctic from satellite data, The Cryosphere, 17, 889–915, doi:10.5194/tc-17-889-2023, 2023.

Bauer, P. and Mugnai, A.: Precipitation profile retrievals using temperature-sounding microwave observations, Journal of Geophysical Research: Atmospheres, 108, 2003JD003 572, doi:10.1029/2003JD003572, 2003.

Bauer, P., Moreau, E., and Di Michele, S.: Hydrometeor Retrieval Accuracy Using Microwave Window and Sounding Channel Observations, Journal of Applied Meteorology, 44, 1016–1032, doi:10.1175/JAM2257.1, 2005.

Bauer, P., Thorpe, A., and Brunet, G.: The quiet revolution of numerical weather prediction, Nature, 525, 47–55, doi:10.1038/nature14956, 2015.

Becker, S., Ehrlich, A., and Wendisch, M.: Meteorological measurements by dropsondes released from POLAR 5 during SORPIC 2010, doi:10.1594/PANGAEA.922004, type: data set, 2020.

Bengtsson, L.: The global atmospheric water cycle, Environmental Research Letters, 5, 025 202, doi:10.1088/1748-9326/5/2/025202, 2010.

Bennartz, R. and Bauer, P.: Sensitivity of microwave radiances at 85–183 GHz to precipitating ice particles, Radio Science, 38, 2002RS002 626, doi:10.1029/2002RS002626, 2003.

Bennartz, R., Shupe, M. D., Turner, D. D., Walden, V. P., Steffen, K., Cox, C. J., Kulie, M. S., Miller, N. B., and Pettersen, C.: July 2012 Greenland melt extent enhanced by low-level liquid clouds, Nature, 496, 83–86, doi:10.1038/nature12002, 2013.

Berg, W.: GPM SSMIS on F18 Common Calibrated Brightness Temperatures L1C 1.5 hours 12 km V07, https://doi.org/10.5067/GPM/SSMIS/F18/1C/07, 2021a.

Berg, W.: GPM SSMIS on F16 Common Calibrated Brightness Temperatures L1C 1.5 hours 12 km V07, https://doi.org/10.5067/GPM/SSMIS/F16/1C/07, 2021b.

Berg, W.: GPM SSMIS on F17 Common Calibrated Brightness Temperatures L1C 1.5 hours 12 km V07, https://doi.org/10.5067/GPM/SSMIS/F17/1C/07, 2021c.

Berg, W.: GPM MHS on NOAA-19 Common Calibrated Brightness Temperatures L1C 1.5 hours 17 km V07, https://doi.org/10.5067/GPM/MHS/NOAA19/1C/07, 2022a.

Berg, W.: GPM AMSR-2 on GCOM-W1 Common Calibrated Brightness Temperature L1C 1.5 hours 10 km V07, https://doi.org/10.5067/GPM/AMSR2/GCOMW1/1C/07, 2022b.

Berg, W.: GPM MHS on METOP-B Common Calibrated Brightness Temperature L1C 1.5 hours 17 km V07, https://doi.org/10.5067/GPM/MHS/METOPB/1C/07, 2022c.

Berg, W.: GPM ATMS on NOAA-20 Common Calibrated Brightness Temperatures L1C 1.5 hours 17 km V07, https://doi.org/10.5067/GPM/ATMS/NOAA20/1C/07, 2022d.

Berg, W.: GPM ATMS on SUOMI-NPP Common Calibrated Brightness Temperature L1C 1.5 hours 16 km V07, https://doi.org/10.5067/GPM/ATMS/NPP/1C/07, 2022e.

Berg, W.: GPM MHS on METOP-A Common Calibrated Brightness Temperature L1C 1.5 hours 17 km V07, https://doi.org/10.5067/GPM/MHS/METOPA/1C/07, 2022f.

Berg, W.: GPM MHS on METOP-C Common Calibrated Brightness Temperature L1C 1.5 hours 17 km V07, https://doi.org/10.5067/GPM/MHS/METOPC/1C/07, 2022g.

Berg, W.: GPM MHS on NOAA-18 Common Calibrated Brightness Temperature L1C 1.5 hours 17 km V07, https://doi.org/10.5067/GPM/MHS/NOAA18/1C/07, 2022h.

Berg, W., Bilanow, S., Chen, R., Datta, S., Draper, D., Ebrahimi, H., Farrar, S., Jones, W. L., Kroodsma, R., McKague, D., Payne, V., Wang, J., Wilheit, T., and Yang, J. X.: Intercalibration of the GPM Microwave Radiometer Constellation, Journal of Atmospheric and Oceanic Technology, 33, 2639–2654, doi:10.1175/JTECH-D-16-0100.1, 2016.

Blackwell, W. J.: New Measurements of Cloud Ice and Snow at 205 Ghz from the Nasa Tropics Pathfinder Mission, in: IGARSS 2022 - 2022 IEEE International Geoscience and Remote Sensing Symposium, pp. 5260–5261, IEEE, Kuala Lumpur, Malaysia, ISBN 978-1-6654-2792-0, doi:10.1109/IGARSS46834.2022.9883989, 2022.

Bliss, A., Miller, J., and Meier, W.: Comparison of Passive Microwave-Derived Early Melt Onset Records on Arctic Sea Ice, Remote Sensing, 9, 199, doi:10.3390/rs9030199, 2017.

Bormann, N.: Accounting for Lambertian reflection in the assimilation of microwave sounding radiances over snow and sea-ice, Quarterly Journal of the Royal Meteorological Society, 148, 2796–2813, doi:10.1002/qj.4337, 2022.

Boukabara, S.-A., Garrett, K., Chen, W., Iturbide-Sanchez, F., Grassotti, C., Kongoli, C., Chen, R., Liu, Q., Yan, B., Weng, F., Ferraro, R., Kleespies, T. J., and Meng, H.: MiRS: An All-Weather 1DVAR Satellite Data Assimilation and Retrieval System, IEEE Transactions on Geoscience and Remote Sensing, 49, 3249–3272, doi:10.1109/TGRS.2011.2158438, 2011.

Boukabara, S.-A., Garrett, K., and Grassotti, C.: Dynamic Inversion of Global Surface Microwave Emissivity Using a 1DVAR Approach, Remote Sensing, 10, 679, doi:10.3390/rs10050679, 2018.

Brath, M., Fox, S., Eriksson, P., Harlow, R. C., Burgdorf, M., and Buehler, S. A.: Retrieval of an ice water path over the ocean from ISMAR and MARSS millimeter and submillimeter brightness temperatures, Atmospheric Measurement Techniques, 11, 611–632, doi:10.5194/amt-11-611-2018, 2018.

Browne, P. A., De Rosnay, P., Zuo, H., Bennett, A., and Dawson, A.: Weakly Coupled Ocean–Atmosphere Data Assimilation in the ECMWF NWP System, Remote Sensing, 11, 234, doi:10.3390/rs11030234, 2019.

Buehler, S. A., Jiménez, C., Evans, K. F., Eriksson, P., Rydberg, B., Heymsfield, A. J., Stubenrauch, C. J., Lohmann, U., Emde, C., John, V. O., Sreerekha, T. R., and Davis, C. P.: A concept for a satellite mission to measure cloud ice water path, ice particle size, and cloud altitude, Quarterly Journal of the Royal Meteorological Society, 133, 109–128, doi:10.1002/qj.143, 2007.

Buehler, S. A., Defer, E., Evans, F., Eliasson, S., Mendrok, J., Eriksson, P., Lee, C., Jiménez, C., Prigent, C., Crewell, S., Kasai, Y., Bennartz, R., and Gasiewski, A. J.: Observing ice clouds in the submillimeter spectral range: the CloudIce mission proposal for ESA's Earth Explorer 8, Atmospheric Measurement Techniques, 5, 1529–1549, doi:10.5194/amt-5-1529-2012, 2012.

Burgard, C., Notz, D., Pedersen, L. T., and Tonboe, R. T.: The Arctic Ocean Observation Operator for 6.9 GHz (ARC3O) – Part 1: How to obtain sea ice brightness temperatures at 6.9 GHz from climate model output, The Cryosphere, 14, 2369–2386, doi:10.5194/tc-14-2369-2020, 2020a.

Burgard, C., Notz, D., Pedersen, L. T., and Tonboe, R. T.: The Arctic Ocean Observation Operator for 6.9 GHz (ARC3O) – Part 2: Development and evaluation, The Cryosphere, 14, 2387–2407, doi:10.5194/tc-14-2387-2020, 2020b.

Calinski, T. and Harabasz, J.: A dendrite method for cluster analysis, Communications in Statistics - Theory and Methods, 3, 1–27, doi:10.1080/03610927408827101, 1974.

Camplani, A., Casella, D., Sanò, P., and Panegrossi, G.: The Passive microwave Empirical cold Surface Classification Algorithm (PESCA): application to GMI and ATMS, Journal of Hydrometeorology, doi:10.1175/JHM-D-20-0260.1, 2021.

Camplani, A., Casella, D., Sanò, P., and Panegrossi, G.: The High lAtitude sNowfall Detection and Estimation aLgorithm for ATMS (HANDEL-ATMS): a new algorithm for snowfall retrieval at high latitudes, Atmospheric Measurement Techniques, 17, 2195–2217, doi:10.5194/amt-17-2195-2024, 2024a.

Camplani, A., Sanò, P., Casella, D., Panegrossi, G., and Battaglia, A.: Arctic Weather Satellite Sensitivity to Supercooled Liquid Water in Snowfall Conditions, Remote Sensing, 16, 4164, doi:10.3390/rs16224164, 2024b.

Caron, M., Touvron, H., Misra, I., Jégou, H., Mairal, J., Bojanowski, P., and Joulin, A.: Emerging Properties in Self-Supervised Vision Transformers, http://arxiv.org/abs/2104.14294, arXiv:2104.14294 [cs], 2021.

Cavalieri, D. J.: A microwave technique for mapping thin sea ice, Journal of Geophysical Research: Oceans, 99, 12 561–12 572, doi:10.1029/94JC00707, 1994.

Cesana, G., Kay, J. E., Chepfer, H., English, J. M., and De Boer, G.: Ubiquitous low-level liquid-containing Arctic clouds: New observations and climate model constraints from CALIPSO-GOCCP, Geophysical Research Letters, 39, 2012GL053 385, doi:10.1029/2012GL053385, 2012.

Chatterjee, D., Acquistapace, C., Deneke, H., and Crewell, S.: Understanding cloud systems structure and organization using a machine's self-learning approach, Artificial Intelligence for the Earth Systems, doi:10.1175/AIES-D-22-0096.1, 2023.

Chatterjee, D., Schnitt, S., Bigalke, P., Acquistapace, C., and Crewell, S.: Capturing the Diversity of Mesoscale Trade Wind Cumuli Using Complementary Approaches From Self-Supervised Deep Learning, Geophysical Research Letters, 51, e2024GL108 889, doi:10.1029/2024GL108889, 2024.

Chylek, P., Folland, C., Klett, J. D., Wang, M., Hengartner, N., Lesins, G., and Dubey, M. K.: Annual Mean Arctic Amplification 1970–2020: Observed and Simulated by CMIP6 Climate Models, Geophysical Research Letters, 49, e2022GL099 371, doi:10.1029/2022GL099371, 2022.

Comiso, J.: Bootstrap Sea Ice Concentrations from Nimbus-7 SMMR and DMSP SSM/I-SSMIS, Version 3, doi:10.5067/7Q8HCCWS4I0R, 2017.

Comiso, J., Cavalieri, D., and Markus, T.: Sea ice concentration, ice temperature, and snow depth using AMSR-E data, IEEE Transactions on Geoscience and Remote Sensing, 41, 243–252, doi:10.1109/TGRS.2002.808317, 2003.

Comiso, J. C.: Sea ice effective microwave emissivities from satellite passive microwave and infrared observations, Journal of Geophysical Research, 88, 7686–7704, doi:10.1029/JC088iC12p07686, 1983.

Comiso, J. C.: Characteristics of Arctic winter sea ice from satellite multispectral microwave observations, Journal of Geophysical Research, 91, 975, doi:10.1029/JC091iC01p00975, 1986.

Comiso, J. C. and Hall, D. K.: Climate trends in the Arctic as observed from space, WIREs Climate Change, 5, 389–409, doi:10.1002/wcc.277, 2014.

Copernicus Marine Service: Arctic Ocean - Sea and Ice Surface Temperature REPROCESSED, doi:10.48670/MOI-00123, 2024.

Cox, G. F. N. and Weeks, W. F.: Salinity Variations in Sea Ice, Journal of Glaciology, 13, 109–120, doi:10.3189/S0022143000023418, 1974.

Crameri, F.: Scientific colour maps, http://doi.org/10.5281/zenodo.1243862, 2018.

Crewell, S. and Löhnert, U.: Accuracy of cloud liquid water path from ground-based microwave radiometry 2. Sensor accuracy and synergy, Radio Science, 38, 8042, doi:10.1029/2002RS002634, 2003.

Crewell, S., Ebell, K., Löhnert, U., and Turner, D. D.: Can liquid water profiles be retrieved from passive microwave zenith observations?, Geophysical Research Letters, 36, 2008GL036 934, doi:10.1029/2008GL036934, 2009.

Crewell, S., Ebell, K., Konjari, P., Mech, M., Nomokonova, T., Radovan, A., Strack, D., Triana-Gómez, A. M., Noël, S., Scarlat, R., Spreen, G., Maturilli, M., Rinke, A., Gorodetskaya, I., Viceto, C., August, T., and Schröder, M.: A systematic assessment of water vapor products in the Arctic: from instantaneous measurements to monthly means, Atmospheric Measurement Techniques, 14, 4829–4856, doi:10.5194/amt-14-4829-2021, 2021.

Day, J. J., Sandu, I., Magnusson, L., Rodwell, M. J., Lawrence, H., Bormann, N., and Jung, T.: Increased Arctic influence on the midlatitude flow during

Scandinavian Blocking episodes, Quarterly Journal of the Royal Meteorological Society, 145, 3846–3862, doi:10.1002/qj.3673, 2019.

De Boer, G., Eloranta, E. W., and Shupe, M. D.: Arctic Mixed-Phase Stratiform Cloud Properties from Multiple Years of Surface-Based Measurements at Two High-Latitude Locations, Journal of the Atmospheric Sciences, 66, 2874–2887, doi:10.1175/2009JAS3029.1, 2009.

De Gélis, I., Prigent, C., Jimenez, C., and Sandells, M.: Forward modelling of passive microwave emissivities over snow-covered areas at continental scale, Remote Sensing of Environment, 328, 114 821, doi:10.1016/j.rse.2025.114821, 2025.

De Rosnay, P., Browne, P., De Boisséson, E., Fairbairn, D., Hirahara, Y., Ochi, K., Schepers, D., Weston, P., Zuo, H., Alonso-Balmaseda, M., Balsamo, G., Bonavita, M., Borman, N., Brown, A., Chrust, M., Dahoui, M., Chiara, G., English, S., Geer, A., Healy, S., Hersbach, H., Laloyaux, P., Magnusson, L., Massart, S., McNally, A., Pappenberger, F., and Rabier, F.: Coupled data assimilation at ECMWF: current status, challenges and future developments, Quarterly Journal of the Royal Meteorological Society, 148, 2672–2702, doi:10.1002/qj.4330, 2022.

Debye, P.: Polare Molekeln, S. Hirzel, 1929.

Debye, P., Anderson, H. R., and Brumberger, H.: Scattering by an Inhomogeneous Solid. II. The Correlation Function and Its Application, Journal of Applied Physics, 28, 679–683, doi:10.1063/1.1722830, 1957.

Denoth, A.: Effect of grain geometry on electrical properties of snow at frequencies up to 100 MHz, Journal of Applied Physics, 53, 7496–7501, doi:10.1063/1.330157, 1982.

Di Tomaso, E., Bormann, N., and English, S.: Assimilation of ATOVS radiances at ECMWF: third year EUMETSAT fellowship report, European Centre for Medium-Range Weather Forecasts, Research Report No. 29, 2013.

Ding, K.-H., Xu, X., and Tsang, L.: Electromagnetic Scattering by Bicontinuous Random Microstructures With Discrete Permittivities, IEEE Transactions on Geoscience and Remote Sensing, 48, 3139–3151, doi:10.1109/TGRS.2010.2043953, 2010.

Domine, F., Taillandier, A., and Simpson, W. R.: A parameterization of the specific surface area of seasonal snow for field use and for models of snowpack evo-

lution, Journal of Geophysical Research: Earth Surface, 112, 2006JF000 512, doi:10.1029/2006JF000512, 2007.

Donlon, C., Galeazzi, C., Midthassel, R., Sallusti, M., Triggianese, M., Fiorelli, B., De Paris, G., Kornienko, A., and Khlystova, I.: The Copernicus Imaging Microwave Radiometer (CIMR): Mission Overview and Status, in: IGARSS 2023 - 2023 IEEE International Geoscience and Remote Sensing Symposium, pp. 989–992, IEEE, Pasadena, CA, USA, ISBN 979-8-3503-2010-7, doi:10.1109/IGARSS52108.2023.10281934, 2023.

Dorff, H., Aubry, C., Ewald, F., Hirsch, L., Jansen, F., Konow, H., Mech, M., Ori, D., Ringel, M., Walbröl, A., Crewell, S., Ehrlich, A., Wendisch, M., and Ament, F.: Unified Airborne Active and Passive Microwave Measurements over Arctic Sea Ice and Ocean during the HALO-(AC)^3 Campaign in Spring 2022 (v2.7), doi:10.1594/PANGAEA.974108, 2024.

Drinkwater, M. and Xiang Liu: Seasonal to interannual variability in Antarctic sea-ice surface melt, IEEE Transactions on Geoscience and Remote Sensing, 38, 1827–1842, doi:10.1109/36.851767, 2000.

Drobot, S. D. and Anderson, M. R.: An improved method for determining snowmelt onset dates over Arctic sea ice using scanning multichannel microwave radiometer and Special Sensor Microwave/Imager data, Journal of Geophysical Research: Atmospheres, 106, 24 033–24 049, doi:10.1029/2000JD000171, 2001.

Duncan, D. I. and Eriksson, P.: An update on global atmospheric ice estimates from satellite observations and reanalyses, Atmospheric Chemistry and Physics, 18, 11 205–11 219, doi:10.5194/acp-18-11205-2018, 2018.

Ebell, K., Löhnert, U., Päschke, E., Orlandi, E., Schween, J. H., and Crewell, S.: A 1-D variational retrieval of temperature, humidity, and liquid cloud properties: Performance under idealized and real conditions, Journal of Geophysical Research: Atmospheres, 122, 1746–1766, doi:10.1002/2016JD025945, 2017.

Ebell, K., Nomokonova, T., Maturilli, M., and Ritter, C.: Radiative Effect of Clouds at Ny-Ålesund, Svalbard, as Inferred from Ground-Based Remote Sensing Observations, Journal of Applied Meteorology and Climatology, 59, 3–22, doi:10.1175/JAMC-D-19-0080.1, 2020.

Ebell, K., Buhren, C., Gierens, R., Chellini, G., Lauer, M., Walbröl, A., Dahlke, S., Krobot, P., and Mech, M.: Impact of weather systems on observed precipitation at Ny-Ålesund (Svalbard), Atmospheric Chemistry and Physics, 25, 7315–7342, doi:10.5194/acp-25-7315-2025, 2025.

ECMWF: ECMWF Strategy 2025-2034, Tech. rep., European Centre for Medium-Range Weather Forecasts, doi:10.21957/05DD9B657E, publisher: ECMWF, 2025.

Ehn, J. K., Hwang, B. J., Galley, R., and Barber, D. G.: Investigations of newly formed sea ice in the Cape Bathurst polynya: 1. Structural, physical, and optical properties, Journal of Geophysical Research: Oceans, 112, 2006JC003 702, doi:10.1029/2006JC003702, 2007.

Ehrlich, A., Bierwirth, E., Istomina, L., and Wendisch, M.: Combined retrieval of Arctic liquid water cloud and surface snow properties using airborne spectral solar remote sensing, Atmospheric Measurement Techniques, 10, 3215–3230, doi:10.5194/amt-10-3215-2017, 2017.

Ehrlich, A., Stapf, J., Lüpkes, C., Mech, M., Crewell, S., and Wendisch, M.: Meteorological measurements by dropsondes released from POLAR 5 during ACLOUD 2017, doi:10.1594/PANGAEA.900204, type: data set, 2019a.

Ehrlich, A., Wendisch, M., Lüpkes, C., Buschmann, M., Bozem, H., Chechin, D., Clemen, H.-C., Dupuy, R., Eppers, O., Hartmann, J., Herber, A., Jäkel, E., Järvinen, E., Jourdan, O., Kästner, U., Kliesch, L.-L., Köllner, F., Mech, M., Mertes, S., Neuber, R., Ruiz-Donoso, E., Schnaiter, M., Schneider, J., Stapf, J., and Zanatta, M.: Collection of data sources for the Arctic CLoud Observations Using airborne measurements during polar Day (ACLOUD) campaign, North-West of Svalbard between 23 May - 26 June 2017, doi:https://doi.org/10.1594/PANGAEA.902603, type: data collection, 2019b.

Ehrlich, A., Wendisch, M., Lüpkes, C., Buschmann, M., Bozem, H., Chechin, D., Clemen, H.-C., Dupuy, R., Eppers, O., Hartmann, J., Herber, A., Jäkel, E., Järvinen, E., Jourdan, O., Kästner, U., Kliesch, L.-L., Köllner, F., Mech, M., Mertes, S., Neuber, R., Ruiz-Donoso, E., Schnaiter, M., Schneider, J., Stapf, J., and Zanatta, M.: A comprehensive in situ and remote sensing data set from the Arctic CLoud Observations Using airborne measurements during polar Day (ACLOUD) campaign, Earth System Science Data, 11, 1853–1881, doi:10.5194/essd-11-1853-2019, 2019c.

Ehrlich, A., Crewell, S., Herber, A., Klingebiel, M., Lüpkes, C., Mech, M., Becker, S., Borrmann, S., Bozem, H., Buschmann, M., Clemen, H.-C., De La Torre Castro, E., Dorff, H., Dupuy, R., Eppers, O., Ewald, F., George, G., Giez, A., Grawe, S., Gourbeyre, C., Hartmann, J., Jäkel, E., Joppe, P., Jourdan, O., Jurányi, Z., Kirbus, B., Lucke, J., Luebke, A. E., Maahn, M., Maherndl, N., Mallaun, C., Mayer, J., Mertes, S., Mioche, G., Moser, M., Müller, H., Pörtge,

V., Risse, N., Roberts, G., Rosenburg, S., Röttenbacher, J., Schäfer, M., Schaefer, J., Schäfler, A., Schirmacher, I., Schneider, J., Schnitt, S., Stratmann, F., Tatzelt, C., Voigt, C., Walbröl, A., Weber, A., Wetzel, B., Wirth, M., and Wendisch, M.: A comprehensive in-situ and remote sensing data set collected during the HALO–(AC)^3 aircraft campaign, doi:10.5194/essd-2024-281, 2024.

Eliasson, S., Buehler, S. A., Milz, M., Eriksson, P., and John, V. O.: Assessing observed and modelled spatial distributions of ice water path using satellite data, Atmospheric Chemistry and Physics, 11, 375–391, doi:10.5194/acp-11-375-2011, 2011.

Ellison, W. J.: Permittivity of Pure Water, at Standard Atmospheric Pressure, over the Frequency Range –25THz and the Temperature Range –100°C, Journal of Physical and Chemical Reference Data, 36, 1–18, doi:10.1063/1.2360986, 2007.

Elsaesser, G. S., O'Dell, C. W., Lebsock, M. D., Bennartz, R., Greenwald, T. J., and Wentz, F. J.: The Multisensor Advanced Climatology of Liquid Water Path (MAC-LWP), Journal of Climate, 30, 10 193–10 210, doi:10.1175/JCLI-D-16-0902.1, 2017.

Entekhabi, D., Njoku, E. G., O'Neill, P. E., Kellogg, K. H., Crow, W. T., Edelstein, W. N., Entin, J. K., Goodman, S. D., Jackson, T. J., Johnson, J., Kimball, J., Piepmeier, J. R., Koster, R. D., Martin, N., McDonald, K. C., Moghaddam, M., Moran, S., Reichle, R., Shi, J. C., Spencer, M. W., Thurman, S. W., Tsang, L., and Van Zyl, J.: The Soil Moisture Active Passive (SMAP) Mission, Proceedings of the IEEE, 98, 704–716, doi:10.1109/JPROC.2010.2043918, 2010.

Eriksson, P., Rydberg, B., Mattioli, V., Thoss, A., Accadia, C., Klein, U., and Buehler, S. A.: Towards an operational Ice Cloud Imager (ICI) retrieval product, Atmospheric Measurement Techniques, 13, 53–71, doi:10.5194/amt-13-53-2020, 2020.

Eriksson, P., Emrich, A., Kempe, K., Riesbeck, J., Aljarosha, A., Auriacombe, O., Kugelberg, J., Hekma, E., Albers, R., Murk, A., Møller Pedersen, S., John, L., Stake, J., McEvoy, P., Rydberg, B., Dybbroe, A., Thoss, A., Canestri, A., Accadia, C., Colucci, P., Gherardi, D., and Kangas, V.: The Arctic Weather Satellite radiometer, Atmospheric Measurement Techniques, 18, 4709–4729, doi:10.5194/amt-18-4709-2025, 2025.

EUMETSAT: ATOVS Level 1b Product Guide, Tech. Rep. v3, European Organisation for the Exploitation of Meteorological Satellites (EUMETSAT), Darmstadt, Germany, 2010.

EUMETSAT: MWR Level 1B – Arctic Weather Satellite Proto-Flight Model - Global, https://data.eumetsat.int/product/EO:EUM:DAT:0905, 2025.

EUMETSAT NWP-SAF: Spectral response functions (SRFs) and MW passbands, https://nwp-saf.eumetsat.int/site/software/rttov/download/coefficients/spectral-response-functions/, 2019.

European Space Agency: Copernicus Sentinel-2 (processed by ESA) MSI Level-2A BOA Reflectance Product, doi:https://doi.org/10.5270/S2_-znk9xsj, 2021.

Evans, K. F. and Stephens, G. L.: Microwave Remote Sensing Algorithms for Cirrus Clouds and Precipitation, Atmospheric Science Paper 540, Department of Atmospheric Science, Colorado State University, Fort Collins, CO, USA, 1993.

Evans, K. F. and Stephens, G. L.: Microwave Radiative Transfer through Clouds Composed of Realistically Shaped Ice Crystals. Part I. Single Scattering Properties, Journal of the Atmospheric Sciences, 52, 2041–2057, doi:10.1175/1520-0469(1995)052<2041:MRTTCC>2.0.CO;2, 1995.

Ewald, F., Kölling, T., Baumgartner, A., Zinner, T., and Mayer, B.: Design and characterization of specMACS, a multipurpose hyperspectral cloud and sky imager, Atmospheric Measurement Techniques, 9, 2015–2042, doi:10.5194/amt-9-2015-2016, 2016.

Ewald, F., Groß, S., Hagen, M., Hirsch, L., Delanoë, J., and Bauer-Pfundstein, M.: Calibration of a 35 GHz airborne cloud radar: lessons learned and intercomparisons with 94 GHz cloud radars, Atmospheric Measurement Techniques, 12, 1815–1839, doi:10.5194/amt-12-1815-2019, 2019.

Fabel, Y., Nouri, B., Wilbert, S., Blum, N., Triebel, R., Hasenbalg, M., Kuhn, P., Zarzalejo, L. F., and Pitz-Paal, R.: Applying self-supervised learning for semantic cloud segmentation of all-sky images, Atmospheric Measurement Techniques, 15, 797–809, doi:10.5194/amt-15-797-2022, 2022.

Fixsen, D. J.: The temperature of the cosmic microwave background, The Astrophysical Journal, 707, 916–920, doi:10.1088/0004-637X/707/2/916, 2009.

Geer, A. J.: Joint estimation of sea ice and atmospheric state from microwave imagers in operational weather forecasting, Quarterly Journal of the Royal Meteorological Society, 150, 3796–3826, doi:10.1002/qj.4797, 2024a.

Geer, A. J.: Simultaneous Inference of Sea Ice State and Surface Emissivity Model Using Machine Learning and Data Assimilation, Journal of Advances in Modeling Earth Systems, 16, e2023MS004 080, doi:10.1029/2023MS004080, 2024b.

George, G., Luebke, A. E., Klingebiel, M., Mech, M., and Ehrlich, A.: Dropsonde measurements from HALO and POLAR 5 during HALO-(AC)^3 in 2022, doi:10.1594/PANGAEA.968891, type: dataset bundled publication, 2024.

Gierens, R., Kneifel, S., Shupe, M. D., Ebell, K., Maturilli, M., and Löhnert, U.: Low-level mixed-phase clouds in a complex Arctic environment, Atmospheric Chemistry and Physics, 20, 3459–3481, doi:10.5194/acp-20-3459-2020, 2020.

Glorot, X., Bordes, A., and Bengio, Y.: Deep Sparse Rectifier Neural Networks, in: Proceedings of the International Conference on Artificial Intelligence and Statistics, edited by Gordon, G., Dunson, D., and Dudík, M., vol. 15, pp. 315–323, PMLR, Fort Lauderdale, FL, USA, https://proceedings.mlr.press/v15/glorot11a.html, 2011.

Gogineni, S. P., Moore, R. K., Grenfell, T. C., Barber, D. G., Digby, S., and Drinkwater, M.: The Effects of Freeze-Up and Melt Processes on Microwave Signatures, in: Microwave Remote Sensing of Sea Ice, pp. 329–341, American Geophysical Union (AGU), ISBN 978-1-118-66395-0, doi:https://doi.org/10.1029/GM068p0329, section: 17 _eprint: https://agupubs.onlinelibrary.wiley.com/doi/pdf/10.1029/GM068p0329, 1992.

Greenwald, T. J., Stephens, G. L., Vonder Haar, T. H., and Jackson, D. L.: A physical retrieval of cloud liquid water over the global oceans using special sensor microwave/imager (SSM/I) observations, Journal of Geophysical Research: Atmospheres, 98, 18 471–18 488, doi:10.1029/93JD00339, 1993.

Grenfell, T. C.: Surface-based passive microwave studies of multiyear sea ice, Journal of Geophysical Research, 97, 3485, doi:10.1029/91JC02651, 1992.

Guedj, S., Karbou, F., Rabier, F., and Bouchard, A.: Toward a Better Modeling of Surface Emissivity to Improve AMSU Data Assimilation Over Antarctica, IEEE Transactions on Geoscience and Remote Sensing, 48, 1976–1985, doi:10.1109/TGRS.2009.2036254, 2010.

Haggerty, J. A. and Curry, J. A.: Variability of sea ice emissivity estimated from airborne passive microwave measurements during FIRE SHEBA, Journal of Geophysical Research: Atmospheres, 106, 15 265–15 277, doi:10.1029/2000JD900485, 2001.

Haggerty, J. A., Curry, J. A., and Liu, G.: Potential for estimating cloud liquid water path over sea ice from airborne passive microwave measurements, Journal of Geophysical Research: Atmospheres, 107, doi:10.1029/2001JD000585, 2002.

Harlow, R.: Millimeter Microwave Emissivities and Effective Temperatures of Snow-Covered Surfaces: Evidence for Lambertian Surface Scattering, IEEE Transactions on Geoscience and Remote Sensing, 47, 1957–1970, doi:10.1109/TGRS.2008.2011893, 2009.

Harlow, R. C.: Sea Ice Emissivities and Effective Temperatures at MHS Frequencies: An Analysis of Airborne Microwave Data Measured During Two Arctic Campaigns, IEEE Transactions on Geoscience and Remote Sensing, 49, 1223–1237, doi:10.1109/TGRS.2010.2051555, 2011.

Harlow, R. C. and Essery, R.: Tundra Snow Emissivities at MHS Frequencies: MEMLS Validation Using Airborne Microwave Data Measured During CLPX-II, IEEE Transactions on Geoscience and Remote Sensing, 50, 4262–4278, doi:10.1109/TGRS.2012.2193132, 2012.

Harris, C. R., Millman, K. J., Van Der Walt, S. J., Gommers, R., Virtanen, P., Cournapeau, D., Wieser, E., Taylor, J., Berg, S., Smith, N. J., Kern, R., Picus, M., Hoyer, S., Van Kerkwijk, M. H., Brett, M., Haldane, A., Del Río, J. F., Wiebe, M., Peterson, P., Gérard-Marchant, P., Sheppard, K., Reddy, T., Weckesser, W., Abbasi, H., Gohlke, C., and Oliphant, T. E.: Array programming with NumPy, Nature, 585, 357–362, doi:10.1038/s41586-020-2649-2, 2020.

Hartmann, J., Lüpkes, C., and Chechin, D.: 1Hz resolution aircraft measurements of wind and temperature during the ACLOUD campaign in 2017, doi:10.1594/PANGAEA.902849, backup Publisher: Alfred Wegener Institute, Helmholtz Centre for Polar and Marine Research, Bremerhaven Type: data set, 2019.

Hector, L. G. and Schultz, H. L.: The Dielectric Constant of Air at Radiofrequencies, Physics, 7, 133–136, doi:10.1063/1.1745374, 1936.

Hersbach, H., Bell, B., Berrisford, P., Hirahara, S., Horányi, A., Muñoz-Sabater, J., Nicolas, J., Peubey, C., Radu, R., Schepers, D., Simmons, A., Soci, C.,

Abdalla, S., Abellan, X., Balsamo, G., Bechtold, P., Biavati, G., Bidlot, J., Bonavita, M., De Chiara, G., Dahlgren, P., Dee, D., Diamantakis, M., Dragani, R., Flemming, J., Forbes, R., Fuentes, M., Geer, A., Haimberger, L., Healy, S., Hogan, R. J., Hólm, E., Janisková, M., Keeley, S., Laloyaux, P., Lopez, P., Lupu, C., Radnoti, G., de Rosnay, P., Rozum, I., Vamborg, F., Villaume, S., and Thépaut, J.-N.: Complete ERA5 from 1940: Fifth generation of ECMWF atmospheric reanalyses of the global climate, doi:10.24381/cds.143582cf, 2017.

Hersbach, H., Bell, B., Berrisford, P., Hirahara, S., Horányi, A., Muñoz-Sabater, J., Nicolas, J., Peubey, C., Radu, R., Schepers, D., Simmons, A., Soci, C., Abdalla, S., Abellan, X., Balsamo, G., Bechtold, P., Biavati, G., Bidlot, J., Bonavita, M., Chiara, G., Dahlgren, P., Dee, D., Diamantakis, M., Dragani, R., Flemming, J., Forbes, R., Fuentes, M., Geer, A., Haimberger, L., Healy, S., Hogan, R. J., Hólm, E., Janisková, M., Keeley, S., Laloyaux, P., Lopez, P., Lupu, C., Radnoti, G., Rosnay, P., Rozum, I., Vamborg, F., Villaume, S., and Thépaut, J.: The ERA5 global reanalysis, Quarterly Journal of the Royal Meteorological Society, 146, 1999–2049, doi:10.1002/qj.3803, 2020.

Hersbach, H., Bell, B., Berrisford, P., Biavati, G., Horányi, A., Muñoz Sabater, J., Nicolas, J., Peubey, C., Radu, R., Rozum, I., Schepers, D., Simmons, A., Soci, C., Dee, D., and Thépaut, J.-N.: ERA5 hourly data on pressure levels from 1940 to present, doi:10.24381/cds.bd0915c6, 2023.

Hewison, T. and English, S.: Airborne retrievals of snow and ice surface emissivity at millimeter wavelengths, IEEE Transactions on Geoscience and Remote Sensing, 37, 1871–1879, doi:10.1109/36.774700, 1999.

Hewison, T., Selbach, N., Heygster, G., Taylor, J., and McGrath, A.: Airborne measurements of Arctic sea ice, glacier and snow emissivity at 24-183 GHz, in: IEEE International Geoscience and Remote Sensing Symposium, vol. 5, pp. 2851–2855, IEEE, Toronto, Ontario, Canada, ISBN 978-0-7803-7536-9, doi:10.1109/IGARSS.2002.1026797, 2002.

Hirahara, Y., Rosnay, P. d., and Arduini, G.: Evaluation of a Microwave Emissivity Module for Snow Covered Area with CMEM in the ECMWF Integrated Forecasting System, Remote Sensing, 12, 2946, doi:10.3390/rs12182946, 2020.

Hollinger, J. P., Troy, B. E., Ramseier, R. O., Asmus, K. W., Hartman, M. F., and Luther, C. A.: Microwave emission from high Arctic sea ice during freeze-up, Journal of Geophysical Research, 89, 8104, doi:10.1029/JC089iC05p08104, 1984.

Hori, M., Aoki, T., Tanikawa, T., Motoyoshi, H., Hachikubo, A., Sugiura, K., Yasunari, T. J., Eide, H., Storvold, R., Nakajima, Y., and Takahashi, F.: In-situ measured spectral directional emissivity of snow and ice in the 8–14 µm atmospheric window, Remote Sensing of Environment, 100, 486–502, doi:10.1016/j.rse.2005.11.001, 2006.

Hotelling, H.: Analysis of a complex of statistical variables into principal components., Journal of Educational Psychology, 24, 417–441, doi:10.1037/h0071325, 1933.

Hou, A. Y., Kakar, R. K., Neeck, S., Azarbarzin, A. A., Kummerow, C. D., Kojima, M., Oki, R., Nakamura, K., and Iguchi, T.: The Global Precipitation Measurement Mission, Bulletin of the American Meteorological Society, 95, 701–722, doi:10.1175/BAMS-D-13-00164.1, 2014.

Hoyer, S. and Hamman, J.: xarray: N-D labeled Arrays and Datasets in Python, Journal of Open Research Software, 5, 10, doi:10.5334/jors.148, 2017.

Huntemann, M., Heygster, G., Kaleschke, L., Krumpen, T., Mäkynen, M., and Drusch, M.: Empirical sea ice thickness retrieval during the freeze-up period from SMOS high incident angle observations, The Cryosphere, 8, 439–451, doi:10.5194/tc-8-439-2014, 2014.

Hunter, J. D.: Matplotlib: A 2D Graphics Environment, Computing in Science & Engineering, 9, 90–95, doi:10.1109/MCSE.2007.55, 2007.

Hwang, B. J., Ehn, J. K., and Barber, D. G.: Impact of ice temperature on microwave emissivity of thin newly formed sea ice, Journal of Geophysical Research: Oceans, 113, 2006JC003 930, doi:10.1029/2006JC003930, 2008.

Høyer, J. L., Lang, A. M., Eastwood, S., Wimmer, W., and Dybkj, G.: Report from Field Inter- Comparison Experiment (FICE) for ice surface temperature, Tech. rep., Danish Meteorological Institute, 2017.

Illingworth, A. J., Barker, H. W., Beljaars, A., Ceccaldi, M., Chepfer, H., Clerbaux, N., Cole, J., Delanoë, J., Domenech, C., Donovan, D. P., Fukuda, S., Hirakata, M., Hogan, R. J., Huenerbein, A., Kollias, P., Kubota, T., Nakajima, T., Nakajima, T. Y., Nishizawa, T., Ohno, Y., Okamoto, H., Oki, R., Sato, K., Satoh, M., Shephard, M. W., Velázquez-Blázquez, A., Wandinger, U., Wehr, T., and Van Zadelhoff, G.-J.: The EarthCARE Satellite: The Next Step Forward in Global Measurements of Clouds, Aerosols, Precipitation, and Radiation, Bulletin of the American Meteorological Society, 96, 1311–1332, doi:10.1175/BAMS-D-12-00227.1, 2015.

Illingworth, A. J., Battaglia, A., Bradford, J., Forsythe, M., Joe, P., Kollias, P., Lean, K., Lori, M., Mahfouf, J.-F., Melo, S., Midthassel, R., Munro, Y., Nicol, J., Potthast, R., Rennie, M., Stein, T. H. M., Tanelli, S., Tridon, F., Walden, C. J., and Wolde, M.: WIVERN: A New Satellite Concept to Provide Global In-Cloud Winds, Precipitation, and Cloud Properties, Bulletin of the American Meteorological Society, 99, 1669–1687, doi:10.1175/BAMS-D-16-0047.1, 2018.

IPCC: Climate Change 2021: The Physical Science Basis. Contribution of Working Group I to the Sixth Assessment Report of the Intergovernmental Panel on Climate Change, Cambridge University Press, Cambridge, United Kingdom and New York, NY, USA, 1 edn., ISBN 978-1-009-15789-6, doi:10.1017/9781009157896, 2021.

Jacob, M., Ament, F., Gutleben, M., Konow, H., Mech, M., Wirth, M., and Crewell, S.: Investigating the liquid water path over the tropical Atlantic with synergistic airborne measurements, Atmospheric Measurement Techniques, 12, 3237–3254, doi:10.5194/amt-12-3237-2019, 2019.

JAXA: Data Users' Manual for the Advanced Microwave Scanning Radiometer 2 (AMSR2) onboard the Global Change Observation Mission 1st - Water "SHIZUKU" (GCOM-W1), Tech. Rep. 4th Edition, Japan Aerospace Exploration Agency, Earth Observation Research Center, 2016.

Jäkel, E. and Ehrlich, A.: Radiance fields of clouds and the Arctic surface measured by a digital camera during ACLOUD 2017, doi:10.1594/PANGAEA.901024, artwork Size: 344 data points Pages: 344 data points, 2019.

Kachi, M., Shimada, R., Ohara, K., Kubota, T., Miura, T., Inaoka, K., Kojima, Y., Aonashi, K., and Ebuchi, N.: The Advanced Microwave Scanning Radiometer 3 (AMSR3) Onboard the Global Observing Satellite for Greenhouse Gases and Water Cycle (GOSAT-GW) Toward Long-Term Water Cycle Monitoring, in: IGARSS 2023 - 2023 IEEE International Geoscience and Remote Sensing Symposium, pp. 561–564, IEEE, Pasadena, CA, USA, ISBN 979-8-3503-2010-7, doi:10.1109/IGARSS52108.2023.10282052, 2023.

Kaleschke, L., Maaß, N., Haas, C., Hendricks, S., Heygster, G., and Tonboe, R. T.: A sea-ice thickness retrieval model for 1.4 GHz radiometry and application to airborne measurements over low salinity sea-ice, The Cryosphere, 4, 583–592, doi:10.5194/tc-4-583-2010, 2010.

Kalesse-Los, H., Schimmel, W., Luke, E., and Seifert, P.: Evaluating cloud liquid detection against Cloudnet using cloud radar Doppler spectra in a pre-trained

artificial neural network, Atmospheric Measurement Techniques, 15, 279–295, doi:10.5194/amt-15-279-2022, 2022.

Kang, E., Sohn, B., Tonboe, R. T., Noh, Y., Kwon, I., Kim, S., Maturilli, M., Kim, H., and Liu, C.: Explicitly determined sea ice emissivity and emission temperature over the Arctic for surface-sensitive microwave channels, Quarterly Journal of the Royal Meteorological Society, 149, 2011–2030, doi:10.1002/qj.4492, 2023.

Kang, E., Sohn, B., Song, H., and Liu, C.: Satellite-Estimated Microwave Emissivity and Emission Temperature Over the Arctic Sea Ice: ANN-Based Algorithm, Journal of Geophysical Research: Atmospheres, 130, e2024JD042 265, doi:10.1029/2024JD042265, 2025.

Kangas, V., D'Addio, S., Klein, U., Loiselet, M., Mason, G., Orlhac, J.-C., Gonzalez, R., Bergada, M., Brandt, M., and Thomas, B.: Ice cloud imager instrument for MetOp Second Generation, in: 2014 13th Specialist Meeting on Microwave Radiometry and Remote Sensing of the Environment (MicroRad), pp. 228–231, IEEE, Pasadena, CA, USA, ISBN 978-1-4799-4644-0 978-1-4799-4645-7, doi:10.1109/MicroRad.2014.6878946, 2014a.

Kangas, V., D'Addio, S., Loiselet, M., Mason, G., Buckley, M., Tennant, G., and Campbell, P.: Microwave Sounder instrument for MetOp Second Generation, in: 2014 13th Specialist Meeting on Microwave Radiometry and Remote Sensing of the Environment (MicroRad), pp. 232–235, IEEE, Pasadena, CA, USA, ISBN 978-1-4799-4644-0 978-1-4799-4645-7, doi:10.1109/MicroRad.2014.6878947, 2014b.

Kanzow, T.: The Expedition PS131 of the Research Vessel POLARSTERN to the Fram Strait in 2022, doi:10.57738/BzPM_0770_2023, place: Bremerhaven Publication Title: Berichte zur Polar- und Meeresforschung = Reports on polar and marine research Volume: 770, 2023.

Karbou, F. and Prigent, C.: Calculation of Microwave Land Surface Emissivity From Satellite Observations: Validity of the Specular Approximation Over Snow-Free Surfaces?, IEEE Geoscience and Remote Sensing Letters, 2, 311–314, doi:10.1109/LGRS.2005.847932, 2005.

Kawanishi, T., Sezai, T., Ito, Y., Imaoka, K., Takeshima, T., Ishido, Y., Shibata, A., Miura, M., Inahata, H., and Spencer, R.: The advanced microwave scanning radiometer for the earth observing system (AMSR-E), NASDA's contribution to the EOS for global energy and water cycle studies, IEEE Transactions on

Geoscience and Remote Sensing, 41, 184–194, doi:10.1109/TGRS.2002.808331, 2003.

Kay, J. E. and L'Ecuyer, T.: Observational constraints on Arctic Ocean clouds and radiative fluxes during the early 21st century, Journal of Geophysical Research: Atmospheres, 118, 7219–7236, doi:10.1002/jgrd.50489, 2013.

Kay, J. E., L'Ecuyer, T., Chepfer, H., Loeb, N., Morrison, A., and Cesana, G.: Recent Advances in Arctic Cloud and Climate Research, Current Climate Change Reports, 2, 159–169, doi:10.1007/s40641-016-0051-9, 2016.

Kilic, L., Prigent, C., Aires, F., Boutin, J., Heygster, G., Tonboe, R. T., Roquet, H., Jimenez, C., and Donlon, C.: Expected Performances of the Copernicus Imaging Microwave Radiometer (CIMR) for an All-Weather and High Spatial Resolution Estimation of Ocean and Sea Ice Parameters, Journal of Geophysical Research: Oceans, 123, 7564–7580, doi:10.1029/2018JC014408, 2018.

Kilic, L., Tonboe, R. T., Prigent, C., and Heygster, G.: Estimating the snow depth, the snow–ice interface temperature, and the effective temperature of Arctic sea ice using Advanced Microwave Scanning Radiometer 2 and ice mass balance buoy data, The Cryosphere, 13, 1283–1296, doi:10.5194/tc-13-1283-2019, 2019.

Kilic, L., Prigent, C., Aires, F., Heygster, G., Pellet, V., and Jimenez, C.: Ice Concentration Retrieval from the Analysis of Microwaves: A New Methodology Designed for the Copernicus Imaging Microwave Radiometer, Remote Sensing, 12, 1060, doi:10.3390/rs12071060, 2020.

Kilic, L., Prigent, C., Jimenez, C., Turner, E., Hocking, J., English, S., Meissner, T., and Dinnat, E.: Development of the SURface Fast Emissivity Model for Ocean (SURFEM-Ocean) Based on the PARMIO Radiative Transfer Model, Earth and Space Science, 10, e2022EA002 785, doi:10.1029/2022EA002785, 2023.

Kim, E., Lyu, C.-H. J., Anderson, K., Vincent Leslie, R., and Blackwell, W. J.: S-NPP ATMS instrument prelaunch and on-orbit performance evaluation, Journal of Geophysical Research: Atmospheres, 119, 5653–5670, doi:10.1002/2013JD020483, 2014.

King, J., Howell, S., Brady, M., Toose, P., Derksen, C., Haas, C., and Beckers, J.: Local-scale variability of snow density on Arctic sea ice, The Cryosphere, 14, 4323–4339, doi:10.5194/tc-14-4323-2020, 2020.

Kingma, D. P. and Ba, J.: Adam: A Method for Stochastic Optimization, doi:10.48550/arXiv.1412.6980, arXiv:1412.6980 [cs], 2017.

Kliesch, L.-L. and Mech, M.: Airborne radar reflectivity and brightness temperature measurements with POLAR 5 during ACLOUD in May and June 2017, doi:10.1594/PANGAEA.899565, type: data set, 2019.

Klingebiel, M., Ehrlich, A., Ruiz-Donoso, E., Risse, N., Schirmacher, I., Jäkel, E., Schäfer, M., Wolf, K., Mech, M., Moser, M., Voigt, C., and Wendisch, M.: Variability and properties of liquid-dominated clouds over the ice-free and sea-ice-covered Arctic Ocean, Atmospheric Chemistry and Physics, 23, 15 289–15 304, doi:10.5194/acp-23-15289-2023, 2023.

Kneifel, S., Maahn, M., Peters, G., and Simmer, C.: Observation of snowfall with a low-power FM-CW K-band radar (Micro Rain Radar), Meteorology and Atmospheric Physics, 113, 75–87, doi:10.1007/s00703-011-0142-z, 2011.

Kneifel, S., Redl, S., Orlandi, E., Löhnert, U., Cadeddu, M. P., Turner, D. D., and Chen, M.-T.: Absorption Properties of Supercooled Liquid Water between 31 and 225 GHz: Evaluation of Absorption Models Using Ground-Based Observations, Journal of Applied Meteorology and Climatology, 53, 1028–1045, doi:10.1175/JAMC-D-13-0214.1, 2014.

Kongoli, C., Boukabara, S.-A., Yan, B., Weng, F., and Ferraro, R.: A New Sea-Ice Concentration Algorithm Based on Microwave Surface Emissivities—Application to AMSU Measurements, IEEE Transactions on Geoscience and Remote Sensing, 49, 175–189, doi:10.1109/TGRS.2010.2052812, 2011.

Konow, H., Jacob, M., Ament, F., Crewell, S., Ewald, F., Hagen, M., Hirsch, L., Jansen, F., Mech, M., and Stevens, B.: A unified data set of airborne cloud remote sensing using the HALO Microwave Package (HAMP), Earth System Science Data, 11, 921–934, doi:10.5194/essd-11-921-2019, 2019.

Kubota, T., Kummerow, C., Panegrossi, G., Ringerud, S., Utsumi, N., and Joseph Turk, F.: Advancing Global Precipitation Data Products: Recommendations from the International Precipitation Working Group, Bulletin of the American Meteorological Society, 106, E564–E570, doi:10.1175/BAMS-D-25-0011.1, 2025.

Kunkee, D. B., Poe, G. A., Boucher, D. J., Swadley, S. D., Hong, Y., Wessel, J. E., and Uliana, E. A.: Design and Evaluation of the First Special Sensor Microwave Imager/Sounder, IEEE Transactions on Geoscience and Remote Sensing, 46, 863–883, doi:10.1109/TGRS.2008.917980, 2008.

Küchler, N., Kneifel, S., Löhnert, U., Kollias, P., Czekala, H., and Rose, T.: A W-Band Radar–Radiometer System for Accurate and Continuous Monitoring of Clouds and Precipitation, Journal of Atmospheric and Oceanic Technology, 34, 2375–2392, doi:10.1175/JTECH-D-17-0019.1, 2017.

Lam, R., Sanchez-Gonzalez, A., Willson, M., Wirnsberger, P., Fortunato, M., Alet, F., Ravuri, S., Ewalds, T., Eaton-Rosen, Z., Hu, W., Merose, A., Hoyer, S., Holland, G., Vinyals, O., Stott, J., Pritzel, A., Mohamed, S., and Battaglia, P.: GraphCast: Learning skillful medium-range global weather forecasting, http://arxiv.org/abs/2212.12794, arXiv:2212.12794 [physics], 2023.

Langlois, A., Mundy, C. J., and Barber, D. G.: On the winter evolution of snow thermophysical properties over land-fast first-year sea ice, Hydrological Processes, 21, 705–716, doi:10.1002/hyp.6407, 2007.

Lawrence, H., Bormann, N., Sandu, I., Day, J., Farnan, J., and Bauer, P.: Use and impact of Arctic observations in the ECMWF Numerical Weather Prediction system, Quarterly Journal of the Royal Meteorological Society, 145, 3432–3454, doi:10.1002/qj.3628, 2019.

Lean, K., Bormann, N., Healy, S., English, S., Schüttemeyer, D., and Drusch, M.: Assessing forecast benefits of future constellations of microwave sounders on small satellites using an ensemble of data assimilations, Quarterly Journal of the Royal Meteorological Society, 151, e4939, doi:10.1002/qj.4939, 2025.

Lecun, Y., Bottou, L., Bengio, Y., and Haffner, P.: Gradient-based learning applied to document recognition, Proceedings of the IEEE, 86, 2278–2324, doi:10.1109/5.726791, 1998.

LeCun, Y., Bengio, Y., and Hinton, G.: Deep learning, Nature, 521, 436–444, doi:10.1038/nature14539, 2015.

Leduc-Leballeur, M., Picard, G., Mialon, A., Arnaud, L., Lefebvre, E., Possenti, P., and Kerr, Y.: Modeling L-Band Brightness Temperature at Dome C in Antarctica and Comparison With SMOS Observations, IEEE Transactions on Geoscience and Remote Sensing, 53, 4022–4032, doi:10.1109/TGRS.2015.2388790, 2015.

Lehning, M., Bartelt, P., Brown, B., Fierz, C., and Satyawali, P.: A physical SNOWPACK model for the Swiss avalanche warning Part II. Snow microstructure, Cold Regions Science and Technology, 2002.

Leinss, S., Löwe, H., Proksch, M., Lemmetyinen, J., Wiesmann, A., and Hajnsek, I.: Anisotropy of seasonal snow measured by polarimetric phase differences in radar time series, The Cryosphere, 10, 1771–1797, doi:10.5194/tc-10-1771-2016, 2016.

Leppäranta, M. and Terhikki, M.: The brine and gas content of sea ice with attention to low salinities and high temperatures, Tech. Rep. 2, Finnish Institute of Marine Research, Helsinki, Finland, http://hdl.handle.net/1834/23905, 1988.

Liang, D., Xu, X., Tsang, L., Andreadis, K. M., and Josberger, E. G.: The Effects of Layers in Dry Snow on Its Passive Microwave Emissions Using Dense Media Radiative Transfer Theory Based on the Quasicrystalline Approximation (QCA/DMRT), IEEE Transactions on Geoscience and Remote Sensing, 46, 3663–3671, doi:10.1109/TGRS.2008.922143, 2008.

Likas, A., Vlassis, N., and J. Verbeek, J.: The global k-means clustering algorithm, Pattern Recognition, 36, 451–461, doi:10.1016/S0031-3203(02)00060-2, 2003.

Liljegren, J., Boukabara, S.-A., Cady-Pereira, K., and Clough, S.: The effect of the half-width of the 22-GHz water vapor line on retrievals of temperature and water vapor profiles with a 12-channel microwave radiometer, IEEE Transactions on Geoscience and Remote Sensing, 43, 1102–1108, doi:10.1109/TGRS.2004.839593, 2005.

Linke, O., Quaas, J., Baumer, F., Becker, S., Chylik, J., Dahlke, S., Ehrlich, A., Handorf, D., Jacobi, C., Kalesse-Los, H., Lelli, L., Mehrdad, S., Neggers, R. A. J., Riebold, J., Saavedra Garfias, P., Schnierstein, N., Shupe, M. D., Smith, C., Spreen, G., Verneuil, B., Vinjamuri, K. S., Vountas, M., and Wendisch, M.: Constraints on simulated past Arctic amplification and lapse rate feedback from observations, Atmospheric Chemistry and Physics, 23, 9963–9992, doi:10.5194/acp-23-9963-2023, 2023.

Liu, Q., Weng, F., and English, S. J.: An Improved Fast Microwave Water Emissivity Model, IEEE Transactions on Geoscience and Remote Sensing, 49, 1238–1250, doi:10.1109/TGRS.2010.2064779, 2011.

Lucas, S., Johannessen, J. A., Cancet, M., Pettersson, L. H., Esau, I., Rheinlænder, J. W., Ardhuin, F., Chapron, B., Korosov, A., Collard, F., Herlédan, S., Olason, E., Ferrari, R., Fouchet, E., and Donlon, C.: Knowledge Gaps and Impact of Future Satellite Missions to Facilitate Monitoring of Changes in the Arctic Ocean, Remote Sensing, 15, 2852, doi:10.3390/rs15112852, 2023.

Luke, E. P., Kollias, P., and Shupe, M. D.: Detection of supercooled liquid in mixed-phase clouds using radar Doppler spectra, Journal of Geophysical Research: Atmospheres, 115, 2009JD012 884, doi:10.1029/2009JD012884, 2010.

Lüpkes, C., Hartmann, J., Chechin, D., and Michaelis, J.: High resolution aircraft measurements of wind and temperature during the AFLUX campaign in 2019, doi:10.1594/PANGAEA.945844, type: data set, 2022.

Maahn, M., Burgard, C., Crewell, S., Gorodetskaya, I. V., Kneifel, S., Lhermitte, S., Van Tricht, K., and Van Lipzig, N. P. M.: How does the spaceborne radar blind zone affect derived surface snowfall statistics in polar regions?, Journal of Geophysical Research: Atmospheres, 119, doi:10.1002/2014JD022079, 2014.

Maahn, M., Turner, D. D., Löhnert, U., Posselt, D. J., Ebell, K., Mace, G. G., and Comstock, J. M.: Optimal Estimation Retrievals and Their Uncertainties: What Every Atmospheric Scientist Should Know, Bulletin of the American Meteorological Society, 101, E1512–E1523, doi:10.1175/BAMS-D-19-0027.1, 2020.

MacQueen, J.: Some methods for classification and analysis of multivariate observations, in: Proceedings of the Fifth Berkeley Symposium on Mathematical Statistics and Probability, edited by Le Cam, L. M. and Neyman, J., vol. 1, pp. 281–297, University of California Press, Berkeley, CA, USA, 1967.

Maezawa, H. and Miyauchi, H.: Rigorous expressions for the Fresnel equations at interfaces between absorbing media, Journal of the Optical Society of America A, 26, 330, doi:10.1364/JOSAA.26.000330, 2009.

Maherndl, N., Moser, M., Lucke, J., Mech, M., Risse, N., Schirmacher, I., and Maahn, M.: Quantifying riming from airborne data during the HALO-(AC)^3 campaign, Atmospheric Measurement Techniques, 17, 1475–1495, doi:10.5194/amt-17-1475-2024, 2024.

Markus, T., Stroeve, J. C., and Miller, J.: Recent changes in Arctic sea ice melt onset, freezeup, and melt season length, Journal of Geophysical Research: Oceans, 114, doi:10.1029/2009jc005436, publisher: American Geophysical Union (AGU), 2009.

Martin, S., Drucker, R., Kwok, R., and Holt, B.: Estimation of the thin ice thickness and heat flux for the Chukchi Sea Alaskan coast polynya from Special Sensor Microwave/Imager data, 1990–2001, Journal of Geophysical Research: Oceans, 109, 2004JC002 428, doi:10.1029/2004JC002428, 2004.

Mathew, N., Heygster, G., Melsheimer, C., and Kaleschke, L.: Surface Emissivity of Arctic Sea Ice at AMSU Window Frequencies, IEEE Transactions on Geoscience and Remote Sensing, 46, 2298–2306, doi:10.1109/TGRS.2008.916630, 2008.

Mathew, N., Heygster, G., and Melsheimer, C.: Surface Emissivity of the Arctic Sea Ice at AMSR-E Frequencies, IEEE Transactions on Geoscience and Remote Sensing, 47, 4115–4124, doi:10.1109/TGRS.2009.2023667, 2009.

Maturilli, M.: High resolution radiosonde measurements from station Ny-Ålesund (2017-04 et seq), doi:10.1594/PANGAEA.914973, backup Publisher: Alfred Wegener Institute - Research Unit Potsdam Type: data set, 2020.

Maturilli, M., Herber, A., and König-Langlo, G.: Surface radiation climatology for Ny-Ålesund, Svalbard (78.9° N), basic observations for trend detection, Theoretical and Applied Climatology, 120, 331–339, doi:10.1007/s00704-014-1173-4, 2015.

Matzler, C.: Microwave permittivity of dry snow, IEEE Transactions on Geoscience and Remote Sensing, 34, 573–581, doi:10.1109/36.485133, 1996.

Matzler, C.: On the Determination of Surface Emissivity From Satellite Observations, IEEE Geoscience and Remote Sensing Letters, 2, 160–163, doi:10.1109/LGRS.2004.842448, 2005.

Matzler, C. and Wegmuller, U.: Dielectric properties of freshwater ice at microwave frequencies, Journal of Physics D: Applied Physics, 20, 1623–1630, doi:10.1088/0022-3727/20/12/013, 1987.

Matzler, C., Ramseier, R., and Svendsen, E.: Polarization effects in seaice signatures, IEEE Journal of Oceanic Engineering, 9, 333–338, doi:10.1109/JOE.1984.1145646, 1984.

May, E., Rydberg, B., Kaur, I., Mattioli, V., Hallborn, H., and Eriksson, P.: The Ice Cloud Imager: retrieval of frozen water column properties, Atmospheric Measurement Techniques, 17, 5957–5987, doi:10.5194/amt-17-5957-2024, 2024.

McKinney, W.: Data Structures for Statistical Computing in Python, in: Proceedings of the 9th Python in Science Conference, pp. 56–61, Austin, Texas, doi:10.25080/Majora-92bf1922-00a, 2010.

Mech, M., Orlandi, E., Crewell, S., Ament, F., Hirsch, L., Hagen, M., Peters, G., and Stevens, B.: HAMP – the microwave package on the High Altitude and

LOng range research aircraft (HALO), Atmospheric Measurement Techniques, 7, 4539–4553, doi:10.5194/amt-7-4539-2014, 2014.

Mech, M., Kliesch, L.-L., Anhäuser, A., Rose, T., Kollias, P., and Crewell, S.: Microwave Radar/radiometer for Arctic Clouds (MiRAC): first insights from the ACLOUD campaign, Atmospheric Measurement Techniques, 12, 5019–5037, doi:10.5194/amt-12-5019-2019, 2019.

Mech, M., Maahn, M., Kneifel, S., Ori, D., Orlandi, E., Kollias, P., Schemann, V., and Crewell, S.: PAMTRA 1.0: the Passive and Active Microwave radiative TRAnsfer tool for simulating radiometer and radar measurements of the cloudy atmosphere, Geoscientific Model Development, 13, 4229–4251, doi:10.5194/gmd-13-4229-2020, 2020.

Mech, M., Ehrlich, A., Herber, A., Lüpkes, C., Wendisch, M., Becker, S., Boose, Y., Chechin, D., Crewell, S., Dupuy, R., Gourbeyre, C., Hartmann, J., Jäkel, E., Jourdan, O., Kliesch, L.-L., Klingebiel, M., Kulla, B. S., Mioche, G., Moser, M., Risse, N., Ruiz-Donoso, E., Schäfer, M., Stapf, J., and Voigt, C.: MOSAiC-ACA and AFLUX - Arctic airborne campaigns characterizing the exit area of MOSAiC, Scientific Data, 9, 790, doi:10.1038/s41597-022-01900-7, 2022a.

Mech, M., Risse, N., Crewell, S., and Kliesch, L.-L.: Radar reflectivities at 94 GHz and microwave brightness temperature measurements at 89 GHz during the AFLUX Arctic airborne campaign in spring 2019 out of Svalbard, doi:10.1594/PANGAEA.944506, type: data set, 2022b.

Mech, M., Risse, N., Crewell, S., Kliesch, L.-L., and Krobot, P.: Microwave brightness temperature measurements during the ACLOUD Arctic airborne campaign in early summer 2017 out of Svalbard, doi:10.1594/PANGAEA.944070, type: data set, 2022c.

Mech, M., Risse, N., Kliesch, L.-L., Crewell, S., Kulla, B. S., and Krobot, P.: Microwave brightness temperature measurements during the AFLUX Arctic airborne campaign in spring 2019 out of Svalbard, doi:10.1594/PANGAEA.944057, type: data set, 2022d.

Mech, M., Risse, N., Marrollo, G., and Paul, D.: ac3airborne, doi:10.5281/zenodo.7305586, 2022e.

Meissner, T. and Wentz, F. J.: The Emissivity of the Ocean Surface Between 6 and 90 GHz Over a Large Range of Wind Speeds and Earth Incidence Angles, IEEE Transactions on Geoscience and Remote Sensing, 50, 3004–3026, doi:10.1109/TGRS.2011.2179662, 2012.

Melsheimer, C. and Spreen, G.: IUP Multiyear Ice Concentration and other sea ice types, Version 1.1 (Arctic)/Version AQ2 (Antarctic) User Guide, https://data.seaice.uni-bremen.de/MultiYearIce/MYIuserguide.pdf, 2022.

Melsheimer, C., Frost, T., and Heygster, G.: Detectability of Polar Mesocyclones and Polar Lows in Data From Space-Borne Microwave Humidity Sounders, IEEE Journal of Selected Topics in Applied Earth Observations and Remote Sensing, 9, 326–335, doi:10.1109/JSTARS.2015.2499083, 2016.

Melsheimer, C., Spreen, G., Ye, Y., and Shokr, M.: First results of Antarctic sea ice type retrieval from active and passive microwave remote sensing data, The Cryosphere, 17, 105–126, doi:10.5194/tc-17-105-2023, 2023.

Merkouriadi, I., Gallet, J., Graham, R. M., Liston, G. E., Polashenski, C., Rösel, A., and Gerland, S.: Winter snow conditions on Arctic sea ice north of Svalbard during the Norwegian young sea ICE (N-ICE2015) expedition, Journal of Geophysical Research: Atmospheres, 122, doi:10.1002/2017JD026753, 2017.

Mewes, D. and Jacobi, C.: Heat transport pathways into the Arctic and their connections to surface air temperatures, Atmospheric Chemistry and Physics, 19, 3927–3937, doi:10.5194/acp-19-3927-2019, 2019.

Mie, G.: Beiträge zur Optik trüber Medien, speziell kolloidaler Metallösungen, Annalen der Physik, 330, 377–445, doi:10.1002/andp.19083300302, 1908.

Milani, L. and Kidd, C.: The State of Precipitation Measurements at Mid-to-High Latitudes, Atmosphere, 14, 1677, doi:10.3390/atmos14111677, 2023.

Morrison, H., De Boer, G., Feingold, G., Harrington, J., Shupe, M. D., and Sulia, K.: Resilience of persistent Arctic mixed-phase clouds, Nature Geoscience, 5, 11–17, doi:10.1038/ngeo1332, 2012.

Munchak, S. J., Ringerud, S., Brucker, L., You, Y., De Gelis, I., and Prigent, C.: An Active–Passive Microwave Land Surface Database From GPM, IEEE Transactions on Geoscience and Remote Sensing, 58, 6224–6242, doi:10.1109/TGRS.2020.2975477, 2020.

Mätzler, C.: Improved Born approximation for scattering of radiation in a granular medium, Journal of Applied Physics, 83, 6111–6117, doi:10.1063/1.367496, 1998.

Mätzler, C.: Relation between grain-size and correlation length of snow, Journal of Glaciology, 48, 461–466, doi:10.3189/172756502781831287, 2002.

Mätzler, C., ed.: Thermal Microwave Radiation: Applications for Remote Sensing, Electromagnetic Waves, Institution of Engineering and Technology, 2006.

Mätzler, C. and Wiesmann, A.: Extension of the Microwave Emission Model of Layered Snowpacks to Coarse-Grained Snow, Remote Sensing of Environment, 70, 317–325, doi:10.1016/S0034-4257(99)00047-4, 1999.

Müller, J. J., Schäfer, M., Rosenburg, S., Ehrlich, A., and Wendisch, M.: High-resolution maps of Arctic surface skin temperature and type retrieved from airborne thermal infrared imagery collected during the HALO-(AC)^3 campaign, doi:10.5194/amt-2024-3967, 2025.

Naoki, K., Ukita, J., Nishio, F., Nakayama, M., Comiso, J. C., and Gasiewski, A.: Thin sea ice thickness as inferred from passive microwave and in situ observations, Journal of Geophysical Research, 113, C02S16, doi:10.1029/2007JC004270, 2008.

NASA ESDIS: NASA Worldview, https://worldview.earthdata.nasa.gov, 2024.

NASA Goddard Space Flight Center and GPM Intercalibration Working Group: NASA Global Precipitation Measurement (GPM) Level 1C Algorithms, Tech. Rep. GPM L1C ATBD (Version 1.9), Goddard Space Flight Center, Greenbelt, Maryland, USA, https://arthurhou.pps.eosdis.nasa.gov/Documents/L1C_ATBD_v1.9_GPMV07.pdf, 2022.

Neuber, R.: A Multi-Disciplinary Arctic Research Facility: From the Koldewey – Rabot – Corbel – Stations to the AWI-IPEV Research Base on Spitsbergen, Polarforschung, 73, 117–123, doi:https://doi.org/10013/epic.33324.d001, 2003.

Nghiem, S. V., Kwok, R., Yueh, S. H., and Drinkwater, M. R.: Polarimetric signatures of sea ice: 1. Theoretical model, Journal of Geophysical Research: Oceans, 100, 13 665–13 679, doi:10.1029/95JC00937, 1995.

Nicolaus, M.: Expedition Programme PS149, pages: 1–42 Place: Bremerhaven Publication Title: Expeditionsprogramm Polarstern, 2025.

Nicolaus, M., Perovich, D. K., Spreen, G., Granskog, M. A., Von Albedyll, L., Angelopoulos, M., Anhaus, P., Arndt, S., Belter, H. J., Bessonov, V., Birnbaum, G., Brauchle, J., Calmer, R., Cardellach, E., Cheng, B., Clemens-Sewall, D., Dadic, R., Damm, E., De Boer, G., Demir, O., Dethloff, K., Divine, D. V., Fong, A. A., Fons, S., Frey, M. M., Fuchs, N., Gabarró, C., Gerland, S.,

Goessling, H. F., Gradinger, R., Haapala, J., Haas, C., Hamilton, J., Hannula, H.-R., Hendricks, S., Herber, A., Heuzé, C., Hoppmann, M., Høyland, K. V., Huntemann, M., Hutchings, J. K., Hwang, B., Itkin, P., Jacobi, H.-W., Jaggi, M., Jutila, A., Kaleschke, L., Katlein, C., Kolabutin, N., Krampe, D., Kristensen, S. S., Krumpen, T., Kurtz, N., Lampert, A., Lange, B. A., Lei, R., Light, B., Linhardt, F., Liston, G. E., Loose, B., Macfarlane, A. R., Mahmud, M., Matero, I. O., Maus, S., Morgenstern, A., Naderpour, R., Nandan, V., Niubom, A., Oggier, M., Oppelt, N., Pätzold, F., Perron, C., Petrovsky, T., Pirazzini, R., Polashenski, C., Rabe, B., Raphael, I. A., Regnery, J., Rex, M., Ricker, R., Riemann-Campe, K., Rinke, A., Rohde, J., Salganik, E., Scharien, R. K., Schiller, M., Schneebeli, M., Semmling, M., Shimanchuk, E., Shupe, M. D., Smith, M. M., Smolyanitsky, V., Sokolov, V., Stanton, T., Stroeve, J., Thielke, L., Timofeeva, A., Tonboe, R. T., Tavri, A., Tsamados, M., Wagner, D. N., Watkins, D., Webster, M., and Wendisch, M.: Overview of the MOSAiC expedition: Snow and sea ice, Elem Sci Anth, 10, 000 046, doi:10.1525/elementa.2021.000046, 2022.

Nielsen-Englyst, P., Høyer, J. L., Kolbe, W. M., Dybkjær, G., Lavergne, T., Tonboe, R. T., Skarpalezos, S., and Karagali, I.: A combined sea and sea-ice surface temperature climate dataset of the Arctic, 1982–2021, Remote Sensing of Environment, 284, 113 331, doi:10.1016/j.rse.2022.113331, 2023.

Nomokonova, T., Ebell, K., Löhnert, U., Maturilli, M., Ritter, C., and O'Connor, E.: Statistics on clouds and their relation to thermodynamic conditions at Ny-Ålesund using ground-based sensor synergy, Atmospheric Chemistry and Physics, 19, 4105–4126, doi:10.5194/acp-19-4105-2019, 2019.

Nomokonova, T., Ebell, K., Löhnert, U., Maturilli, M., and Ritter, C.: The influence of water vapor anomalies on clouds and their radiative effect at Ny-Ålesund, Atmospheric Chemistry and Physics, 20, 5157–5173, doi:10.5194/acp-20-5157-2020, 2020.

NORSEX Group: Norwegian Remote Sensing Experiment in a Marginal Ice Zone, Science, 220, 781–787, doi:10.1126/science.220.4599.781, number: 4599 Publisher: American Association for the Advancement of Science, 1983.

Norwegian Polar Institute: Kartdata Svalbard 1:100 000 (S100 Kartdata) / Map Data, doi:10.21334/npolar.2014.645336c7, 2014.

Notz, D. and SIMIP Community: Arctic Sea Ice in CMIP6, Geophysical Research Letters, 47, doi:10.1029/2019GL086749, 2020.

Notz, D. and Stroeve, J.: Observed Arctic sea-ice loss directly follows anthropogenic CO_2 emission, Science, 354, 747–750, doi:10.1126/science.aag2345, 2016.

NWP SAF: Pass band data for MW coefficient files, https://nwp-saf.eumetsat.int/site/software/rttov/download/coefficients/spectral-response-functions/, 2024.

Onstott, R. G., Grenfell, T. C., Matzler, C., Luther, C. A., and Svendsen, E. A.: Evolution of microwave sea ice signatures during early summer and midsummer in the marginal ice zone, Journal of Geophysical Research, 92, 6825, doi:10.1029/JC092iC07p06825, 1987.

O'Dell, C. W., Wentz, F. J., and Bennartz, R.: Cloud Liquid Water Path from Satellite-Based Passive Microwave Observations: A New Climatology over the Global Oceans, Journal of Climate, 21, 1721–1739, doi:10.1175/2007JCLI1958.1, 2008.

Pan, J., Durand, M., Sandells, M., Lemmetyinen, J., Kim, E. J., Pulliainen, J., Kontu, A., and Derksen, C.: Differences Between the HUT Snow Emission Model and MEMLS and Their Effects on Brightness Temperature Simulation, IEEE Transactions on Geoscience and Remote Sensing, 54, 2001–2019, doi:10.1109/TGRS.2015.2493505, 2016.

Paszke, A., Gross, S., Massa, F., Lerer, A., Bradbury, J., Chanan, G., Killeen, T., Lin, Z., Gimelshein, N., Antiga, L., Desmaison, A., Köpf, A., Yang, E., DeVito, Z., Raison, M., Tejani, A., Chilamkurthy, S., Steiner, B., Fang, L., Bai, J., and Chintala, S.: PyTorch: An Imperative Style, High-Performance Deep Learning Library, doi:10.48550/arXiv.1912.01703, arXiv:1912.01703 [cs], 2019.

Paţilea, C., Heygster, G., Huntemann, M., and Spreen, G.: Combined SMAP–SMOS thin sea ice thickness retrieval, The Cryosphere, 13, 675–691, doi:10.5194/tc-13-675-2019, 2019.

Pedregosa, F., Varoquaux, G., Gramfort, A., Michel, V., Thirion, B., Grisel, O., Blondel, M., Prettenhofer, P., Weiss, R., Dubourg, V., Vanderplas, J., Passos, A., and Cournapeau, D.: Scikit-learn: Machine Learning in Python, Journal of Machine Learning Research, 12, 2825–2830, 2011.

Penny, S. G., Akella, S., Chevallier, M., Counillon, F., Draper, C., Frolov, S., Fujii, Y., Kumar, A., Laloyaux, P., Martin, M., MetOffice, U., Peña, M., de Rosnay, P., Subramanian, A., Anderson, J., Carrassi, A., Kalnay, E., and Todling,

R.: Coupled data assimilation for integrated earth system analysis and prediction: goals, challenges, and recommendations, Tech. Rep. 2017-3, World Meteorological Organization (WMO), https://repository.library.noaa.gov/view/noaa/28431/noaa_28431_DS1.pdf, 2017.

Perovich, D. K., Elder, B. C., and Richter-Menge, J. A.: Observations of the annual cycle of sea ice temperature and mass balance, Geophysical Research Letters, 24, 555–558, doi:10.1029/97GL00185, 1997.

Perro, C., Duck, T. J., Lesins, G., Strong, K., and Drummond, J. R.: Arctic Surface Properties and Their Impact on Microwave Satellite Water Vapor Column Retrievals, IEEE Transactions on Geoscience and Remote Sensing, 58, 8332–8344, doi:10.1109/TGRS.2020.2986302, 2020.

Persson, P. O. G.: Onset and end of the summer melt season over sea ice: thermal structure and surface energy perspective from SHEBA, Climate Dynamics, 39, 1349–1371, doi:10.1007/s00382-011-1196-9, 2012.

Pfreundschuh, S., Fox, S., Eriksson, P., Duncan, D., Buehler, S. A., Brath, M., Cotton, R., and Ewald, F.: Synergistic radar and sub-millimeter radiometer retrievals of ice hydrometeors in mid-latitude frontal cloud systems, Atmospheric Measurement Techniques, 15, 677–699, doi:10.5194/amt-15-677-2022, 2022.

Pfreundschuh, S., Guilloteau, C., Brown, P. J., Kummerow, C. D., and Eriksson, P.: GPROF V7 and beyond: assessment of current and potential future versions of the GPROF passive microwave precipitation retrievals against ground radar measurements over the continental US and the Pacific Ocean, Atmospheric Measurement Techniques, 17, 515–538, doi:10.5194/amt-17-515-2024, 2024.

Picard, G., Le Toan, T., Quegan, S., Caraglio, Y., and Castel, T.: Radiative transfer modeling of cross-polarized backscatter from a pine forest using the discrete ordinate and eigenvalue method, IEEE Transactions on Geoscience and Remote Sensing, 42, 1720–1730, doi:10.1109/TGRS.2004.831229, 2004.

Picard, G., Brucker, L., Roy, A., Dupont, F., Fily, M., Royer, A., and Harlow, C.: Simulation of the microwave emission of multi-layered snowpacks using the Dense Media Radiative transfer theory: the DMRT-ML model, Geoscientific Model Development, 6, 1061–1078, doi:10.5194/gmd-6-1061-2013, 2013.

Picard, G., Sandells, M., and Löwe, H.: SMRT: an active–passive microwave radiative transfer model for snow with multiple microstructure and scattering formulations (v1.0), Geoscientific Model Development, 11, 2763–2788, doi:10.5194/gmd-11-2763-2018, 2018.

Picard, G., Löwe, H., Domine, F., Arnaud, L., Larue, F., Favier, V., Le Meur, E., Lefebvre, E., Savarino, J., and Royer, A.: The Microwave Snow Grain Size: A New Concept to Predict Satellite Observations Over Snow-Covered Regions, AGU Advances, 3, e2021AV000 630, doi:10.1029/2021AV000630, 2022.

Pithan, F., Medeiros, B., and Mauritsen, T.: Mixed-phase clouds cause climate model biases in Arctic wintertime temperature inversions, Climate Dynamics, 43, 289–303, doi:10.1007/s00382-013-1964-9, 2014.

Platnick, S., Li, J. Y., King, M. D., Gerber, H., and Hobbs, P. V.: A solar reflectance method for retrieving the optical thickness and droplet size of liquid water clouds over snow and ice surfaces, Journal of Geophysical Research: Atmospheres, 106, 15 185–15 199, doi:10.1029/2000JD900441, 2001.

Polder, D. and van Santen, J. H.: The effective permeability of mixtures of solids, Physica, 12, 257–271, 1946.

Prigent, C., Rossow, W. B., and Matthews, E.: Microwave land surface emissivities estimated from SSM/I observations, Journal of Geophysical Research, 102, 21 867–21 890, doi:10.1029/97JD01360, 1997.

Prigent, C., Rossow, W. B., and Matthews, E.: Global maps of microwave land surface emissivities: Potential for land surface characterization, Radio Science, 33, 745–751, doi:10.1029/97RS02460, 1998.

Prigent, C., Aires, F., and Rossow, W. B.: Retrieval of Surface and Atmospheric Geophysical Variables over Snow-Covered Land from Combined Microwave and Infrared Satellite Observations, Journal of Applied Meteorology, 42, 368–380, doi:10.1175/1520-0450(2003)042<0368:ROSAAG>2.0.CO;2, 2003.

Prigent, C., Liang, P., Tian, Y., Aires, F., Moncet, J.-L., and Boukabara, S. A.: Evaluation of modeled microwave land surface emissivities with satellite-based estimates, Journal of Geophysical Research: Atmospheres, 120, 2706–2718, doi:10.1002/2014JD021817, 2015.

Prigent, C., Aires, F., Wang, D., Fox, S., and Harlow, C.: Sea-surface emissivity parametrization from microwaves to millimetre waves, Quarterly Journal of the Royal Meteorological Society, 143, 596–605, doi:10.1002/qj.2953, 2017.

Proksch, M., Löwe, H., and Schneebeli, M.: Density, specific surface area, and correlation length of snow measured by high-resolution penetrometry, Journal of Geophysical Research: Earth Surface, 120, 346–362, doi:10.1002/2014JF003266, 2015a.

Proksch, M., Mätzler, C., Wiesmann, A., Lemmetyinen, J., Schwank, M., Löwe, H., and Schneebeli, M.: MEMLS3&a: Microwave Emission Model of Layered Snowpacks adapted to include backscattering, Geoscientific Model Development, 8, 2611–2626, doi:10.5194/gmd-8-2611-2015, 2015b.

Pulliainen, J., Grandell, J., and Hallikainen, M.: HUT snow emission model and its applicability to snow water equivalent retrieval, IEEE Transactions on Geoscience and Remote Sensing, 37, 1378–1390, doi:10.1109/36.763302, 1999.

Rabe, B. and Geibert, W.: The Expedition PS144 of the Research Vessel POLARSTERN to the Arctic Ocean in 2024, doi:10.57738/BzPM_0794_2025, pages: 1–312 Place: Bremerhaven Publication Title: Berichte zur Polar- und Meeresforschung = Reports on polar and marine research Volume: 794, 2025.

Rahimi, R., Ebtehaj, A., Panegrossi, G., Milani, L., Ringerud, S. E., and Turk, F. J.: Vulnerability of Passive Microwave Snowfall Retrievals to Physical Properties of Snowpack: A Perspective From Dense Media Radiative Transfer Theory, IEEE Transactions on Geoscience and Remote Sensing, 60, 1–13, doi:10.1109/TGRS.2022.3184530, 2022.

Rantanen, M., Karpechko, A. Y., Lipponen, A., Nordling, K., Hyvärinen, O., Ruosteenoja, K., Vihma, T., and Laaksonen, A.: The Arctic has warmed nearly four times faster than the globe since 1979, Communications Earth & Environment, 3, 168, doi:10.1038/s43247-022-00498-3, 2022.

Reber, B., Mätzler, C., and Schanda, E.: Microwave signatures of snow crusts Modelling and measurements, International Journal of Remote Sensing, 8, 1649–1665, doi:10.1080/01431168708954805, 1987.

Risse, N.: nrisse/si-emis: Code related to: Assessing the sea ice microwave emissivity up to submillimeter waves from airborne and satellite observations (1.0.1), https://doi.org/10.5281/zenodo.11535477, 2024.

Risse, N.: Data related to: Cloud liquid water path detectability and retrieval accuracy from airborne passive microwave observations over Arctic sea ice, doi:10.5281/zenodo.15848709, 2025a.

Risse, N.: nrisse/si-clouds: Code related to: Cloud liquid water path detectability and retrieval accuracy from airborne passive microwave observations over Arctic sea ice, doi:10.5281/zenodo.17064296, 2025b.

Risse, N., Mech, M., and Crewell, S.: Sea ice microwave emissivity observed from the Polar 5 aircraft during the airborne field campaigns ACLOUD and AFLUX, https://doi.pangaea.de/10.1594/PANGAEA.965569, 2024a.

Risse, N., Mech, M., Prigent, C., Spreen, G., and Crewell, S.: Assessing sea ice microwave emissivity up to submillimeter waves from airborne and satellite observations, The Cryosphere, 18, 4137–4163, doi:10.5194/tc-18-4137-2024, 2024b.

Rivoire, L., Marty, R., Carrel-Billiard, T., Chambon, P., Fourrié, N., Audouin, O., Martet, M., Birman, C., Accadia, C., and Ackermann, J.: A global observing-system simulation experiment for the EPS–Sterna microwave constellation, Quarterly Journal of the Royal Meteorological Society, 150, 2991–3012, doi:https://doi.org/10.1002/qj.4747, _eprint: https://rmets.onlinelibrary.wiley.com/doi/pdf/10.1002/qj.4747, 2024.

Rodgers, C. D.: Inverse Methods for Atmospheric Sounding: Theory and Practice, vol. 2 of *Series on Atmospheric, Oceanic and Planetary Physics*, World Scientific, Singapore; River Edge, NJ, ISBN 981-281-371-3, 2000.

Rose, T., Crewell, S., Löhnert, U., and Simmer, C.: A network suitable microwave radiometer for operational monitoring of the cloudy atmosphere, Atmospheric Research, 75, 183–200, doi:10.1016/j.atmosres.2004.12.005, 2005.

Rosenburg, S., Lange, C., Jäkel, E., Schäfer, M., Ehrlich, A., and Wendisch, M.: Retrieval of snow layer and melt pond properties on Arctic sea ice from airborne imaging spectrometer observations, Atmospheric Measurement Techniques, 16, 3915–3930, doi:10.5194/amt-16-3915-2023, 2023.

Rosenkranz, P. W.: Water vapor microwave continuum absorption: A comparison of measurements and models, Radio Science, 33, 919–928, doi:10.1029/98RS01182, 1998.

Rosenkranz, P. W.: A Model for the Complex Dielectric Constant of Supercooled Liquid Water at Microwave Frequencies, IEEE Transactions on Geoscience and Remote Sensing, 53, 1387–1393, doi:10.1109/TGRS.2014.2339015, 2015.

Rostosky, P., Spreen, G., Gerland, S., Huntemann, M., and Mech, M.: Modeling the Microwave Emission of Snow on Arctic Sea Ice for Estimating the Uncertainty of Satellite Retrievals, Journal of Geophysical Research: Oceans, 125, doi:10.1029/2019JC015465, 2020.

Rousseeuw, P. J.: Silhouettes: A graphical aid to the interpretation and validation of cluster analysis, Journal of Computational and Applied Mathematics, 20, 53–65, doi:10.1016/0377-0427(87)90125-7, 1987.

Royer, A., Roy, A., Montpetit, B., Saint-Jean-Rondeau, O., Picard, G., Brucker, L., and Langlois, A.: Comparison of commonly-used microwave radiative transfer models for snow remote sensing, Remote Sensing of Environment, 190, 247–259, doi:10.1016/j.rse.2016.12.020, 2017.

Rumelhart, D. E., Hintont, G. E., and Williams, R. J.: Learning representations by back-propagating errors, Nature, 323, 533–536, 1986.

Rückert, J., Rostosky, P., Huntemann, M., Clemens-Sewall, D., Ebell, K., Kaleschke, L., Lemmetyinen, J., Macfarlane, A., Naderpour, R., Stroeve, J., Walbröl, A., and Spreen, G.: Sea ice concentration satellite retrievals influenced by surface changes due to warm air intrusions: A case study from the MOSAiC expedition., preprint, Oceanography and Atmospheric Sciences and Meteorology, doi:10.31223/X5VW85, 2023a.

Rückert, J. E., Huntemann, M., Tonboe, R. T., and Spreen, G.: Modeling Snow and Ice Microwave Emissions in the Arctic for a Multi-Parameter Retrieval of Surface and Atmospheric Variables From Microwave Radiometer Satellite Data, Earth and Space Science, 10, e2023EA003 177, doi:10.1029/2023EA003177, 2023b.

Rückert, J. E., Walbröl, A., Risse, N., Krobot, P., Haseneder-Lind, R., Mech, M., Ebell, K., and Spreen, G.: Microwave sea ice and ocean brightness temperature and emissivity between 22 and 243 GHz from ship-based radiometers, Annals of Glaciology, 66, e8, doi:10.1017/aog.2025.1, 2025.

Sandells, M., Lowe, H., Picard, G., Dumont, M., Essery, R., Floury, N., Kontu, A., Lemmetyinen, J., Maslanka, W., Morin, S., Wiesmann, A., and Matzler, C.: X-Ray Tomography-Based Microstructure Representation in the Snow Microwave Radiative Transfer Model, IEEE Transactions on Geoscience and Remote Sensing, 60, 1–15, doi:10.1109/TGRS.2021.3086412, 2022.

Sandells, M., Rutter, N., Wivell, K., Essery, R., Fox, S., Harlow, C., Picard, G., Roy, A., Royer, A., and Toose, P.: Simulation of Arctic snow microwave emission in surface-sensitive atmosphere channels, The Cryosphere, 18, 3971–3990, doi:10.5194/tc-18-3971-2024, 2024.

Sandells, M., Mätzler, C., Arduini, G., Gélis, I. d., English, S., Kern, S., Lee, S.-M., Macfarlane, A. R., Meloche, J., Picard, G., Prigent, C., Rückert, J., Spreen, G., Tonboe, R., Vuyovich, C., and Weng, F.: Snow and Sea Ice Reference-Quality Emission and Backscatter Modeling, Bulletin of the American Meteorological Society, 106, E1972 – E1980, doi:10.1175/BAMS-D-25-0148.1, place: Boston MA, USA Publisher: American Meteorological Society, 2025.

Sandven, S., Spreen, G., Heygster, G., Girard-Ardhuin, F., Farrell, S. L., Dierking, W., and Allard, R. A.: Sea Ice Remote Sensing—Recent Developments in Methods and Climate Data Sets, Surveys in Geophysics, 44, 1653–1689, doi:10.1007/s10712-023-09781-0, 2023.

Saunders, R., Hocking, J., Turner, E., Rayer, P., Rundle, D., Brunel, P., Vidot, J., Roquet, P., Matricardi, M., Geer, A., Bormann, N., and Lupu, C.: An update on the RTTOV fast radiative transfer model (currently at version 12), Geoscientific Model Development, 11, 2717–2737, doi:10.5194/gmd-11-2717-2018, 2018.

Scarlat, R. C., Heygster, G., and Pedersen, L. T.: Experiences With an Optimal Estimation Algorithm for Surface and Atmospheric Parameter Retrieval From Passive Microwave Data in the Arctic, IEEE Journal of Selected Topics in Applied Earth Observations and Remote Sensing, 10, 3934–3947, doi:10.1109/JSTARS.2017.2739858, 2017.

Scarlat, R. C., Spreen, G., Heygster, G., Huntemann, M., Paţilea, C., Pedersen, L. T., and Saldo, R.: Sea Ice and Atmospheric Parameter Retrieval From Satellite Microwave Radiometers: Synergy of AMSR2 and SMOS Compared With the CIMR Candidate Mission, Journal of Geophysical Research: Oceans, 125, doi:10.1029/2019JC015749, 2020.

Schemann, V. and Ebell, K.: Simulation of mixed-phase clouds with the ICON large-eddy model in the complex Arctic environment around Ny-Ålesund, Atmospheric Chemistry and Physics, 20, 475–485, doi:10.5194/acp-20-475-2020, 2020.

Schirmacher, I., Kollias, P., Lamer, K., Mech, M., Pfitzenmaier, L., Wendisch, M., and Crewell, S.: Assessing Arctic low-level clouds and precipitation from above – a radar perspective, Atmospheric Measurement Techniques, 16, 4081–4100, doi:10.5194/amt-16-4081-2023, 2023.

Schäfer, M., Wolf, K., Ehrlich, A., Hallbauer, C., Jäkel, E., Jansen, F., Luebke, A. E., Müller, J., Thoböll, J., Röschenthaler, T., Stevens, B., and Wendisch, M.: VELOX – a new thermal infrared imager for airborne remote sensing of cloud and surface properties, Atmospheric Measurement Techniques, 15, 1491–1509, doi:10.5194/amt-15-1491-2022, 2022.

Schäfer, M., Rosenburg, S., Ehrlich, A., Röttenbacher, J., and Wendisch, M.: Two-dimensional cloud-top and surface brightness temperature at spectral band BT3 (10.74 +/- 0.39 µm) with 1 Hz temporal resolution de-

rived at flight altitude from VELOX during the HALO-(AC)³ field campaign, doi:10.1594/PANGAEA.963382, 2023a.

Schäfer, M., Rosenburg, S., Ehrlich, A., Röttenbacher, J., and Wendisch, M.: Two-dimensional cloud-top and surface brightness temperature with 1 Hz temporal resolution derived at flight altitude from VELOX during the HALO-(AC)³ field campaign, doi:10.1594/PANGAEA.963401, type: dataset publication series, 2023b.

Schäfer, M., Rosenburg, S., Ehrlich, A., Röttenbacher, J., and Wendisch, M.: One-dimensional cloud-top or surface brightness temperature with 20 Hz temporal resolution derived at flight altitude from VELOX-KT19 during the HALO-(AC)³ field campaign, doi:10.1594/PANGAEA.967378, 2024.

Screen, J. A. and Simmonds, I.: The central role of diminishing sea ice in recent Arctic temperature amplification, Nature, 464, 1334–1337, doi:10.1038/nature09051, 2010.

Screen, J. A., Deser, C., and Simmonds, I.: Local and remote controls on observed Arctic warming, Geophysical Research Letters, 39, 2012GL051 598, doi:10.1029/2012GL051598, 2012.

Serreze, M. C. and Francis, J. A.: The Arctic Amplification Debate, Climatic Change, 76, 241–264, doi:10.1007/s10584-005-9017-y, 2006.

Serreze, M. C., Barrett, A. P., Stroeve, J. C., Kindig, D. N., and Holland, M. M.: The emergence of surface-based Arctic amplification, The Cryosphere, 2009.

Shokr, M.: Field observations and model calculations of dielectric properties of Arctic sea ice in the microwave C-band, IEEE Transactions on Geoscience and Remote Sensing, 36, 463–478, doi:10.1109/36.662730, 1998.

Shokr, M., Asmus, K., and Agnew, T.: Microwave Emission Observations from Artificial Thin Sea Ice: The Ice-Tank Experiment, IEEE Transactions on Geoscience and Remote Sensing, 47, 325–338, doi:10.1109/TGRS.2008.2005585, 2009.

Shupe, M. D.: A ground-based multisensor cloud phase classifier, Geophysical Research Letters, 34, 2007GL031 008, doi:10.1029/2007GL031008, 2007.

Shupe, M. D. and Intrieri, J. M.: Cloud Radiative Forcing of the Arctic Surface: The Influence of Cloud Properties, Surface Albedo, and Solar Zenith Angle, Journal of Climate, 17, 616–628, doi:10.1175/1520-0442(2004)017<0616:CRFOTA>2.0.CO;2, 2004.

Shupe, M. D., Walden, V. P., Eloranta, E., Uttal, T., Campbell, J. R., Starkweather, S. M., and Shiobara, M.: Clouds at Arctic Atmospheric Observatories. Part I: Occurrence and Macrophysical Properties, Journal of Applied Meteorology and Climatology, 50, 626–644, doi:10.1175/2010JAMC2467.1, 2011.

Shupe, M. D., Turner, D. D., Zwink, A., Thieman, M. M., Mlawer, E. J., and Shippert, T.: Deriving Arctic Cloud Microphysics at Barrow, Alaska: Algorithms, Results, and Radiative Closure, Journal of Applied Meteorology and Climatology, 54, 1675–1689, doi:10.1175/JAMC-D-15-0054.1, 2015.

Sledd, A., Shupe, M. D., Solomon, A., and Cox, C. J.: Surface Energy Balance Responses to Radiative Forcing in the Central Arctic From MOSAiC and Models, Journal of Geophysical Research: Atmospheres, 130, e2024JD042 578, doi:10.1029/2024JD042578, 2025.

Smith, A., Jahn, A., Burgard, C., and Notz, D.: Improving model-satellite comparisons of sea ice melt onset with a satellite simulator, The Cryosphere, 16, 3235–3248, doi:10.5194/tc-16-3235-2022, 2022.

Soriot, C., Picard, G., Prigent, C., Frappart, F., and Domine, F.: Year-round sea ice and snow characterization from combined passive and active microwave observations and radiative transfer modeling, Remote Sensing of Environment, 278, 113 061, doi:10.1016/j.rse.2022.113061, 2022.

Soriot, C., Prigent, C., Jimenez, C., and Frappart, F.: Arctic Sea Ice Thickness Estimation From Passive Microwave Satellite Observations Between 1.4 and 36 GHz, Earth and Space Science, 10, doi:10.1029/2022EA002542, 2023.

Soriot, C., Vancoppenolle, M., Prigent, C., Jimenez, C., and Frappart, F.: Winter arctic sea ice volume decline: uncertainties reduced using passive microwave-based sea ice thickness, Scientific Reports, 14, 21 000, doi:10.1038/s41598-024-70136-9, 2024.

Spreen, G., Kaleschke, L., and Heygster, G.: Sea ice remote sensing using AMSR-E 89-GHz channels, Journal of Geophysical Research, 113, C02S03, doi:10.1029/2005JC003384, 2008.

Stapf, J., Ehrlich, A., Jäkel, E., and Wendisch, M.: Aircraft measurements of broadband irradiance during the ACLOUD campaign in 2017, doi:10.1594/PANGAEA.900442, type: data set, 2019.

Stapf, J., Ehrlich, A., and Wendisch, M.: Aircraft measurements of broadband irradiance during the AFLUX campaign in 2019, doi:10.1594/PANGAEA.932020, 2021.

Stephens, G. L., Vane, D. G., Boain, R. J., Mace, G. G., Sassen, K., Wang, Z., Illingworth, A. J., O'connor, E. J., Rossow, W. B., Durden, S. L., Miller, S. D., Austin, R. T., Benedetti, A., Mitrescu, C., and the CloudSat Science Team: THE CLOUDSAT MISSION AND THE A-TRAIN: A New Dimension of Space-Based Observations of Clouds and Precipitation, Bulletin of the American Meteorological Society, 83, 1771–1790, doi:10.1175/BAMS-83-12-1771, 2002.

Stephens, G. L., Vane, D. G., Tanelli, S., Im, E., Durden, S., Rokey, M., Reinke, D., Partain, P., Mace, G. G., Austin, R., L'Ecuyer, T., Haynes, J., Lebsock, M., Suzuki, K., Waliser, D., Wu, D., Kay, J., Gettelman, A., Wang, Z., and Marchand, R.: CloudSat mission: Performance and early science after the first year of operation, Journal of Geophysical Research: Atmospheres, 113, 2008JD009 982, doi:10.1029/2008JD009982, 2008.

Stevens, B., Ament, F., Bony, S., Crewell, S., Ewald, F., Gross, S., Hansen, A., Hirsch, L., Jacob, M., Kölling, T., Konow, H., Mayer, B., Wendisch, M., Wirth, M., Wolf, K., Bakan, S., Bauer-Pfundstein, M., Brueck, M., Delanoë, J., Ehrlich, A., Farrell, D., Forde, M., Gödde, F., Grob, H., Hagen, M., Jäkel, E., Jansen, F., Klepp, C., Klingebiel, M., Mech, M., Peters, G., Rapp, M., Wing, A. A., and Zinner, T.: A High-Altitude Long-Range Aircraft Configured as a Cloud Observatory: The NARVAL Expeditions, Bulletin of the American Meteorological Society, 100, 1061–1077, doi:10.1175/BAMS-D-18-0198.1, 2019.

Stogryn, A. and Desargant, G.: The dielectric properties of brine in sea ice at microwave frequencies, IEEE Transactions on Antennas and Propagation, 33, 523–532, doi:10.1109/TAP.1985.1143610, 1985.

Stramler, K., Del Genio, A. D., and Rossow, W. B.: Synoptically Driven Arctic Winter States, Journal of Climate, 24, 1747–1762, doi:10.1175/2010JCLI3817.1, 2011.

Stroeve, J., Holland, M. M., Meier, W., Scambos, T., and Serreze, M.: Arctic sea ice decline: Faster than forecast, Geophysical Research Letters, 34, 2007GL029 703, doi:10.1029/2007GL029703, 2007.

Stroeve, J., Nandan, V., Willatt, R., Dadic, R., Rostosky, P., Gallagher, M., Mallett, R., Barrett, A., Hendricks, S., Tonboe, R., McCrystall, M., Serreze, M., Thielke, L., Spreen, G., Newman, T., Yackel, J., Ricker, R., Tsamados, M., Macfarlane, A., Hannula, H.-R., and Schneebeli, M.: Rain on snow (ROS) understudied in sea ice remote sensing: a multi-sensor analysis of ROS dur-

ing MOSAiC (Multidisciplinary drifting Observatory for the Study of Arctic Climate), The Cryosphere, 16, 4223–4250, doi:10.5194/tc-16-4223-2022, 2022.

Stroeve, J. C., Markus, T., Boisvert, L., Miller, J., and Barrett, A.: Changes in Arctic melt season and implications for sea ice loss, Geophysical Research Letters, 41, 1216–1225, doi:10.1002/2013gl058951, publisher: American Geophysical Union (AGU), 2014.

Sweeney, A. J., Fu, Q., Po-Chedley, S., Wang, H., and Wang, M.: Internal Variability Increased Arctic Amplification During 1980–2022, Geophysical Research Letters, 50, e2023GL106 060, doi:10.1029/2023GL106060, 2023.

Tan, I., Sotiropoulou, G., Taylor, P. C., Zamora, L., and Wendisch, M.: A Review of the Factors Influencing Arctic Mixed-Phase Clouds: Progress and Outlook, doi:10.1002/essoar.10508308.1, 2021.

Tan, S., Aksoy, M., Brogioni, M., Macelloni, G., Durand, M., Jezek, K. C., Wang, T.-L., Tsang, L., Johnson, J. T., Drinkwater, M. R., and Brucker, L.: Physical Models of Layered Polar Firn Brightness Temperatures From 0.5 to 2 GHz, IEEE Journal of Selected Topics in Applied Earth Observations and Remote Sensing, 8, 3681–3691, doi:10.1109/JSTARS.2015.2403286, 2015.

Thielke, L., Huntemann, M., Hendricks, S., Jutila, A., Ricker, R., and Spreen, G.: Sea ice surface temperatures from helicopter-borne thermal infrared imaging during the MOSAiC expedition, Scientific Data, 9, 364, doi:10.1038/s41597-022-01461-9, 2022.

Thorndike, R. L.: Who belongs in the family?, Psychometrika, 18, 267–276, doi:10.1007/BF02289263, 1953.

Tian-Kunze, X., Kaleschke, L., Maaß, N., Mäkynen, M., Serra, N., Drusch, M., and Krumpen, T.: SMOS-derived thin sea ice thickness: algorithm baseline, product specifications and initial verification, The Cryosphere, 8, 997–1018, doi:10.5194/tc-8-997-2014, 2014.

Timco, G. and Frederking, R.: A review of sea ice density, Cold Regions Science and Technology, 24, 1–6, doi:10.1016/0165-232X(95)00007-X, 1996.

Tjernström, M. and Graversen, R. G.: The vertical structure of the lower Arctic troposphere analysed from observations and the ERA-40 reanalysis, Quarterly Journal of the Royal Meteorological Society, 135, 431–443, doi:10.1002/qj.380, 2009.

Tonboe, R. T.: The simulated sea ice thermal microwave emission at window and sounding frequencies, Tellus A, 62, 333–344, doi:10.1111/j.1600-0870.2010.00434.x, 2010.

Tonboe, R. T., Heygster, G., Pedersen, L. T., and Andersen, S.: Sea ice emission modelling, in: Thermal Microwave Radiation: Applications for Remote Sensing, edited by Mätzler, C., Electromagnetic Waves, pp. 382–400, Institution of Engineering and Technology, 2006.

Tonboe, R. T., Dybkjær, G., and Høyer, J. L.: Simulations of the snow covered sea ice surface temperature and microwave effective temperature, Tellus A: Dynamic Meteorology and Oceanography, 63, 1028–1037, doi:10.1111/j.1600-0870.2011.00530.x, 2011.

Torquato, S. and Kim, J.: Nonlocal Effective Electromagnetic Wave Characteristics of Composite Media: Beyond the Quasistatic Regime, Physical Review X, 11, 021 002, doi:10.1103/PhysRevX.11.021002, 2021.

Triana-Gómez, A. M., Heygster, G., Melsheimer, C., Spreen, G., Negusini, M., and Petkov, B. H.: Improved water vapour retrieval from AMSU-B and MHS in the Arctic, Atmospheric Measurement Techniques, 13, 3697–3715, doi:10.5194/amt-13-3697-2020, 2020.

Tsang, L., Chen, C., Chang, A. T. C., Guo, J., and Ding, K.: Dense media radiative transfer theory based on quasicrystalline approximation with applications to passive microwave remote sensing of snow, Radio Science, 35, 731–749, doi:10.1029/1999RS002270, 2000.

Tsang, L., Pan, J., Liang, D., Li, Z., and Cline, D.: Modeling Active Microwave Remote Sensing of Snow using Dense Media Radiative Transfer (DMRT) Theory with Multiple Scattering Effects, in: 2006 IEEE International Symposium on Geoscience and Remote Sensing, pp. 477–480, IEEE, Denver, CO, USA, ISBN 978-0-7803-9510-7, doi:10.1109/IGARSS.2006.127, 2006.

Tschudi, M., Meier, W. N., Stewart, J. S., Fowler, C., and Maslanik, J.: Polar Pathfinder Daily 25 km EASE-Grid Sea Ice Motion Vectors, doi:10.5067/INAWUWO7QH7B, 2019.

Tschudi, M. A., Meier, W. N., and Stewart, J. S.: An enhancement to sea ice motion and age products at the National Snow and Ice Data Center (NSIDC), The Cryosphere, 14, 1519–1536, doi:10.5194/tc-14-1519-2020, 2020.

Tucker, W. B., Grenfell, T. C., Onstott, R. G., Perovich, D. K., Gow, A. J., Snuchman, R. A., and Sutherland, L. L.: Microwave and physical properties of sea ice in the winter Marginal Ice Zone, Journal of Geophysical Research, 96, 4573, doi:10.1029/90JC02269, 1991.

Turner, D., Cadeddu, M., Lohnert, U., Crewell, S., and Vogelmann, A.: Modifications to the Water Vapor Continuum in the Microwave Suggested by Ground-Based 150-GHz Observations, IEEE Transactions on Geoscience and Remote Sensing, 47, 3326–3337, doi:10.1109/TGRS.2009.2022262, 2009.

Turner, D. D., Vogelmann, A. M., Austin, R. T., Barnard, J. C., Cady-Pereira, K., Chiu, J. C., Clough, S. A., Flynn, C., Khaiyer, M. M., Liljegren, J., Johnson, K., Lin, B., Long, C., Marshak, A., Matrosov, S. Y., McFarlane, S. A., Miller, M., Min, Q., Minimis, P., O'Hirok, W., Wang, Z., and Wiscombe, W.: Thin Liquid Water Clouds: Their Importance and Our Challenge, Bulletin of the American Meteorological Society, 88, 177–190, doi:10.1175/BAMS-88-2-177, 2007.

Turner, D. D., Kneifel, S., and Cadeddu, M. P.: An Improved Liquid Water Absorption Model at Microwave Frequencies for Supercooled Liquid Water Clouds, Journal of Atmospheric and Oceanic Technology, 33, 33–44, doi:10.1175/JTECH-D-15-0074.1, 2016.

UK Met Office: GHRSST Level 4 OSTIA Global Foundation Sea Surface Temperature Analysis (GDS version 2), https://doi.org/10.5067/GHOST-4FK02, 2012.

UK Met Office: Cartopy: A cartographic python library with Matplotlib support, http://scitools.org.uk/cartopy/docs/latest/, 2023.

Ulaby, F. T., Moore, R. K., and Fung, A.: Microwave remote sensing, active and passive, Artech House Inc., Norwood, MA, USA, ISBN 0 89006 192 0, 1986.

Untersteiner, N.: Natural desalination and equilibrium salinity profile of perennial sea ice, Journal of Geophysical Research, 73, 1251–1257, doi:10.1029/JB073i004p01251, 1968.

Vaisala: Vaisala Dropsonde RD94, https://www.vaisala.com/sites/default/files/documents/RD94-Dropsonde-Datasheet-B210936EN-A-LoRes.pdf, 2010.

Vant, M. R., Ramseier, R. O., and Makios, V.: The complex-dielectric constant of sea ice at frequencies in the range 0.1–40 GHz, Journal of Applied Physics, 49, 1264–1280, doi:10.1063/1.325018, 1978.

Vargel, C., Royer, A., St-Jean-Rondeau, O., Picard, G., Roy, A., Sasseville, V., and Langlois, A.: Arctic and subarctic snow microstructure analysis for microwave brightness temperature simulations, Remote Sensing of Environment, 242, 111 754, doi:10.1016/j.rse.2020.111754, 2020.

Virtanen, P., Gommers, R., Oliphant, T. E., Haberland, M., Reddy, T., Cournapeau, D., Burovski, E., Peterson, P., Weckesser, W., Bright, J., Van Der Walt, S. J., Brett, M., Wilson, J., Millman, K. J., Mayorov, N., Nelson, A. R. J., Jones, E., Kern, R., Larson, E., Carey, C. J., Polat, I., Feng, Y., Moore, E. W., VanderPlas, J., Laxalde, D., Perktold, J., Cimrman, R., Henriksen, I., Quintero, E. A., Harris, C. R., Archibald, A. M., Ribeiro, A. H., Pedregosa, F., Van Mulbregt, P., SciPy 1.0 Contributors, Vijaykumar, A., Bardelli, A. P., Rothberg, A., Hilboll, A., Kloeckner, A., Scopatz, A., Lee, A., Rokem, A., Woods, C. N., Fulton, C., Masson, C., Häggström, C., Fitzgerald, C., Nicholson, D. A., Hagen, D. R., Pasechnik, D. V., Olivetti, E., Martin, E., Wieser, E., Silva, F., Lenders, F., Wilhelm, F., Young, G., Price, G. A., Ingold, G.-L., Allen, G. E., Lee, G. R., Audren, H., Probst, I., Dietrich, J. P., Silterra, J., Webber, J. T., Slavič, J., Nothman, J., Buchner, J., Kulick, J., Schönberger, J. L., De Miranda Cardoso, J. V., Reimer, J., Harrington, J., Rodríguez, J. L. C., Nunez-Iglesias, J., Kuczynski, J., Tritz, K., Thoma, M., Newville, M., Kümmerer, M., Bolingbroke, M., Tartre, M., Pak, M., Smith, N. J., Nowaczyk, N., Shebanov, N., Pavlyk, O., Brodtkorb, P. A., Lee, P., McGibbon, R. T., Feldbauer, R., Lewis, S., Tygier, S., Sievert, S., Vigna, S., Peterson, S., More, S., Pudlik, T., Oshima, T., Pingel, T. J., Robitaille, T. P., Spura, T., Jones, T. R., Cera, T., Leslie, T., Zito, T., Krauss, T., Upadhyay, U., Halchenko, Y. O., and Vázquez-Baeza, Y.: SciPy 1.0: fundamental algorithms for scientific computing in Python, Nature Methods, 17, 261–272, doi:10.1038/s41592-019-0686-2, 2020.

Voss, S., Heygster, G., and Ezraty, R.: Improving sea ice type discrimination by the simultaneous use of SSM/I and scatterometer data, Polar Research, 22, 35–42, 2003.

Vuyovich, C. M., Jacobs, J. M., Hiemstra, C. A., and Deeb, E. J.: Effect of spatial variability of wet snow on modeled and observed microwave emissions, Remote Sensing of Environment, 198, 310–320, doi:10.1016/j.rse.2017.06.016, 2017.

Walbröl, A., Crewell, S., Engelmann, R., Orlandi, E., Griesche, H., Radenz, M., Hofer, J., Althausen, D., Maturilli, M., and Ebell, K.: Atmospheric temperature, water vapour and liquid water path from two microwave radiometers during MOSAiC, Scientific Data, 9, 534, doi:10.1038/s41597-022-01504-1, 2022.

Walbröl, A., Michaelis, J., Becker, S., Dorff, H., Ebell, K., Gorodetskaya, I., Heinold, B., Kirbus, B., Lauer, M., Maherndl, N., Maturilli, M., Mayer, J., Müller, H., Neggers, R. A. J., Paulus, F. M., Röttenbacher, J., Rückert, J. E., Schirmacher, I., Slättberg, N., Ehrlich, A., Wendisch, M., and Crewell, S.: Contrasting extremely warm and long-lasting cold air anomalies in the North Atlantic sector of the Arctic during the HALO-(AC)^3 campaign, Atmospheric Chemistry and Physics, 24, 8007–8029, doi:10.5194/acp-24-8007-2024, 2024.

Wang, D., Prigent, C., Aires, F., and Jimenez, C.: A Statistical Retrieval of Cloud Parameters for the Millimeter Wave Ice Cloud Imager on Board MetOp-SG, IEEE Access, 5, 4057–4076, doi:10.1109/ACCESS.2016.2625742, 2017a.

Wang, D., Prigent, C., Kilic, L., Fox, S., Harlow, C., Jimenez, C., Aires, F., Grassotti, C., and Karbou, F.: Surface Emissivity at Microwaves to Millimeter Waves over Polar Regions: Parameterization and Evaluation with Aircraft Experiments, Journal of Atmospheric and Oceanic Technology, 34, 1039–1059, doi:10.1175/JTECH-D-16-0188.1, 2017b.

Wang, L., Wolken, G. J., Sharp, M. J., Howell, S. E. L., Derksen, C., Brown, R. D., Markus, T., and Cole, J.: Integrated pan-Arctic melt onset detection from satellite active and passive microwave measurements, 2000-2009: INTEGRATED PAN-ARCTIC MELT ONSET, Journal of Geophysical Research: Atmospheres, 116, n/a–n/a, doi:10.1029/2011JD016256, 2011.

Wang, M. and Overland, J. E.: A sea ice free summer Arctic within 30 years: An update from CMIP5 models, Geophysical Research Letters, 39, 2012GL052 868, doi:10.1029/2012GL052868, 2012.

Warmerdam, F.: The Geospatial Data Abstraction Library, in: Open Source Approaches in Spatial Data Handling, edited by Hall, G. B. and Leahy, M. G., pp. 87–104, Springer Berlin Heidelberg, Berlin, Heidelberg, ISBN 978-3-540-74831-1, doi:10.1007/978-3-540-74831-1_5, 2008.

Warren, S. G.: Optical properties of snow, Reviews of Geophysics, 20, 67–89, doi:10.1029/RG020i001p00067, 1982.

Warren, S. G., Rigor, I. G., Untersteiner, N., Radionov, V. F., Bryazgin, N. N., Aleksandrov, Y. I., and Colony, R.: Snow Depth on Arctic Sea Ice, Journal of Climate, 12, 1814–1829, doi:10.1175/1520-0442(1999)012<1814:SDOASI>2.0.CO;2, 1999.

Waskom, M.: seaborn: statistical data visualization, doi:10.5281/zenodo.4645478, 2021.

Weber, A., Kölling, T., Pörtge, V., Baumgartner, A., Rammeloo, C., Zinner, T., and Mayer, B.: Polarization upgrade of specMACS: calibration and characterization of the 2D RGB polarization-resolving cameras, Atmospheric Measurement Techniques, 17, 1419–1439, doi:10.5194/amt-17-1419-2024, 2024a.

Weber, A., Pörtge, V., Zinner, T., and Mayer, B.: Spectral radiance measurements with the hyperspectral and polarized imaging system specMACS during the HALO-(AC)³ field campaign, doi:10.1594/PANGAEA.966992, 2024b.

Wehr, T., Kubota, T., Tzeremes, G., Wallace, K., Nakatsuka, H., Ohno, Y., Koopman, R., Rusli, S., Kikuchi, M., Eisinger, M., Tanaka, T., Taga, M., Deghaye, P., Tomita, E., and Bernaerts, D.: The EarthCARE mission – science and system overview, Atmospheric Measurement Techniques, 16, 3581–3608, doi:10.5194/amt-16-3581-2023, 2023.

Wendisch, M., Macke, A., Ehrlich, A., Lüpkes, C., Mech, M., Chechin, D., Dethloff, K., Velasco, C. B., Bozem, H., Brückner, M., Clemen, H.-C., Crewell, S., Donth, T., Dupuy, R., Ebell, K., Egerer, U., Engelmann, R., Engler, C., Eppers, O., Gehrmann, M., Gong, X., Gottschalk, M., Gourbeyre, C., Griesche, H., Hartmann, J., Hartmann, M., Heinold, B., Herber, A., Herrmann, H., Heygster, G., Hoor, P., Jafariserajehlou, S., Jäkel, E., Järvinen, E., Jourdan, O., Kästner, U., Kecorius, S., Knudsen, E. M., Köllner, F., Kretzschmar, J., Lelli, L., Leroy, D., Maturilli, M., Mei, L., Mertes, S., Mioche, G., Neuber, R., Nicolaus, M., Nomokonova, T., Notholt, J., Palm, M., Pinxteren, M. v., Quaas, J., Richter, P., Ruiz-Donoso, E., Schäfer, M., Schmieder, K., Schnaiter, M., Schneider, J., Schwarzenböck, A., Seifert, P., Shupe, M. D., Siebert, H., Spreen, G., Stapf, J., Stratmann, F., Vogl, T., Welti, A., Wex, H., Wiedensohler, A., Zanatta, M., and Zeppenfeld, S.: The Arctic Cloud Puzzle: Using ACLOUD/PASCAL Multiplatform Observations to Unravel the Role of Clouds and Aerosol Particles in Arctic Amplification, Bulletin of the American Meteorological Society, 100, 841–871, doi:10.1175/BAMS-D-18-0072.1, place: Boston MA, USA Publisher: American Meteorological Society, 2019.

Wendisch, M., Handorf, D., Tegen, I., Neggers, R., and Spreen, G.: Glimpsing the Ins and Outs of the Arctic Atmospheric Cauldron, Eos, 102, doi:10.1029/2021EO155959, 2021.

Wendisch, M., Brückner, M., Crewell, S., Ehrlich, A., Notholt, J., Lüpkes, C., Macke, A., Burrows, J. P., Rinke, A., Quaas, J., Maturilli, M., Schemann, V., Shupe, M. D., Akansu, E. F., Barrientos-Velasco, C., Bärfuss, K., Blechschmidt, A.-M., Block, K., Bougoudis, I., Bozem, H., Böckmann, C., Bracher,

A., Bresson, H., Bretschneider, L., Buschmann, M., Chechin, D. G., Chylik, J., Dahlke, S., Deneke, H., Dethloff, K., Donth, T., Dorn, W., Dupuy, R., Ebell, K., Egerer, U., Engelmann, R., Eppers, O., Gerdes, R., Gierens, R., Gorodetskaya, I. V., Gottschalk, M., Griesche, H., Gryanik, V. M., Handorf, D., Harm-Altstädter, B., Hartmann, J., Hartmann, M., Heinold, B., Herber, A., Herrmann, H., Heygster, G., Höschel, I., Hofmann, Z., Hölemann, J., Hünerbein, A., Jafariserajehlou, S., Jäkel, E., Jacobi, C., Janout, M., Jansen, F., Jourdan, O., Jurányi, Z., Kalesse-Los, H., Kanzow, T., Käthner, R., Kliesch, L. L., Klingebiel, M., Knudsen, E. M., Kovács, T., Körtke, W., Krampe, D., Kretzschmar, J., Kreyling, D., Kulla, B., Kunkel, D., Lampert, A., Lauer, M., Lelli, L., von Lerber, A., Linke, O., Löhnert, U., Lonardi, M., Losa, S. N., Losch, M., Maahn, M., Mech, M., Mei, L., Mertes, S., Metzner, E., Mewes, D., Michaelis, J., Mioche, G., Moser, M., Nakoudi, K., Neggers, R., Neuber, R., Nomokonova, T., Oelker, J., Papakonstantinou-Presvelou, I., Pätzold, F., Pefanis, V., Pohl, C., van Pinxteren, M., Radovan, A., Rhein, M., Rex, M., Richter, A., Risse, N., Ritter, C., Rostosky, P., Rozanov, V. V., Donoso, E. R., Saavedra Garfias, P., Salzmann, M., Schacht, J., Schäfer, M., Schneider, J., Schnierstein, N., Seifert, P., Seo, S., Siebert, H., Soppa, M. A., Spreen, G., Stachlewska, I. S., Stapf, J., Stratmann, F., Tegen, I., Viceto, C., Voigt, C., Vountas, M., Walbröl, A., Walter, M., Wehner, B., Wex, H., Willmes, S., Zanatta, M., and Zeppenfeld, S.: Atmospheric and Surface Processes, and Feedback Mechanisms Determining Arctic Amplification: A Review of First Results and Prospects of the (AC)3 Project, Bulletin of the American Meteorological Society, 104, E208–E242, doi:10.1175/BAMS-D-21-0218.1, 2023.

Wendisch, M., Crewell, S., Ehrlich, A., Herber, A., Kirbus, B., Lüpkes, C., Mech, M., Abel, S. J., Akansu, E. F., Ament, F., Aubry, C., Becker, S., Borrmann, S., Bozem, H., Brückner, M., Clemen, H.-C., Dahlke, S., Dekoutsidis, G., Delanoë, J., De La Torre Castro, E., Dorff, H., Dupuy, R., Eppers, O., Ewald, F., George, G., Gorodetskaya, I. V., Grawe, S., Groß, S., Hartmann, J., Henning, S., Hirsch, L., Jäkel, E., Joppe, P., Jourdan, O., Jurányi, Z., Karalis, M., Kellermann, M., Klingebiel, M., Lonardi, M., Lucke, J., Luebke, A., Maahn, M., Maherndl, N., Maturilli, M., Mayer, B., Mayer, J., Mertes, S., Michaelis, J., Michalkov, M., Mioche, G., Moser, M., Müller, H., Neggers, R., Ori, D., Paul, D., Paulus, F., Pilz, C., Pithan, F., Pöhlker, M., Pörtge, V., Ringel, M., Risse, N., Roberts, G. C., Rosenburg, S., Röttenbacher, J., Rückert, J., Schäfer, M., Schäfer, J., Schemannn, V., Schirmacher, I., Schmidt, J., Schmidt, S., Schneider, J., Schnitt, S., Schwarz, A., Siebert, H., Sodemann, H., Sperzel, T., Spreen, G., Stevens, B., Stratmann, F., Svensson, G., Tatzelt, C., Tuch, T., Vihma,

T., Voigt, C., Volkmer, L., Walbröl, A., Weber, A., Wehner, B., Wetzel, B., Wirth, M., and Zinner, T.: Overview: Quasi-Lagrangian observations of Arctic air mass transformations – Introduction and initial results of the HALO–(AC)^3 aircraft campaign, doi:10.5194/egusphere-2024-783, 2024.

Wentz, F. J. and Meissner, T.: Algorithm theoretical basis document: AMSR ocean algorithm, version 2, Technical Report 121599A-1, Remote Sensing Systems, Santa Rosa, CA, USA, https://eospso.gsfc.nasa.gov/sites/default/files/atbd/atbd-amsr-ocean.pdf, 2000.

Wesche, C., Steinhage, D., and Nixdorf, U.: Polar aircraft Polar5 and Polar6 operated by the Alfred Wegener Institute, Journal of large-scale research facilities JLSRF, 2, A87, doi:10.17815/jlsrf-2-153, 2016.

Westwater, E. R., Han, Y., Shupe, M. D., and Matrosov, S. Y.: Analysis of integrated cloud liquid and precipitable water vapor retrievals from microwave radiometers during the Surface Heat Budget of the Arctic Ocean project, Journal of Geophysical Research: Atmospheres, 106, 32 019–32 030, doi:10.1029/2000JD000055, 2001.

Wiesmann, A. and Mätzler, C.: Microwave Emission Model of Layered Snowpacks, Remote Sensing of Environment, 70, 307–316, doi:10.1016/S0034-4257(99)00046-2, 1999.

Wiesmann, A., Mätzler, C., and Weise, T.: Radiometric and structural measurements of snow samples, Radio Science, 33, 273–289, doi:10.1029/97RS02746, 1998.

Wirth, M. and Groß, S.: Aircraft measurements of backscatter ratio, particle depolarization and water vapour molecular density profiles over Arctic sea ice and ocean during the HALO-(AC)^3 campaign in spring 2022, doi:10.1594/PANGAEA.967086, 2024.

Wirth, M., Fix, A., Mahnke, P., Schwarzer, H., Schrandt, F., and Ehret, G.: The airborne multi-wavelength water vapor differential absorption lidar WALES: system design and performance, Applied Physics B, 96, 201–213, doi:10.1007/s00340-009-3365-7, 2009.

Wivell, K., Fox, S., Sandells, M., Harlow, C., Essery, R., and Rutter, N.: Evaluating Snow Microwave Radiative Transfer (SMRT) model emissivities with 89 to 243 GHz observations of Arctic tundra snow, The Cryosphere, 17, 4325–4341, doi:10.5194/tc-17-4325-2023, 2023.

WMO: WMO sea ice nomenclature, terminology, codes and illustrated glossary, Tech. Rep. WMO-No. 259, Secretariat WMO, Geneva, https://library.wmo.int/idurl/4/41953, 2014.

Xie, X., Crewell, S., Löhnert, U., Simmer, C., and Miao, J.: Polarization signatures and brightness temperatures caused by horizontally oriented snow particles at microwave bands: Effects of atmospheric absorption, Journal of Geophysical Research: Atmospheres, 120, 6145–6160, doi:10.1002/2015JD023158, 2015.

Yamashita, R., Nishio, M., Do, R. K. G., and Togashi, K.: Convolutional neural networks: an overview and application in radiology, Insights into Imaging, 9, 611–629, doi:10.1007/s13244-018-0639-9, 2018.

Zhou, W., Leung, L. R., and Lu, J.: Steady threefold Arctic amplification of externally forced warming masked by natural variability, Nature Geoscience, 17, 508–515, doi:10.1038/s41561-024-01441-1, 2024.

Ólason, E., Boutin, G., Williams, T., Korosov, A., Regan, H., Rheinlænder, J., Rampal, P., Flocco, D., Samaké, A., Davy, R., Spain, T., and Chua, S.: The next generation sea-ice model neXtSIM, version 2, doi:10.5194/egusphere-2024-3521, 2025.

Acknowledgements

I would like to thank my supervisor, Prof. Dr. Susanne Crewell, for the detailed scientific input throughout this journey and for providing me with the opportunity to study this exciting topic. Your expertise and guidance allowed me to explore my own ideas with curiosity and independence.

I would like to extend my gratitude to Dr. Mario Mech for his endless support. Your dedication to managing complex field campaigns and collecting novel observations was essential for this thesis. I also want to thank you for providing me with the opportunity to join several field campaigns. Your welcoming nature made work both in the field and in the office enjoyable and rewarding.

I extend my sincere gratitude to Dr. Catherine Prigent, who agreed to join my thesis advisory committee, for stimulating insightful discussions during every meeting. Your expertise on the surface microwave signature at global scales helped to connect the small-scale field observations with larger features.

I further thank Prof. Dr. Ghislain Picard for agreeing to be one of the examiners of this thesis and Prof. Dr. Christian Sohler for accepting to lead the examination committee.

I would like to thank Prof. Dr. Manfred Wendisch and everybody involved for orchestrating the $(\mathcal{AC})^3$ project. Engaging in this community over the past years was truly inspiring.

To Dr. Dwaipayan Chatterjee and Dr. Christoph Böhm for our thoughtful and often humorous chats about and beyond science. I learned a lot from you, and your invaluable support allowed me to solve challenges in a fun way. The idea for the machine learning application in Chapter 4 is an outcome of the countless discussions with DC and Christoph.

I would also like to heartily thank my office mate, Dr. Andreas Walbröl. It was great working with you and receiving detailed feedback and suggestions by simply turning around my screen. You also helped me to settle in Cologne, for which I am very thankful. Moreover, Andreas' meticulous work ensured high-quality atmospheric profiles used in Chapter 4.

I extend a special thanks to Pavel Krobot for his dedication to ensuring successful field observations. Pavel designed and implemented the novel radiometer setup for R/V *Polarstern*. Thank you for the enjoyable and uplifting times we shared during field work and lunch.

A heartfelt thank you goes to Dagmar Janzen, who provides the most generous support in any administrative tasks. Dagmar always helped me very quickly with any question or form that needed to be processed.

A big thank you goes to everyone who was involved in the AWARES working

group and Arctic subgroup during the past years. Our regular scientific exchange provided a great opportunity for feedback and to learn from each other.

To the crew and technicians of the *Polar 5* aircraft, *HALO* aircraft, and R/V *Polarstern*. Collecting field data in the Arctic would be impossible without your hard work, dedication, and patience.

To open source software developers for providing a reliable and sophisticated framework to study the Earth system.

Finally, I want to thank my family for their unconditional support. And much of this would not have been possible without Suehyun.